INTEGRATION OF ROCK PHYSICS AND SEISMIC INVERSION FOR CARBONATE RESERVOIR CHARACTERIZATION

A Dissertation

by

TINGTING ZHANG

Submitted to the Office of Graduate and Professional Studies of
Texas A&M University
in partial fulfillment of the requirements for the degree of

DOCTOR OF PHILOSOPHY

Chair of Committee,	Yuefeng Sun
Committee Members,	Walter Ayers
	Micheal Pope
	Mark Everett
	Benchun Duan
Head of Department,	Rick Giardino

December 2014

Major Subject: Geophysics

ABSTRACT

Carbonate reservoir characterization based on rock physics and seismic inversion helps in better understanding the influence of deposition and diagenesis on rock property. In this dissertation, I first study a modern carbonate platform to understand the relationship between dolomitization and sea level change and oceanography; I then analyze the geological control of diagenesis carbonate pore types on elastic properties, such as velocity and impedance, and finally I study the geophysical signatures and inversion of highly fractured zones in deeply buried carbonates using logs and seismic data.

On the Southern Marion platform, dolostone with large pores generally has high permeability, high sonic velocity, and high acoustic impedance at given porosity compared to limestone. Acoustic impedance inversion picks out three dolomitization events, matching well with three high stands of sea level events, to illustrate that the high stand of sea level induces the formation of dolomitization zones with large pores. This study demonstrates the positive feedback loop of dolomitization and ocean current circulation, as well as the relationship between dolomitization and sea level change.

The pore types in carbonates complicate the porosity-velocity and porosity-permeability relationships, lowering the prediction accuracy of porosity from porosity-impedance relationships. The application of the Sun rock physics model in an ultra-deep carbonate reservoir showed that the product of porosity and pore structure parameter has a much better linear relationship with velocity/impedance than porosity with

velocity/impedance. This finding reveals that porosity—together with pore structure parameter, dominates the elastic rock properties in carbonates, not porosity alone.

The major storage spaces are fractures and fracture related dissolution pores (cavities, molds, and vugs) in Hexiwu carbonate buried hill, in the Bohai Bay basin, China. Log analysis shows fractured zones, with open- and large-angle fractures, have porosity less than 5%, bulk modulus less than 55 GPa, and acoustic impedance less than 15,500 (g/cc)×(m/s). These typical fractured zones have a high pore structure parameter—higher than 6—using the Sun model. Seismic inversion for porosity and pore structure parameter shows that the fractured and high-porosity zones are subject to the structural setting in this area, which is controlled by the regional tectonics in the Bohai Bay basin. The proposed methodology is applicable to fractured reservoirs in similar geological settings.

DEDICATION

This dissertation is dedicated to my husband, Feng Xiao, my mother, Aizhi Wang, my father, Yueshun Zhang, and my sister Yingying Zhang, for their love, encouragement and support.

ACKNOWLEDGEMENTS

I would like to express my sincere gratitude to my committee chair Dr. Yuefeng Sun for his guidance and comment on my research. Without his support, I might not be able to work on this interesting and important research topic and it would be harder for me to finish my doctoral study. His sincerity toward sciences and scientific writing will benefit me through my professional life. I will also like to thank my committee members Dr. Walter Ayers, Dr. Micheal Pope, Dr. Benchun Duan, and Dr. Mark Everett for their guidance and support in the course of this research.

Thanks are also be given to my colleagues Dr. Qifeng Dou, Zhao Zhang, Liqin Sang, Qifei Huang, Hongyu Tian, Allen Li for the discussions and help on course work and research, as well as for their support to make my life be enjoyable at Texas A&M University. I would also thank IT staff Ryan Young and Steve Tran for their technical support on software maintenance.

I am indebted to Hess, Aramco, Marathon, Berg-Hughes Center, and the Reservoir Geophysics Program for their generous financial support to help me realize my dream. I would also like to thank Schlumberger (SIS and WesternGeco) and BP for their internship opportunity for me to gain valuable work experience. My gratitude also goes to Sinopec, PetroChina, ODP, and Miami University for their data support. Special thanks to software providers Schlumberger, CGGVeritas, and Halliburton for their generous support of Petrel, Techlog, HRS, and Landmark.

Finally, none of this would have become possible without the support and encouragement from my mother, father, and sister. They are the motivator driving me to go forward when I am stuck and they are also the coolant calming me down from self-satisfaction when I achieve something. They are always there for me no matter I am facing life ups or downs. I am grateful to them for what they did for me. I promise I will always be with them no matter what we are facing in the future.

NOMENCLATURE

k	bulk modulus
k_d	dry bulk modulus
k_s	solid bulk modulus
k_f	fluid bulk modulus
k_g	gas bulk modulus
μ	shear modulus
μ_d	dry shear modulus
μ_s	solid shear modulus
ϕ	porosity
Dphi	density porosity
S_w	water saturation
γ	pore structure parameter
γ_μ	shear pore structure parameter
C	pore structure ratio
V_p	p-velocity
V_s	s-velocity
ρ	density
AI	acoustic impedance
EI	elastic impedance
GI	gradient impedance

θ	incident angle
V_s/V_p	s-velocity and p-velocity ratio

TABLE OF CONTENTS

Page

LIST OF FIGURES

Page

LIST OF TABLES

Page

CHAPTER I

INTRODUCTION

Carbonate reservoirs account for 60% oil and 40% gas reserves worldwide. However, due to the limitation of production and development techniques, as well as the intense permeability heterogeneity in carbonate reservoirs, the oil and gas recovery rate is generally lower than 25%, which is much lower than that in sandstone reservoirs. Porosity alone without considering pore type variations (including fractures) usually cannot determine the efficiency of fluid flow in the porous medium and so permeability. Therefore, research on the quantification of pore type diversity and permeability heterogeneity in carbonates is of great significance for the oil/gas field production and development.

Great effort of research has been carried out on the subsurface data set, mostly core samples and borehole logs, for the purpose of extracting more information on rock petrophysical properties (e.g. porosity, permeability, pore shape, grain size, and density, etc.) of interested formations in the subsurface. In carbonates, however, diagenesis often produces a more complex pore structure system and profoundly increases the heterogeneity in carbonate rocks, in addition to porosity, grain size, fluid content, and lithology (e.g., Sun, 2007; Weger et al., 2009; Xu and Payne, 2009). Weger (2009) proposed a digital image analysis (DIA) method for the measurement of quantitative pore-structure parameters from thin sections and summarized four key parameters for the quantification of pore-structure in carbonates. Sun (2000, 2001, and 2004) introduced a

rock physics model (Sun model), based on poroelasticity, to quantify the pore-structure effect on sonic velocity and permeability in reservoir rocks. The application of the Sun rock physics model succeeded in both siliciclastics and deep buried carbonates for pore-structure quantification and permeability prediction (Adesokan and Sun, 2010; Dou et al., 2011a, 2011b; Sun et al, 2011; Zhang et al., 2012; Zhang et al., 2012). In my dissertation work, I intend to extend the investigation by using the Sun model for quantifying the effect of fractures on log and seismic responses, in addition to dolomitization, diagenesis, pore types and others.

1.1 Research objectives

This dissertation is aimed to characterize carbonate reservoirs (shallow or deep buried) by integrating Sun rock physics model (Sun, 2000, 2001, and 2004) and seismic data. Complicated pore structure system increases the heterogeneity level of carbonate rocks, adding great difficulty to characterize a carbonate reservoir by conventional technology from seismic volume, such as impedance inversion and porosity prediction. The introduction of pore structure parameter, independent of porosity, by Sun (2000, 2001, and 2004) provides a powerful tool to quantify the pore type variations in carbonate rocks.

This dissertation consists of three parts. In Part I, a 500-m-thick dolomitized upper succession, which is early to late Miocene in age, of the Southern Marion Plateau, NE Australiais, is investigated by log analysis, Sun model application, and seismic inversion. The purpose of this study is to analyze in shallow buried carbonates what is

the second dominant factor (mineralogy, pore structure, or fluid) controlling elastic properties besides porosity, to investigate the dolomitization mechanism in this geological setting, to study its relationship with seal level change and ocean current circulation in the subsurface strata, and finally to map the interested zones of dolostone by seismic inversion.

The major problem I address in part II is how to characterize a carbonate reservoir with variable pore types from poststack seismic inversion. The dataset used is borehole logs and poststack seismic volume from Yuanba gas field, Sichuan Basin, China. The target strata is the Feixiangguan Foramtion of Permian, which is deeply buried up to 6000 meter. The combined result of deposition and diagenesis on Feixiangguan carbonates increases the pore type variations in the rock to such an extent that pore structure together with porosity has a major control on rock properties. Based on this understanding, it is not wise and accurate to estimate porosity directly from impedance inversion. What reservoir parameter can be more accurately predicted based on poststack impedance inversion, considering the wide availability of poststack seismic data? What is the geological meaning of this reservoir parameter? These two questions are addressed in this part.

In part III, Sun rock physics model and prestack seismic inversion are integrated for the purpose of detecting naturally fractured zones in deep buried carbonate hill of Hexiwu field, Bohai Bay basin of China. Fractures and fracture related dissolution pores (cavities, molds, and/or vugs) provide the major storage spaces for hydrocarbons in deeply buried carbonate hill of Hexiwu field, Bohai Bay basin, China. The traditional

methods have great difficulty in detecting fractured zones. What are the petrophysical and geophysical characterisitics of fractured zones in carbonate buried hill? How to identify fractured zones from seismic data? These two issues are the core of my study in part III.

1.2 Summary of the dissertation

Diagenesis, including compaction, cementation, dissolution, dolomitization, and fracturing and so on, modifies the lithology, as well as the pore system in carbonate rocks after deposition. Dolomitization is an important diagenetic type as it usually changes porosity and permeability tremendously in many subsurface carbonate formations. Thus, the study on dolomitization mechanism is of great significance for reservoir property analysis. In Part I, using the data set from the Southern Marion platform (ODP Leg 194), offshore NE Australia, core and log analysis is carried out, the effect of dolomitization on sonic properties is studied using rock physics models, and seismic inversion is implemented to map the interest zones. The research demonstrates the dolomitization process is related to sea level change and oceanography. Rising sea level facilitates the dolomitization process to form dolostone with large pores, of which three belts follow the ocean bottom topography. Ocean current circulation supplies the driving-force for fluid-flow within the platform to assist the dolomitization process.

In carbonates, complex pore system (microposity, vuggy, moldic, interparticle, intercrystalline, and fracture, etc.) complicates the porosity-velocity and porosity-permeability relationships, which lower the prediction accuracy of porosity from

porosity-impedance relationships. In Part II, the Sun rock physics model is applied to an ultra-deep carbonate reservoir in Sichuan Basin. The research reveals the product of porosity and frame flexibility factor, which is also called pore structure parameter as a proxy factor of pore structure in carbonates, has a much better relationship with velocity and impedance. This finding indicates that porosity together with pore structure parameter dominates the elastic rock properties in carbonates.

Fractured carbonate reservoirs in ultra-deep basins are investigated, which have become strategic exploration targets recently. In Part III, deeply-buried carbonate hills in Hexiwu depression of the Bohai Bay basin, China, are studied. The Hexiwu carbonate hill underwent several tectonic movements, including Lingyuan, Tieling, Jixian, and Caledonian orogeny, and Indosinian-Himalayan movement. Faults and fractures are well-developed in this area due to the uplifting and regional compression. Strong diagenesis closes original and even secondary pores in residual carbonate rocks during multiple uplifting and subsidence. The major hydrocarbon storage spaces are interpreted to be dissolution pores (cavities, molds, and vugs) associated with minor faults and open fractures by core examination, log analysis, and seismic interpretation. Fracture detection, therefore, is the most important work in this area for hydrocarbon reservoirs. Borehole log analysis and Sun model application shows carbonate rocks with open fractures usually have impedance lower than 15,500 (g/cc)×(m/s), bulk modulus lower than 55 GPa, and pore structure parameter values higher than 6. These analytical results will be used in the prestack seismic inversion for acoustic impedance, porosity, and pore structure parameter to predict fractured zones in carbonate buried hills. The proposed

methodology of identifying geophysical signatures of fractured zones and fractured zone characterization based on log and prestack seismic inversion is applicable to fractured reservoirs or even unconventional reservoirs in similar structural settings.

CHAPTER II

DOLOMITIZATION ASSOCIATED WITH SEA LEVEL AND OCEAN CURRENT CIRCULATION IN THE SOUTHERN MARION PLATFORM, OFFSHORE NE AUSTRALIA

2.1 Summary

On the Southern Marion carbonate platform, dolomitization is triggered by the circulation of normal or slightly modified seawater and is related to changes in sedimentation rate and sea level change. Dolomitization further modifies formation permeability and fluid flow patterns. Dolostone/calcareous dolostone with large vuggy or moldic porosity is formed by fabric-preserving dissolution and recrystallization, which increase the pore space and facilitate the fluid flow effectively, with permeability ranging from 1 to 10,000 mD. Using a rock physics parameter, the frame flexibility factor (γ), as a proxy of pore structure, we find that this group of dolostone with larger pores, higher permeability, and higher sonic velocity for a given porosity usually has a lower value of frame flexibility factor—less than 2—than limestone of similar porosity, which, after strong compaction and cementation, occludes fluid flow, prevents dolomitization, and has permeability as low as 0.02 mD.

Acoustic impedance inversion confirms the asymmetric geometry of the Southern Marion platform is shaped by the oceanographic currents, which are caused by the southward-flowing East Australian Current. Three layers of dolostone with large pores in the upper platform reveal strong fluid flow within the carbonate platform,

leading to dolomitization and dissolution. These three strongly dolomitized zones follow the platform topography, indicating that the diagenetic fluid flow is driven by oceanographic currents. Three large-pore-formation dolomitization events match well with three high stands of sea level events, illustrating that the high stand of sea level induces the formation of dolomitization zones with large pores. This study demonstrates the positive feedback loop of dolomitization and ocean current circulation, as well as the relationship between dolomitization and sea level change, which could be applicable for better understanding subsurface fluid-rock interactions and dolomitization pore systems in other carbonate environments.

2.2 Introduction

The scientific purpose of Ocean Drilling Program Leg 194 is to investigate the influence of sea level and oceanography on subtropical carbonate platform growing on Marion Plateau, offshore NE Australia. The Previous works include the study on carbonate asymmetric platform build up mechanism (Isern et al., 2004), porosity and permeability relations (Ehrenberg et al., 2004, 2006a), the research on biosedimentary and paleoenvironmental evolution (Conesa et al., 2001), the analysis on carbonate platform growth, demise and dolomitization (Ehrenberg et al., 2006b), and the measurement and quantification of pore-structure parameters from thin sections (Weger et al., 2009).

Limited by the structure-less seismic data in the Southern Marion platform, dolomitization mechanism and its relationship with ocean current circulation has not

been further investigated. In this report, we integrated rock physics analysis and seismic inversion in the Southern Marion platform for the motivation of summarizing the major diagenesis types (especially dolomitization) in shallow carboantes, analyzing the rock properties of dolostone and limestone, quantifying the major controls to characterize typical dolostone intervals, and therefore mapping typical dolostone zones by seismic inversion. This piece of work is of significance to understand the dolomitization mechamism and its relationship with sea level change and oceanography.

2.3 Method

Due to the high level of heterogeneity in carbonates, an increasing amount of effort has been made towards pore-structure delineation and quantification. Weger et al. (2009) proposed a digital image analysis (DIA) method for the measurement of quantitative pore-structure parameters from thin sections and summarized four key parameters for the quantification of pore-structure in carbonates. The feasibility of this method is remarkable on core data, but limited for seismic related works. Sun (2000, 2001, and 2004) introduced a rock physics model (Sun model), based on poroelasticity, to quantify the pore-structure effect on sonic velocity and permeability in reservoir rocks. The application of this rock physics model succeeded in both siliciclastics and deep buried carbonates for pore-structure quantification and permeability prediction (Adesokan and Sun, 2010; Dou et al., 2011a, 2011b; Sun et al, 2011; Zhang et al., 2012; Zhang et al., 2012). In this paper, the Sun model is applied to the shallow buried carbonates in the Southern Marion platform for the purpose of analyzing the major

controls on rock properties and investigating how dolomitization is related to sea level and oceanography.

The shear wave log data was not acquired in the field. As a key input of the Sun model, the estimation of shear velocity log is fundamental. In this research, by integrating Gassmann's Equation and Sun model shear wave velocity is estimated from compressional velocity, density, and lithology description. One assumption is that the systematic error existing between core measurements and logs has the same influence on different lithologies. Following is the detailed procedure to estimate the shear velocity.

The Gassmann's Equation can be re-written in the following format to show its clear physical meaning (Han and Batzel, 2004),

$$k = k_d + \Delta k_d \tag{2.1}$$

$$\Delta k_d = \frac{k_s (1 - \frac{k_d}{k_s})^2}{1 - \phi - \frac{k_d}{k_s} + \phi \frac{k_s}{k_f}} \tag{2.2}$$

where k_s, k_f, k_d, k are the bulk moduli of the mineral grain, fluid, dry rock and saturated rock frame respectively; ϕ is the density porosity; Δk_d is the increment of bulk modulus after the rock is saturated with fluid.

According to the Sun model (Dou et al., 2011b), for gas saturated/dry carbonate rocks, we have

$$k_d \approx k_s (1 - \phi)^{\gamma} \tag{2.3}$$

$$\mu_d \approx \mu_s (1 - \phi)^{\gamma_\mu} \tag{2.4}$$

$$\mu \approx \mu_d \tag{2.5}$$

Thus, from these three equations (Equation 2.3, 2.4, and 2.5) we have

$$\mu \approx \mu_s \left(\frac{k_d}{k_s}\right)^C \tag{2.6}$$

$$C = \frac{\gamma_\mu}{\gamma} \tag{2.7}$$

where μ, μ_s are the saturated and dry-rock shear moduli; γ, γ_μ are the frame flexibility factors; C is the gamma ratio, defined as the ratio of shear frame flexibility factor over compressional frame flexibility factor (γ_μ/γ). Sun (2004) reported that the gamma ratio is a constant for similar lithology when porosity is not too low. In this study, core data analysis gives 1.3 and 0.9 for dolostone and limestone respectively (Figure 2.1). The lithology log was estimated by combining density log, PEF log, and the lithology description (Anselmetti et al., 2001). k_s, k_f, and μ_s were estimated by Wood's Equation.

We can compute P-velocity from K_d, Δk_d, and μ by using Equation 2.8, if K_d is known. Δk_d and μ are calculated by using Equation 2.2 and 2.6 respectively.

$$V_p^{\,*} = \sqrt{\frac{k_d + \Delta k_d + \frac{4}{3}\mu}{\rho}} \tag{2.8}$$

where $V_p^{\,*}$ is the computed P-velocity, while V_p represents the P-velocity log.

The initial value of k_d is defined by Equation 2.6 and 2.8 by assuming C=1, Δk_d=0 and V_p=$V_p^{\,*}$. Then, an increment from a pre-defined database is iteratively added to the initial value of k_d to minimize the error between the computed P-velocity and P-

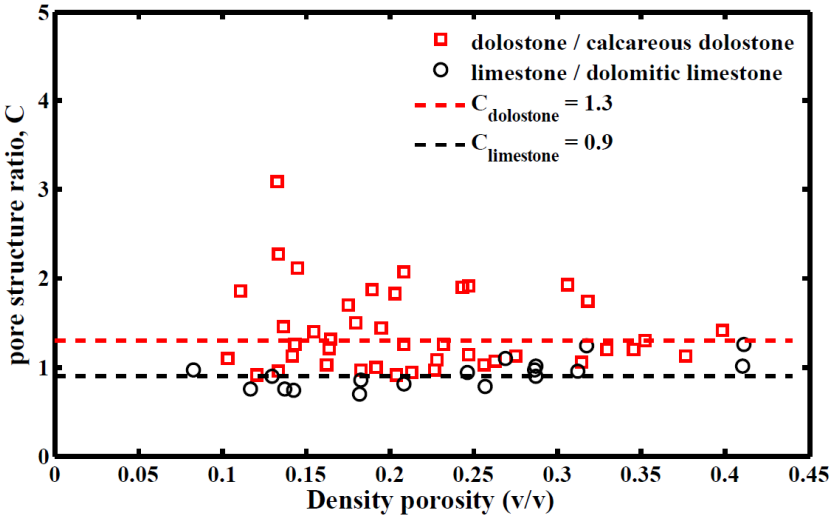

Figure 2.1. Gamma ratio C versus density porosity in Marion Plateau carbonate platform. Data points are from core samples.

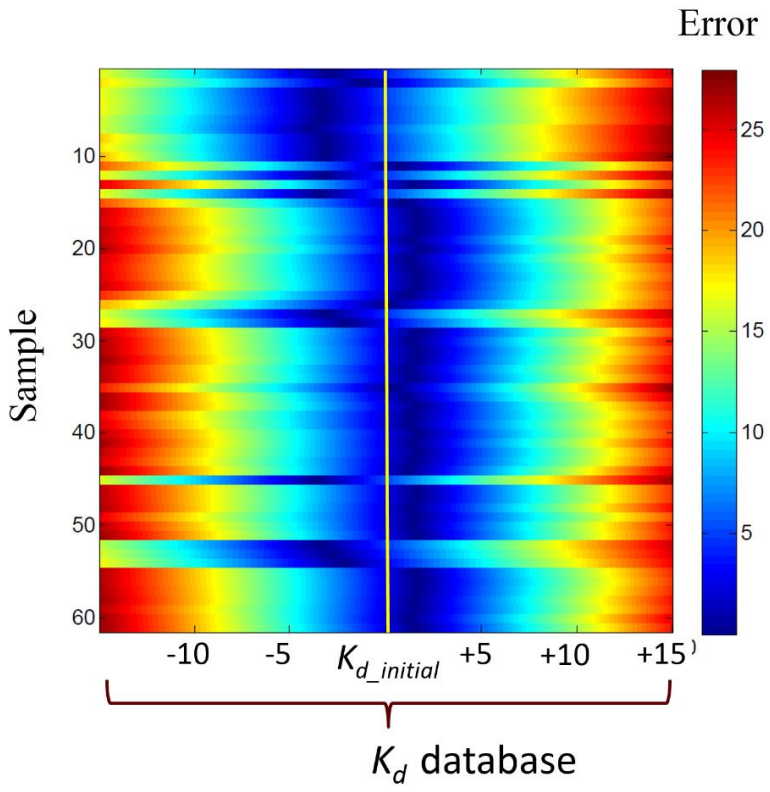

Figure 2.2. The error map shows the best K_d to estimate S-velocity. The yellow line is the initial K_d.

velocity log (Equation 2.9). The error is shown in Figure 2.2.

$$\text{error} = \left| V_p - V_p^{\,*} \right| \tag{2.9}$$

After acquiring the best k_d, μ is calculated by Equation 2.6. Finally the S-velocity is estimated by equation:

$$V_s = \sqrt{\frac{\mu}{\rho}} \tag{2.10}$$

Figure 2.3 shows the comparison between the measured and estimated S-velocity for core samples. Overall, the estimated S-velocity is very close to the measured S-velocity regardless of density porosity.

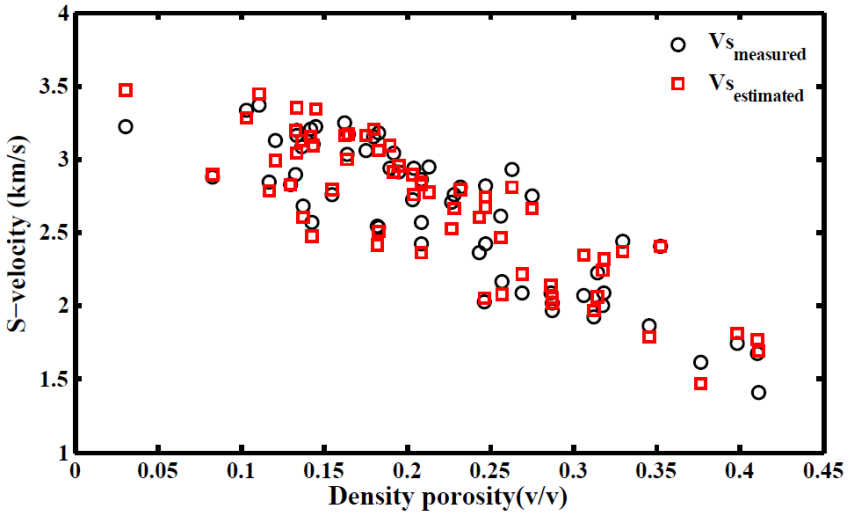

Figure 2.3. Comparison between measured and estimated S-velocity. Data points are from core samples.

Figure 2.4 shows the estimated S-velocity log as well as the P-velocity, density, and density porosity log. Vs/Vp ratio, bulk modulus and shear modulus are further

calculated. Large variation of Vs/Vp ratio and low values of bulk and shear moduli are the characteristics of modern carbonate rocks.

We input P-velocity, estimated S-velocity and density to Sun model for the estimation of frame flexibility factors (γ, γ_μ). The major equations in Sun model are summarized as following:

$$\gamma = 1 + \frac{\ln f}{\ln(1-\phi)} \tag{2.11}$$

where f is an intermediate frame flexibility factor defined as

$$f = \frac{1}{1-\phi} * \left(1 - \frac{F_k * (1 - \frac{K_f}{K_s}) * \phi}{1 - \frac{K_f}{K_s} F_k}\right) \tag{2.12}$$

where F_k is defined as

$$F_k = \frac{1}{\phi} * \frac{K_s - K}{K_s - K_f} \tag{2.13}$$

$$\gamma_\mu = 1 + \frac{\ln f_\mu}{\ln(1-\phi)} \tag{2.14}$$

where f_μ is another intermediate frame flexibility factor defined as

$$f = \frac{1}{1-\phi} * \frac{\mu}{\mu_s} \tag{2.15}$$

According to Sun (2000, 2004), frame flexibility factor is independent of rock porosity. The variation of frame flexibility factor represents the different pore structure for carbonates with similar lithology and porosity (Sun, 2001).

Limited by the unavailability of prestack seismic data, poststack seismic inversion is carried out to investigate how dolomitization is related to sea level change and oceanography in the Southern Marion platform.

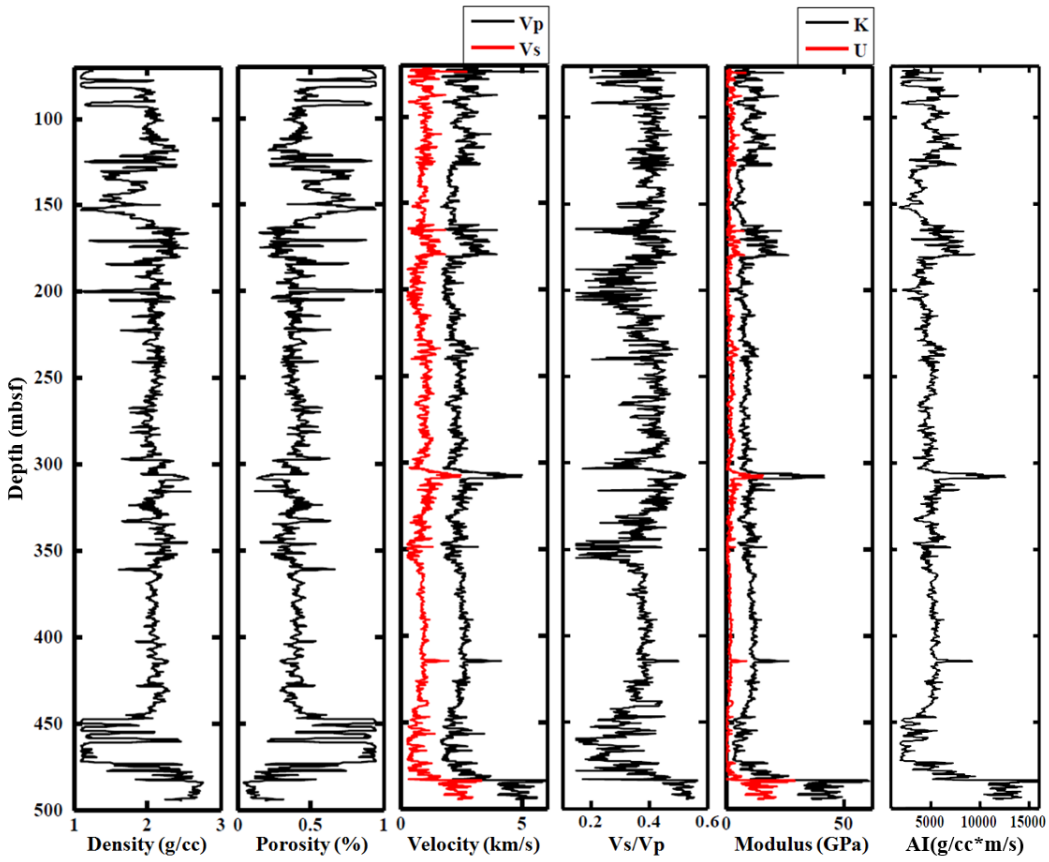

Figure 2.4. Logging summary of Site 1196. Porosity is calculated from density. S-velocity (Vs) is estimated based on Sun model and Gassmann's Equation.

2.4 Data

The Southern Marion Plateau is one of the carbonate platforms of Marion Plateau, located off (1196 and 1199) were drilled on top of this platform, penetrating a 663-m carbonate succession of bioclastic and reefal sedimentary bodies. This study

focuses on the dolomitized 500-m-thick upper succession of Site 1196, which is early to late Miocene in age.

Core measurement data are limited on Marion Plateau due to the low recovery. All samples (60) available were employed to estimate S-velocity log, summarize the diagenesis types, and quantify the major factors influencing the rock properties. Out of all 60 samples, 42 samples are dolostone/calcareous dolostone rocks, and 18 samples are limestone rocks. Petrophysical measurements on core samples used in this study have been reported by Weger et al. (2009). Compressional and shear wave velocities were measured on distilled water saturated samples by using an ultrasonic transmitter-receiver pair with piezoelectric transducers forming the core of the equipment. Porosity was measured by computing the difference between the measured volume of the core plug and the real volume determined by helium injection in a Boyle's law porosimeter. Gas permeability (Klinkenberg-corrected permeability in units of millidarcy) was measured at a confining pressure of 20 bars.

Figure 2.5 shows the velocity profiles measured at Site 1196 according to ODP Leg 194 logging summary. P-velocity measured on core samples are at least 1.1 times faster than downhole measurements. The reason is the low core recovery of mainly cemented carbonates and the systematic error between core and logging measurements (ODP Leg194 Downhole Logging Summary). For the purpose of integrating core measurement and logging data to analysis the rock properties, the core measured velocities are divided by a factor of 1.1 to match the high logging velocities.

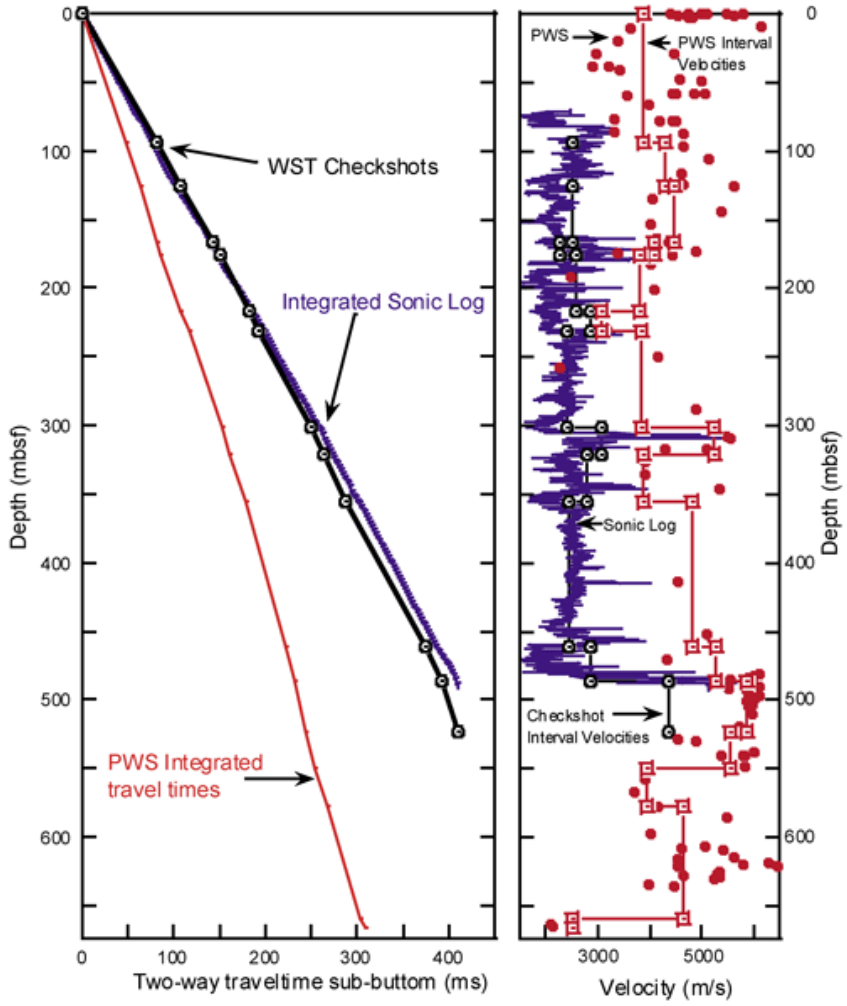

Figure 2.5. Velocity profiles measured at Site 1196 (From ODP Leg 194 logging summary).

High-resolution seismic data has been collected over the Marion Plateau, northeast Australia, for the purpose of investigating how sea level and oceanography control the carbonate platform building. Mar_07 is the 2D seismic line cutting through the Southern Marion platform (Figure 2.11). The massive and table-like structures in carbonate platform give tremendous difficulty in interpretation of the platform inner geometry, attributes analysis and seismic inversion. The extraction of first multiple wave

shows a better bedding feature within the platform, which add more information and feasibility to investigate the dolomitization mechanism in the Southern Marion platform.

2.5 Results

2.5.1 Rock physics analysis on core samples

Limestone samples have small scattering on both crossplots of bulk modulus versus density porosity and shear modulus versus density porosity (Figure 2.6), which confirms porosity is the dominant controlling factor influencing the elastic properties of limestone samples. Thin section examination on limestone samples reveals the dominant pore types are intra-particle, moldic, inter-particle, and micro-porosity. Three typical thin sections (g, h, and i) are marked in Figure 2.6 and 2.7. The major diagenesis in limestone includes compaction, dissolution, cementation, and fabric-preserving dissolution. Based on Sun model, the estimation of frame flexibility factor for limestone samples gives compressional frame flexibility factor higher than 3 and shear frame flexibility factor higher than 3.5.

Porosity is also the dominant factor controlling the elastic properties of dolostone samples (Figure 2.6). However, dolostone samples have bigger scattering on the crossplot of bulk modulus versus density porosity and shear modulus versus density porosity than those of limestone, which is largely due to the pore size, pore shape, and pore connectivity variation. Six typical dolostone samples (a, b, c, d, e, and f) are marked in Figure 2.6, and their thin sections are shown in Figure 2.7. When porosity is around 20.5%, dolostone samples d, e, and f have large difference in bulk and shear moduli.

According to their thin sections, dolostone samples with large moldic, vuggy or intra-particle pores have higher bulk modulus than those with small pores.

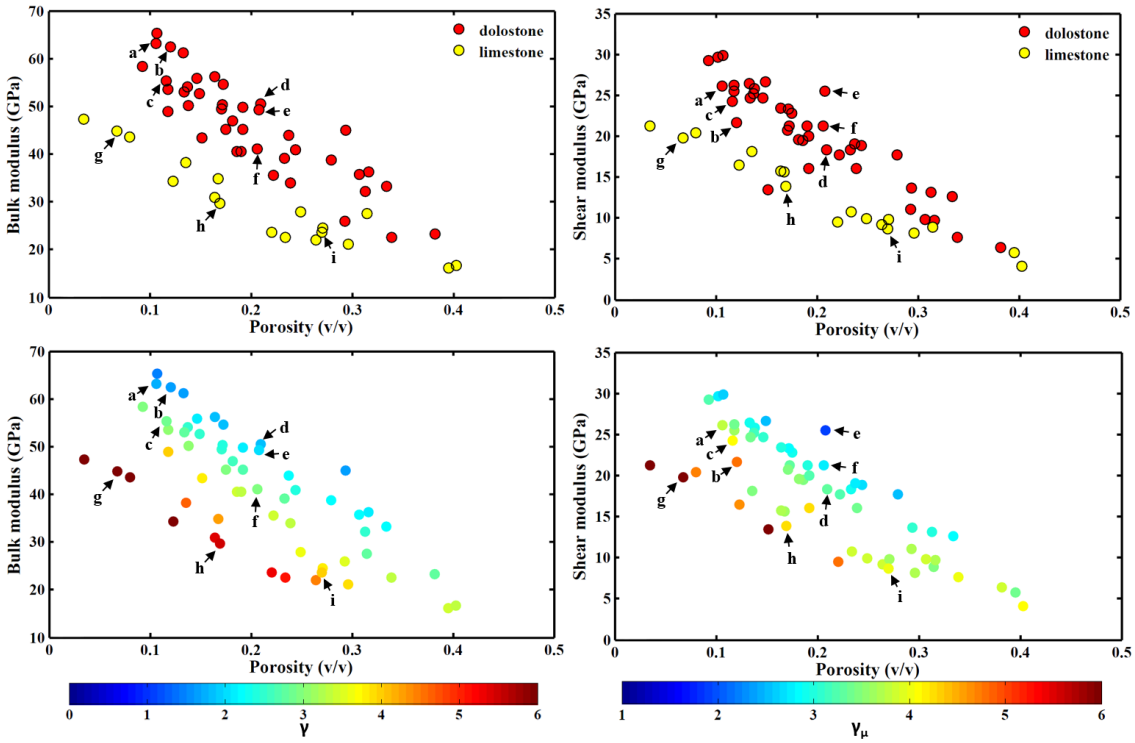

Figure 2.6. Crossplots of bulk and shear moduli versus porosity. Data points are from core samples. The annotated samples are thin sections in Figure 2.7.

Their measured permeability indicates that dolostones with large pores tend to have high permeability values. The low porosity samples a and c show the similar trend. Comparison of the permeability of samples b and c indicates that the presence of inter-particle or inter-crystal pores greatly increases the rock permeability.

The compressional frame flexilibity factors of dolostone samples with large pores are estimated to be lower than 2. In this case, compressional frame flexibility

factor quantifies the pore size in carbonate rocks. The shear modulus of these six samples places them differently from what bulk modulus does. The shear modulus decreases when macro-pore connectivity increases (more inter-particle pores).

2.5.2 Rock physics analysis on log data of Site 1196

Based on S-velocity estimation and Sun model application, compressional and shear frame flexibility factors are calculated based on the log data (Figure 2.4). Figure 2.8 show the bulk, shear moduli versus density porosity respectively for dolostone and limestone intervals. The color indicator is compressional and shear frame flexibility factor respectively for bulk and shear moduli versus porosity. Due to the poor cementation of shallow buried carbonates, some zones have very high porosity up to 90% (Figure 2.4). For the purpose of analyzing the rock properties of cemented carbonate rocks in modern settings, the crossplots only plot the data points with density porosity lower than 60%.

Generally, the increase in density porosity results in the decrease of bulk and shear moduli (Figure 2.8). The increase of compressional and shear frame flexibility factors correlates to bulk and shear moduli decrease at given porosity. The Sun model application shows that compressional frame flexibility factor has a range of 0 to 7 while shear frame flexibility factor has a range of 0 to 8 for dolostone intervals (Figure2.8). Limestone intervals have a narrower range for both compressional and shear frame flexibility factor. They are 2 to 7 and 2 to 8 respectively. The comparison indicates limestone intervals have less pore structure variation than dolostone intervals. Compared to the crossplots in Figure 2.6, the compressional and shear frame flexibility factors of

log data are slightly different from those of core data. One reason for this is the much larger population of data points and the inclusion of poor cemented rocks. In this case, the pore system becomes more complex for log data. The second reason is the measurement difference between these two categories of data, which results in a systematic difference. The correction of dividing the core velocity by a factor of 1.1 is to compromise this systematic difference.

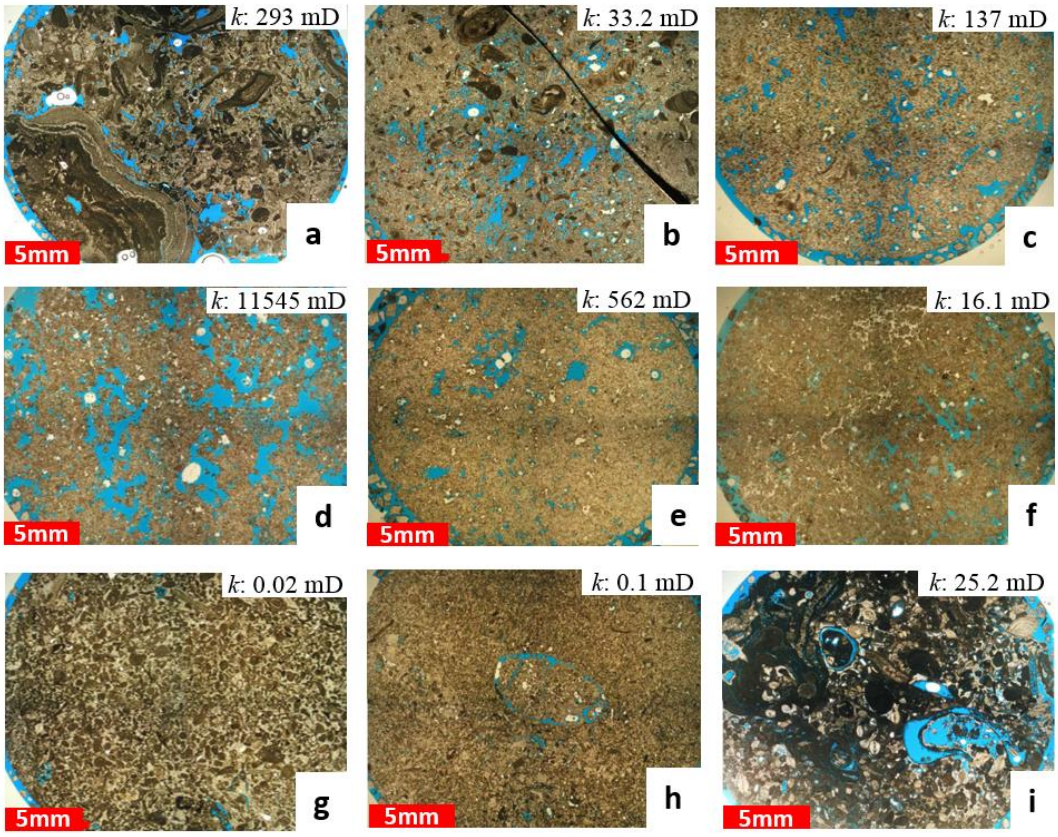

Figure 2.7. Thin sections of annotated core samples in Figure 2.6.
a, b, c, d, e, and f are dolostone samples. g, h, and i are limestone samples.

Pore structure variation is responsible for the strong scattering of bulk and shear moduli at given porosity for dolostone intervals. On both crossplots, the diamonds represent the core samples with large moldic/intra-particle pores. Their bulk and shear moduli are higher than other dolostone at the same porosity. Their frame flexibility factors are smaller than 2. One typical thick layer in Well 1196 is from 160 to 180 mbsf (Figure 2.4) with relative low porosity (~25%), high P-velocity (~3200 m/s), and high bulk modulus (greater than 30 GPa).

The squares are from the white sucrosic dolostone interval of Site 1196 (412.7~470.4 mbsf) (Shipboard Scientific Party, 2001). Their bulk and shear moduli have limited variation. However, their density porosity varies from 30 to 44%. Their frame flexibility factors are higher than 3 for both cases, as well as have limited variations in value.

The crossplots of bulk and shear moduli versus density porosity in limestone zones show slight scattering of data points compared to those in dolostone intervals. However, the shear moduli versus density porosity has a wider scattering. According to the former thin section analysis in limestone samples (Figure 2.7), the dominant pore types in limestone include moldic, intra-particle, inter-particle, and microporosity. The scattering difference between these two crossplots in limestone intervals can be interpreted as shear modulus is more sensitive to pore size, pore shape and pore connectivity. More measured core samples in the Southern Marion platform are needed to verify this point. Both crossplots in limestone intervals show compression and shear

frame flexibility factor higher than 2, which indicates the dolostone with large pores (γ <= 2) can be separated from the mixture of other dolostone and limestone.

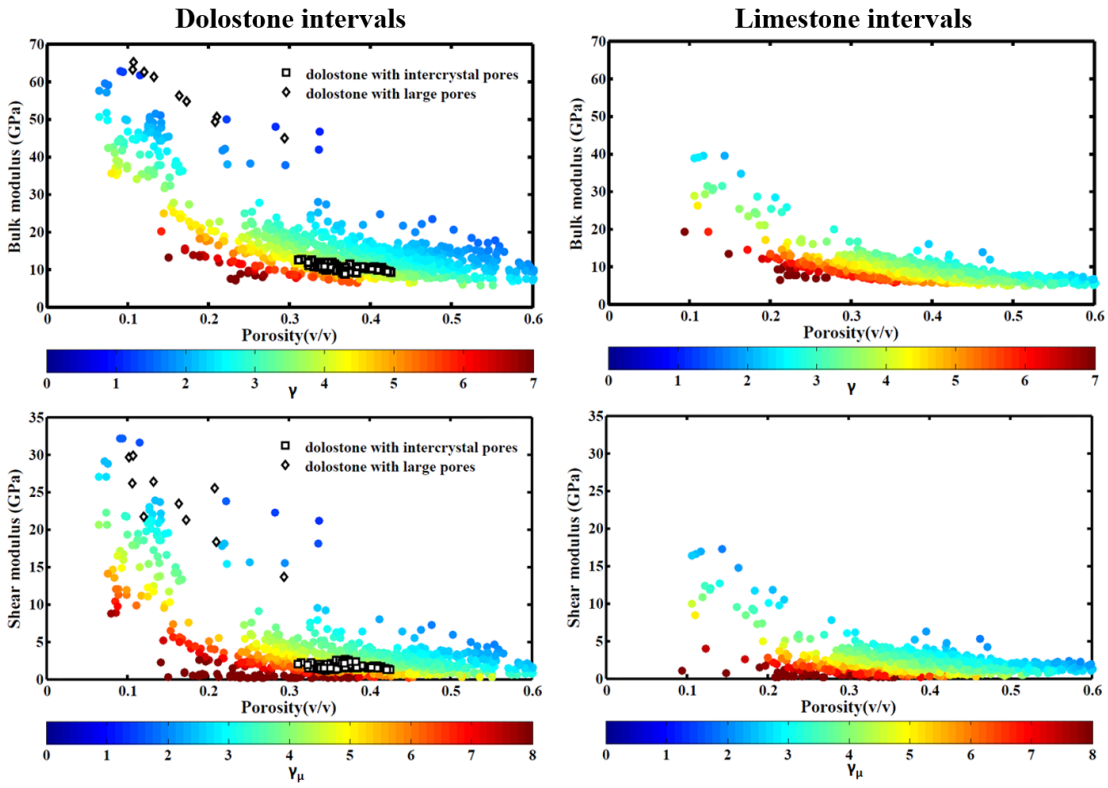

Figure 2.8. Crossplots of bulk and shear moduli versus density porosity in dolostone and limestone intervals respectively. Data points with porosity higher than 0.6 are excluded for poor cementation.

2.5.3 Permeability

Permeability in carbonates is significant for controlling fluid flow pathways. In the oil and gas field development stage, it is a key parameter to control production. A good understanding of porosity-permeability relations in modern carbonates is also important in studying deep buried carbonates.

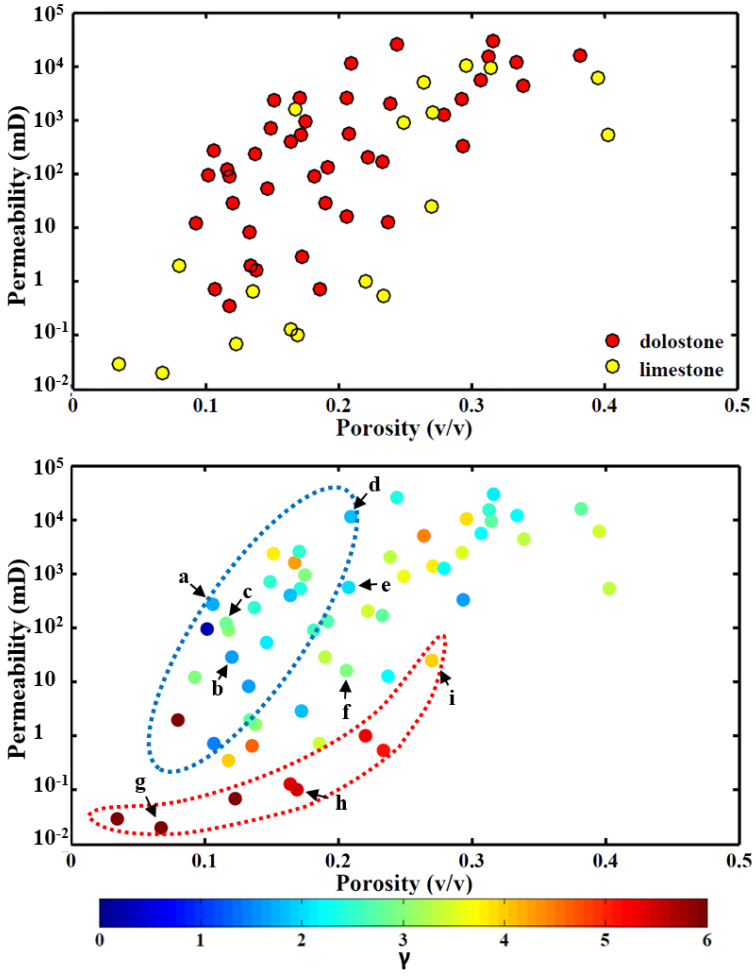

Figure 2.9. Crossplots of permeability versus porosity. Top figure is colored by lithology while the bottom one is colored by pore structure parameter (γ). Data points are from core samples.

For limestone samples g, h, and i in Figure 2.6, the measured porosity varies from 6.8 to 25.2%, and the measured permeability varies from 0.02 to 25.2 mD (Figure 2.7). Porosity is more dominant in controlling permeability in limestone rocks. When porosity is lower than 25%, permeability in limestone is generally lower than that in dolostone (Figure 2.9). In the high porosity range, mineralogy has limited contribution to permeability variation.

For dolostone samples in Figure 2.6, the measured permeability values are labeled on thin sections in Figure 2.7. The permeability magnitude of dolostone samples varies from tens of millidarcy to thousands of millidarcy. For dolostone samples with similar pore structure (sample c and e), porosity is the dominant factor affecting permeability. Dolostone samples with larger pores tend to have higher permeability (sample d, e, and f). For dolostone samples with large pores (sample a, b, and c), the percentage of inter-particle, inter-crystal porosity and fracture/micro-fracture also controls the permeability.

The crossplot of permeability versus porosity with compressional frame flexibility factor as color indicator shows that compressional frame flexibility factor can be used to separate two groups of carbonate rocks for permeability prediction (Figure 2.9). One group is limestone rocks within the red circle. They have high compressional frame flexibility factor values but low permeability compared to dolostone rocks. The second group is dolostone rocks with large pores within the blue circle. Although their porosity is comparatively low, their permeability is generally higher than other samples at the same porosity.

2.5.4 Acoustic impedance inversion

Although the application of Sun model on core and logging data found out a small value of compressional frame flexibility factor (<=2) can be used to separate dolostone with large pores when porosity is lower than 20% from other types of dolostone and limestone, prestack seismic inversion cannot be carried out for mapping this typical dolostone due to the shortage of prestack seismic data. Considering that

dolostone zones with large pores have high P-impedance, poststack seismic data will be used to estimate their distribution within the platform.

Figure 2.11 shows the primary wave and first multiple wave on Line Mar_07. First multiple wave has been corrected according to the ocean topography. Careful investigation found out first multiple wave offers a better imaging within the carbonate platform. Primary wave shows massive and table-like structures in carbonate platform. First multiple wave shows a better bedding pattern especially in the upper platform. One reason could be that first multiple wave is covered by less noise, and offers a better data for carbonate platform geometry interpretation and seismic inversion. Figure 2.12 shows the first multiple shifted to the time domain of primary wave and the acoustic impedance inversion result based on first multiple.

According to Isern et al. (2004), the dominant energy source shaping the platform asymmetric geometry is the oceanographic currents, which thins the strata on left side. First multiple wave clearly shows the asymmetric geometry. The P-impedance inversion result based on model-based inversion algorism shows an even better asymmetric geometry, although the P-impedance of the lower platform is contaminated by noise. Three high P-impedance belts are identified within the platform and interpreted as high high P-impedance, low porosity dolostone with large pores by incorporating logging data at Site 1196. The bottom two correspond well to the high values of P-impedance log at Well 1196. The bottom one is at a depth of around 310 mbsf at Site 1196 and the middle one is at a depth of 160 to 180 mbsf (Figure 2.4). The top one has a relatively high impedance at Site 1196, which matches well with the high P-impedance

log at a depth around 120 mbsf. The bottom one is the shortest one as it is truncated by the noise.

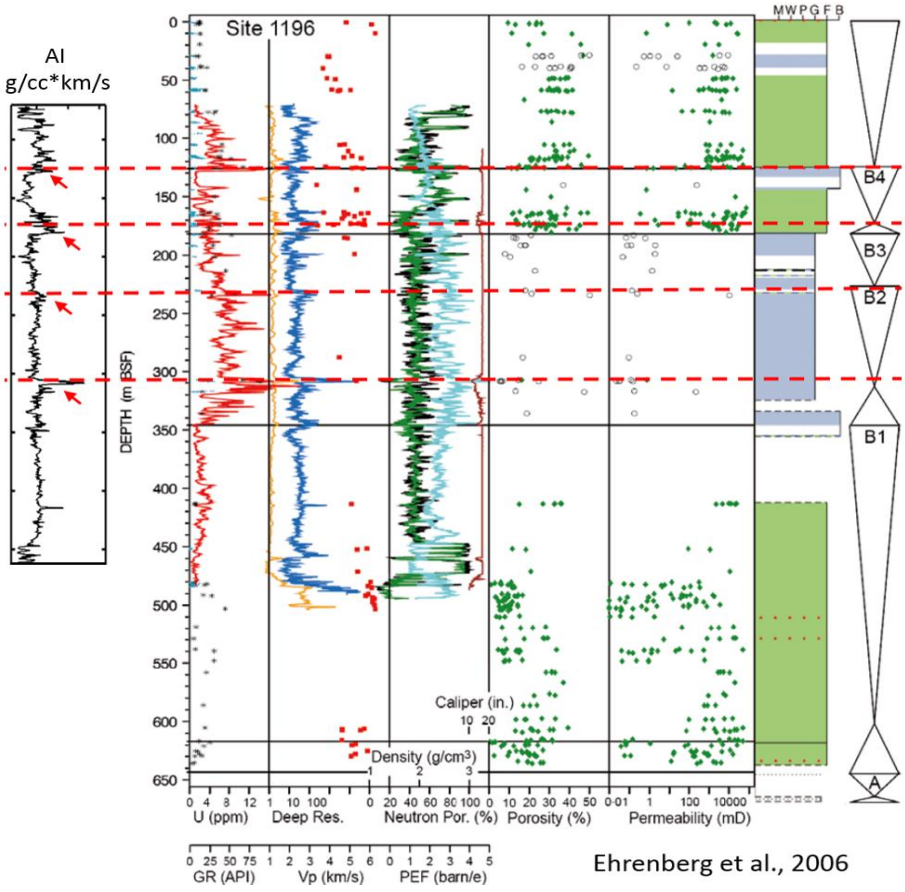

Figure 2.10. The tie of impedance log with sequence cycles interpreted by Ehrenberg et al. (2006).

According to Ehrenberg et al. (2006a), six sea level fluctuations are interpreted based on logging and core data (Figure 2.10). Four of them are tying well with high impedance picks. Ignoring the bottom two where no logging data acquired, four high sea level events are matching the high impedance picks in Figure 2.12 (dashed lines). Due to the limitation of first multiple, the inverted P-impedance is much lower than P-

impedance log at Site 1196, which adds difficulty to quantitatively interpret the dolostone zones with large pore. However, due to the characteristic of dolostone with large pores, which is high P-impedance, high P-velocity, low frame flexibility factor, and low porosity, by considering the P-impedance log at Site 1196 it is reasonable to take 4000 (g/cc)×(m/s) as a threshold to separated high P-impedance values for dolostone with large pores on P-impedance profile. Three red dashed lines in Figure 2.12 meet this condition. The high stand of sea level, in this case, is not the must condition for the formation of dolostone with large pores, but it definitely facilitates the dolomitization process, as well as the dissolution to form large pores. Overall, three dolostone zones follow the ocean topography, which illustrates that the diagenetic fluid flow is driven by the oceanographic currents and follows the sedimentary structure within the platform. The black arrows in Figure 11 indicate the fluid circulation direction.

2.6 Conclusions

On the Southern Marion carbonate platform, the circulation of normal or slightly modified seawater assists the dolomitization process, which is related to changes in sedimentation rate and sea level change. The dolomitization type and magnitude have a positive relationship with formation permeability, fluid-flow patterns, and sea level. One typical group of dolostone is dolostone/calcareous dolostone with large intraparticle, vuggy, or moldic porosity. It is formed by fabric-preserving dissolution and recrystallization, which increase the pore space and permeability effectively by up to several thousand mD. Quantification of pore structure effect shows a lower value of

frame flexibility factor ($\gamma < 2$). Another typical group of dolostone is sucrosic dolostone produced by fabric-destructive recrystallization, which retains the primary porosity but has a tremendous increase in permeability (~12,000 mD). The frame flexibility factor calculation gives a higher value than that of fabric-preserving dolostone ($3 < \gamma < 4.5$).

In limestone intervals, compaction, cementation, and dissolution dominate diagenesis. Fabric preserving dissolution increases porosity while cementation and compaction reduce original porosity. Limestone permeability has a strong positive relationship with porosity, and it can be as low as 0.02 mD. The frame flexibility factor estimation gives values higher than 2, which is higher than that of dolostone with large pores.

The extraction of the first multiple wave and its application on P-impedance inversion clearly confirm that the asymmetric geometry of the Southern Marion platform is created by oceanographic currents, which blow southeast ward. The mapping of three dolostone zones with large pores in the upper platform match three high stands of sea level events interpreted at Site 1196, revealing that the high stand of sea level can assist the dolomitization process to form large pores. Three dolostone zones follow the ocean topography, further demonstrating that the fluid flow system within the platform is driven by oceanographic currents. With increased permeability, dolostone intervals continue to facilitate the fluid flow within the platform and therefore to accelerate further dolomitization in carbonate rocks. The study on how dolomitization is related to sea level change and ocean current circulation is applicable for better understanding of

subsurface fluid-rock interactions and dolomitization mechanism in other carbonate environments.

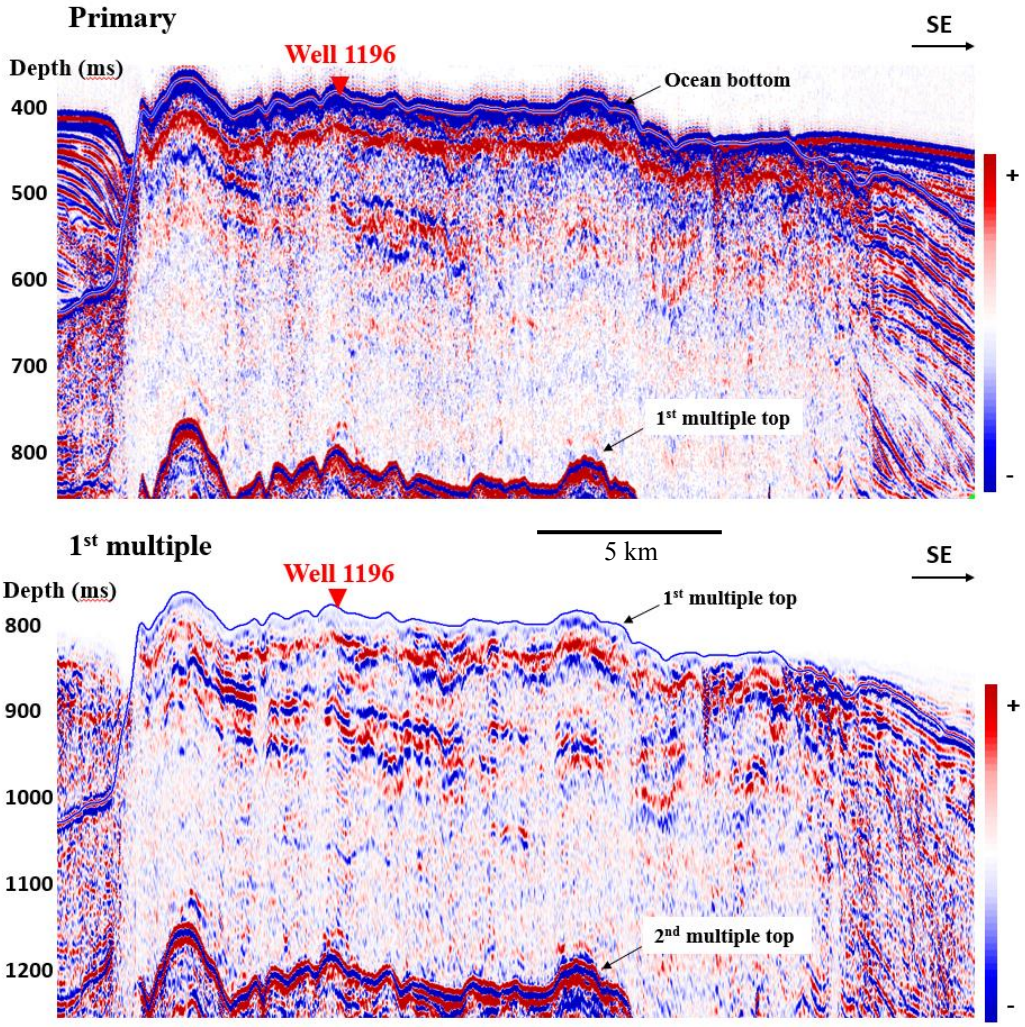

Figure 2.11. Primary wave and first multiple wave through the Southern Marion platform. The first multiple top is corrected according to the ocean topography.

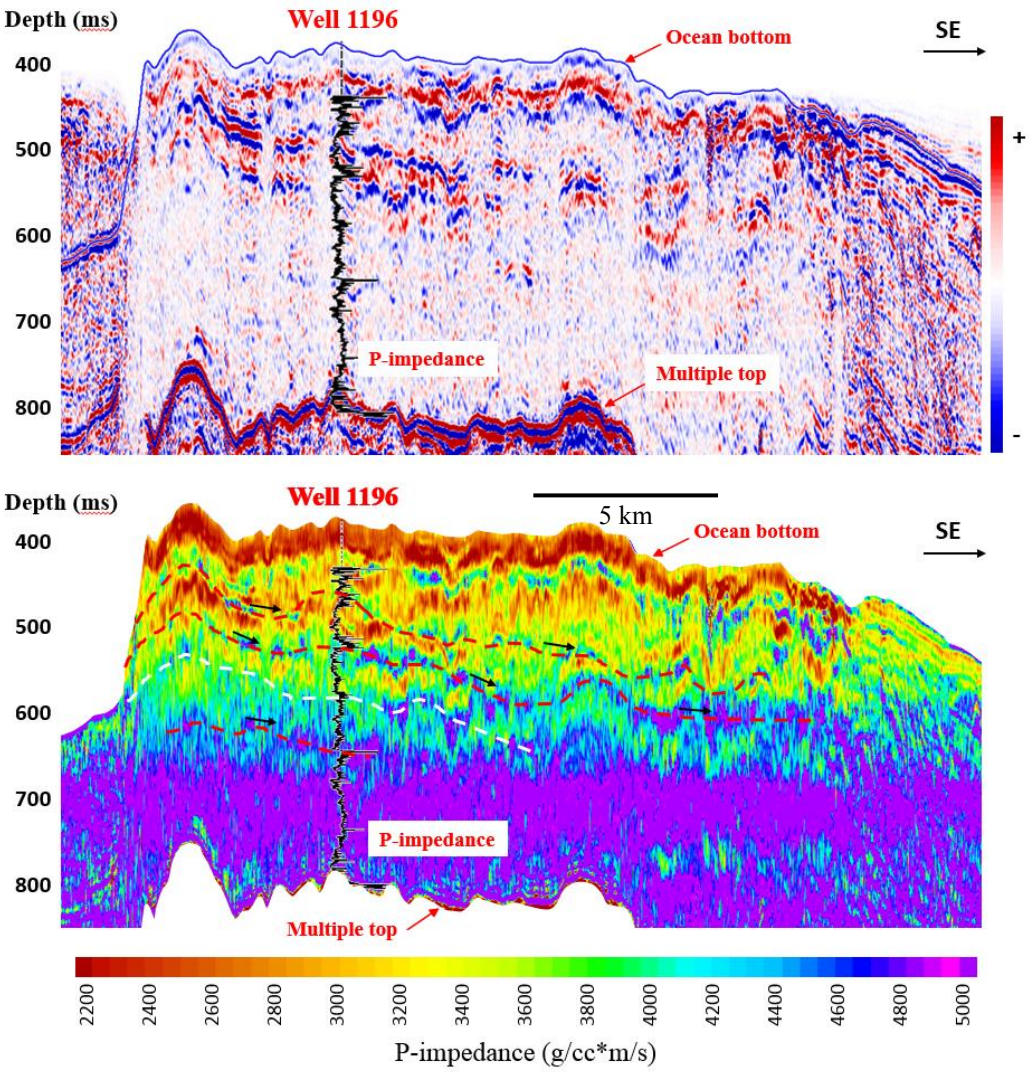

Figure 2.12. The first multiple (top) corrected to the primary wave's depth and the P-impedance inversion result (bottom). Four dashed lines mark four high P-impedance belts, which match well with four high stands of sea level events. Three red dashed lines mark the dolostone zones with large pores within the platform.

CHAPTER III

IMPROVING POROSITY-VELOCITY RELATIONSHIPS USING CARBONATE PORE TYPES

3.1 Summary

Acoustic impedance in carbonates is influenced by factors such as porosity, pore structure/fracture, fluid content, and lithology. Occurrence of moldic and vuggy pores, fractures and other pore structures due to diagenesis in carbonate rocks can greatly complicate the relationships between impedance and porosity. Using a frame flexibility factor (γ) derived from a poroelastic model to characterize pore structure in reservoir rocks, we found that its product with porosity could result in a much better correlation with sonic velocity ($Vp = A\text{-}B\times\gamma\phi$) and acoustic impedance ($AI = C\text{-}D\times\gamma\phi$), where *A, B, C* and *D* is 6.60, 0.03, 18.3, and 0.09 respectively for the deep low-porosity carbonate reservoir studied in this paper. These new relationships could also be useful to improve seismic inversion of ultra-deep hydrocarbon reservoirs in other similar environments.

3.2 Introduction

Oil and gas exploration is increasingly shifting towards ultra-deep depositional environments. Recent pre-salt discoveries in offshore Brazil and giant discoveries of gas fields in Sichuan, China are in deep carbonate platforms with heterogeneous reservoir quality. Seismic inversion proves to play an important role in predicting lithology and fluid variations in these and similar deep geologic formations.

The fact that relationships between acoustic impedance and reservoir properties in carbonates are difficult to establish is well known (e.g., Anselmetti and Eberli, 1993; Lucia, 1999). Such relationships have been found useful for sandstone reservoirs as pore space in clastic rocks tends to be relatively homogeneous in many cases. In carbonates, however, diagenesis often produces a complex pore structure and profoundly increases the heterogeneity in carbonate rocks, in addition to porosity, grain size, fluid content, and lithology (e.g., Sun, 2007; Weger et al., 2009; Xu and Payne, 2009). In addition, our knowledge on the petrophysical properties of carbonate reservoir rocks in ultra-deep environments and their seismic responses needs improvement.

In this paper, we use a rock physics model introduced by Sun (2000) to analyze the relationships among velocity, acoustic impedance, pore structure, fluid content and porosity for a carbonate gas reservoir at a depth of about 7km in the Sichuan Basin, China. We find that the product of porosity and frame flexibility factor results in a better correlation with velocity or acoustic impedance.

3.3 Theory and method

Based on an extended Biot theory of poroelasticity, Sun (2000, 2004) derived a simplified rock physics model for carbonate rocks. In this model, a frame flexibility factor (γ) is introduced to characterize the effect of pore structure on seismic velocity. In comparison to the wave velocity, this frame flexibility factor depends less on porosity. This model has been successfully used in seismic reservoir characterization of worldwide carbonate fields for its effectiveness in quantifying pore structures in

carbonate rocks (e.g., Bracco Gartner et al., 2005; Sun, 2007; El-Wazeer et al., 2010; Dou et al., 2011b).

The formula to be used for calculation of the frame flexibility factor is:

$$\gamma = 1 + \frac{\ln f}{\ln(1-\phi)} \tag{3.1}$$

where ϕ is porosity; f is one frame flexibility factor defined as

$$f = \frac{1}{1-\phi} * \left(1 - \frac{F_k * (1 - \frac{K_f}{K_s}) * \phi}{1 - \frac{K_f}{K_s} F_k}\right) \tag{3.2}$$

where K_s is solid matrix bulk modulus; K_f is fluid bulk modulus; and F_k is defined as

$$F_k = \frac{1}{\phi} * \frac{K_s - K}{K_s - K_f} \tag{3.3}$$

where K is the bulk modulus.

For dry or highly gas-saturated rocks, bulk modulus and shear modulus can be approximately expressed as functions of the product of porosity (ϕ) and frame flexibility factor (γ) as follows:

$$k \approx k_s(1-\gamma\phi) \tag{3.4}$$

$$\mu \approx \mu_s(1-c\gamma\phi) \tag{3.5}$$

To the first-order approximation, these relationships in Equation 3.4 and 3.5 theoretically predict that both bulk and shear moduli are inversely proportional to the product of porosity and frame flexibility factor. Correspondingly, as functions of bulk, shear moduli and density, the P-velocity and acoustic impedance should have a stronger

and better dependence on the product of frame flexibility factor and porosity than on porosity alone.

Additionally, we assume the lithology of carbonate rocks are dolostone for the studied gas reservoirs in this paper. The bulk modulus K_s of the solid matrix is taken to be 86.5 GPa. The fluid bulk modulus K_f is calculated by using Wood's Equation (Equation 3.6) (Wood, 1955) and assuming K_w=2.25 GPa for water and K_g =0.133 Gpa for gas.

$$\frac{1}{k_f} = \frac{S_w}{k_w} + \frac{1 - S_w}{k_g} \tag{3.6}$$

Using Equation 3.1-3.3 and 3.6, the frame flexibility factor can be calculated using core or well log data.

3.4 Data analysis and results

The log data sets used in this study are from an onshore gas reservoir at a depth of about 7km, Sichuan Basin, in the southwest part of China. The well logs are composed of P-wave velocity, S-wave velocity, density, porosity, fluid saturation, mineralogy, and caliper. The data analyzed are from two major gas reservoir units. These gas reservoirs were mainly developed in the reef crests, and the dolomitization process in later diagenesis helped in forming relatively high porosity up to about 12%. Owing to the extent of dolomitization, the two reservoir units have highly variable reservoir quality in terms of lateral and vertical changes of porosity and permeability. The cap and base rocks are mainly low-porosity limestone as well as the seal between the two units.

Using sonic logs (*Vp* and *Vs*), density, porosity, and fluid saturation logs, the pore-structure parameter (γ) is estimated using Eqs. 3.1-3.3 and 3.6. Figure 3.1 is a plot of P-velocity versus density porosity for different frame flexibility factor shown in labeled colors. At a porosity of 4%, the P-velocity has a large variation with a maximum difference of about 1.98 km/s. This variation can be explained with different pore structure types. Depending less on porosity, frame flexibility factor is a parameter that could be used to quantitatively characterize the pore structure effect on velocity. At given porosity, if the pores are large and isolated (large vugs or molds), the carbonate rock will have a higher P-velocity, and the frame flexibility factor will have a lower value; if the pores have smaller size and are connected (intercrystalline or interparticle), the carbonate rock may have a relative low P-velocity, and the frame flexibility factor has a relative high value; if the carbonate rock is fractured, the P-velocity of the rock may be particularly low, and the frame flexibility factor is then particularly high. Thus for a given porosity, the higher the frame flexibility factor and the higher the permeability. Correspondingly, the high value of the product of porosity and frame flexibility factor may represent high permeability zone where hydrocarbons can migrate and/or be stored.

Figure 3.2a shows the plot of sonic P-velocity versus porosity with water saturation indicated by color. The data are from well logs available in the studied depth interval. The data points are widely scattered on the plot. When porosity is around 4%, P-velocity has a variation of 1.98 (km/s) due to pore type changes (Dou et al., 2011b). For the data points above the best-fit line, the porosity inverted from P-velocity by using

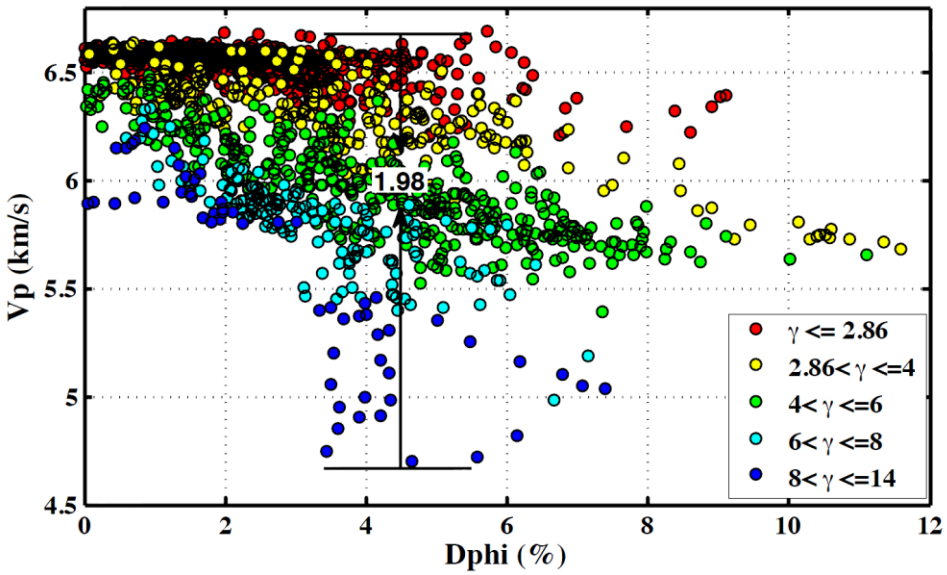

Figure 3.1. Crossplot of P-velocity versus density porosity for different frame flexibility factor shown by color.

the best-fit line could be lower than it should be; for the points below the best-fit line, the inverted porosity could be higher. The linear relationship between P-velocity and porosity (Vp=-0.11×ϕ+6.63) has an R-square only around 0.37. Thus, conventional inversion methods that use best-fit lines to estimate porosity from sonic wave velocity cannot be applied to the studied reservoirs.

In contrast to the velocity-porosity crossplot shown in Figure 3.2a, Figure 3.2b shows the crossplot of sonic P-wave velocity versus the product of porosity and frame flexibility factor (labeled as product). It is evident that the correlation between velocity and the product is much better than that between velocity and porosity alone shown in Figure 2a. Where the product of porosity and frame flexibility factor is about 0.248, P-velocity has a variation of 0.9 (km/s). Depending less on lithology, the relationship between P-velocity and the product of porosity and frame flexibility factor is

$$Vp = A - B \times \gamma\phi \qquad (3.7)$$

where A and B are 6.60 and 0.03, respectively for the studied reservoir units. The R-square equals 0.85.

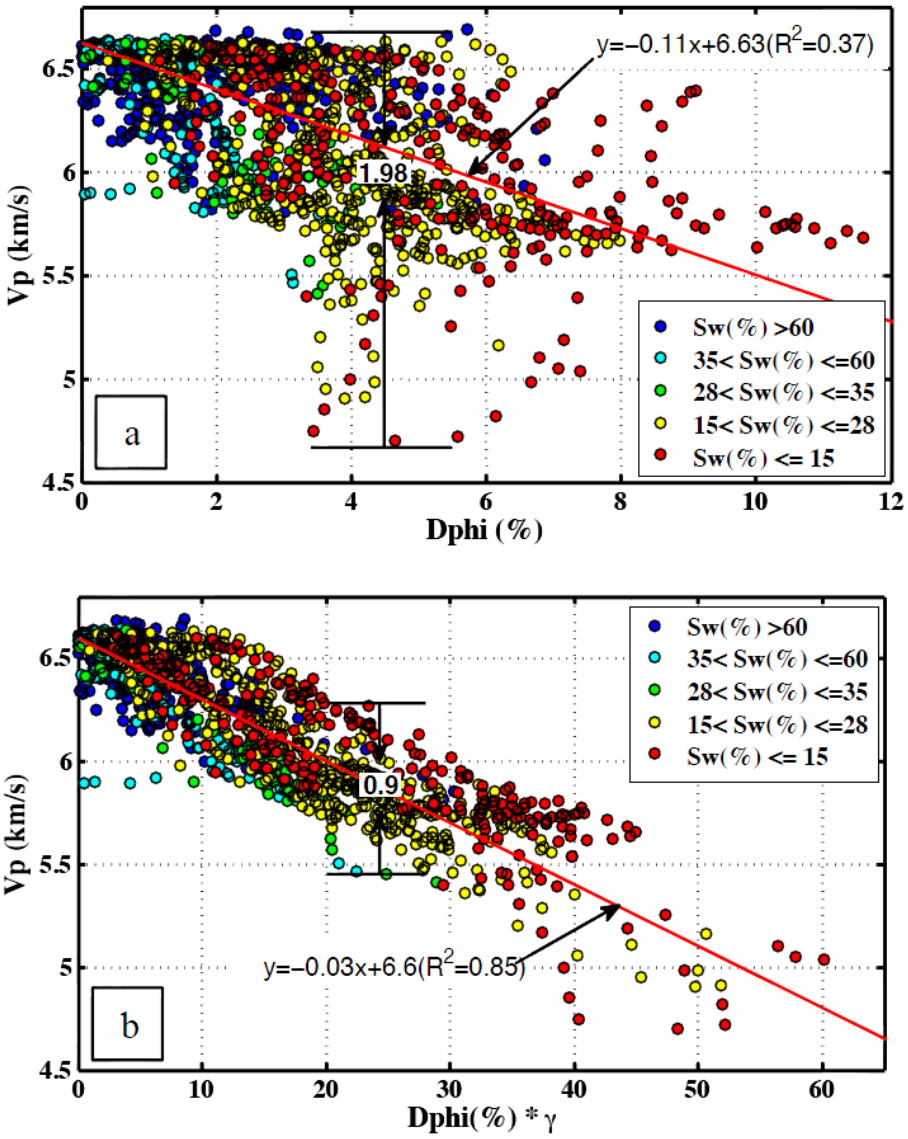

Figure 3.2. a) Crossplot of P-velocity versus porosity for different water saturation (Sw) shown by color. b) Crossplot of P-velocity versus the product of porosity and frame flexibility factor for different water saturation (Sw) shown by color.

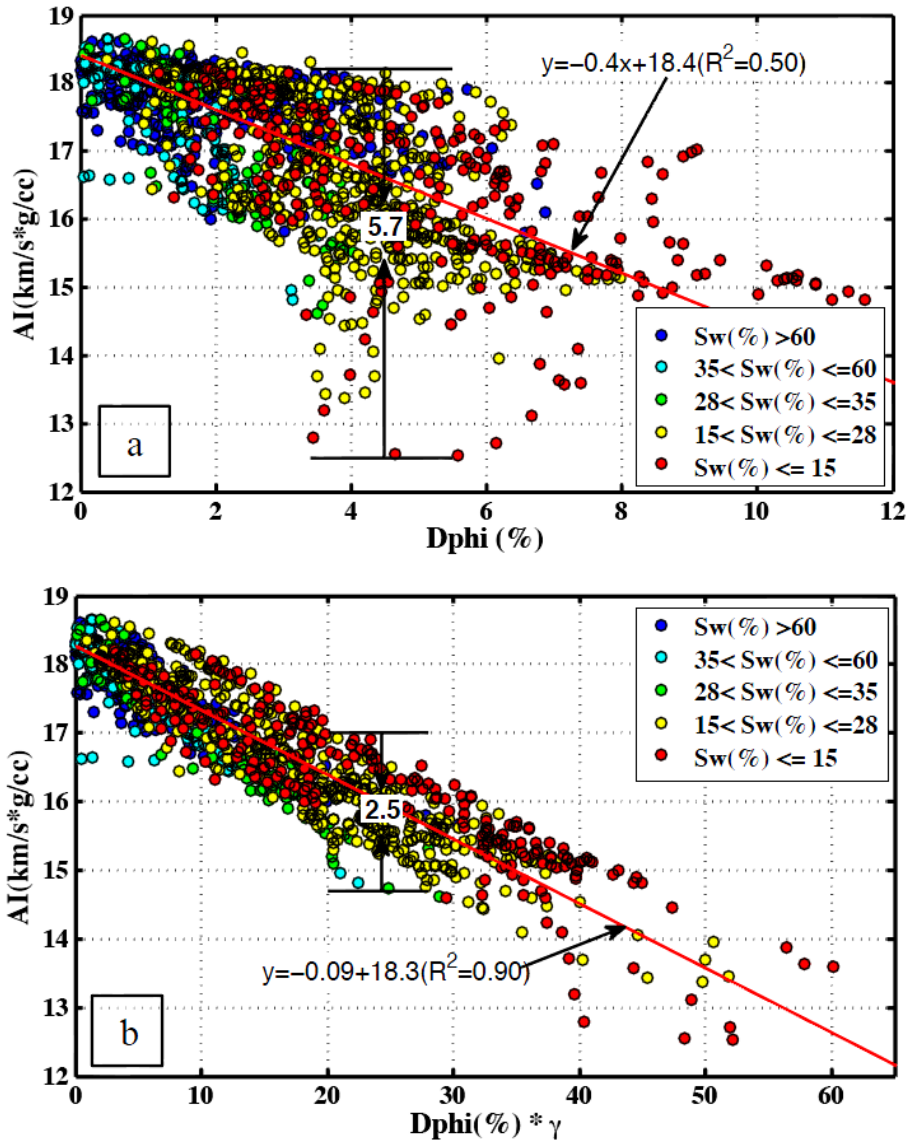

Figure 3.3. a) Crossplot of acoustic impedance versus porosity for different water saturation (Sw) shown by color. b) Crossplot of acoustic impedance versus the product of porosity and frame flexibility factor for different water saturation (Sw) shown by color.

It is noted that the data points from the non-gas zones (blue) are much more localized into the small region where the product of porosity and frame flexibility factor is low. This is because water-saturated zones usually have lower frame flexibility factor

values than the gas-saturated zones. Gas-saturation increases as the product of porosity and frame flexibility factor increases.

Figure 3.3a shows the acoustic impedance (a product of P-wave velocity and density, labeled as P-impedance) versus porosity with water saturation indicated by color. Like the velocity-porosity crossplot, the crossplot of P-impedance and porosity shows similar large scatters. When porosity is around 4%, P-impedance has a large variation of 5.7 (g/cc)×(km/s). Again, for the data points above the best-fit line, the porosity inverted from P-impedance if the best-fit line is used could be lower than it should be; for the points below the best-fit line, the porosity could be higher. The R-square of the linear relationship between P-velocity and porosity is only 0.5. Thus, conventional acoustic impedance inversion methods that use best-fit lines could not provide accurate estimation of porosity from seismic data in such cases.

In contrast to the P-impedance-porosity crossplot shown in Figure 3.3a, Figure 3.3b shows the crossplot of P-impedance versus the product of porosity and frame flexibility factor (labeled as product). It can be seen that the correlation between impedance and the product shown in Figure 3.3b is improved dramatically and is much better than that between impedance and porosity alone shown in Figure 3.3a. Depending less on lithology, the relationship between P-impedance and the product of porosity and frame flexibility factor is

$$AI = C\text{-}D \times \gamma\phi \qquad (3.8)$$

where C and D are 18.3 and 0.09, respectively for the studied reservoir units. The R-square is 0.90.

As for the velocity-product crossplot in Figure 3.2b, the data points from the non-gas zones (blue) on the P-impedance and product crossplot in Figure 3.3b are also much more localized into the small region where the product of porosity and frame flexibility factor is low. The correlation between P-impedance and the product of porosity and frame flexibility factor shown in Figure 3.3b is actually better than the correlation between velocity and the product of porosity and frame flexibility factor because of the effect of density. This further indicates that gas-saturation tends to increase with the product of porosity and frame flexibility factor.

The relationships between velocity or acoustic impedance and product of porosity and frame flexibility factor could improve seismic inversion results if this product can be suitably inverted from seismic data. Figure 3.4 shows a profile of the inverted product of porosity and frame flexibility factor through Well A. The posted log curve is the water saturation. At the well location, the inverted product of porosity and frame flexibility factor corresponds well to the water saturation log.

3.5 Conclusions and remarks

Field study of ultra-deep carbonate gas reservoirs in Sichuan basin of China demonstrates that the frame flexibility factor derived from an extended Biot theory is of great importance for understanding the porosity-velocity complexity in carbonate reservoirs. The correlation between velocity and the product of frame flexibility factor and porosity is much better than that between velocity and porosity alone. The correlation between P-impedance and the product of porosity and frame flexibility factor

is even better than the correlation between velocity and the product of porosity and frame flexibility factor. These results prove to be useful for seismic inversion and they should be applicable to ultra-deep hydrocarbon reservoirs in other similar settings.

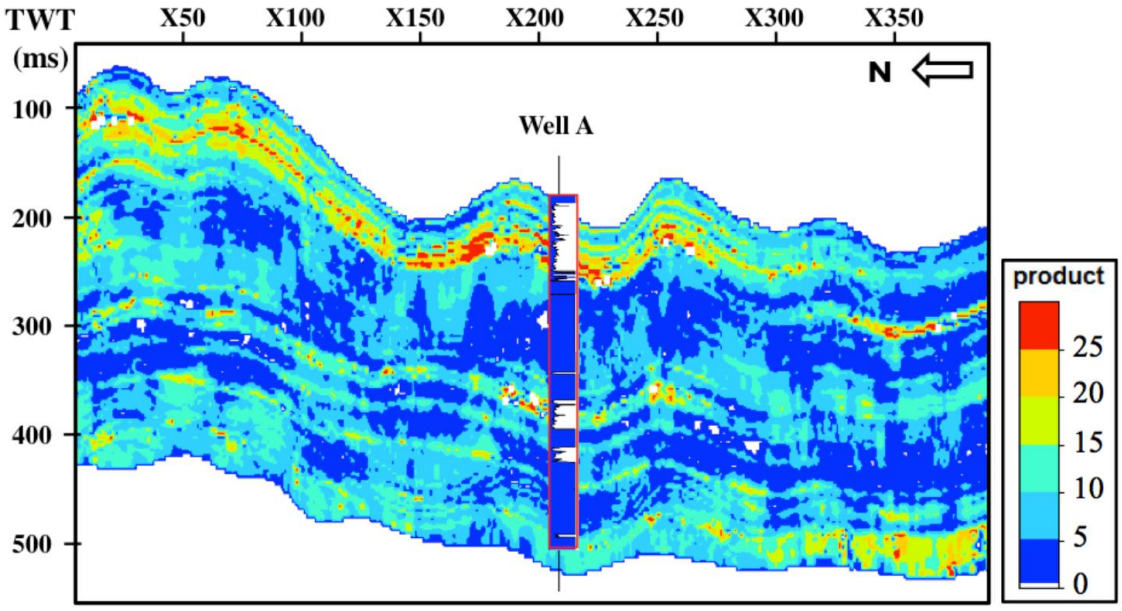

Figure 3.4. The profile of the inverted product of porosity and frame flexibility factor through well A. The posted log curve is water saturation, and the vertical red line is the well path.

CHAPTER IV

PREDICTING FRACTURED ZONES USING ROCK PHYSICS BASED PRESTACK SEISMIC INVERSION IN A DEEP BURIED CARBONATE HILL OF BOHAI BAY BASIN, CHINA

4.1 Summary

Fractures and fracture-related dissolution pores (cavities, molds, and/or vugs) provide the major conduit and/or storage space for hydrocarbons in the deeply buried carbonate hill of Hexiwu field, Bohai Bay basin, China. Using standard and image logs available, it is found that low acoustic impedance and bulk modulus are typical signatures of fractured zones and high-porosity rocks. Fracture detection using high-resolution enhanced prestack seismic data becomes essential to find porous and/or highly permeable zones in the deep formation of Hexiwu field.

Analysis of two adjacent wells, where standard logs, shear wave logs, and FMI logs are available, shows that fractured zones usually occur where porosity is less than 5%. Fractured zones generally have much lower bulk modulus than tight limestone at similar porosity. Moreover, fracture angle strongly influences the elastic properties of rocks. At given porosities, fractured zones with large-angle fractures tend to have lower bulk and shear moduli than those with low-angle fractures. In addition, fractured zones with open fractures clearly have lower bulk moduli than those with sealed fractures at similar porosities whereas the shear moduli similar. Fractured zones with open and

large-angle fractures in the studied low-porosity (less than 5%) carbonate rocks usually have bulk moduli lower than 55 GPa and P-impedance lower than 15,500 (g/cc)×(m/s).

Fractured zones as thin as 20-m-thick can be imaged using resolution-enhanced 3D prestack seismic data available for the study. 3D distribution of fractured zones in Hexiwu buried hill reveals that the distribution of fractures is closely related to the fault structure, and is controlled by the regional tectonics. The described methodology may also be applicable for fracture detection in other deep conventional and unconventional reservoirs.

4.2 Introduction and geological background

The hydrocarbon exploration in buried carbonate hills started in 1975 in the Bohai Bay basin. Since then more than 20 carbonate hill reservoirs (Renqiu, Yanling, Balizhuang, Hejian, Nanmeng, Longhuzhuang, Yongqing, Suqiao, Hezhuang, Shenxi, and Jingqiu and so on) have been discovered (Zhao et al., 2012). All of them are classified as easily discovered buried-hill head reservoirs due to their shallow burial, their relationships with control faults, and their large reservoir thickness. Nowadays, the exploration target has changed to difficult-to-discover buried-hill slope reservoirs and buried-hill internal reservoirs for more oil/gas accumulations. The complex sedimentary and structural setting, primary sedimentology and stratigraphy studies, limited deep drilling wells, and the low-resolution of seismic data acquired add extreme difficulty to discover those difficult-to-discover reservoirs.

4.2.1 Tectonic setting

Bohai Bay basin, which has an area of about 200,000 km^2, is located in the eastern part of China (Figure 4.1). It is one of the most petroliferous basins in China. Bohai Bay Basin is predominantly a Cenozoic rifting basin or extensional basin (Qi and Yang, 2010), and mainly bounded by Yanshan folded belt in the north, by Taihangshan uplift in the west, Liaodong uplift, Ludong uplift, and Luxi uplift in the east. Based on the distribution of Paleogene deposits, the Bohai Bay basin is subdivided into eight depressions and five uplifts (Qi and Yang, 2010, Figure 4.2). Jizhong Depression is in the northwestern part of Bohai Bay basin. Langgu Sag (shown by a green box in Figure 4.2) is one of major sags in Jizhong Depression. The tectonic pattern of carbonate burial

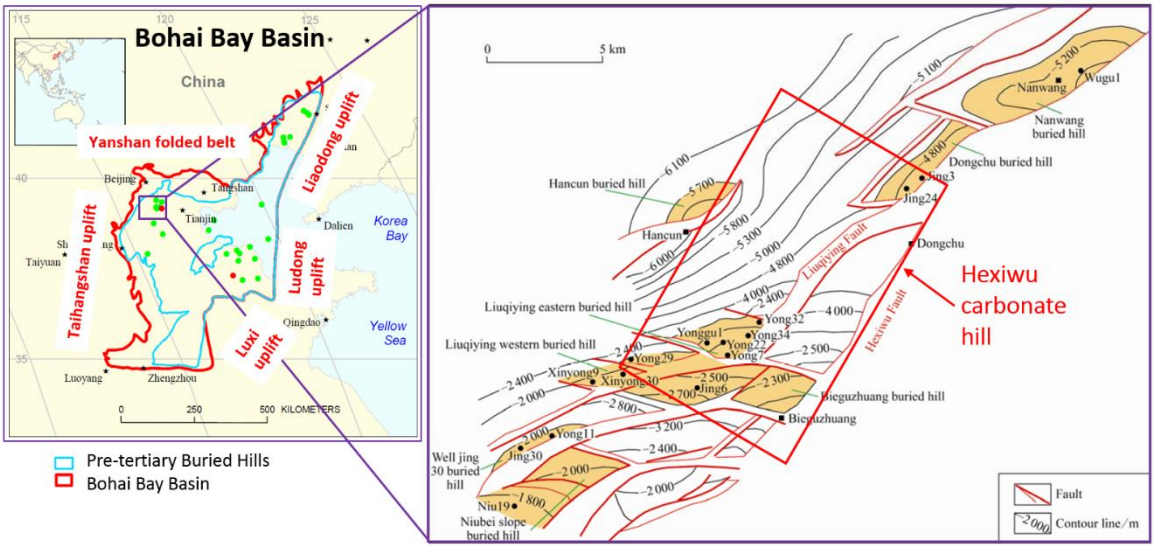

Figure 4.1. The right figure shows the structure map of Langgu Sag. The red box indicates the location of the Hexiwu carbonate hill (modified from Guo et al., 2009). The left figure shows the tectonic setting of the Bohai Bay basin. Langgu Sag is in the northwest part of the Bohai Bay basin (modified from the map of USGS Energy Resources Program).

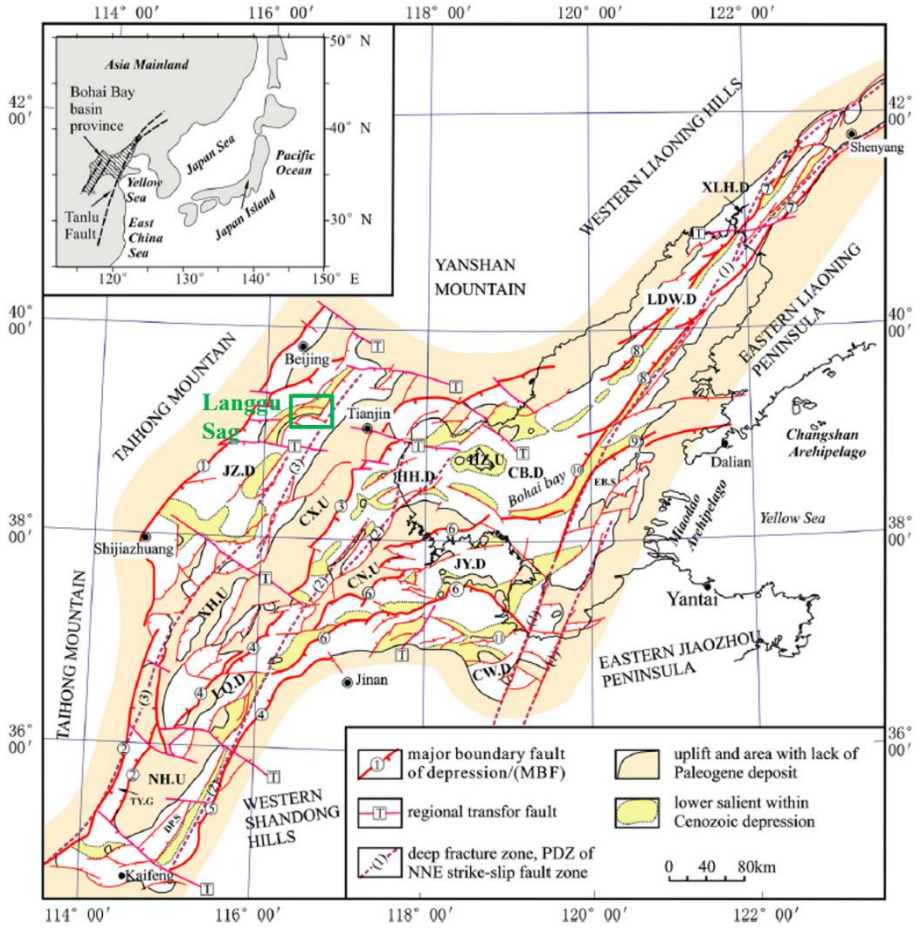

Figure 4.2. The structure map of the Bohai Bay basin (From Qi and Yang, 2010). According to Qi and yang (2010), the simplified names of tectonic units: JZ.D for Jizhong Depression, CX.U for Cangxian Uplift, HH.D for Huanghua Depression, LQ.D for Linqin Depression, XH.U for Xunheng Uplift, DP.S for Dongpu Sag, NH.U for Neihuang Uplift, TY.G for Tangyin Graben, XLH.D for Xialiaohe Depression, LDW.D for Liaodongwan Depression, HZ.U for Haizhong Uplift, CB.D for Central Bohai Depression, EB.S for E. Bohai Sag, CN.U for Chenning Uplift, JY.D for Jiyang Depression, CW.D for Changwei Depression. The simplified names of master boundary faults: ① is the MBF of Jizhong Depression, ② is the MBF of Tangyin Graben, ③ is the MBF of Huanghua Depression, ④ is the MBF of Linqin Depression, ⑤ is the MBF of Dongpu Sag, ⑥ is the MBF of Jiyang Depression, ⑦ is the MBF of Xiaoliaohe Depression, ⑧ is the MBF of Liaodongwan Depression, ⑨ is the MBF of East Bohai Sag, ⑩ is t⑪MBF of Central Bohai Sag, is the MBF of Changwei Depression. The names of master right-lateral strike-slip faults: (1) is the Shenyang-Weifang strike-slip fault zone (northern part of the Tanlu Deep Fracture Zone), (2) is the Huanghua-Dongming strike-slip fault zone (Lanliao Deep Fracture Zone), (3) is the Baxian-Shulu-Handan strike-slip fault zone (Shulu-Handan Deep Fracture Zone).

hills in Jizhong Depression is controlled by the tectonic evolution of Jizhong Depression. Based on previous research (Du et al., 2002, Ren et al., 2002, Editorial committee of Petroleum Geology of China, 1987, Lu et al., 2011), the evolution of Jizhong Depression can be divided into five stages: 1) the forming stage (mid- and late-Proterozoic (Pt_{2-3}) and Paleozoic (Pz)) that constitutes the buried-hill's substances; 2) the initial forming stage (Mesozoic (Mz)) of the buried hills; 3) the dominant development stage (early- and mid-Eocene (E_2k-E_3s_2)) of the buried hills; 4) the adjusting and forming stage (late-Eocene (E_3s_1- E_3d); and 5) the deep-buried stage (Neogene and Quarternary (N-Q)).

Table 4.1. Main structural movements and development phase of karsts in Jizhong Depression (Guo et al., 2009).

Name of structural movement	Karsts phase	Main property of movement	Sedimentary hiatus	Karsts strata	Paleoclimate
Indo-China - Himalayan	V	Horizontal compression	Carboniferous-before Paleogene	All strata in buried hill	Dry alternating with warm and humid
Caledonian - Hercynian	IV	Elevation and subsidence	Late deposition period of Fengfeng Formation – before deposition of Benxi Formation	Top of Fengfeng Formation	Warm and humid
Jixian	III	Elevation and subsidence	Late deposition period of Jingeryu Formation – before deposition of Fujunshan Formation	Top of Jingeryu Formation	?
Tieling	II	Elevation and subsidence	Late deposition period of Tieling Formation – before deposition of Xiamaling Formation	Top of Tieling Formation	Warm and humid
Lingyuan	I	Elevation and subsidence	Late deposition period of Wumishan Formation – before deposition of Hongshuizhuang Formation	Top of Wumishan Formation	Warm and humid

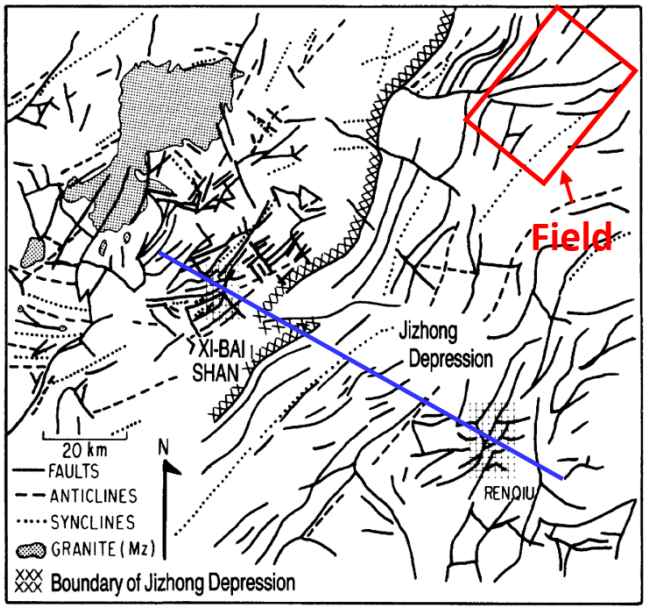

Figure 4.3. Outline map of regional structures in Jizhong Depression (Modified from Fei and Wang, 1984). The red box indicates the research area.

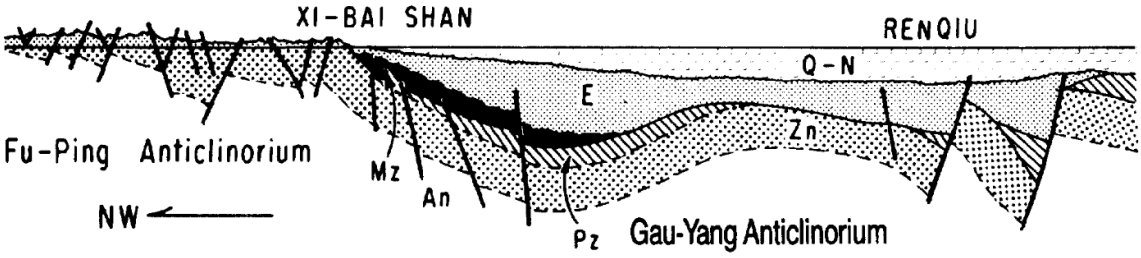

Figure 4.4. A profile view of faulting system in Jizhong Depression (Fei and Wang, 1984). It is marked as a blue line in Figure 4.3.

The Hexiwu carbonate hill is located in the middle part of Langgu Sag, Jizhong Depression of Bohai Bay basin (Figure 4.1). Guo et al. (2009) analyzed the main structural movements and development phase of karsts in Jixian to Paleogene system in the Hexiwu area (Table 4.1). During Lingyuan, Tieling, Jixian, and Caledonian-Hercynian period, Hexiwu area mainly experienced elevation and subsidence vertically

and five major unconformities were formed. From Indo-China to Himalayan period, horizontal compression was dominant in this area and facilitated the development of minor faults and fractures.

Figure 4.3 and 4.4 shows the complicated structure in Jizhong Depression. Most of the faults are north/northeast oriented, including the boundary faults of Jizhong Depression. Guo et al. (2009) studied the fracture orientation of two wells—Jing3 and Yong29-2—in the Hexiwu area. He found out the fractures were primarily developed in NE and NW direction. Based on Wang and Zhu's research (2003), the NW fractures were formed during Yanshan tectonic period and the NE fractures were formed during Himalayan period.

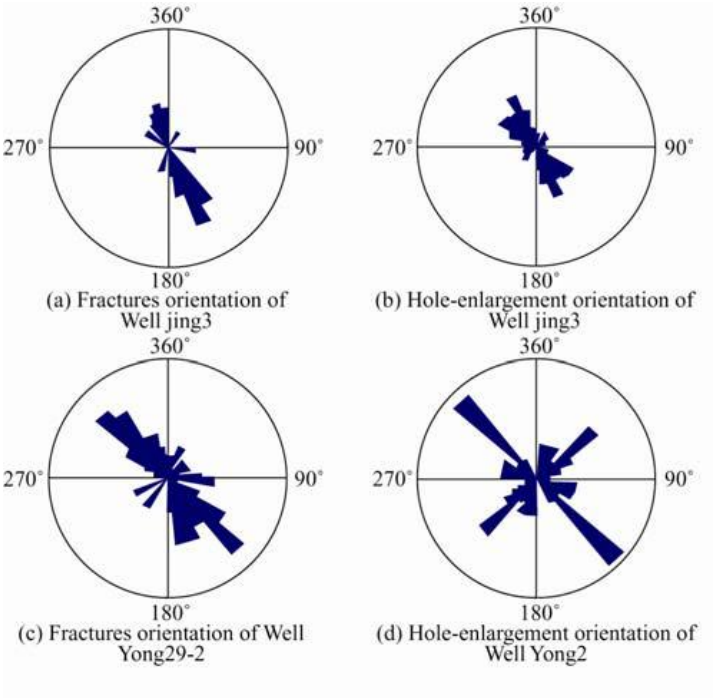

Figure 4.5. Fracture orientation and hole-enlargement orientation (Guo et al., 2009).

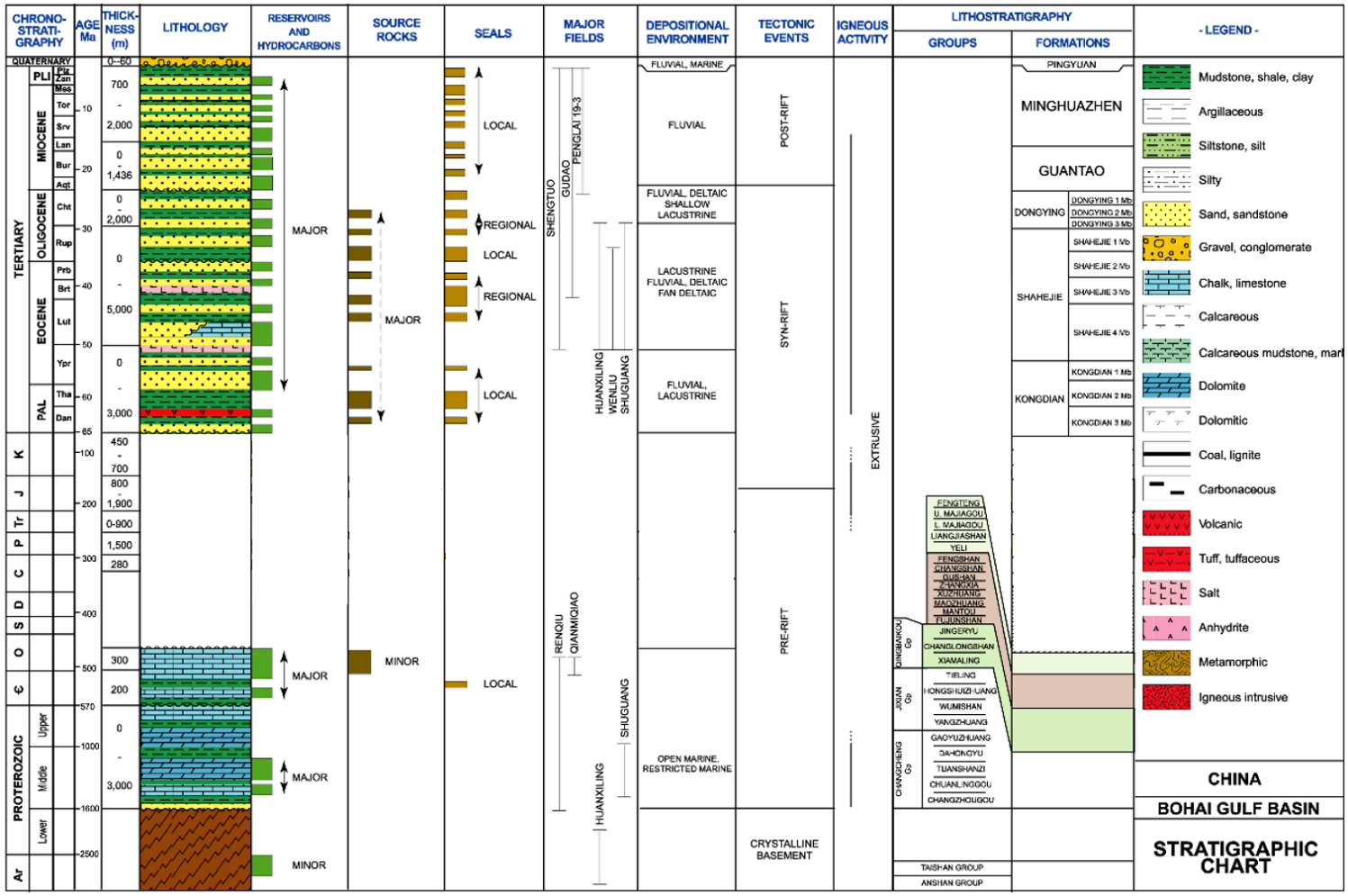

Figure 4.6. Sequence stratigraphy in Hexiwu area (Modified from USGS Energy Resources Program).

4.2.2 Petroleum system

The multiple elevation and subsidence due to tectonic movements created more than five unconformities (Guo et al., 2009) in Jizhong Depression. One major unconformity is separating Ordovician carbonates and overburden strata. In the Hexiwu area, the major strata of carbonate hill comes from the Ordovician (Figure 4.6). Three formations—Fengfeng, Upper Majiagou, and Lower Majiagou Formation—are subdivided in this area. The overburden strata from Silurian to Cretaceous are eroded away during elevation.

The Hexiwu buried hill has undergone the destruction and reconstruction of long time, multistage, and strong diagenesis during burial. The primary pore space in the rock was closed due to intense cementation and compaction. The residual storage space in carbonate hill reservoirs is mainly from dissolution pores, such as cavities, fractures, molds and vugs associated with fractures (Guo et al., 2009).

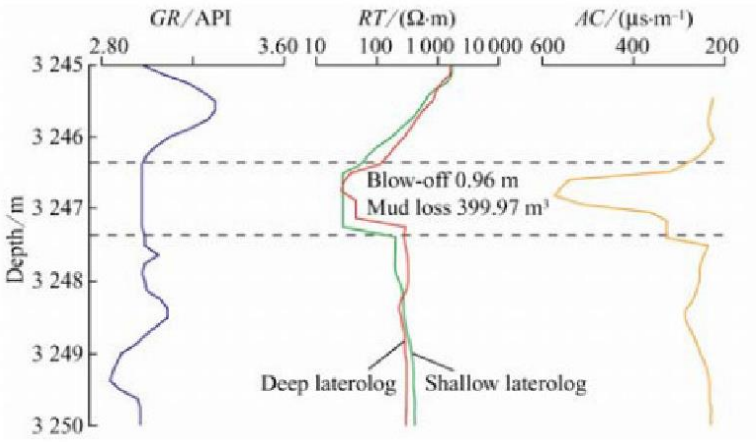

Figure 4.7. Log response of large caves in Majiagou Formation of Well Yong 34 in Langgu Sag (Guo et al., 2009).

Cavity refers to dissolved pores and caves, which have a size of more than 2 mm (Guo et al., 2009). One feature of cavities is that they have irregular shape and different size from millimeter to meter or even larger. According to its size, dissolved cavity can be divided into three categories: 1) larger cavity with diameter more than 50 cm (Figure 4.7), 2) middle cavity with diameter between 10 cm to 50 cm, and 3) small cavity with diameter larger than 2 mm but smaller than 10 cm. The occurrence of dissolved cavity usually accompanied the erosion of carbonate strata during the tectonic elevation period, and it is a major member of storage space in buried-hill head reservoirs (Zhao et al., 2012).

Multiple elevation and subsidence and the compressional stress field in the Hexiwu area created well-developed fractures in carbonate buried hill. Fractures generally have limited contribution to storage space (less than 2%), but it has tremendous and positive influence on permeability. Based on Guo et al.'s (2009) classification, three types of fractures are defined. They are 1) pressolved fractures, 2) dissolved fractures, and 3) structural fractures (Figure 4.8). Pressolved fractures also refer to as satures. They are commonly observed in limestone, but less in dolostone. Dissolved fractures were mainly formed during late period and related to structural fractures. Structural fractures, closely relating to folds and faults, were formed under regional horizontal compressional stress during the Indo-China and Himalayan period. Figure 4.8 shows two typical thin sections presenting structural fractures from the Hexiwu area. One has open structural fractures from Fengfeng Formation of Yong 11. The other one has multiple-stage fractures filled by calcite from Wugu 2. For the

exploration of buried-hill slope reservoirs and buried-hill internal reservoirs, the detection of open structural fracture is a key step.

Molds and vugs, associated with fractures, are dissolved pores with diameter smaller than 2 mm. According to Guo et al. (2009), inter-crystalline dissolved pores, non-fabric dissolved pores, and intergranular dissolved pores are commonly observed under microscopes and scanning electron microscopies. Molds and vugs are usually developed with fractures and satures (Figure 4.9). They provide the major storage space for buried-hill slope reservoirs and buried-hill internal reservoirs.

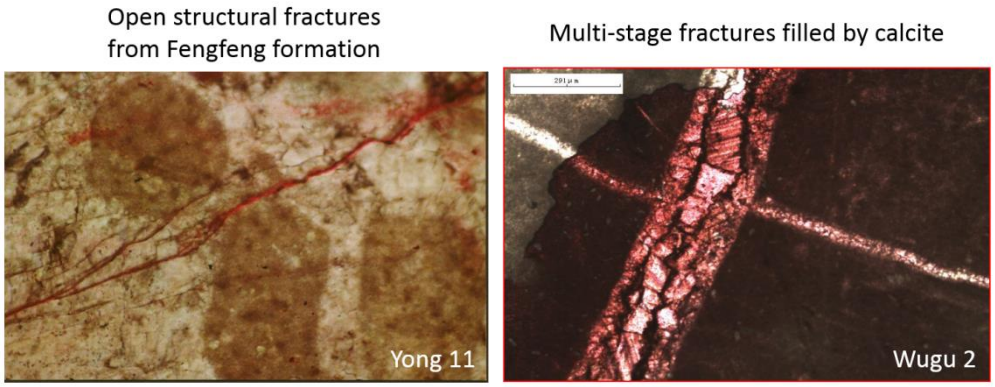

Figure 4.8. Thin sections show fractures in the Hexiwu area.

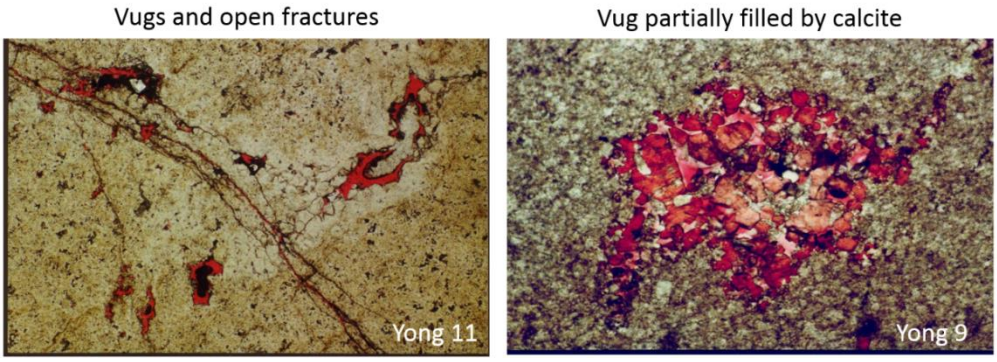

Figure 4.9. Thin sections show vugs in the Hexiwu area.

The main source rock charging carbonate buried-hill reservoirs is lacustrine shale in the Paleogene Shahejie Formation unit Es_3, and the next are units Es_4 and Es_1 (Figure 4.6) (Zhai and Zha, 1981, Zha, 1984). The maximum thickness of source beds is up to 1,000 m in the depocenter. The main kerogen types are humic in northern part of Jizhong Depression, and mixed in the southern and middle parts. Organic matter is abundant and has a high conversion rate for any kerogen type. The sealing rock is also Paleogene lacustrine shale (Figure 4.6). It is well proved that the hydrocarbon migration is through faults and/or unconformities to charge carbonate buried-hill (Zha, 1984).

4.2.3 Reservoir types

According to Zha (1984), the reservoir types in carbonate buried-hill can be subdivided into 11 groups (Figure 4.10): (A) oil and gas pools on the hilltop, which is also called buried-hill head reservoirs, including massive, bedded, wedge shaped, and irregular; (B) oil and gas pools on the slope of the buried hill, which is also called buried-hill slope reservoirs, in wedged shape and irregular shape; and (C) oil and gas pools within the buried-hill, which is also called buried-hill internal reservoirs, including semisubtle massive, semisubtle bedded, semisubtle irregular, subtle massive, and subtle bedded.

The major effort in the past is to discover oil and gas pools on the hilltop, such as Renqiu field. Therefore, there is a potential to find oil and gas on the slope of the buried-hill and within the buried-hill. It is clear that fractures play important roles in both porosity and permeability increment for buried-hill slope reservoirs and buried-hill internal reservoirs. Thus, fracture detection in the Hexiwu area is a key step to discover

more reservoirs in buried-hill. In this chapter, I analyze the geophysical signatures of fracture zone, propose the inversion method based on rock physics model, and carry out prestack seismic inversion for fracture zone prediction.

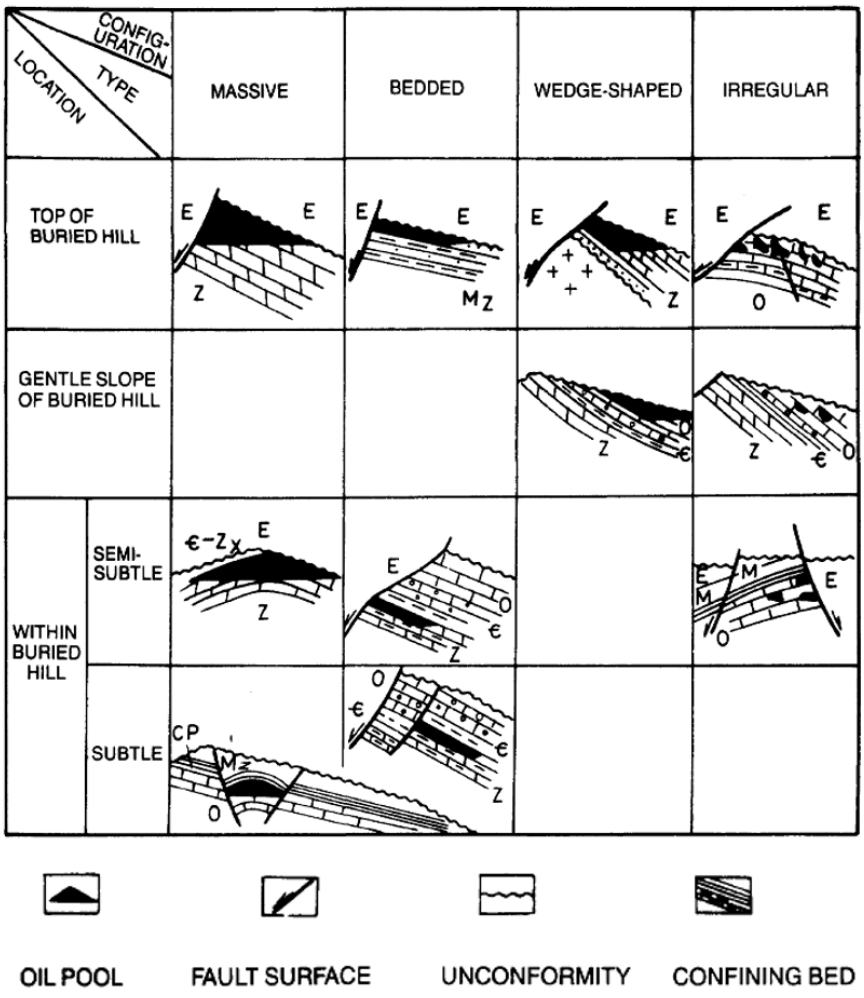

Figure 4.10. Types of buried-hill oil/gas pool (from Zha, 1984).

4.3 Data

Hexiwu area is a highly-explored oil/gas filed. However, the past exploration effort was primarily on Paleogene lacustrine sandstone, which is shallow buried and has low exploration and production risk. We have very few paper and electronic records of core measurements. And the core of few wells from Ordovician carbonate hill is also limited in length and usually breaks into small pieces. It is impossible to do more core measurements for petrophysical parameters, like P-velocity, S-velocity, and so on. Additionally, most of logging data are only recording the sandstone layers, except Jing 3, Jing 24, Jing 30, Wugu 2, and Wugu 4. Only Wugu 2 and Wugu 4 have sonic logs. I use Jing 3, Wugu 2, and Wugu 4 to build initial model for acoustic impedance inversion from poststack seismic data. Considering the methodology of combining prestack seismic inversion and Sun rock physic model, we can only use Wugu 2 and Wugu 4. The limited core and logging data add difficulty to fracture zone detection in this area.

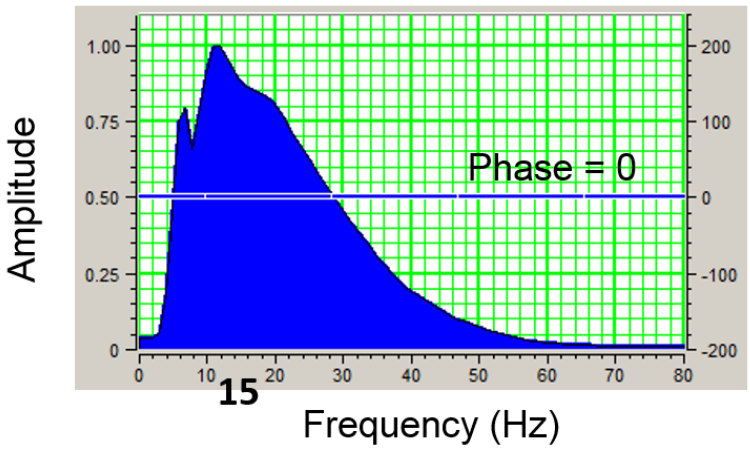

Figure 4.11. The amplitude spectrum of poststack seismic volume in Fengfeng, Upper Majiagou, and Lower Majiagou Formation.

The existing seismic data (CRP and poststack) has low-resolution with a central frequency of 15 Hz in our target formations (Fengfeng, Upper Majigou, and Lower Majiagou Formation) (Figure 4.11). The acoustic impedance inversion from low-resolution seismic data based on model based inversion method fails to identify the two highly-fractured zones (identified with low P-velocity) at well Wugu 2 location (Figure 4.12).

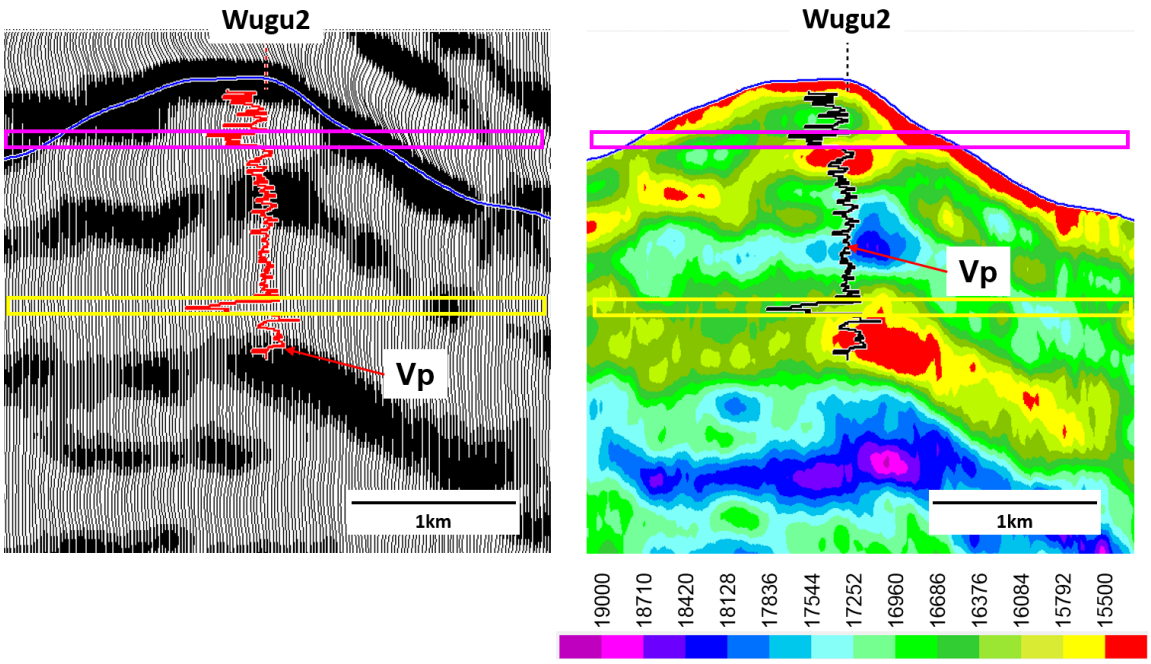

Figure 4.12. Acoustic impedance inversion result (right figure) from low-resolution seismic data (left figure). The inserted well is Wugu 2, and the inserted log is P-velocity. Two marked layers are interpreted as highly-fractured zones based on logging data.

One method proposed by Sun (2003) to increase the resolution of seismic data is applied in the Hexiwu project. The detailed introduction and one previous application of this method on Puguang gas field to identify thin gas beds is attached in appendix A.

Figure 4.13 shows the high-resolution processing result of conventional poststack seismic data in the Hexiwu field. The top figure is the conventional seismic data while the bottom one is the high-resolution seismic data. In the yellow box, it is clear that the high-resolution seismic data has much more reflections than conventional seismic data. The amplitude spectrum extraction shows the frequency range of high-resolution seismic data is improved to as high as 55 Hz, which is much higher than that of conventional seismic data. The high-resolution seismic data is one key input for fracture zone prediction in the Hexiwu structural belt.

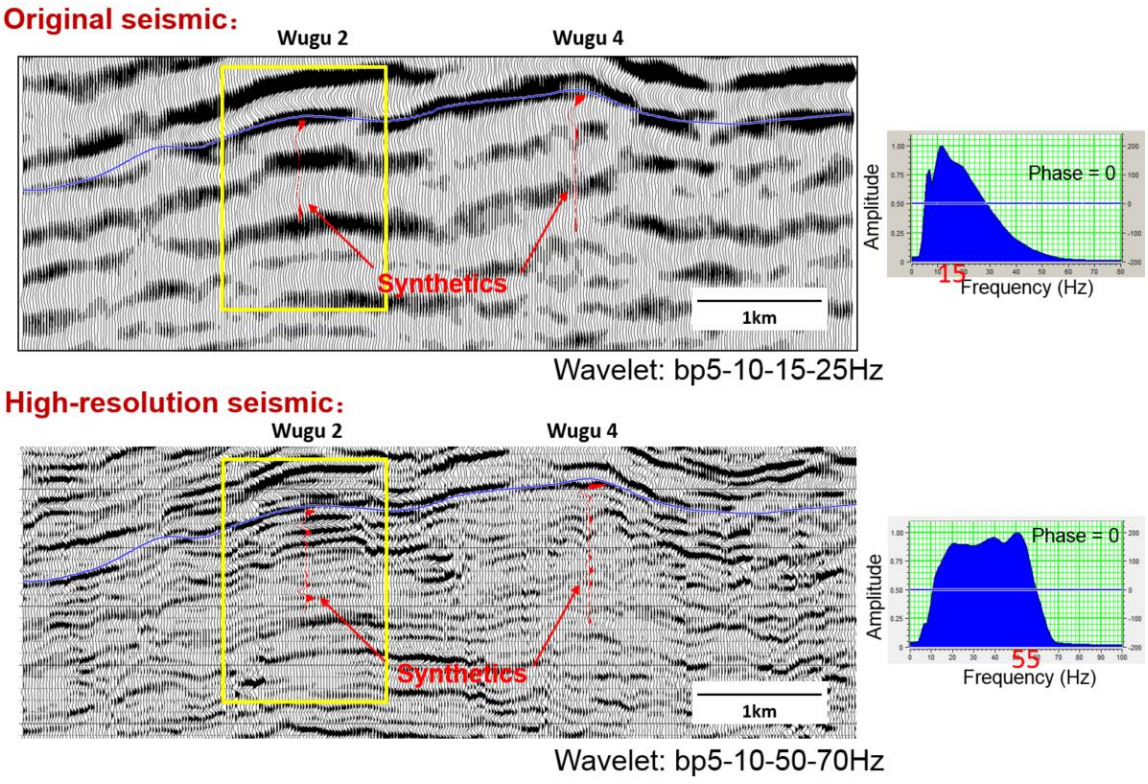

Figure 4.13. The comparison between conventional seismic data and high-resolution processed seismic data.

4.4 Method

Rock physics analysis and seismic inversion are two important and necessary steps to detect fractured zones in Hexiwu carbonate hill. Sun rock physic model (Sun, 2000, 2001, and 2004) has been introduced in the method part of part II and part III. It is derived based on poroelasticity to quantify the pore-structure effect on sonic velocity and permeability in reservoir rocks. It provides a theoretical and practical bridge to tie petrophysical measurements (such as density, P-velocity, S-velocity, porosity, and permeability) to seismic data, which makes it possible to predict the pore structure variations (vuggy, moldic, inter-particle, inter-crystal, micro-porosity, and fracture, and so on) in sedimentary rocks, especially in carbonates that have more complicated pore type complexes. The log analysis will analyze the pore structure features of fractured zones and seismic inversion will help in identifying fractured zones in a map view.

4.4.1 Log analysis

Wugu 2 and Wugu 4 are only two wells penetrating Fengfeng, Upper Majiagou, and Lower Majiagou Formation and having sonic logs. Only Wugu 2 has FMI log. The main idea of doing log analysis is to identify the unique petrophysical identity of certain features (such as different mineralogy zone, different fluid zone, and fracture zone, and so on) by highlighting those features on the crossplots of any two petrophysical parameters. The common crossplots I usually draw include the crossplot of sonic velocity versus porosity, moduli versus porosity, impedance versus porosity, sonic velocity versus the product of porosity and pore structure parameter, moduli versus the

product of porosity and pore structure parameter, and impedance versus the product of porosity and pore structure parameter and so on.

4.4.2 Poststack seismic inversion

The poststack seismic inversion method used in this chapter is model-based inversion (Figure 4.14). This inversion method provides stable and fast inversion result. After acquiring acoustic impedance (AI), the methodology in Chapter III is applied and the product of porosity and pore structure parameter is estimated for reservoir characterization.

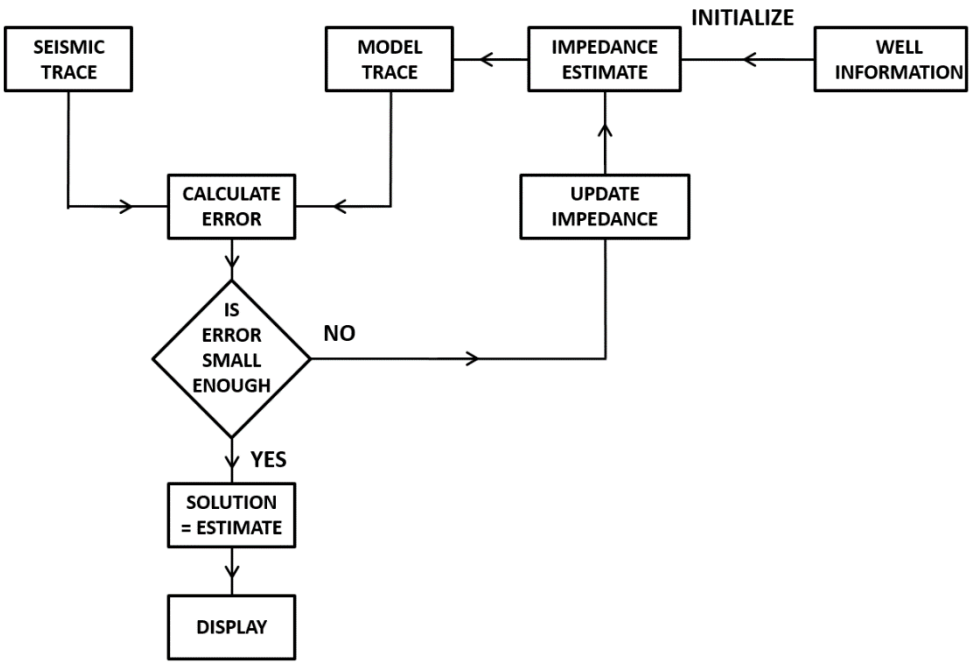

Figure 4.14. The flow chart of model-based inversion method (modified from Russell, 1988).

4.4.3 Prestack seismic inversion

Dou (2011), in his dissertation, proposed a two-step method for the estimation of porosity and pore structure parameter in an ultra-deep carbonate reservoir. One limitation is the shear impedance inversion from far-angle seismic set. Due to the large depth (greater than 5000 m), the largest angle that can be processed with real amplitude is only around 20 degree, which is far less than required for the accurate inversion for shear impedance.

In this dissertation, the two-step method will be implemented. In the first step, however, I will use gradient impedance to substitute shear impedance to improve the inversion accuracy.

4.4.3.1 Theoretical methodology

Connolly (2010) defined the gradient impedance based on the AVO theory of intercept and gradient (Equation 4.1), which can be inverted from the gradient volume. The common processing of gradient volume is to take the difference of the largest angle and the lowest angle set in angle gathers.

$$GI = Vp * Vs^{-8k} * \rho^{-4k} \tag{4.1}$$

where k is the Vs-Vp ratio square.

The substitution of shear impedance (SI) by gradient impedance (GI) will compromise the limitation in Dou's method (2011) and therefore will help the estimation of porosity and pore structure parameter more accurately.

According to Connolly (1999), elastic impedance is defined in Equation 4.2.

$$EI = Vp^{(1+\tan^2\theta)} * Vs^{(-8k\sin^2\theta)} * \rho^{(1-4k\sin^2\theta)} \tag{4.2}$$

where θ is the incident angle. It is approximating the impedance at different incident angle. When incident angle is zero, we have acoustic impedance. Acoustic impedance is expressed as

$$AI = \rho * Vp \tag{4.3}$$

The relationship among AI, EI, and GI can be expressed as

$$GI = \frac{EI - AI}{\theta} \tag{4.4}$$

Suppose k=0.25, that is Vs is half of Vp for certain lithology, the combination of AI and GI will have the following Equation 4.5.

$$AI * GI = (\frac{Vs}{Vp})^{-2} \tag{4.5}$$

Thus, we have

$$\frac{Vs}{Vp} = \sqrt{\frac{1}{AI * GI}} \tag{4.6}$$

Put Equation 4.6 to 4.1, 4.2, and 4.3, the P-velocity can be resolved as

$$Vp = (\frac{AI * GI^{4k\sin^2\theta}}{EI})^{\tan^2\theta - 4k\sin^2\theta} \tag{4.7}$$

Continuously, we have density and S-velocity expressed as

$$\rho = \frac{AI}{Vp} \tag{4.8}$$

$$Vs = Vp * \sqrt{\frac{1}{AI * GI}} \tag{4.9}$$

The second step is to apply Sun model and estimate porosity and pore structure parameters. The key equations in Sun model are summarized in Chapter II and Chapter III. Finally, the fractured zones will be predicted by combining the geology and inversion results.

This methodology is mathematically working to calculate P-wave, S-wave, and density from P-impedance (AI), elastic impedance (EI), and gradient impedance (GI). In reality, the calculation of P-wave is not stable due to the small values of exponents in 4.7 (<< 1). A better way of doing prestack seismic inversion for porosity and pore structure evaluation in Huabei field is written in detail in the following part.

4.4.3.2 Practical methodology

In this part, all the data are logs or log computed parameters. The purpose is to verify the feasibility of the proposed methodology.

Gradient impedance is calculated from low incident angle elastic impedance and large incident angle elastic impedance logs based on Equation 4.4 (Figure 4.15). Therefore, the Vs-Vp ratio is estimated by Equation 4.6, which is the X-axis in Figure 4.16. The comparison between Vs-Vp ratio and estimated Vs-Vp ratio clearly shows that the estimated Vs-Vp ratio is very close to the real Vs-Vp ratio, which is one key step in this work. This estimation method of Vs-Vp ratio can also be used to find AVO Class III reservoirs.

The next step is to estimate bulk modulus and shear modulus. It is found out that there is a linear relationship between P-impedance and bulk modulus with the restriction of the estimated Vs-Vp ratio (Figure 4.17). The estimated result is compared with bulk

modulus computed from density and P-, S-velocity logs in Figure 4.18. The bulk modulus is well estimated with R^2 0.9 for Wugu2 and 0.87 for Wugu 4 respectively.

Considering the expressions of P-velocity and S-velocity with bulk modulus, shear modulus, and density, the shear modulus can be expressed in Equation 4.10. The calculated shear modulus is compared to shear modulus from density and S-velocity logs in Figure 4.19. The shear modulus is also well estimated with R^2 0.87 for Wugu2 and 0.8 for Wugu 4 respectively.

$$\mu = \frac{(\frac{Vs}{Vp})^2 K}{1 - \frac{4}{3}(\frac{Vs}{Vp})^2} \tag{4.10}$$

The next key step is to estimate porosity from impedance logs and estimated bulk modulus and shear modulus. Combine the expressions of computing pore structure parameters in Sun model, it is easy to have

$$(\frac{\mu}{\mu_s})^{\frac{\gamma}{\gamma_\mu}} = \frac{k}{k_s} - \frac{(\frac{(k_s - k)}{k_s})^2 \frac{k_f}{k_s - k_f}}{\phi - \frac{(k_s - k)}{k_s}\frac{k_f}{k_s - k_f}} \tag{4.11}$$

where K_s and K_f are bulk modulus of the solid frame and fluid, μ_s is the shear modulus of solid frame.

The ratio of shear pore structure parameter and pore structure parameter can be expressed as

$$\frac{\gamma_\mu}{\gamma} = \frac{\log \mu - \log \mu_s}{\log k - \log k_s} + O(\phi) \qquad (4.12)$$

where $O(\phi)$ is a function of porosity and bulk modulus.

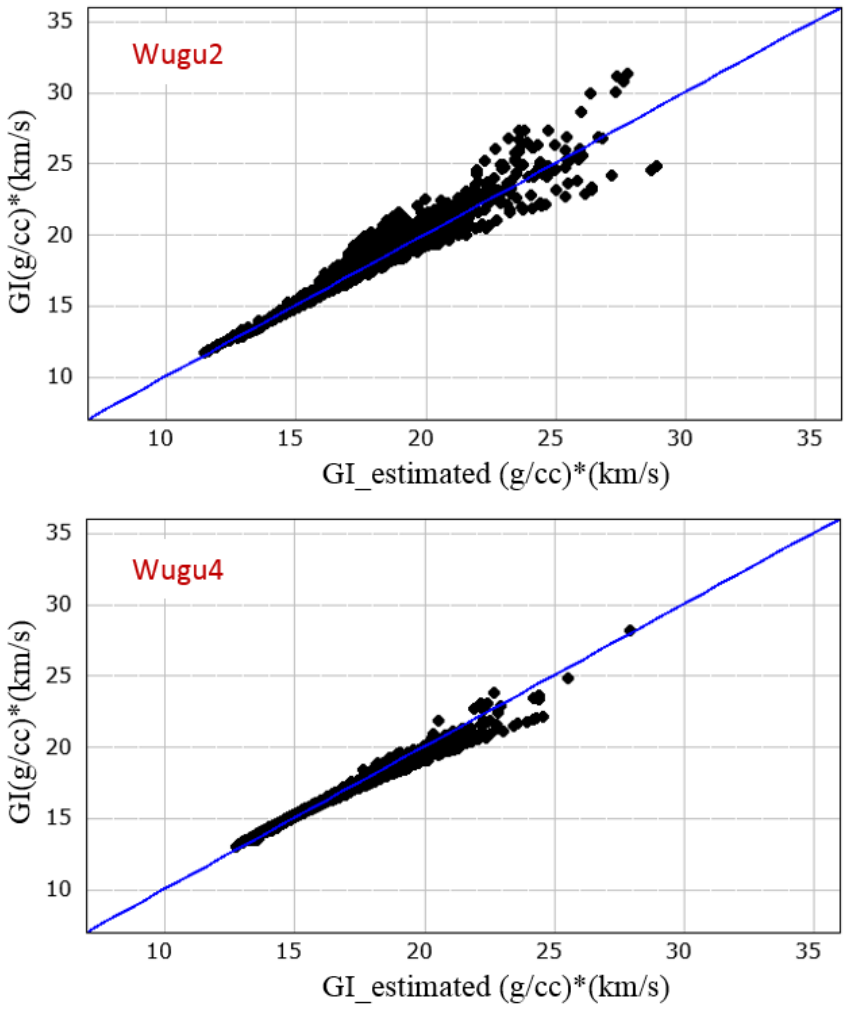

Figure 4.15. The comparison between GI from density, P- and S-velocity logs and estimated GI from elastic impedance.

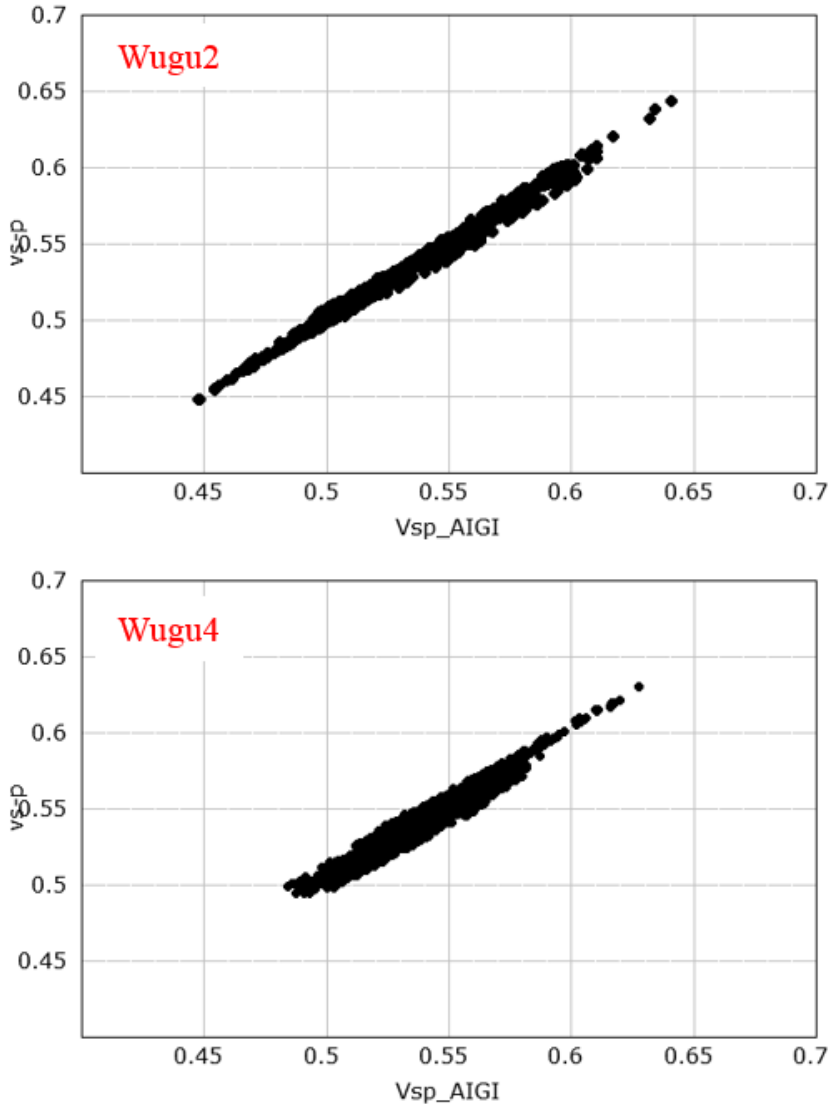

Figure 4.16. The comparison between Vs-Vp ratio and estimated Vs-Vp ratio.

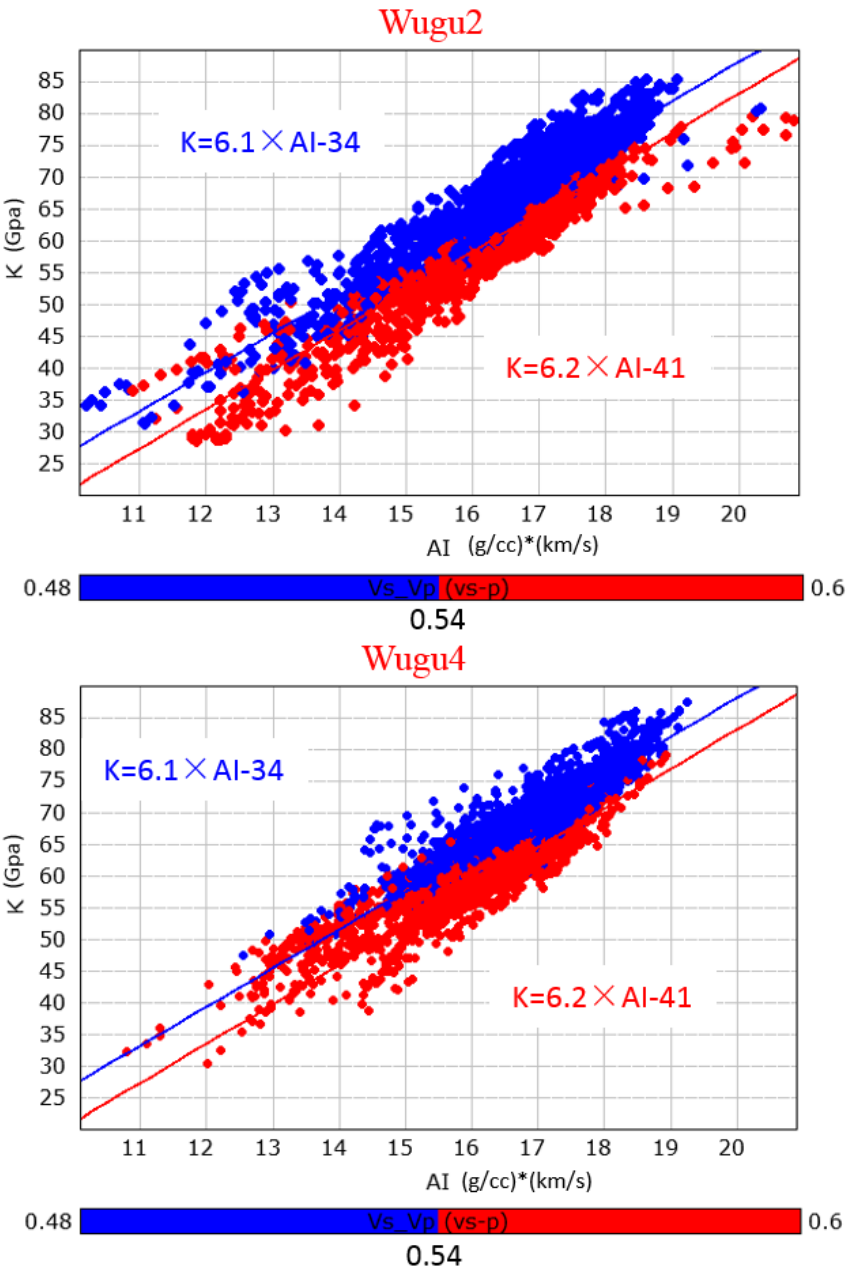

Figure 4.17. The linear relationship between P-impedance and bulk modulus for Wugu 2 and Wugu 4.

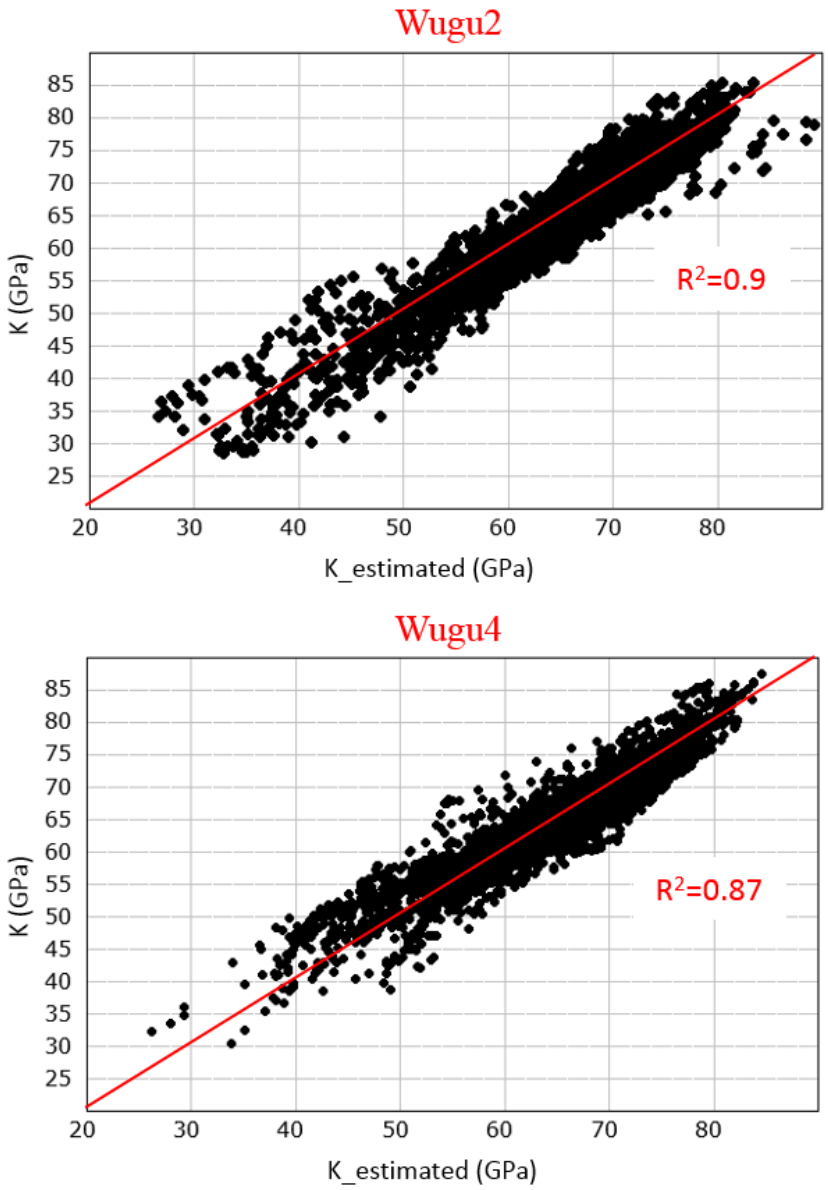

Figure 4.18. The comparison between the bulk modulus and the estimated bulk modulus.

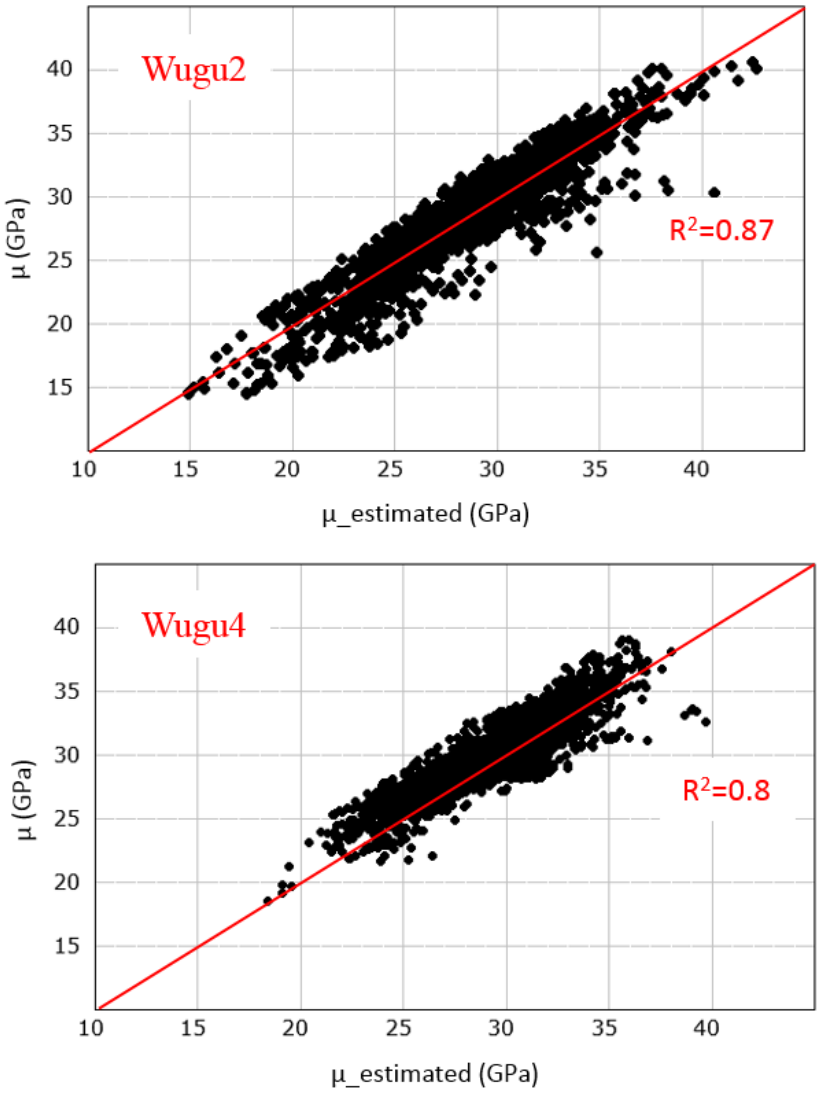

Figure 4.19. The comparison between the shear modulus and the estimated shear modulus.

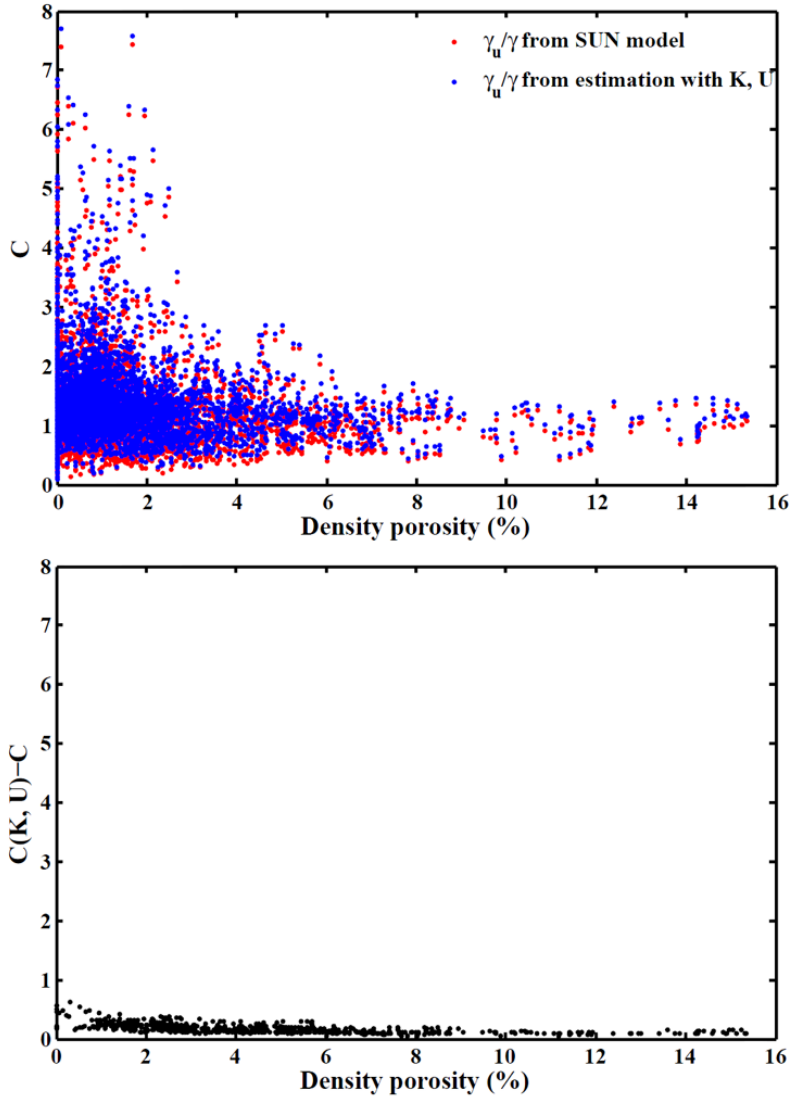

Figure 4.20. The crossplot of C (shear pore structure parameter versus pore structure parameter) versus density porosity (top). The crossplot of C difference between that from Sun model and that from Equation 4.12 by neglecting $O(\phi)$ versus density porosity (bottom). The data is from Well Wugu 2.

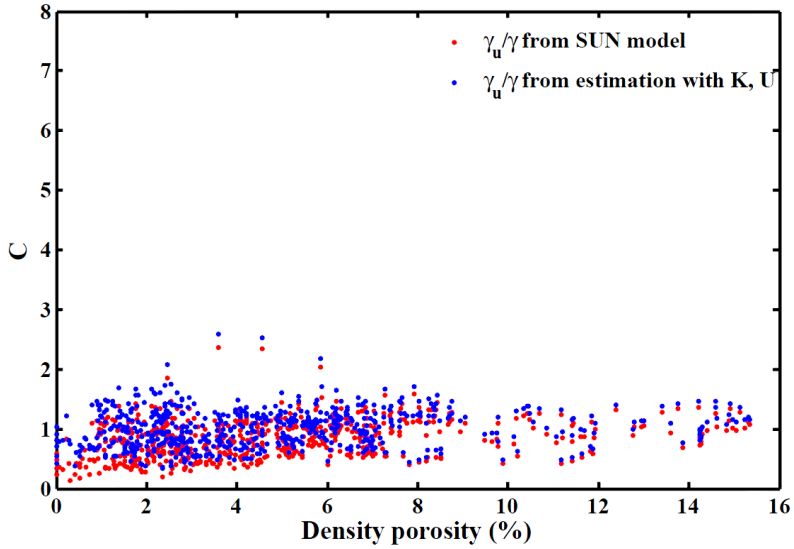

Figure 4.21. The crossplot of C (shear pore structure parameter versus pore structure parameter) versus density porosity. The data is from Well Wugu 2 with P-impedance lower than 15,500 (g/cc)×(m/s).

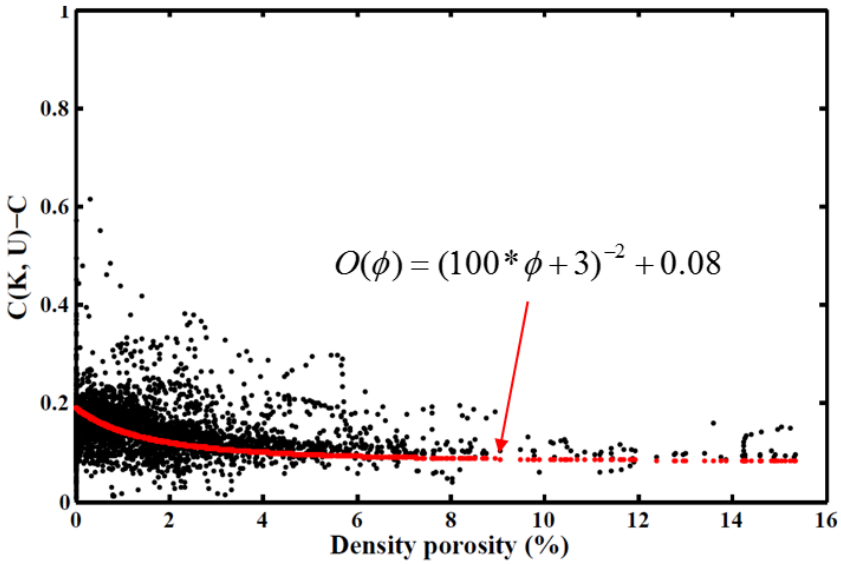

Figure 4.22. The zoom in of the crossplot of C difference versus density porosity in Figure 4.20. The trend line can be expressed with $O(\phi) = (100 * \phi + 3)^{-2} + 0.1$. The data is from Well Wugu 2.

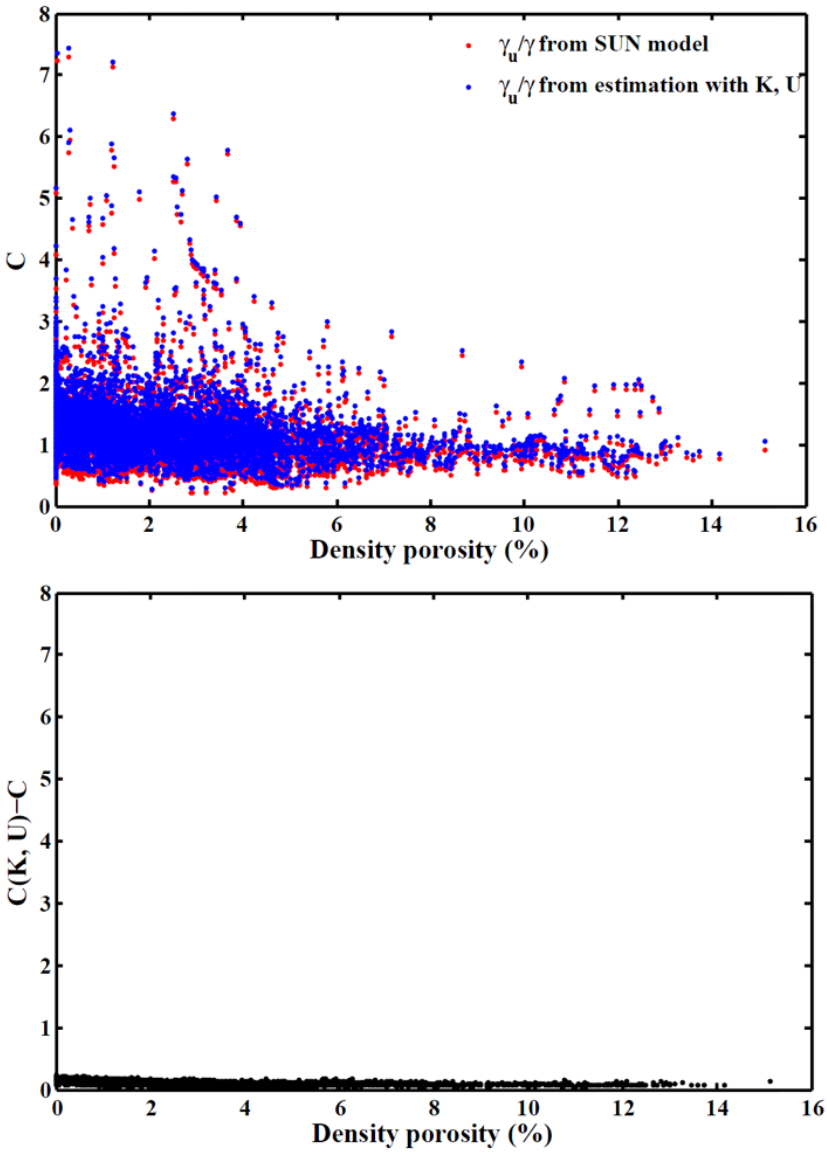

Figure 4.23. The crossplot of C (shear pore structure parameter versus pore structure parameter) versus density porosity (top). The crossplot of C difference between that from Sun model and that from Equation 4.12 by neglecting $O(\phi)$ versus density porosity (bottom). The data is from Well Wugu 4.

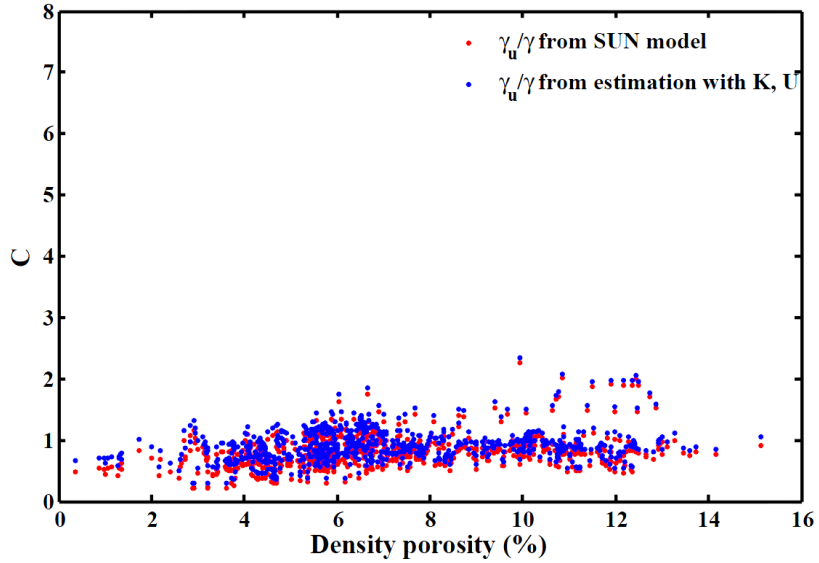

Figure 4.24. The crossplot of C (shear pore structure parameter versus pore structure parameter) versus density porosity. The data is from Well Wugu 4 with P-impedance lower than 15,500 (g/cc)×(m/s).

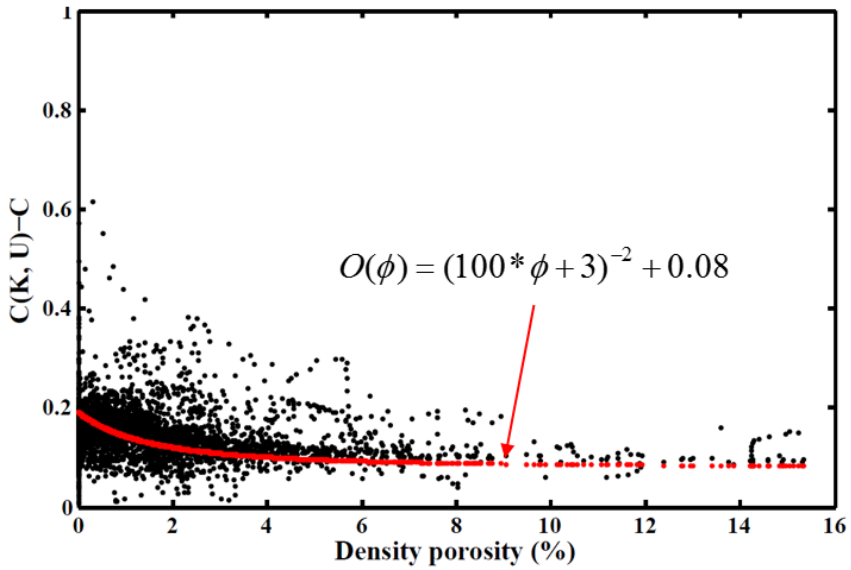

Figure 4.25. The zoom in of the crossplot of C difference versus density porosity in Figure 4.23. The trend line can be expressed with $O(\phi) = (100 * \phi + 3)^{-2} + 0.1$. The data is from Well Wugu 4.

Sun (2000, 2001, and 2004) defined the ratio of shear pore structure parameter and pore structure parameter as C. It has strong dependency on lithology. For sandstone reservoirs, it has a value of 9/8 approximately. If neglect $O(\phi)$ in Equation 4.12, the C is computed from *K,* μ and in blue in Figure 4.20, 4.21, 4.23, and 4.24. The C parameter calculated from Sun model is in red in Figure 4.20, 4.21, 4.23, and 4.24.

From Figure 4.20 -4.25, it is explicit that the C difference between that from Sun model and that from Equation 4.12 by neglecting $O(\phi)$ is pretty small and ignorable. The zoom-in view in Figure 4.22 and 4.25 shows that the C difference can be expressed as a function of porosity as below

$$O(\phi) = (100 * \phi + 3)^{-2} + 0.08 \qquad (4.13)$$

The crossplot of P-impedance versus the product of porosity and pore structure parameter shows a linear relationship between these two parameters (Figure 4.47). The theory and one typical application have been introduced in Chapter III. In the Hexiwu field, we also have

$$\phi\gamma = aAI + b \qquad (4.14)$$

where a =-11.1 and b=197.8.

Therefore, by combining Equation 4.12 and 4.14, the product of porosity and shear pore structure parameter can be expressed as

$$\phi\gamma_{\mu} = (aAI + b)\left(\frac{\log\mu - \log\mu_s}{\log k - \log k_s} + O(\phi)\right) \qquad (4.15)$$

In the Sun model, the shear pore structure parameter has a relationship with shear modulus as

$$\frac{\mu}{\mu_s} = (1-\phi)^{\gamma_\mu} \tag{4.16}$$

If we extend $(1-\phi)^{\gamma_\mu}$ by Taylor series to the second order as

$$(1-\phi)^{\gamma_\mu} \approx 1 - \phi\gamma_\mu + \frac{\gamma_\mu(\gamma_\mu - 1)\phi^2}{2} \tag{4.17}$$

Therefore, we have

$$\phi \approx \frac{1 - \phi\gamma_\mu + \frac{(\gamma_\mu\phi)^2}{2} - \frac{\mu}{\mu_s}}{\frac{1}{2}\phi\gamma_\mu} \tag{4.18}$$

By combining Equation 4.15 and 4.18, we can compute porosity. However, because of the existence of $O(\phi)$ in Equation 4.15, there is no straightforward answer. To solve this problem I propose an iterative algorithm to compute porosity.

Algorithm:

Step 1: Set $O_0(\phi) = 0$, we have $(\phi\gamma_\mu)_1 = (aAI + b)\frac{\log\mu - \log\mu_s}{\log k - \log k_s}$;

Step 2: Then we have $\phi_1 \approx \frac{1 - (\phi\gamma_\mu)_1 + \frac{((\gamma_\mu\phi)_1)^2}{2} - \frac{\mu}{\mu_s}}{\frac{1}{2}(\phi\gamma_\mu)_1}$;

For i=2 : N;

Step 3: Set $O_{i-1}(\phi) = (100 * \phi_{i-1} + 3)^{-2} + 0.1$, then

$$(\phi\gamma_\mu)_i = (aAI + b)\frac{\log\mu - \log\mu_s}{\log k - \log k_s} + O_{i-1}(\phi);$$

Step 4: Then $\phi_i \approx \dfrac{1-(\phi\gamma_\mu)_i + \dfrac{((\gamma_\mu\phi)_i)^2}{2} - \dfrac{\mu}{\mu_s}}{\dfrac{1}{2}(\phi\gamma_\mu)_i}$;

Step 5: When error ($e = \left|\phi_i - \phi_{i-1}\right|$) is small enough, stop the loop.

The computed porosity of Wugu 2 and Wugu 4 are compared to density porosity logs in Figure 4.26 and 4.27. The computed pore structure parameters are compared to pore structure parameters from Sun model in Figure 4.28 and 4.29 of Wugu 2 and Wugu 4 respectively.

The workflow of prestack seismic inversion for the evaluation of fracture reservoir of carbonate hill in the Hexiwu area is summarized in Figure 4.30. This methodology works well for well logs. The success of its application on seismic inversion is largely due to the seismic data quality.

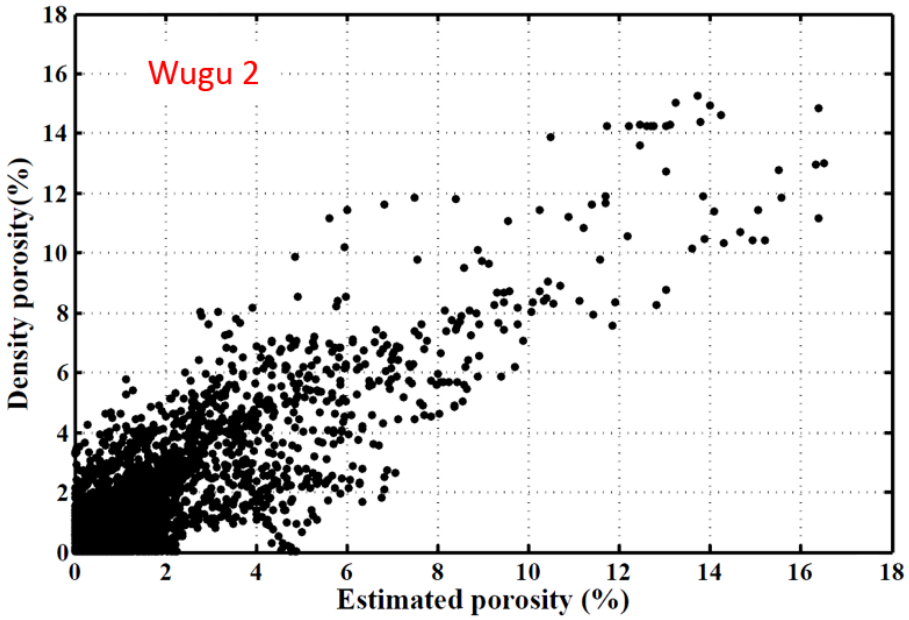

Figure 4.26. The crossplot of density porosity versus estimated porosity of Wugu 2.

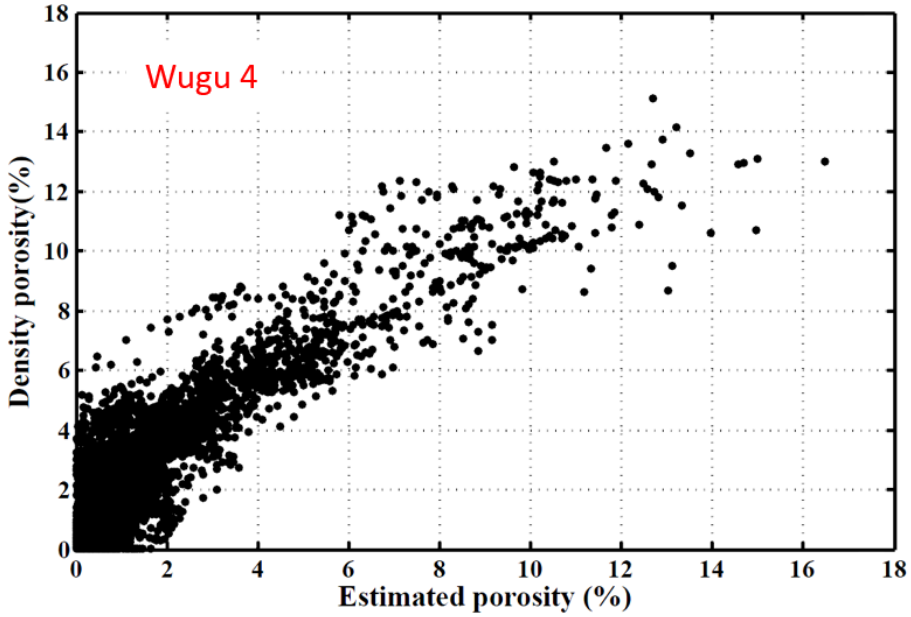

Figure 4.27. The crossplot of density porosity versus estimated porosity of Wugu 4.

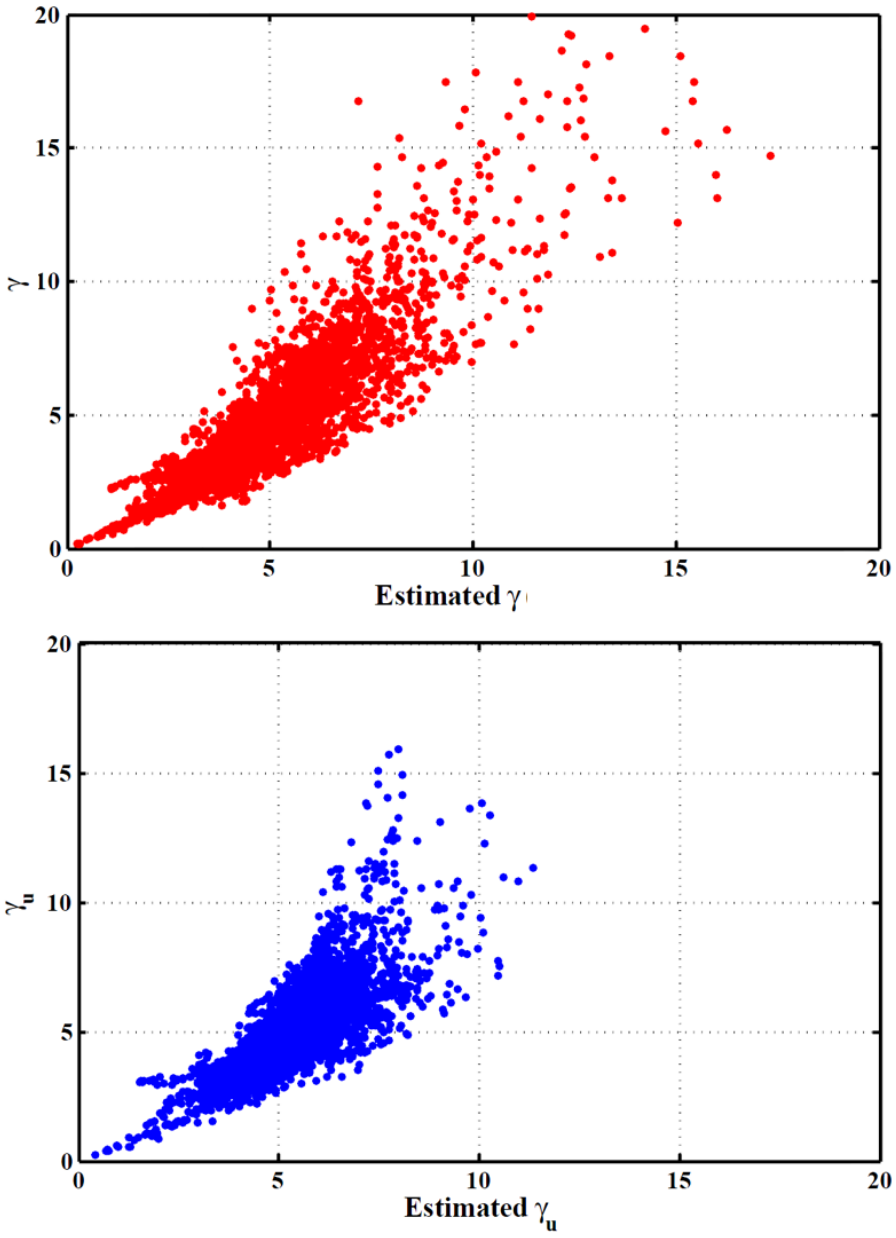

Figure 4.28. The crossplots of pore structure parameters versus estimated pore structure parameters respectively of Wugu 2.

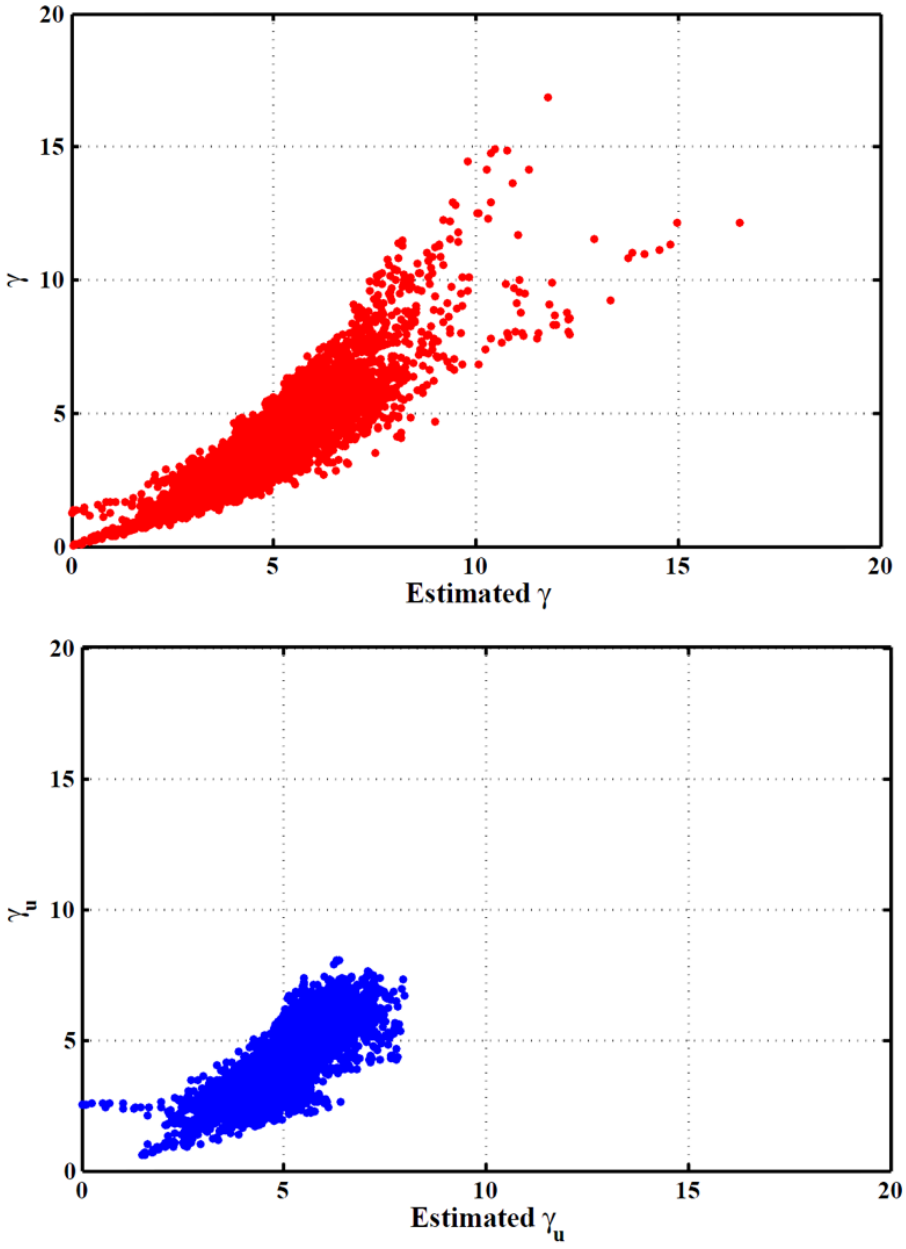

Figure 4.29. The crossplots of pore structure parameters versus estimated pore structure parameters respectively of Wugu 4.

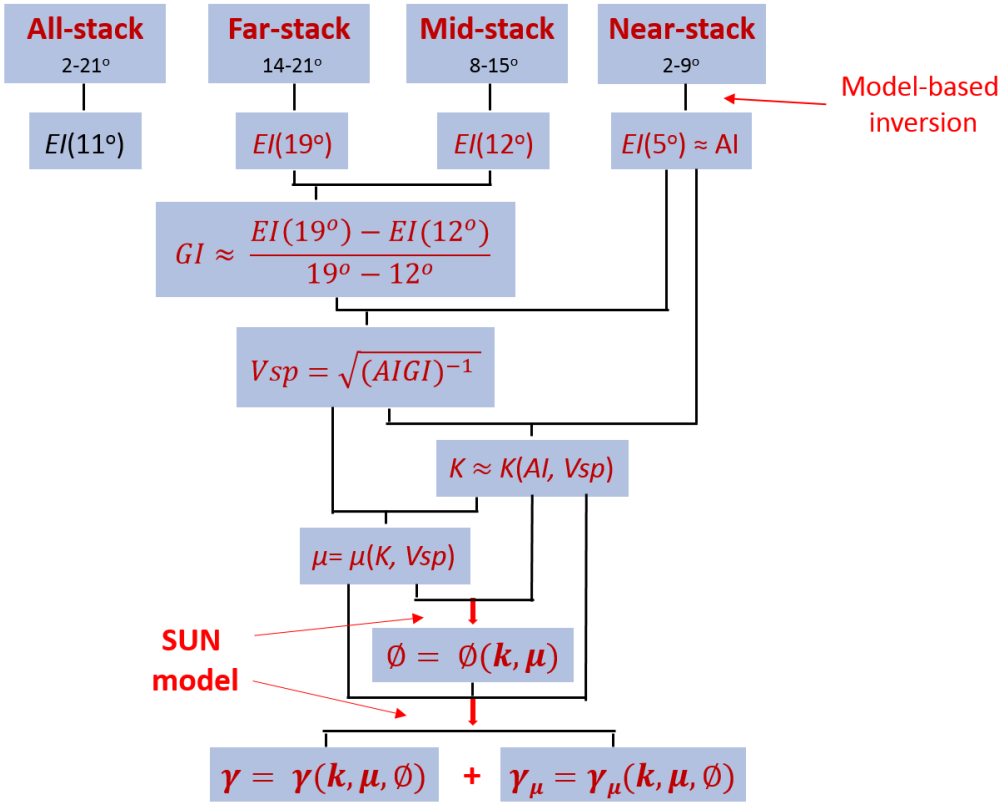

Figure 4.30. The work flow of prestack seismic inversion for the evaluation of fracture reservoir of carbonate buried hill in the Hexiwu area.

4.5 Results

4.5.1 Log analysis

Limestone and dolostone are two dominant lithology types in the Hexiwu buried-hill. Tight and/or low-porosity (less than 5%) limestone generally has lower bulk density than tight and/or low-porosity dolostone (Figure 4.31). The average bulk density of tight and/or low-porosity limestone is around 2.68 (g/cc) while that of tight and/or low-porosity dolostone is around 2.78 (g/cc). The bulk modulus of tight and/or low-porosity limestone has a narrow range from 62 to 82 GPa. Comparatively, the bulk modulus of tight or low-porosity dolostone has a wider range from 50 to 86 GPa. One reason could be that the dolostone intervals have different percentage of calcite. The second one could be the pore structure variation. And the third could be the different fluid content.

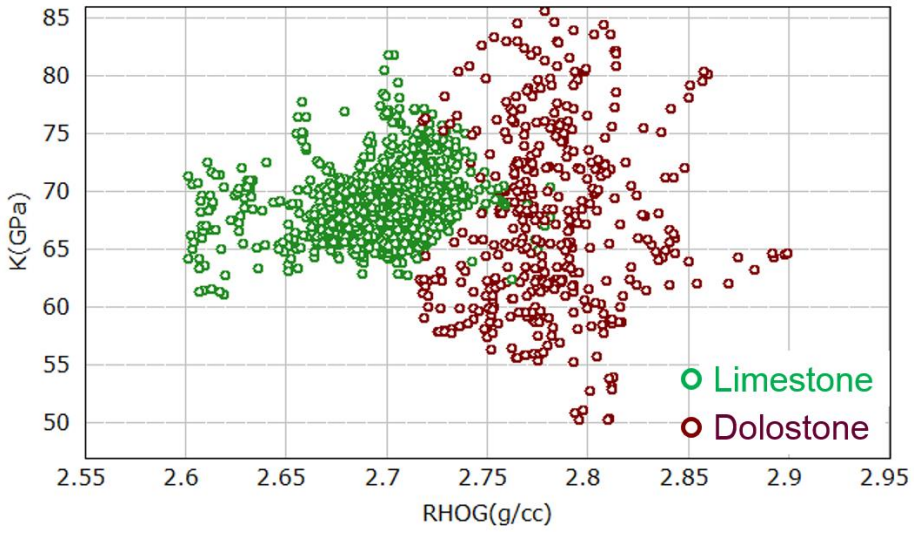

Figure 4.31. The comparison between tight or low-porosity limestone and dolostone on bulk density and modulus. The data is from Wugu 4.

Three porosity logs are available in Wugu 4. They are neutron porosity (CNL), ELAN porosity (PORT), and density porosity (DPHI). ELAN porosity, provided by the Hexiwu oilfield, is an estimated porosity by inputting the mineralogy, neutron porosity, density, and sonic velocity and so on. Comparing these three types of porosity, it is noticeable that neutron porosity offers the highest porosity while density porosity shows the lowest porosity for the same data points in Figure 4.32. In the low porosity range, the crossplots of bulk/shear modulus versus porosity show that tight and/or low-porosity dolostone has a generally higher bulk/shear modulus compared to tight and/or low-porosity limestone. It is well explained by the fact that dolomite is much more rigid than calcite, which determines dolostone has high resistance to compressional/shear stress.

Figure 4.33 shows the crossplots of bulk/shear modulus versus density porosity with water saturation and Vs-Vp ratio as color indicators respectively. Logging data is from Wugu 4. From top two figures, it is clear that in the porosity range of 2 to 5%, part of low water saturated data points are sitting on high bulk/shear modulus (bulk modulus greater than 75 GPa; shear modulus greater than 34 GPa). Considering the analysis based on Figure 4.32, those data points are mainly from dolostone intervals. The bottom two figures show that those data points have low Vs-Vp ratios comparatively. Therefore, at low porosity, if Vs-Vp ratio is given, oil/gas saturated dolostone intervals can be separated from water saturated limestone and dolostone. This idea has been successfully applied in Yuanba field, Sichuan Basin, China in Dou's dissertation (2011).

The major purpose of the Hexiwu buried-hill research is to detect the fractured zones, as the dominant storage space is provided by fracture related cavity, vugs, and

molds and fractures can increase permeability in carbonates. Fractured and tight carbonate zones exhibit different elastic property. The crossplot of bulk modulus versus density porosity in Figure 4.35 clearly shows that fractured zone (Figure 4.34A) has lower bulk modulus than tight limestone (Figure 4.34B), even though they have similar density porosity (0 ~ 2.5%).

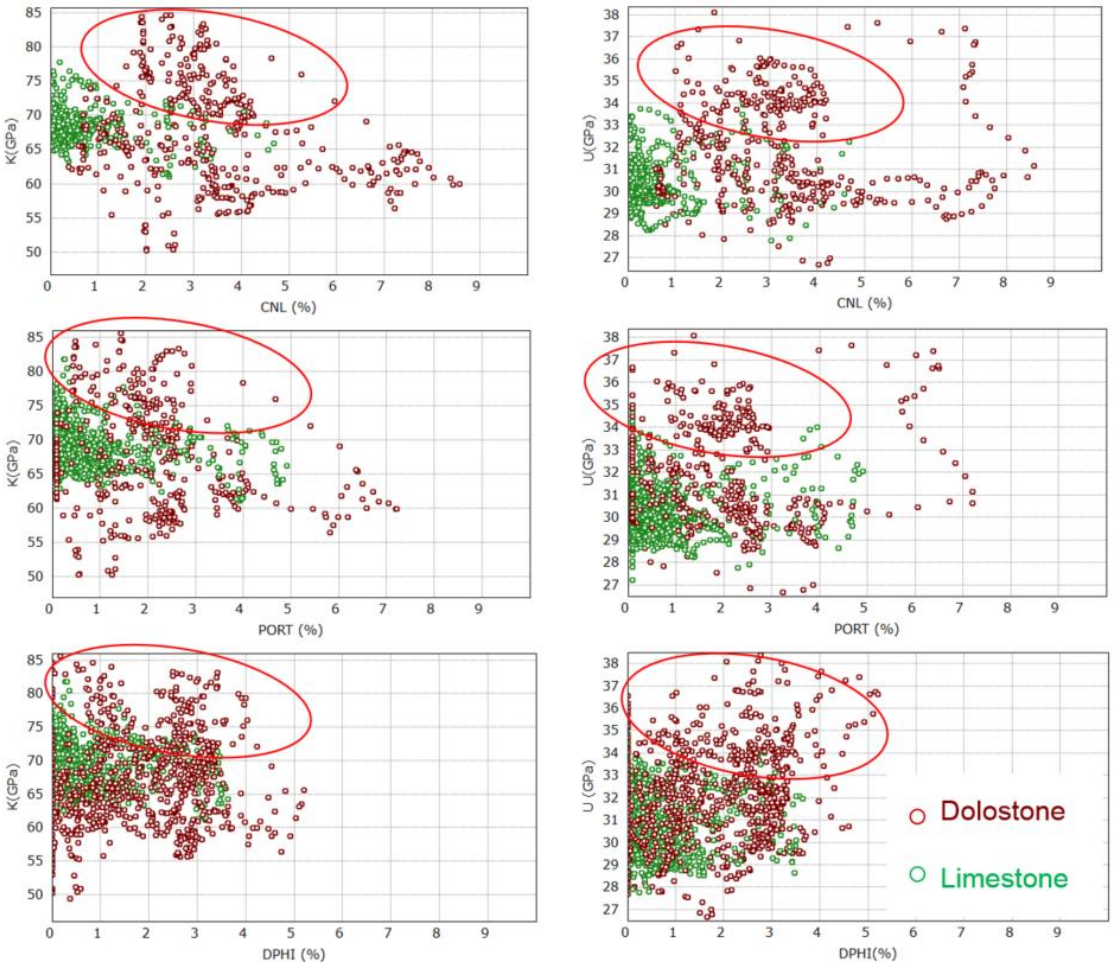

Figure 4.32. Crossplots of bulk/shear modulus versus neutron porosity (CNL, top), ELAN porosity (PORT, middle), and density porosity (DPHI, bottom). The circled datapoints are from dolostone intervals, which have higher bulk/shear modulus than limestone at the same porosity. Data points are from Wugu 4.

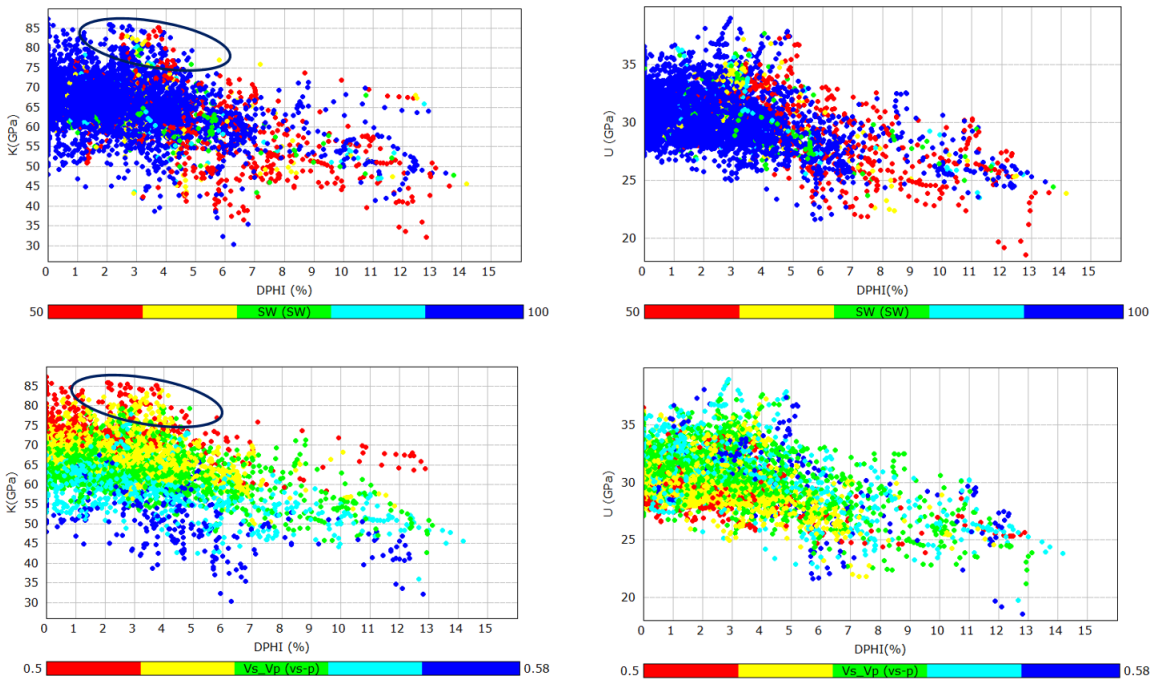

Figure 4.33. The crossplots of bulk/shear modulus versus density porosity with water saturation (top two) and Vs-Vp ratio (bottom two) as color indicators respectively. Data points are from Wugu 4.

The crossplot of shear modulus versus density porosity doesn't exhibit the same pattern. The samples from fracture zone and tight limestone zone are mixed together, even though the shear modulus of fracture zone has a large variation. Therefore, bulk modulus is more sensitive to fracture than shear modulus.

The fracture angle is a key factor influencing the elastic property of carbonate rocks. Considering the dips of fractures, they can be divided into two categories: 1) low-angle fracture (Figure 4.36); and 2) high-angle fracture (Figure 4.37). The purple box in Figure 4.36 is circling a rock section with vuggy porosity. Low-angle fracture zone, high-angle fracture zone, and vuggy zone have different influences on wave propagation. The low-angle fracture zone and the high-angle fracture zone have similar porosity of

3% and 2% respectively (Figure 4.37). However, their bulk/shear modulus have certain differences. High-angle fracture zone tends to have low bulk/shear modulus while low-angle fracture zone has high bulk/shear modulus, which indicates high-angle fractures have stronger negative influence on wave propagation than low-angle fractures do. The vuggy zone is mixed with low-angle fracture zone, which means they have similar effect on wave propagation.

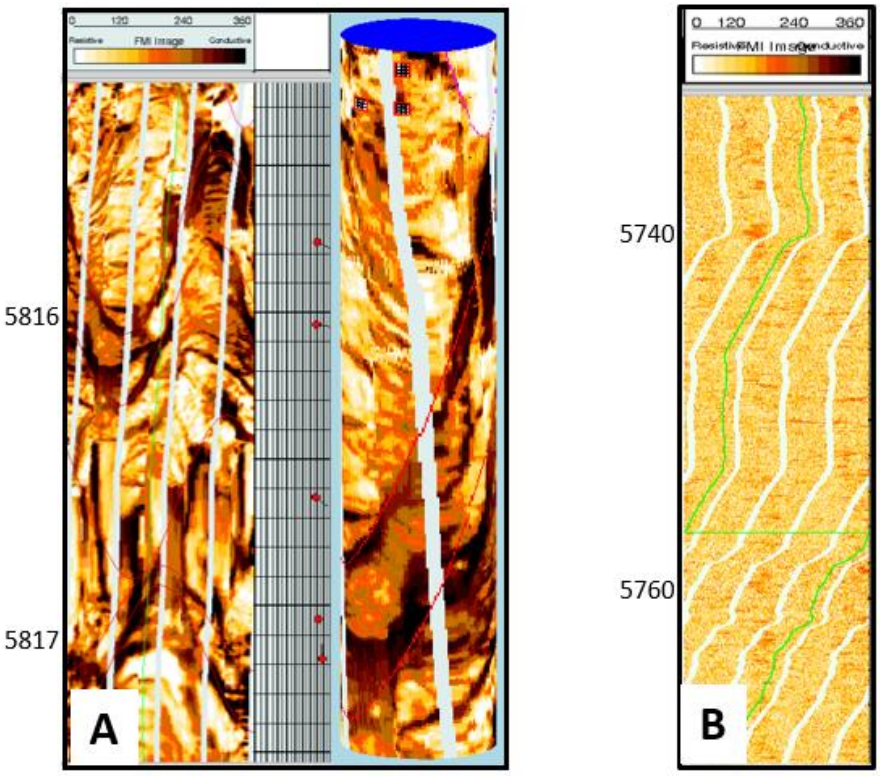

Figure 4.34. Section views of FMI from Wugu 2. A is a section with open fractures. B is a section with tight limestone.

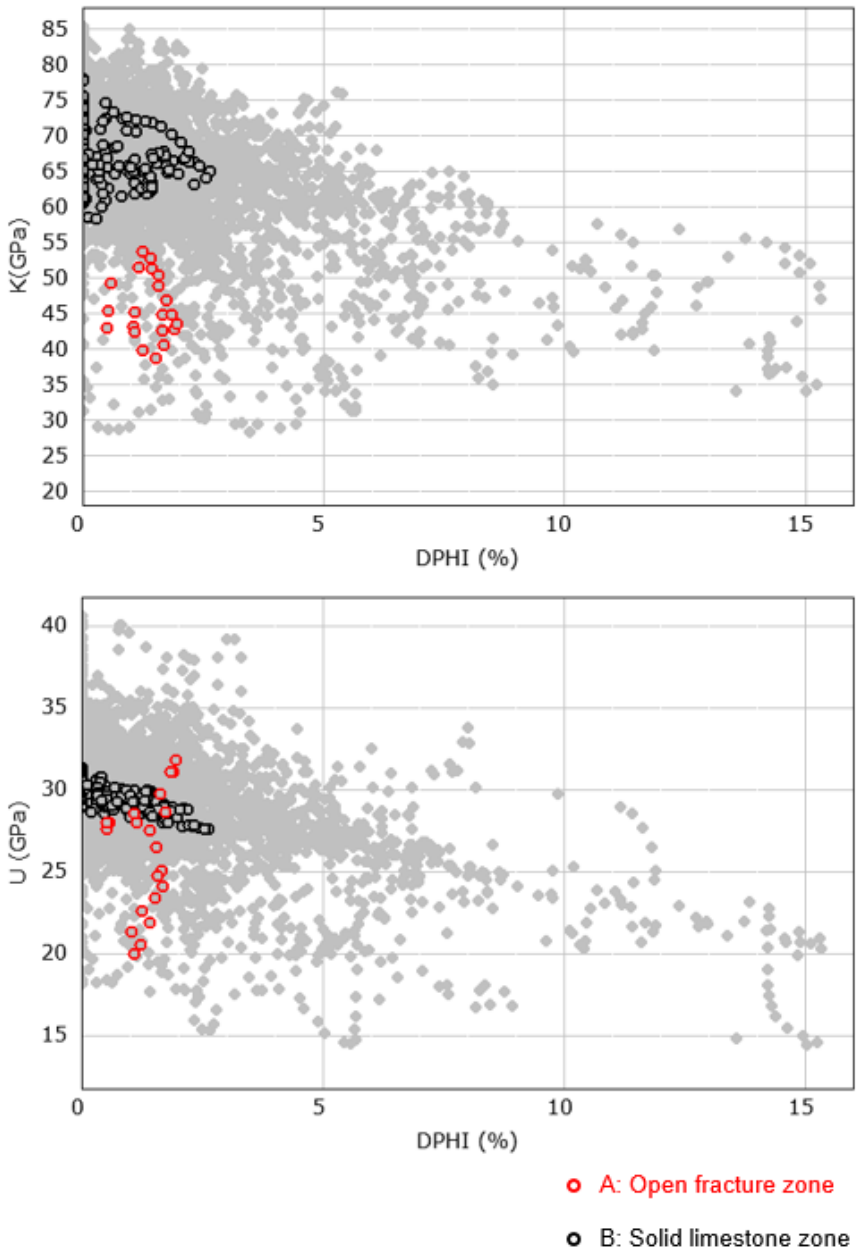

Figure 4.35. Crossplots of bulk/shear modulus versus density porosity with highlighted samples from interval A and B in Figure 4.34.

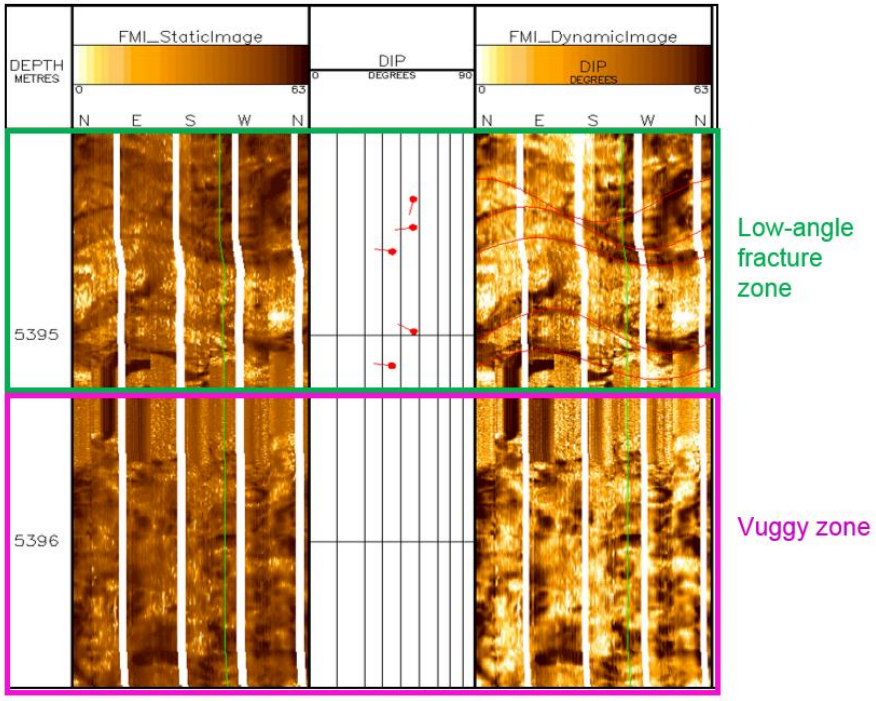

Figure 4.36. A section view of FMI image from Wugu 4. Green box is a low-angle fracture zone while the purple box is vuggy zone.

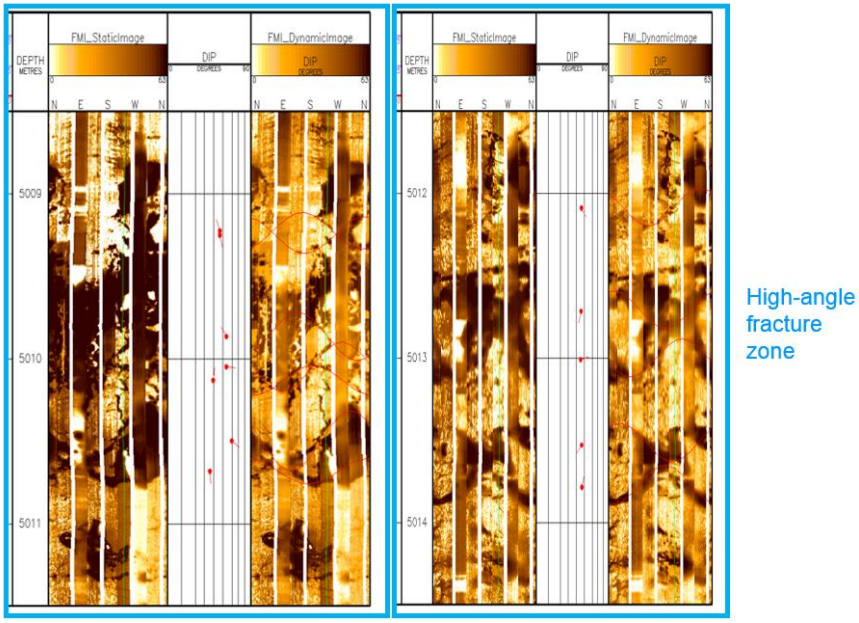

Figure 4.37. A section view of FMI from Wugu 4. Blue box is a high-angle fracture zone.

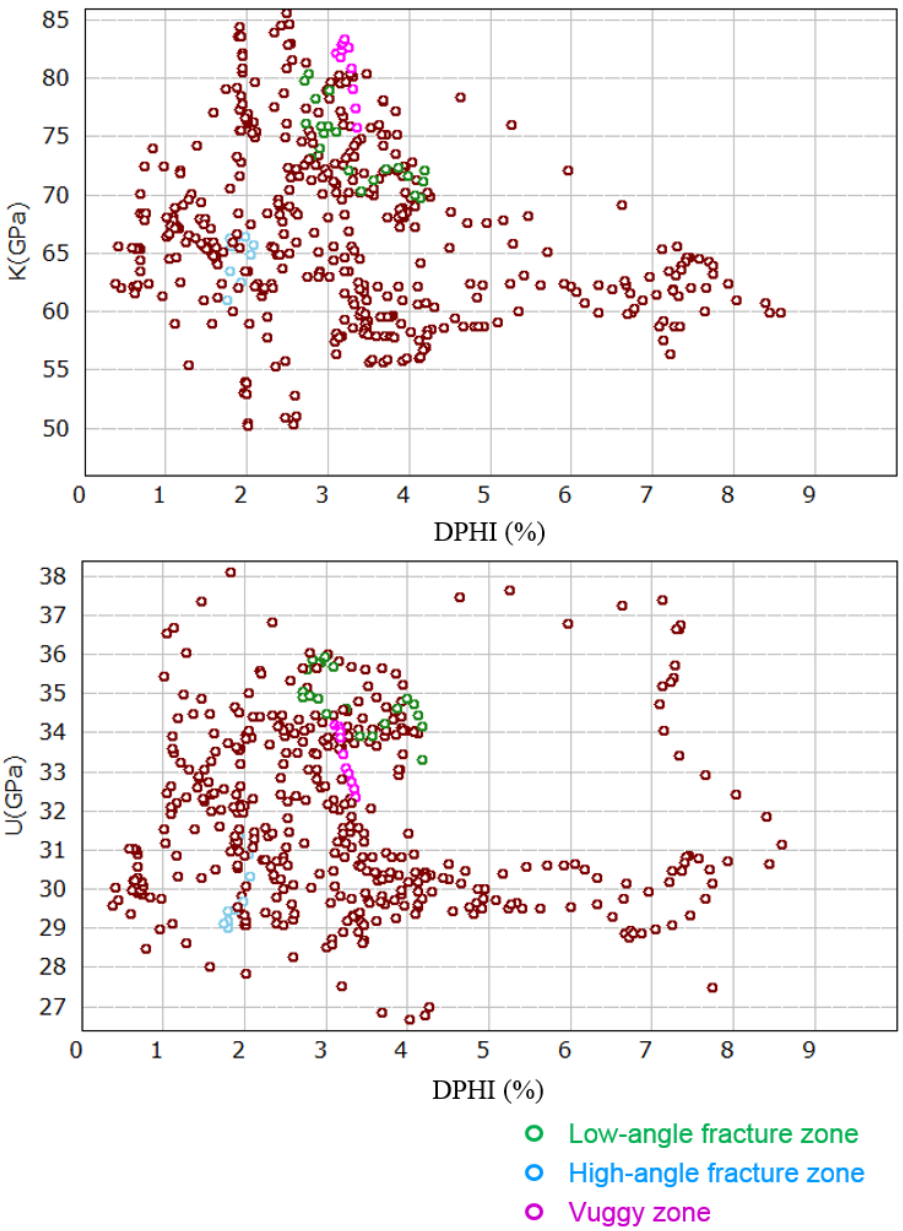

Figure 4.38. The Crossplots of bulk/shear modulus versus density porosity. Data points are from Wugu 4. The low-angle fracture zone and vuggy zone are shown in Figure 4.36. The high-angle fracture zone is shown in Figure 4.37.

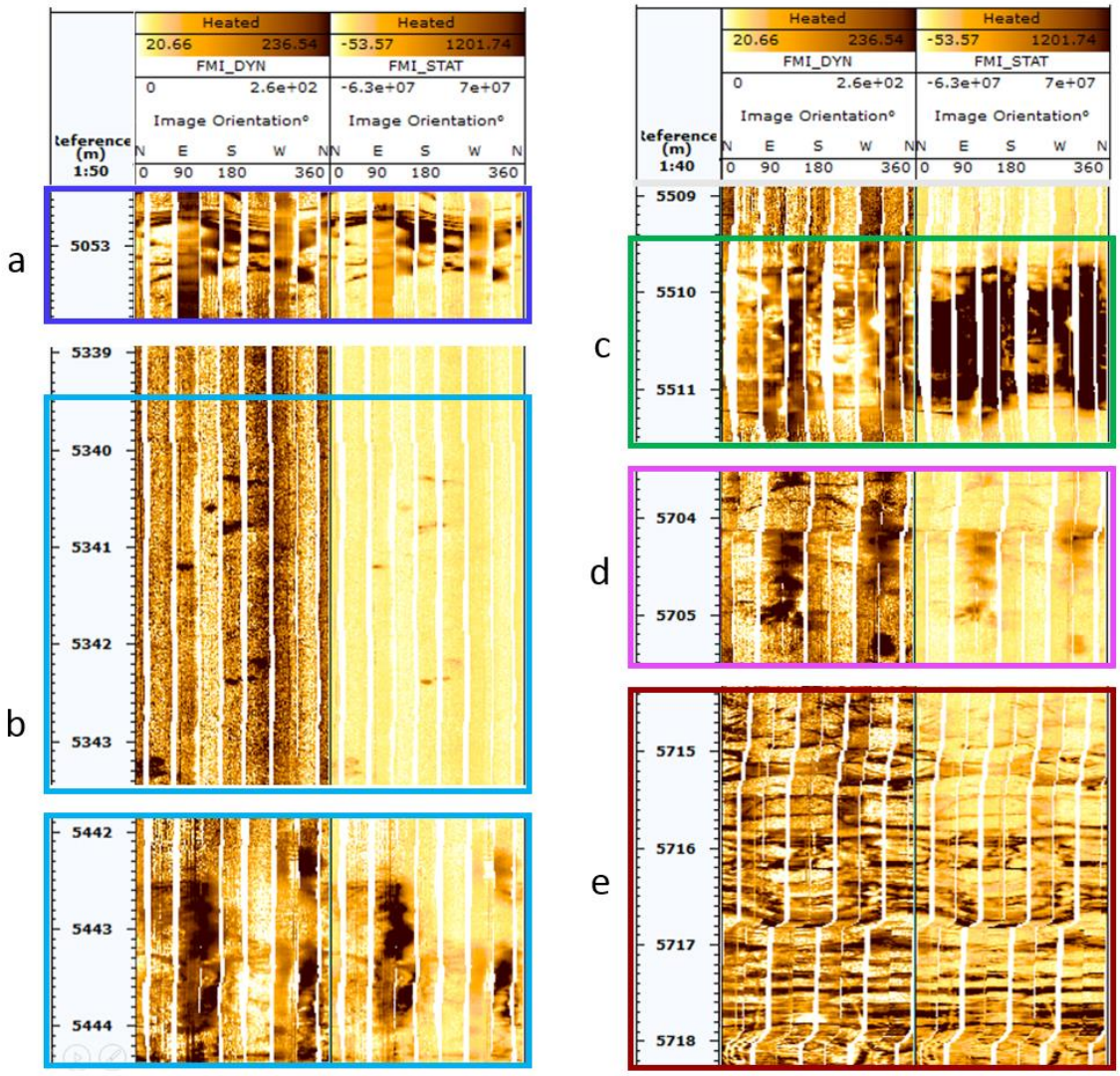

Figure 4.39. Six section views of FMI from Wugu 4. a) fractures with vugs; b) vugs; c) big vugs with minor fractures; d) small vugs with minor fractures; and e) fractures.

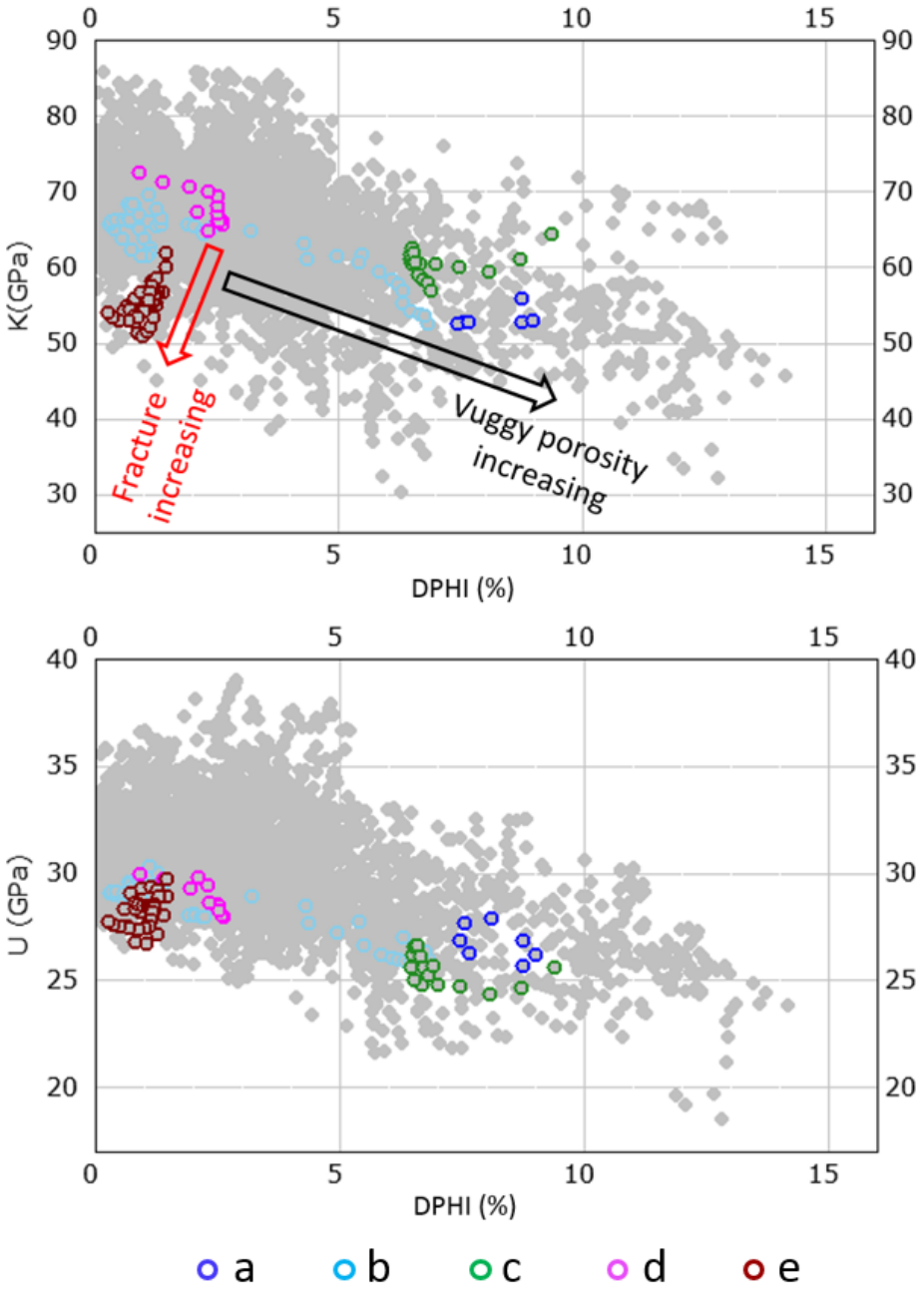

Figure 4.40. The crossplots of bulk/shear modulus versus density porosity. The data is from Wugu 4. The FMI of a), b), c), d), and e) are shown in Figure 4.39.

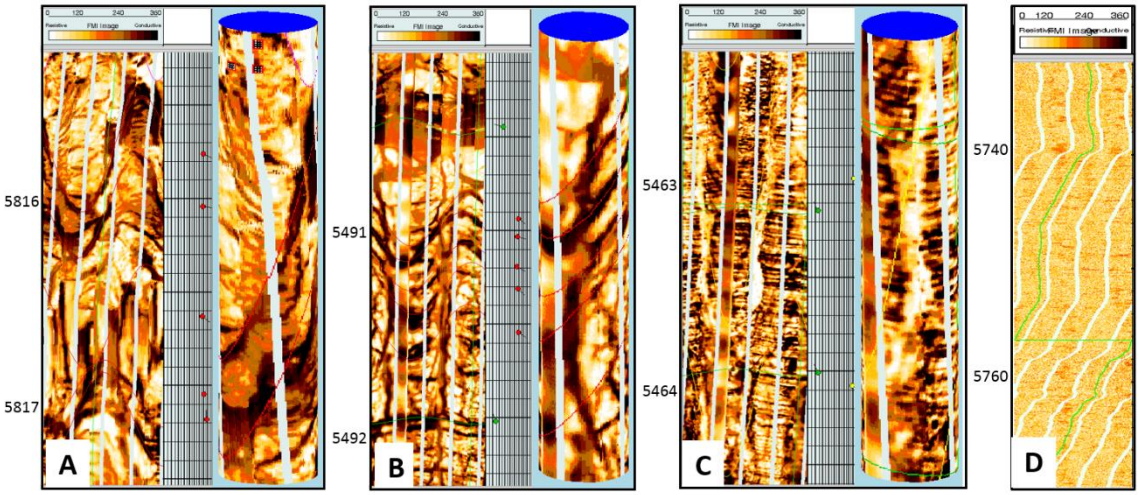

Figure 4.41. Three sections of FMI from Wugu 2. A and B have open fractures. C is close fractures. D is tight limestone.

The presence of fractures and vugs influences the bulk/shear modulus differently. Five section views of FMI from Wugu 4 include a) fractures with vugs; b) small vugs + big vugs; c) big vugs with minor fractures; d) small vugs with minor fractures; and e) fractures (Figure 4.39). Their different distributions on the crossplot of bulk modulus versus density porosity confirm that the fractures can decrease the bulk modulus at given porosities, meanwhile the large vugs decrease the bulk modulus and increase the porosity. However, their location on the crossplot of shear modulus versus density porosity doesn't follow the general rules. The fractures in Figure 4.39 are mostly low-angle fractures. They are more sensitive to bulk modulus than to shear modulus.

Open fractures and close fractures should have different influence on rock properties, like bulk/shear modulus, P-/S-velocity, and P-/S-impedance and so on. Figure 4.41 shows two open fracture sections (A and B), one close fracture section (C), and one tight limestone section (D) from Wugu 2. These open fractures mostly have high dip

angle. The rocks from section A, B, C, and D have similar porosity (1%~3%) in Figure 4.42. However, the bulk modulus of section A and B (less than 55 GPa) have lower values than that of section C and D (greater than 55 GPa). The shear moduli of section A, B, C, and D are mixed together while the shear moduli of fractured zones (section A and B) have a large variation. Therefore, bulk modulus is more sensitive to open fractures than to close fractures and tight carbonates while shear modulus is not.

The crossplot of bulk modulus versus shear modulus shows that section A and B are distributed in the lower left corner while section C and D are located in the upper right part. It is logical that carbonate rocks with open high-angle fractures have both low bulk modulus and shear modulus. A black line is tentatively drawn to separate high porosity carbonates and/or open high-angle fracture carbonates from low porosity carbonates with/without close fractures. If all those data points below the black line on the crossplots of acoustic impedance versus density porosity of Wugu 2 and Wugu 4 are highlighted (Figure 4.44), it is clear that Wugu 2 has more data highlighted than Wugu 4, which indicates Wugu 2 is more fractured than Wugu 4. The previous FMI interpretation proves that Wugu 2 has more fractured zones than Wugu 4. Moreover, it is also clear that those low bulk/shear modulus data points (red points) have low acoustic impedance lower than 15.5 (g/cc)×(km/s). Those data points who have acoustic impedance lower than 15.5 (g/cc)×(km/s) but above the black line on the crossplot of bulk modulus versus shear modulus have comparative high porosity. They are also an important part of carbonate reservoir rocks. Therefore, we can separate those data points, which have acoustic

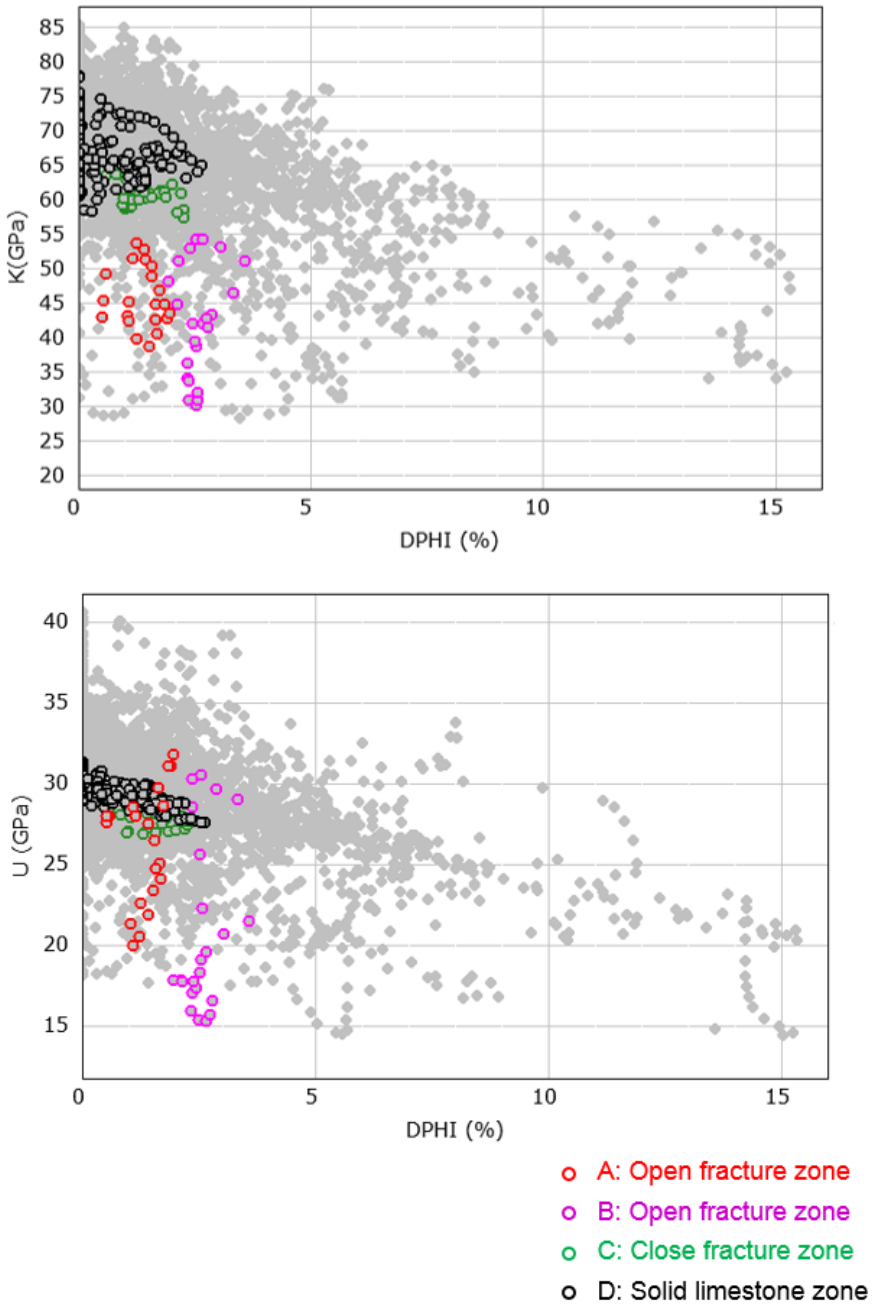

Figure 4.42. The crossplots of bulk/shear modulus versus density porosity. The data is from Wugu 2. Red and purple circles present open fracture zone and they are pointing to A and B respectively in Figure 4.41. Green circles present close fracture zone and they are pointing to C in Figure 4.41. Black circles stand for tight limestone zone D in Figure 4.41.

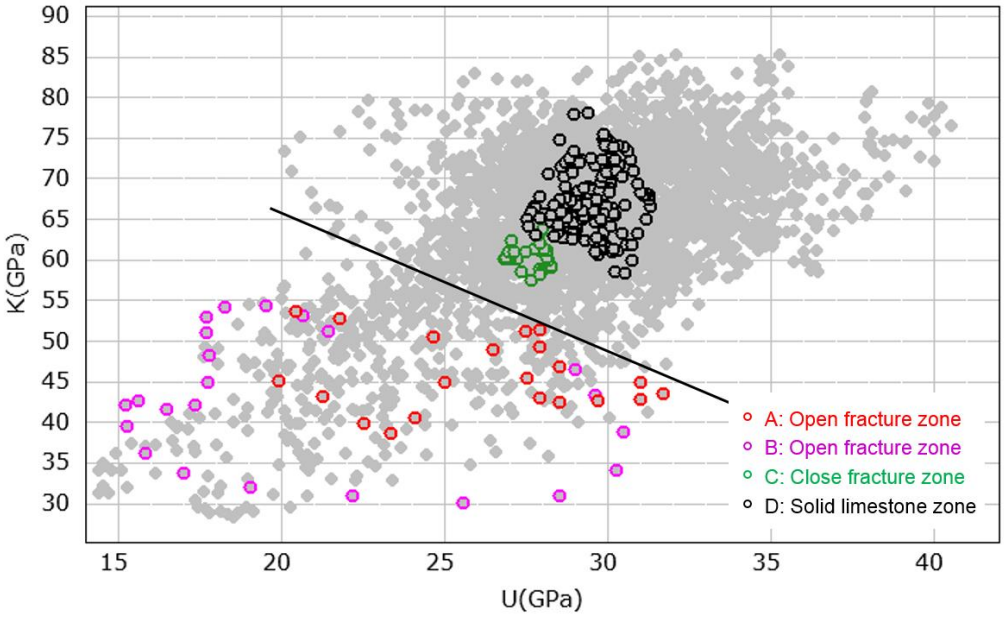

Figure 4.43. The crossplot of bulk modulus versus shear modulus. The data is from Wugu 2. Red and purple circles present open fracture zone and they are pointing to A and B respectively in Figure 4.41. Green circles present close fracture zone and they are pointing to C in Figure 4.41. Black circles stand for tight limestone zone D in Figure 4.41.

impedance lower than 15.5 (g/cc)×(km/s), into two categories: 1) high porosity reservoir rocks; and 2) low porosity reservoir rocks with open fractures (Figure 4.45).

The application of Sun model (Sun, 2000, 2001, and 2004) on Wugu 2 and Wugu 4 finds out pore structure parameter (γ) is independent of porosity and quantifies different structure belts at given porosity (Figure 4.46). Considering the Yuanba gas field (Dou, 2011b), those data points, which have low pore structure parameter values (less than 3.5) and have porosity values between 2 to 5%, might be oil/gas saturated dolostone (Figure 4.32 and 4.33). The increase of pore structure parameter corresponding to the pore type variation and the presence of fractures (Figure 4.40). In this case, the definition of low porosity fracture zone can be achieved by using three

criteria: 1) porosity lower than 5%; 2) acoustic impedance lower than 15.5 (g/cc)×(km/s); and 3) pore structure parameter higher than 6.

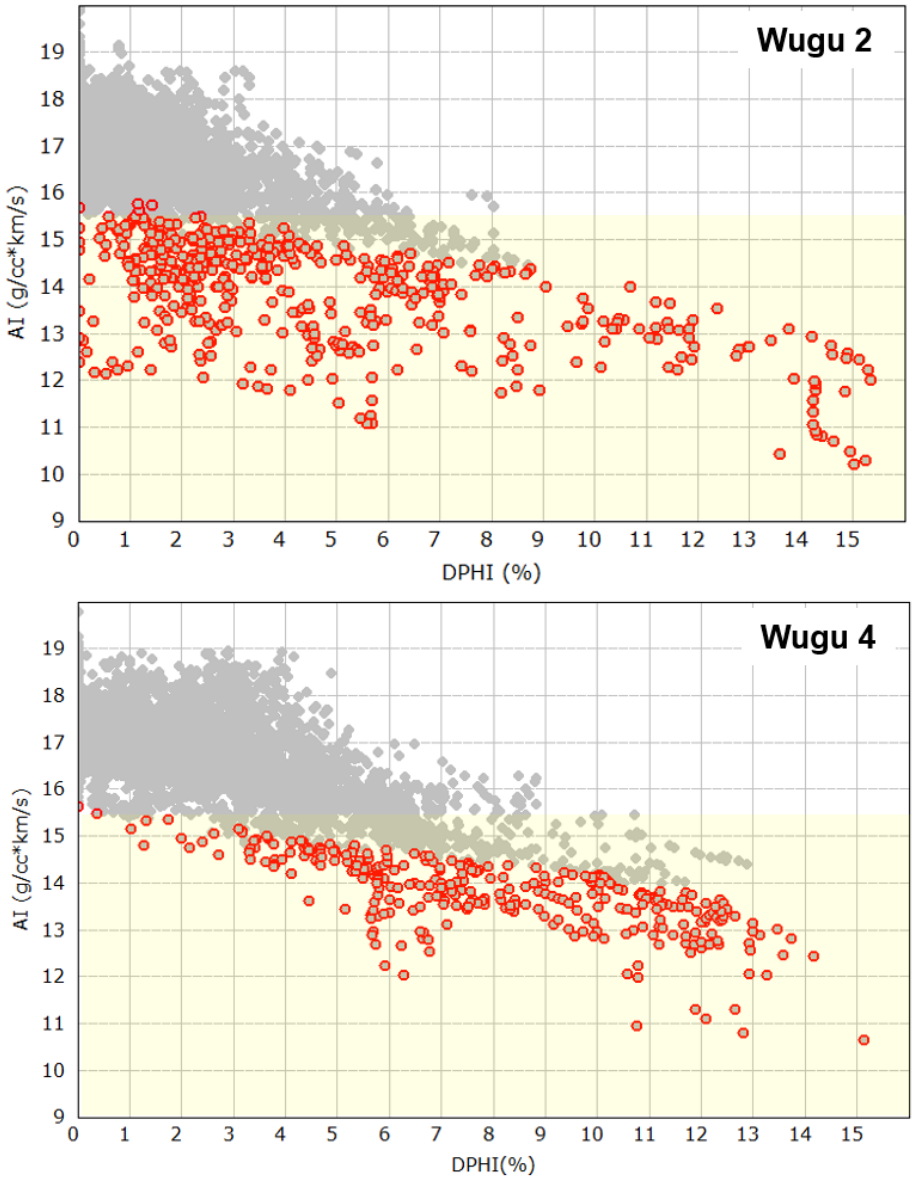

Figure 4.44. The crossplots of acoustic impedance versus density porosity. The top figure is plotting Wugu 2 and the bottom plotting Wugu 4. The yellow zone covers the data points that have acoustic impedance lower than 15.5 (g/cc)×(km/s).

In chapter III, a product of porosity and pore structure parameter is defined to characterize carbonate reservoirs. The same methodology is applied on Wugu 2 and Wugu 4 logging data (Figure 4.47). Wugu 2 and Wugu 4 have the same relationship between acoustic impedance and the product of porosity and pore structure parameter. It is AI=0.09×Dphi(%)×γ+17.8 with R^2 0.753 and 0.743 respectively for Wugu 2 and Wugu 4. Those data points, which have high values of the product of porosity and pore structure parameter, are from the carbonate reservoir zone with high porosity or open fractures (Figure 4.45).

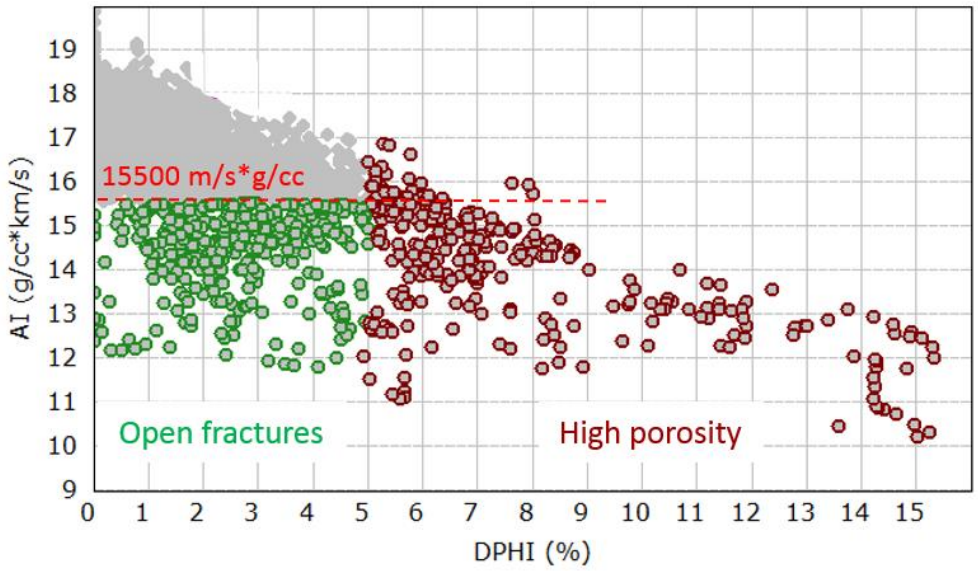

Figure 4.45. The crossplot of acoustic impedance versus density porosity. The plotted data is from Wugu 2. The green color present open fractured zones. The red color present high porosity reservoir zones.

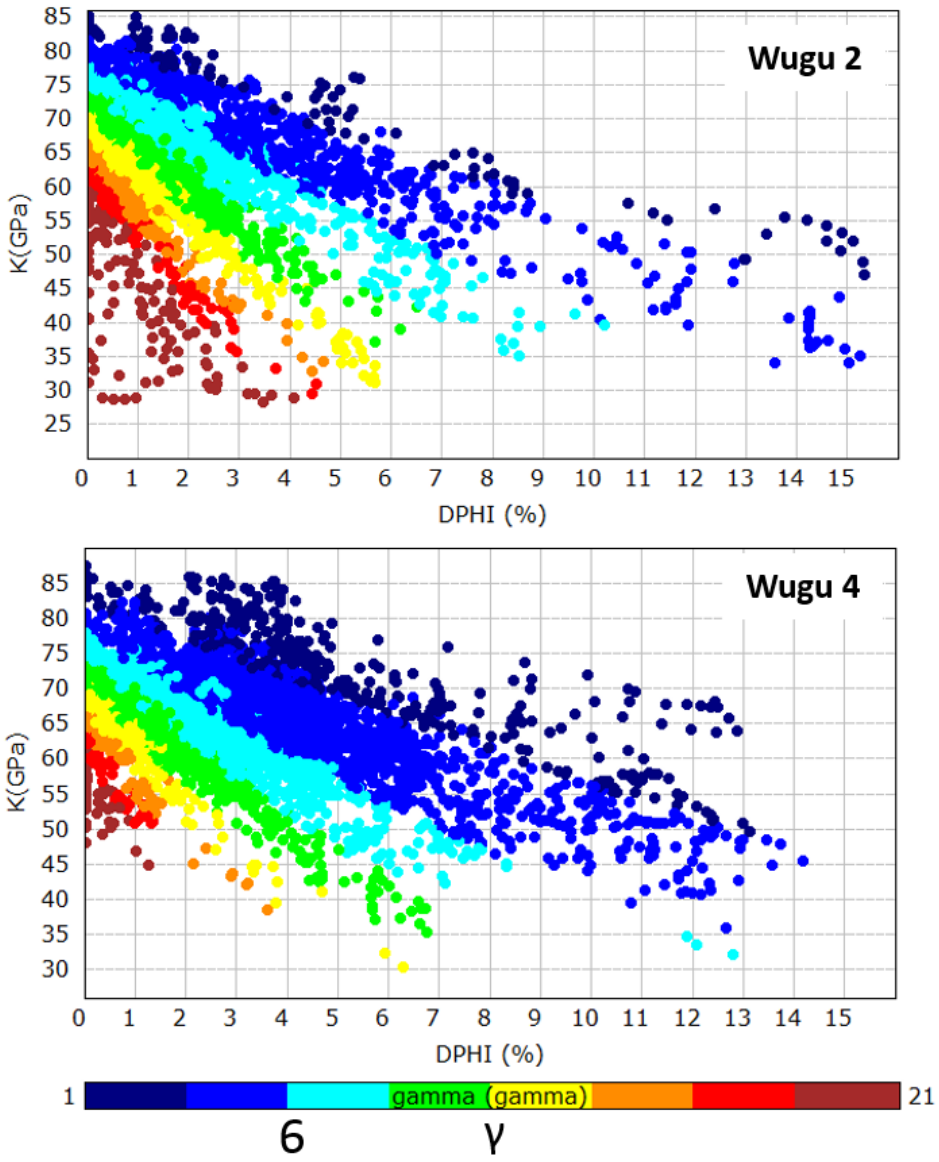

Figure 4.46. The crossplots of bulk modulus versus density porosity of Wugu 2 and Wugu 4. The color indicator is pore structure parameter.

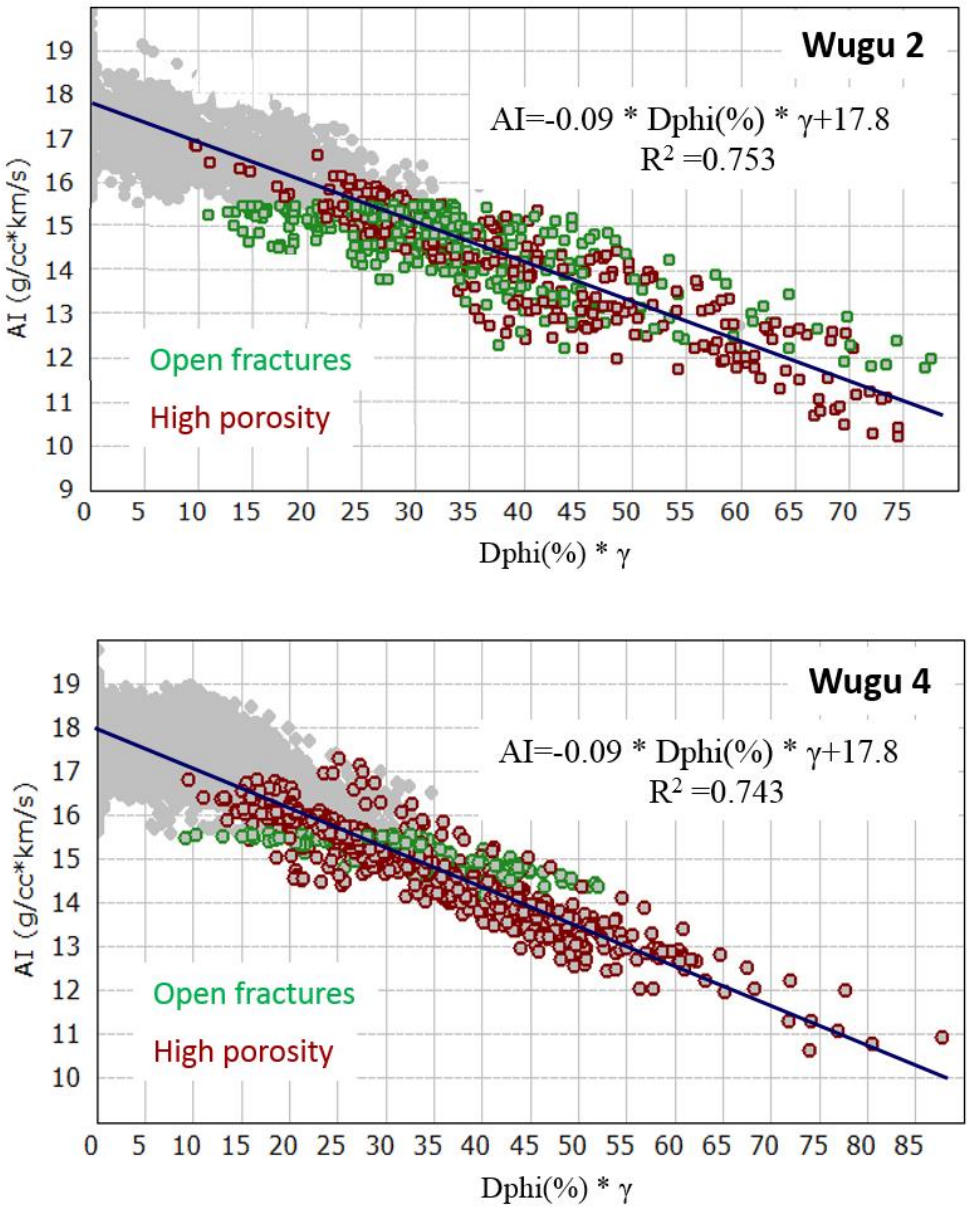

Figure 4.47. The crossplots of acoustic impedance versus the product of porosity and pore structure parameter of Wugu 2 and Wugu 4. The green points are from open fracture zone and the red points are from high porosity zone.

4.5.2 Poststack seismic inversion

4.5.2.1 Synthetic seismogram

The method used to do poststack seismic inversion is model-based seismic inversion (Russell, 1988). One primary step is to compute synthetic seismogram, which ties the well logging data (in depth) to seismic data (in time). Considering the time length of two wells used in poststack seismic inversion shorter than 400 ms (Figure 4.50, 4.51, and 4.52), it is better to create a band-pass wavelet to tie wells to seismic (Figure 4.48). The frequency range of band-pass wavelet is 5-15-50-70 Hz, which corresponds well to the amplitude spectrum of high-resolution seismic data in the target formations (Fengfeng,

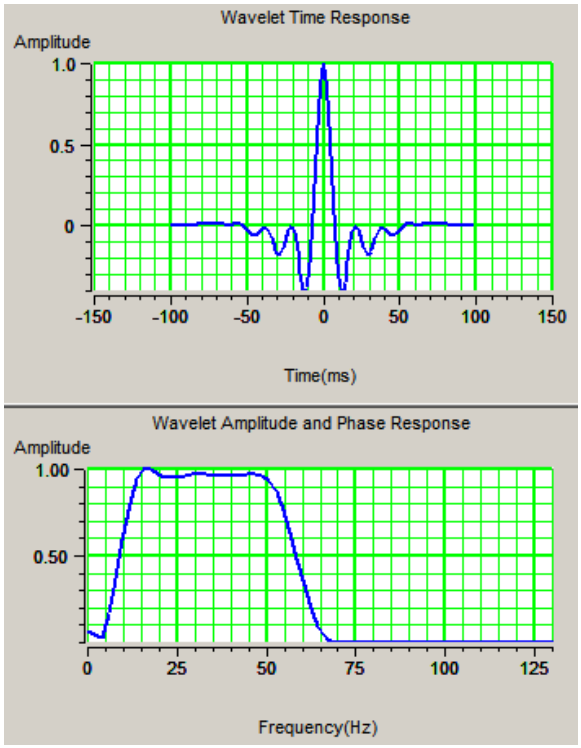

Figure 4.48. The band-pass wavelet used in synthetic seismogram.

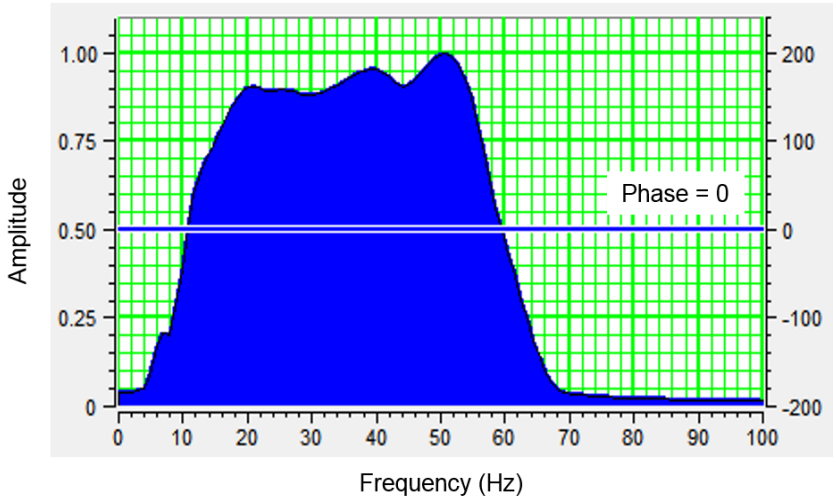

Figure 4.49. The amplitude spectrum of high-resolution seismic data in the target formations.

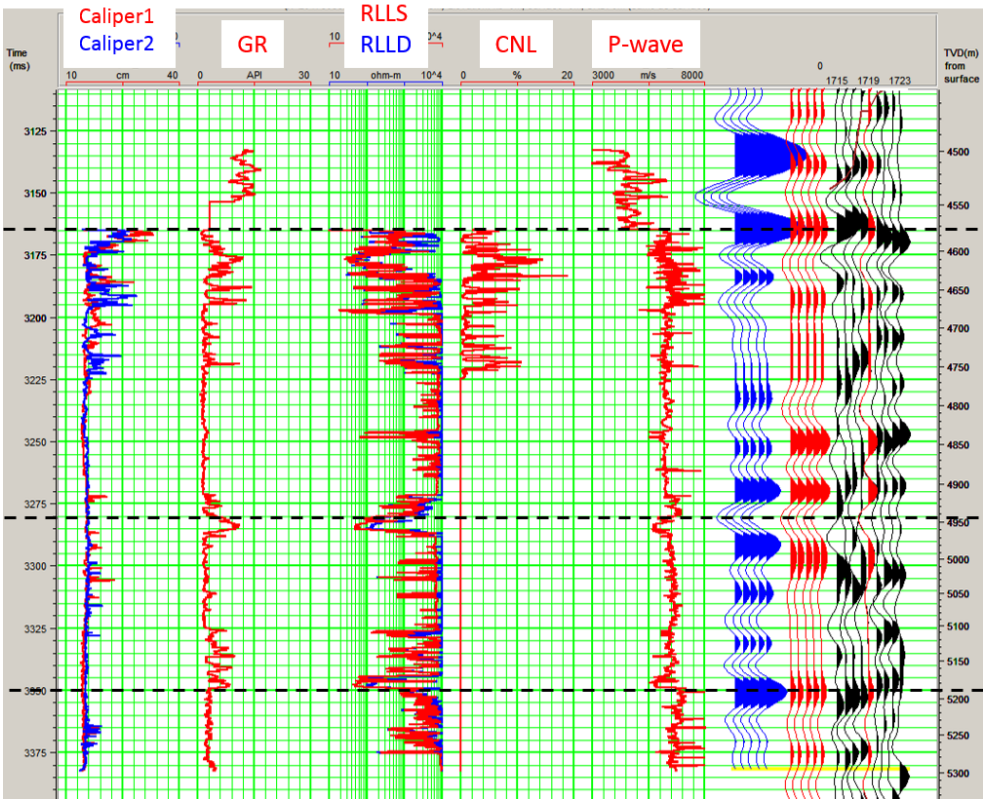

Figure 4.50. The synthetic seismogram of Jing 3. The blue wiggles are synthetics and the red are the repetition of seismic trace at well location.

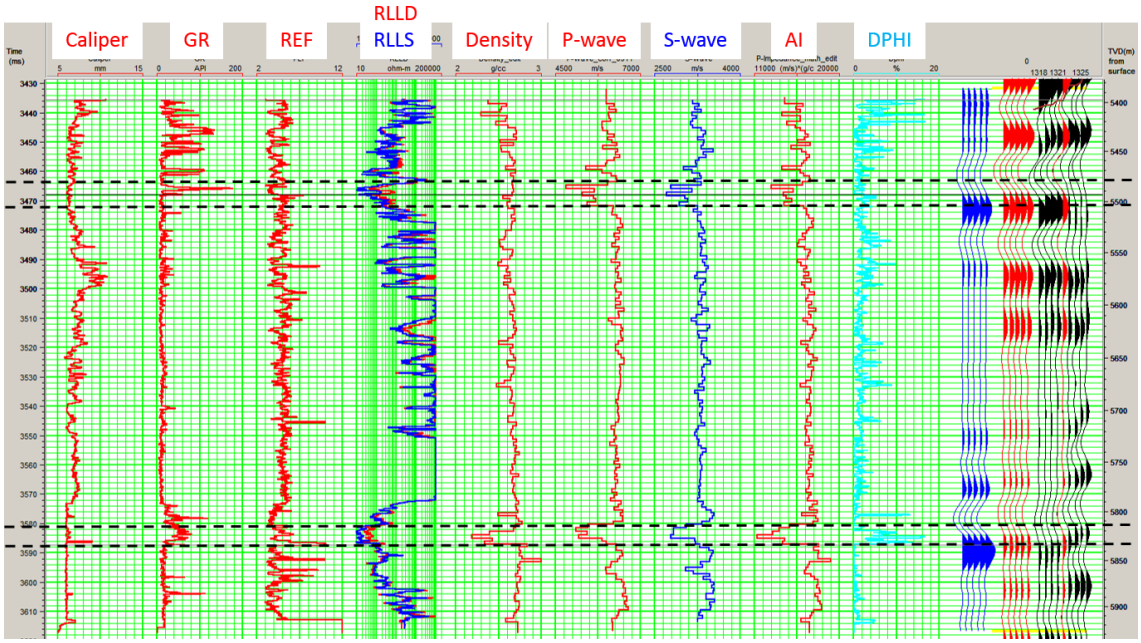

Figure 4.51. The synthetic seismogram of Wugu 2. The blue wiggles are synthetics and the red are the repetition of seismic trace at well location.

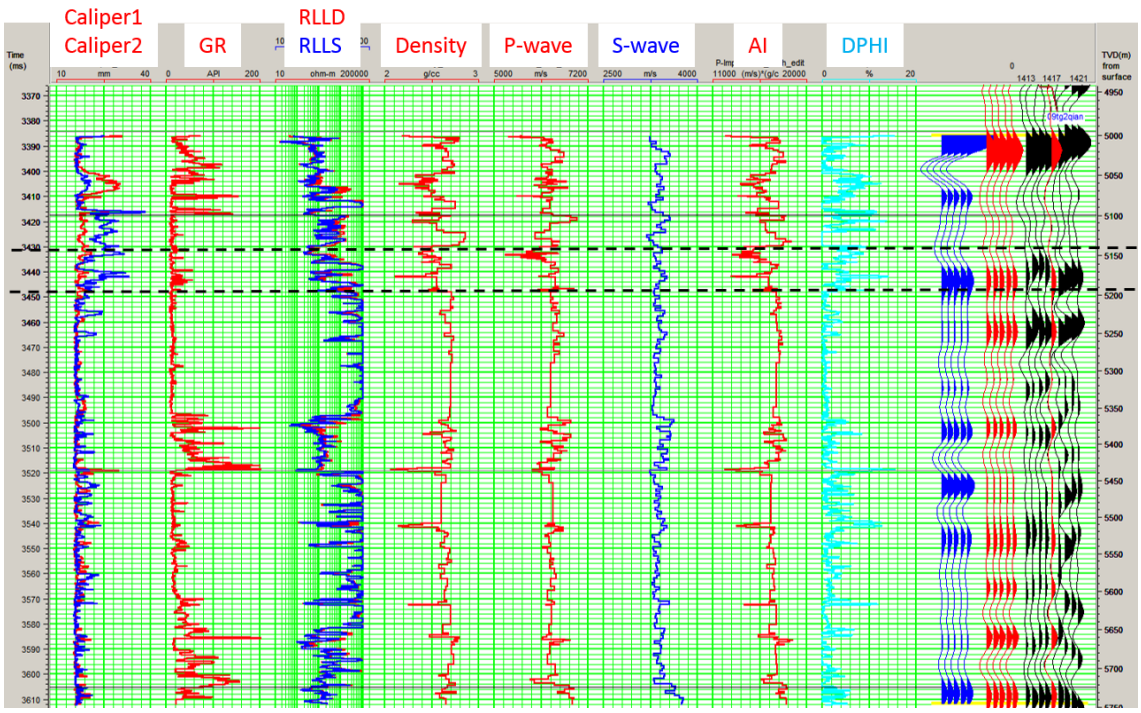

Figure 4.52. The synthetic seismogram of Wugu 4. The blue wiggles are synthetics and the red are the repetition of seismic trace at well location.

Upper Majiagou, and Lower Majiagou Formation) (Figure 4.49). The synthetic seismogram of Jing 3, Wugu 2, and Wugu 4 are listed in Figure 4.50, 4.51, and 4.52 respectively. The synthetics (blue wiggles) of three wells have good match with the high-resolution seismic trace (red wiggles) at well location.

The average thickness of the two fractured zones of Wugu 2 is around 20 meters. It is impossible to identify them with conventional seismic data. The tops of two fracture/high-porosity zones of Wugu 2 interpreted with low P-velocity, S-velocity, and P-impedance are pointing to troughs of synthetics and high-resolution seismic traces respectively (Figure 4.51). The seismic resolution is much more enhanced after high-resolution processing to identify thin layers of fractured zones.

4.5.2.2 Model building, inversion and inversion QC

Figure 4.53 and 4.54 show the conventional and high-resolution seismic profile cutting through Jing 30, Xinyong 9, Xinyong 30, Yong 22, Wuug 2, Wugu 4, Jing 24, and Jing 3 respectively. The low frequency initial model built with Jing 3, Wugu 2, and Wugu 4 is shown in Figure 4.53. The model-based inversion results are shown in Figure 4.56 and 4.57 respectively from conventional and high-resolution seismic data. The general view of conventional acoustic impedance inversion result has thick beds of low impedance while that of high-resolution acoustic impedance inversion result has thin beds. Most drilling wells except Xinyong 9 were drilled on regional or local structural highs. Major low-impedance zones are in or immediately below the regional unconformity. Internal low-impedance zones are also shown on both profiles (Figure

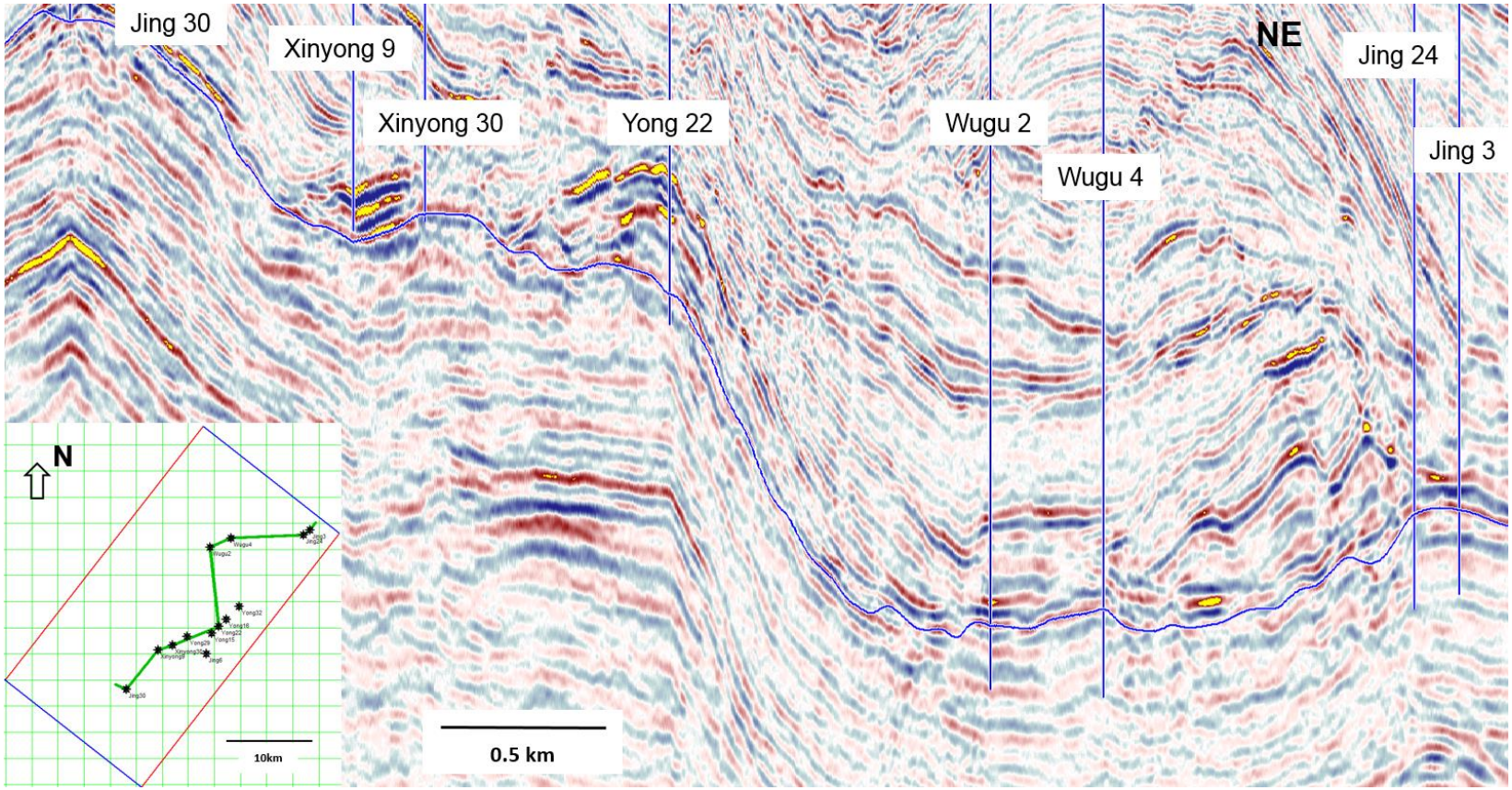

Figure 4.53. A conventional seismic profile cutting through Jing 30, Xinyong 9, Xinyong 30, Yong 22, Wuug 2, Wugu 4, Jing 24, and Jing 3.

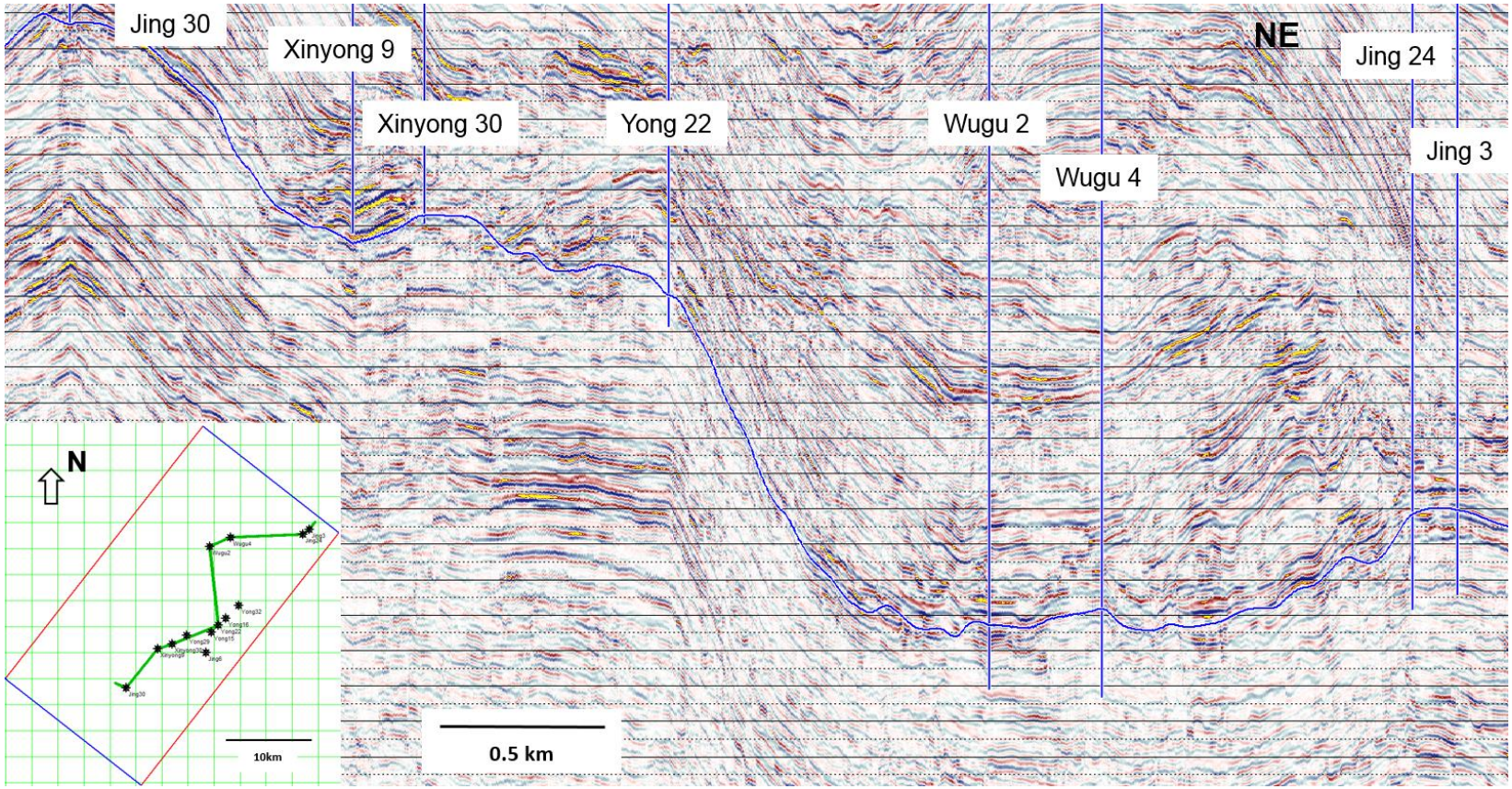

Figure 4.54. A high-resolution seismic profile cutting through Jing 30, Xinyong 9, Xinyong 30, Yong 22, Wuug 2, Wugu 4, Jing 24, and Jing 3.

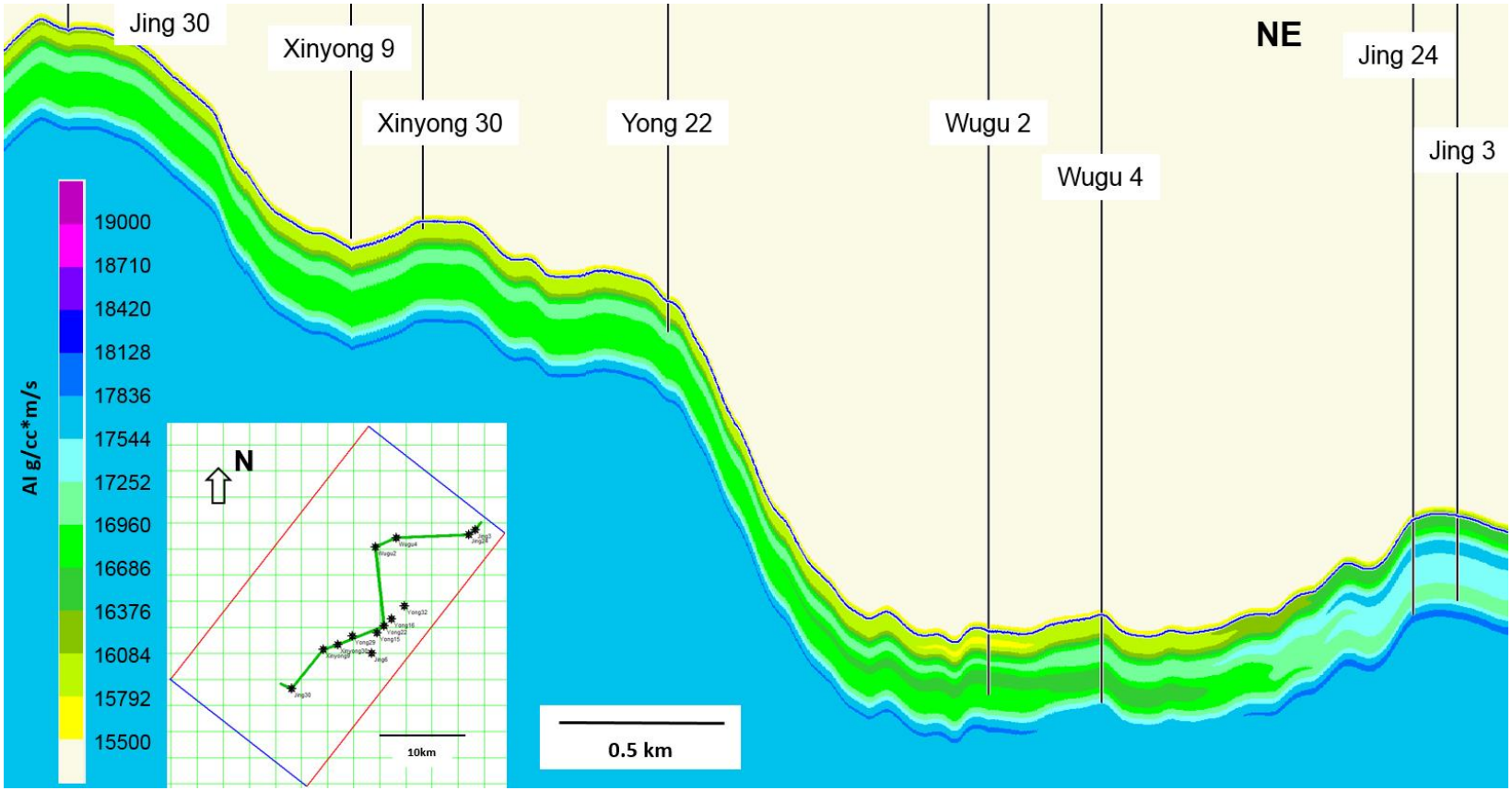

Figure 4.55. A profile of initial model for acoustic impedance inversion cutting through Jing 30, Xinyong 9, Xinyong 30, Yong 22, Wuug 2, Wugu 4, Jing 24, and Jing 3.

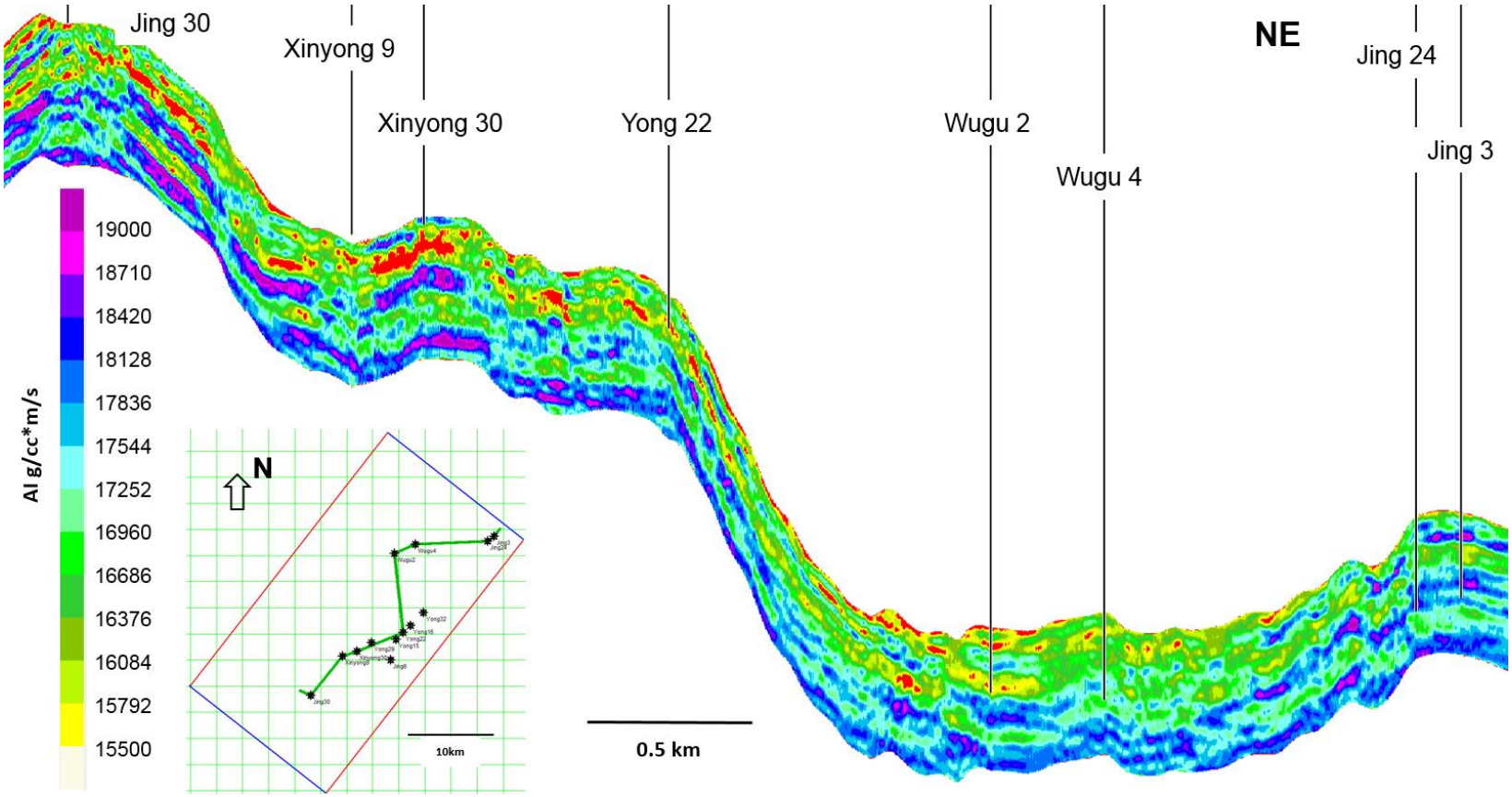

Figure 4.56. A profile of acoustic impedance inversion result from conventional seismic data cutting through Jing 30, Xinyong 9, Xinyong 30, Yong 22, Wuug 2, Wugu 4, Jing 24, and Jing 3.

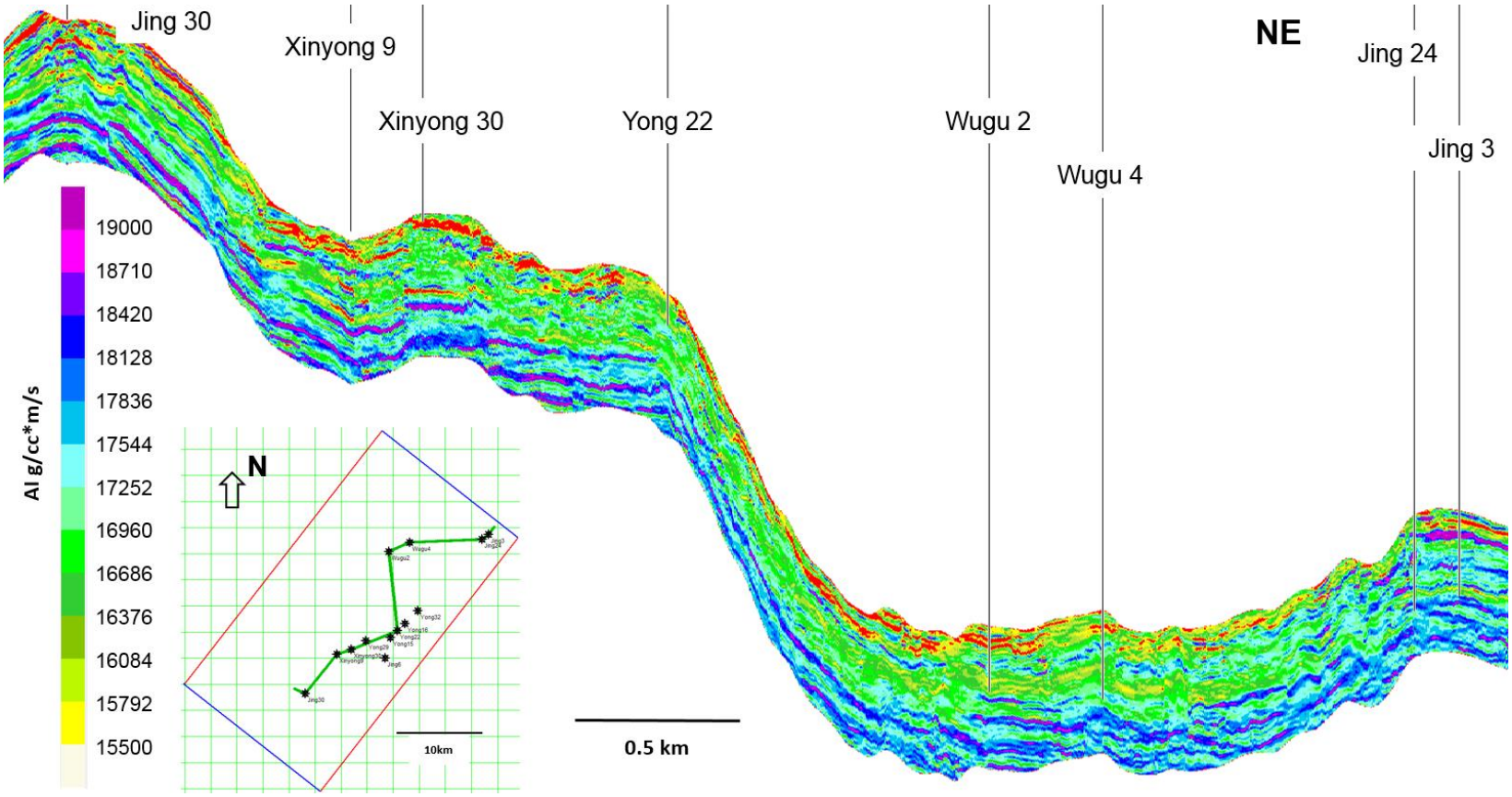

Figure 4.57 A profile of acoustic impedance inversion result from high-resolution seismic data cutting through Jing 30, Xinyong 9, Xinyong 30, Yong 22, Wuug 2, Wugu 4, Jing 24, and Jing 3.

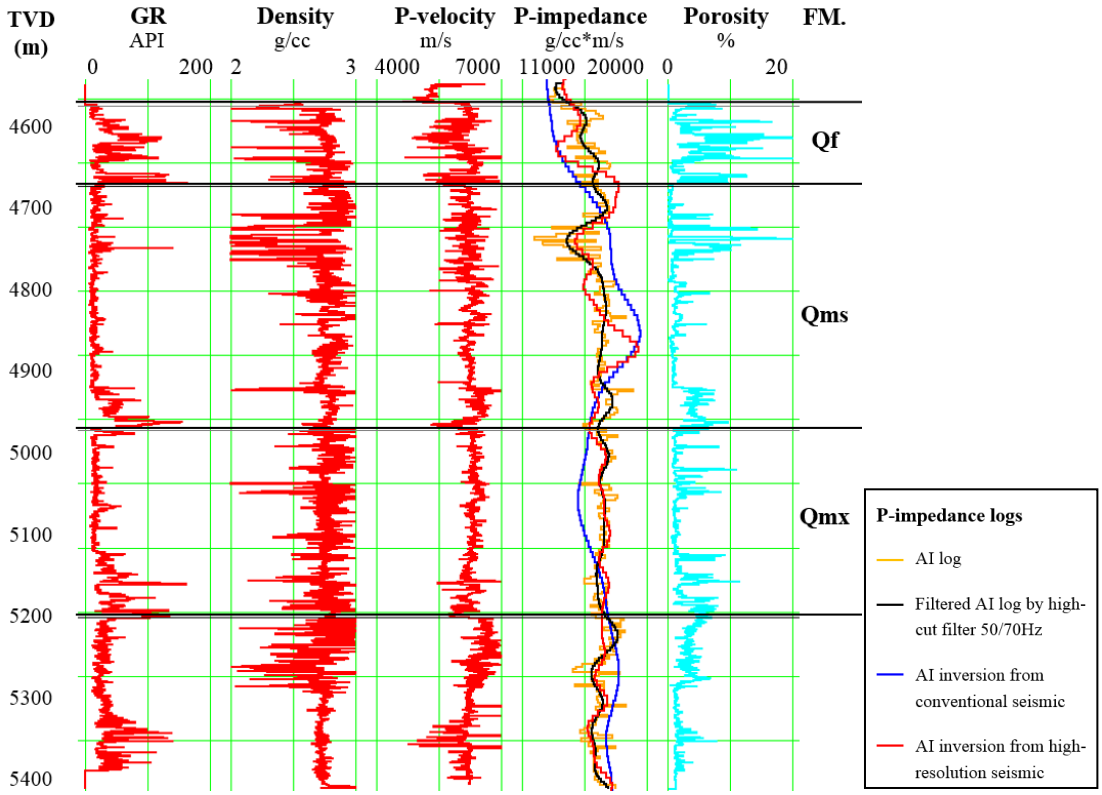

Figure 4.58. The inversion result QC at Jing 3.

4.56 and 4.57). The detailed interpretation on high-resolution seismic inversion will be stated in the following.

The inversion results from conventional seismic and high-resolution seismic are quality-controlled in Figure 4.58, 4.59, and 4.60. In the P-impedance trace, four impedances logs are listed: 1) acoustic impedance log (AI); 2) filtered acoustic impedance (AI) log by high-cut filter (50/70 Hz); 3) acoustic impedance (AI) inversion from conventional seismic; and 4) acoustic impedance (AI) inversion from high-resolution seismic data. Overall, the acoustic impedance inversion from high-resolution seismic has the best similarity with the filtered acoustic impedance log while the

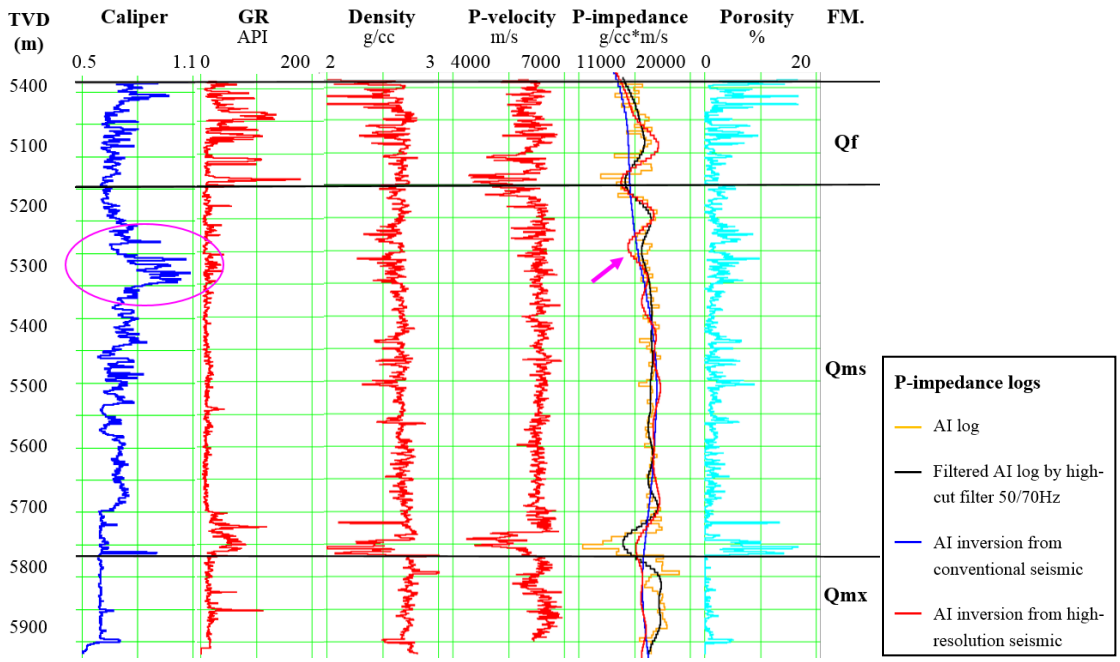

Figure 4.59. The inversion result QC at Wugu 2.

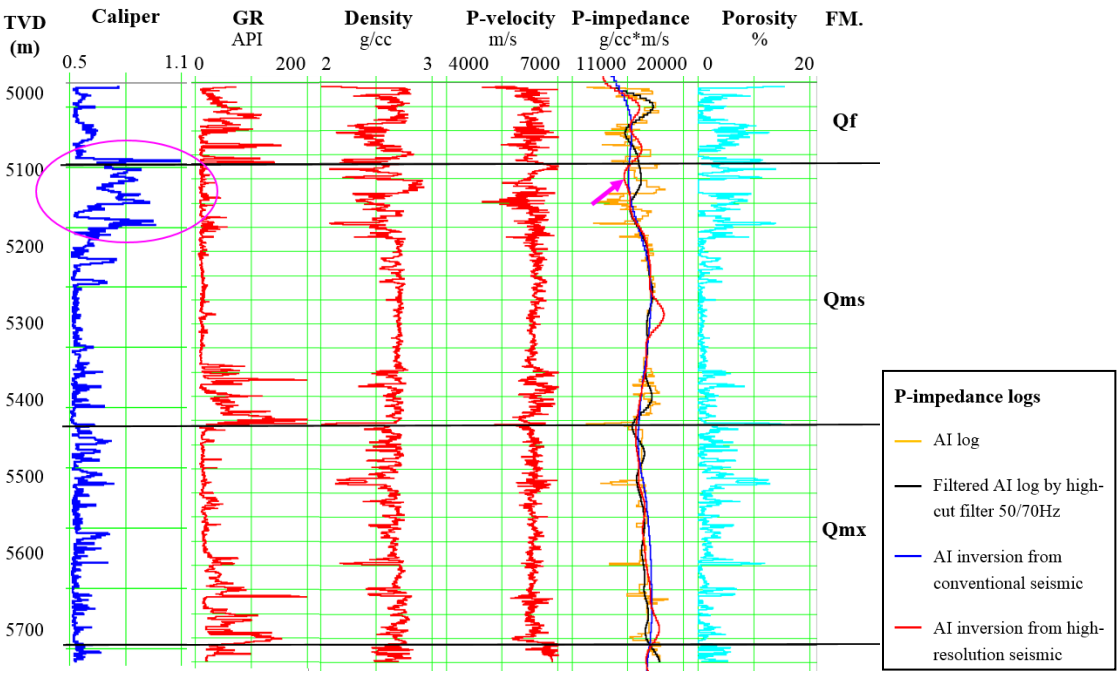

Figure 4.60. The inversion result QC at Wugu 4.

acoustic impedance inversion from conventional seismic loses the accuracy of recovering the impedance at well location. For intervals that have high porosity, they usually have low values for acoustic impedance log and also the acoustic impedance inversion from high-resolution seismic. One interval of the acoustic impedance inversion from high-resolution seismic of Wugu 2 and Wugu 4 has lower impedance values than that of filtered acoustic impedance log (marked by purple arrow in Figure 4.59 and 4.60). Careful examination shows that acoustic impedance log is influenced by the washout zone at these two intervals of Wugu 2 and Wugu 4 (marked by purple circles in Figure 4.57 and 4.58), which makes the acoustic impedance log has higher values than the real impedance log.

4.5.2.3 Inversion results

The conventional seismic data has low central frequency and fails to resolve thin layers of facture zones in the Hexiwu buried-hill (Figure 4.12 and 4.61). The high-resolution seismic data has improved frequency range and has the ability to identify thin layers (purple box and yellow box in Figure 4.61). The inserted log in Figure 4.61 is acoustic impedance log. The low impedance belt immediately below the purple box is from the seismic data. The reason why the acoustic impedance log doesn't have low impedance is that the density and P-velocity logs lose accuracy due to the caliper increasing at that depth (Figure 4.59). The resolution of seismic inversion is the key to identify fractured zones in the Hexiwu buried-hill.

Stratigraphy interpretation based on conventional acoustic impedance inversion has great difficulty due to its low resolution (Figure 4.62). Two formation boundaries are

interpreted based on logging data with one key feature of low impedance. The filtered acoustic impedance log is inserted in Figure 4.62 to augment the sequence boundary interpretation. The formation boundary between Fengfeng and Upper Majiagou Formation is clear as a continuous low-impedance belt, which corresponds to one low sea level period. However, the formation boundary between Upper Majiagou and Lower Majiagou Formation is hard to identify as no continuous low-impedance belt exists. With the acoustic impedance inversion from high-resolution seismic, it is easy to interpret two formation boundaries as two continuous low-impedance belts.

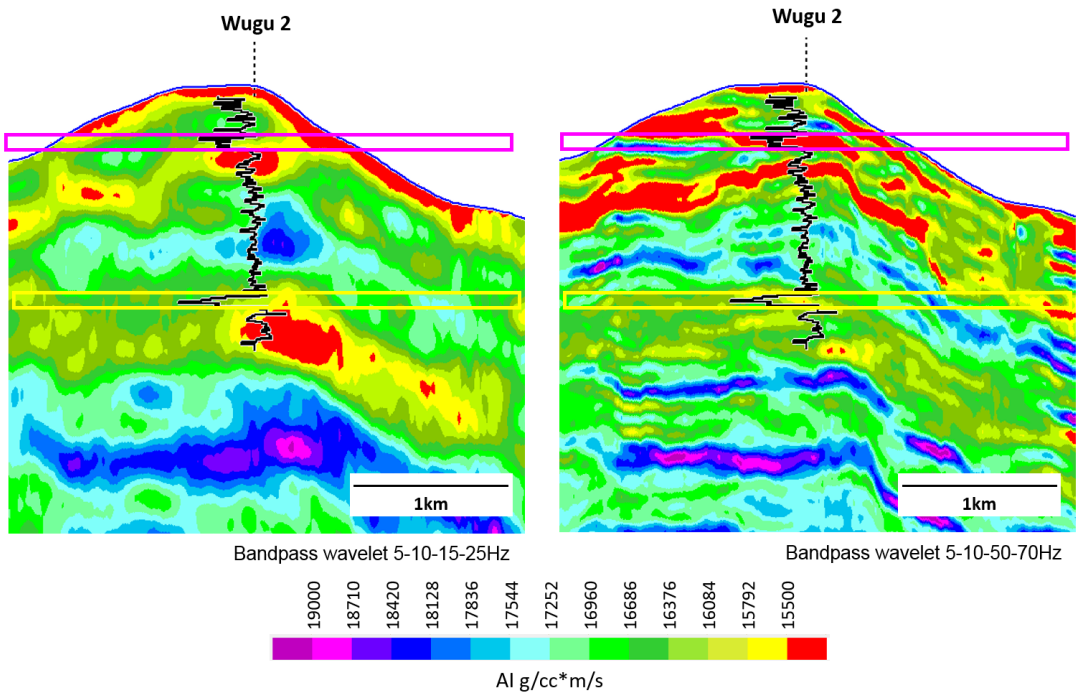

Figure 4.61. The acoustic impedance inversion results comparison at Wugu 2 between conventional seismic and high-resolution seismic data. Two layers of fracture zone are marked by a purple box and a yellow box. Inserted log is P-impedance.

Based on high-resolution seismic inversion, two major sea level cycles can be interpreted. Low sea level produces low-impedance rocks while high sea level produces high-impedance rocks. Therefore, the high-resolution acoustic impedance volume can be used to do sequence stratigraphy interpretation and facies mapping as well.

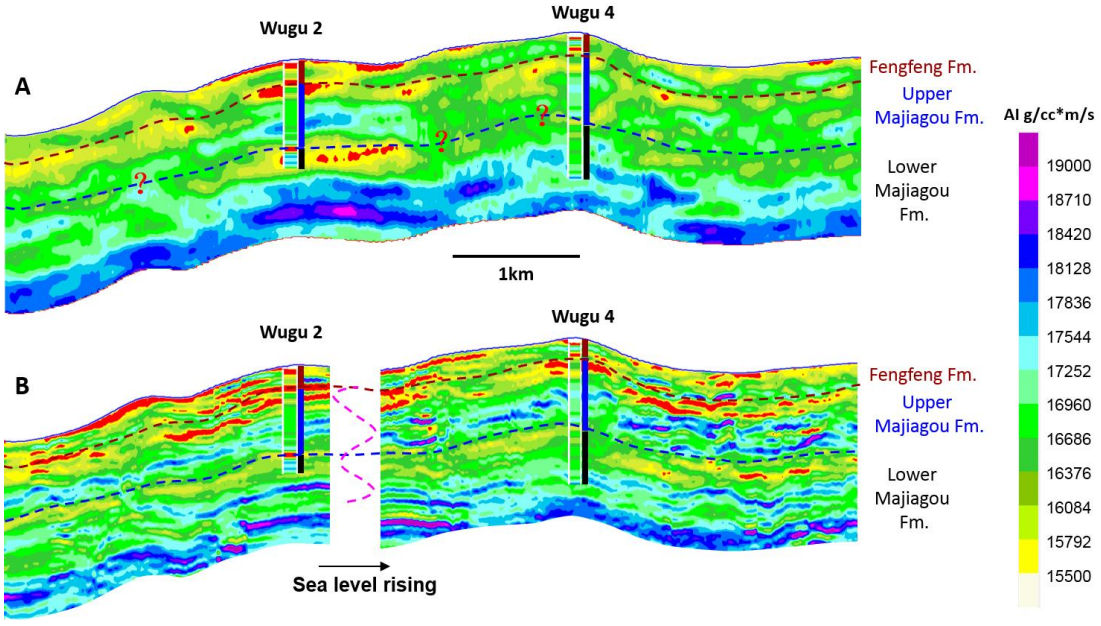

Figure 4.62. The interpretation of conventional (A) and high-resolution seismic inversion (B). The inserted log is filtered acoustic impedance with high-cut filter (20/30 Hz).

Due to several times of elevation and subsidence, a major unconformity is created to separate Ordovician carbonates and Paleogene sandstones in the Hexiwu area. Along the unconformity, a cavity belt is developed by dissolution of meteoric water (Guo et al., 2009). One slice of high-resolution acoustic impedance is generated along the cavity zone (Figure 4.63). On this impedance surface, four notable low-impedance

zones (A, B, C, and D) are picked out for detailed interpretation. Structurally, A and B are located on structural highs; C on the slope; and D in the trough.

Zone A, which is located in the southeast part of the Hexiwu area, is a thick layer of low-impedance immediately below the regional unconformity. It has the largest area out of four zones. Two typical lines (inline 1090 and xline 3100) are picked out in Figure 4.64 for detailed interpretation. Zone A is defined as a buried-hill head reservoir, because it is sitting on a structural high and bounded by the regional unconformity only. Currently no well is drilled on this top. It has great potential to trap oil/gas if source rock and migration path are coupling well for this zone.

Zone B is also a local structural high, close to Zone A, on map of Figure 4.61. Inline 1350 and xline 2890 are cutting through this zone (Figure 4.65). One profile of inline 1350, buried-hill head reservoir is bounded by a minor fault on the right. This area develops several minor faults, which can be seen both from inline 1350 and xline 2890. Besides the same buried-hill head reservoir on inline 1350, several buried-hill internal reservoirs can be recognized on xline 2890. Their common feature is that their one end or both is/are bounded by minor fault/faults. Those minor faults can be migration path for oil/gas to trap in those reservoirs.

Zone C is on the southwest flank of the Hexiwu area (Figure 4.63). Its top low-impedance zone is truncated by the unconformity (Figure 4.66). The formation of this type of reservoir is caused by erosion during the elevation and dissolution during the burial. Their size are restricted by the dissolution in the strata. Buried-hill slope reservoir

can also be bounded by fault on the other ends. The unconformity and bounded fault can be oil/gas migration paths to charge these type of reservoirs.

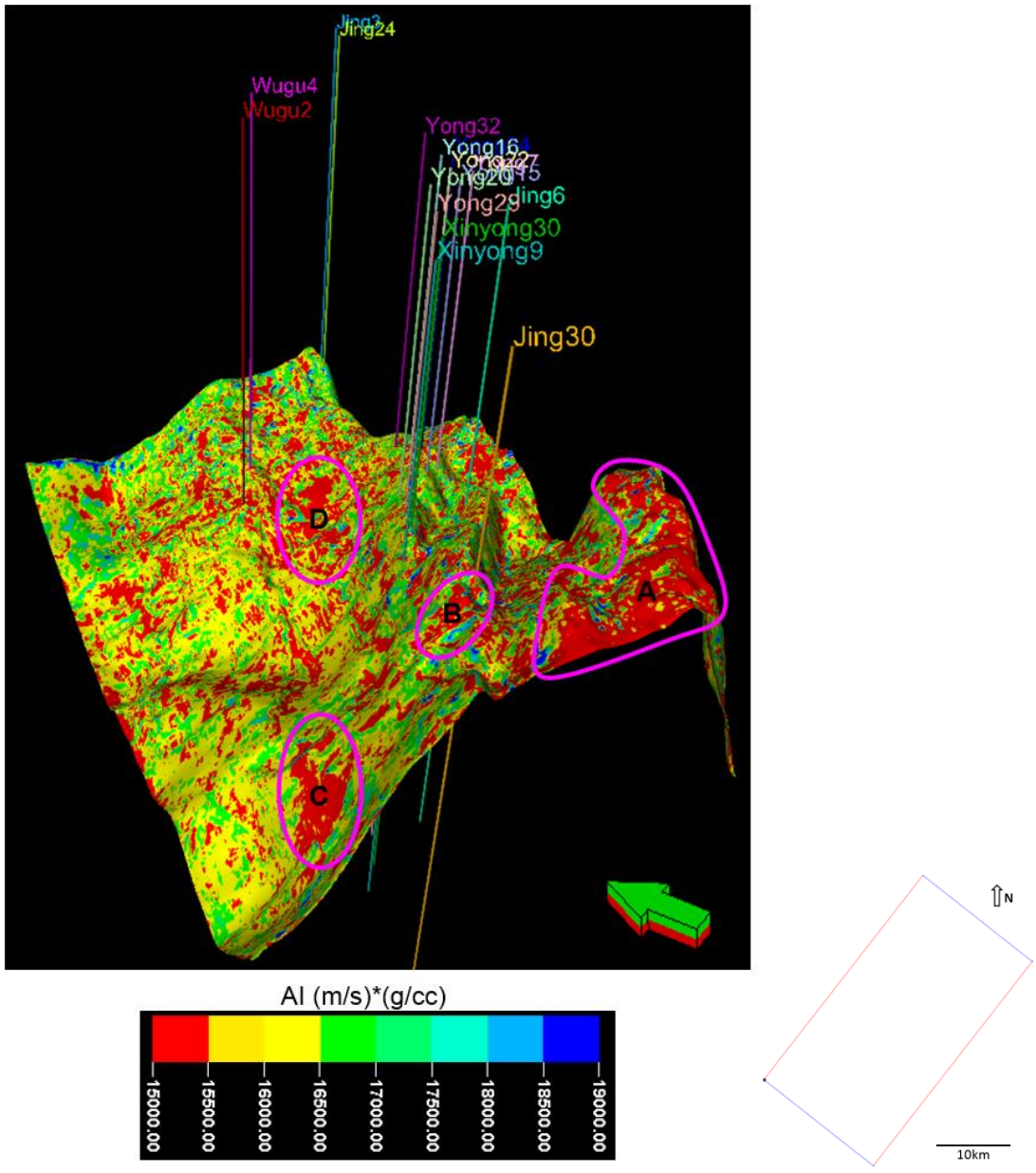

Figure 4.63. The interpretation of high-resolution seismic inversion. The slice is cutting through the top cavity zone.

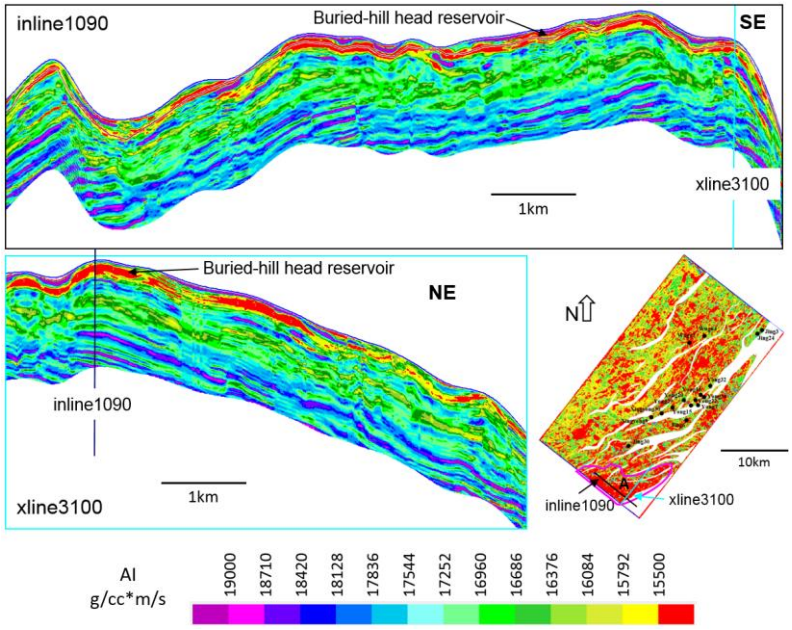

Figure 4.64. The inline and xline view and interpretation of zone A, which is the low-impedance zone immediately below the unconformity.

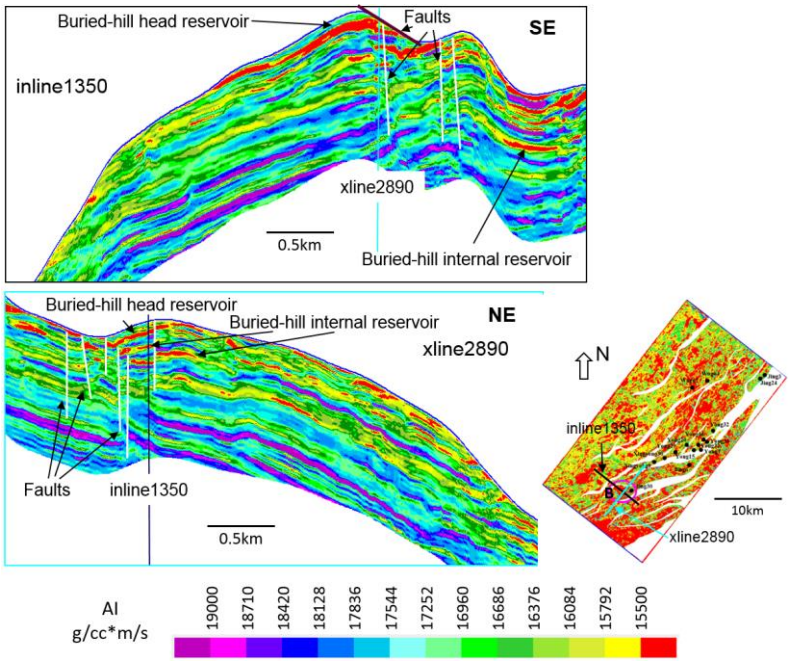

Figure 4.65. The inline and xline view and interpretation of zone B, which is the low-impedance and/or high-impedance zone immediately below and parallel to the unconformity.

Zone D, sitting in the trough area, is located in the northeast part of the Hexiwu field (Figure 4.63). On the profile of inline 2110, several buried-hill slope reservoirs and one buried-hill internal reservoir can be identified (Figure 4.67). Xline 2970 doesn't show obvious faults. Minor faults play important role in bounding both buried-hill slope and internal reservoirs. The unconformity and/or faults can be migration paths to charge buried-hill slope reservoirs while the minor faults can be migration paths to charge buried-hill internal reservoirs. Both buried-hill slope and internal reservoirs are the major exploration targets of the next stage.

The product of porosity and pore structure parameter has a better relationship with acoustic impedance than porosity does. A good example has been show in Chapter III. Its application in Hexiwu carbonate buried-hill shows that high values of the product can be interpreted to be high-porosity or highly fractured reservoirs (Figure 4.47). After acoustic impedance inversion from high-resolution seismic data, the product of porosity and pore structure parameter is calculated and shown in Figure 4.68. In the area of Jing 30, Xinyong 9, Xinyong 30, Wugu 2, Wugu 4, and Jing 3, high product zones are on the top part of the profile, which is the cavity zone. On the map view of Figure 4.69, Zone A, Zone B, Zone C, and Zone D are recognized with high values of the product, which means those zones can either be high-porosity zone or highly fractured zone. This slice is also cutting through the top cavity zone immediately below the regional unconformity as the impedance map in Figure 6.63. They are all potential oil/gas reservoirs for the production of next stage.

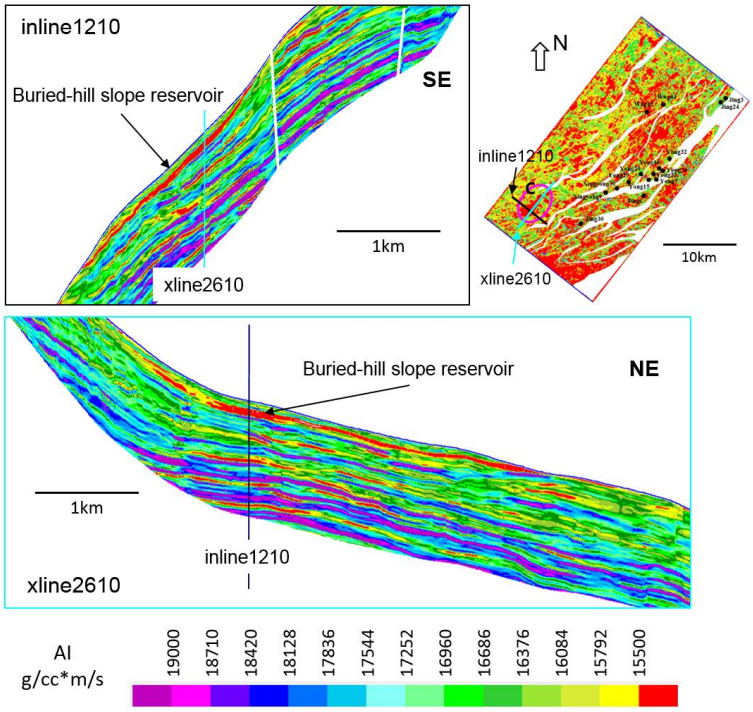

Figure 4.66. The inline and xline view and interpretation of zone C, which is the low-impedance and/or high-impedance zone immediately below and parallel to the unconformity.

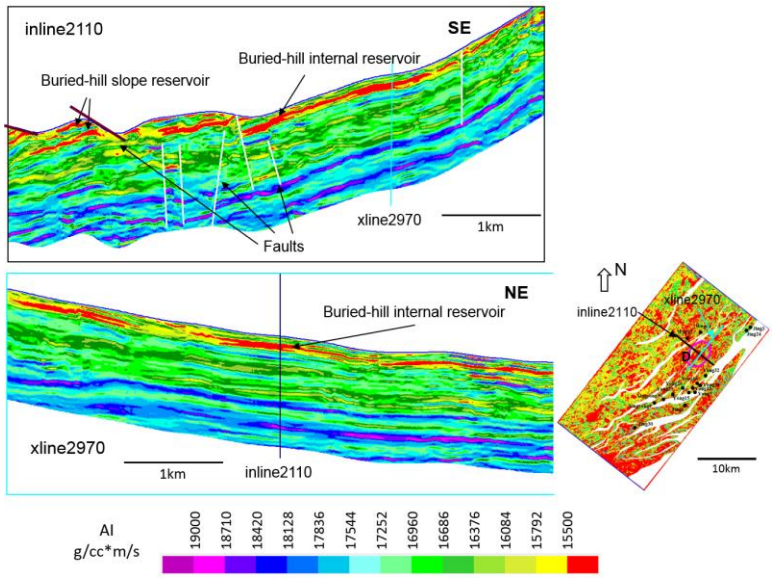

Figure 4.67. The inline and xline view and interpretation of zone D, which is the low-impedance and/or high-impedance zone immediately below and parallel to the unconformity.

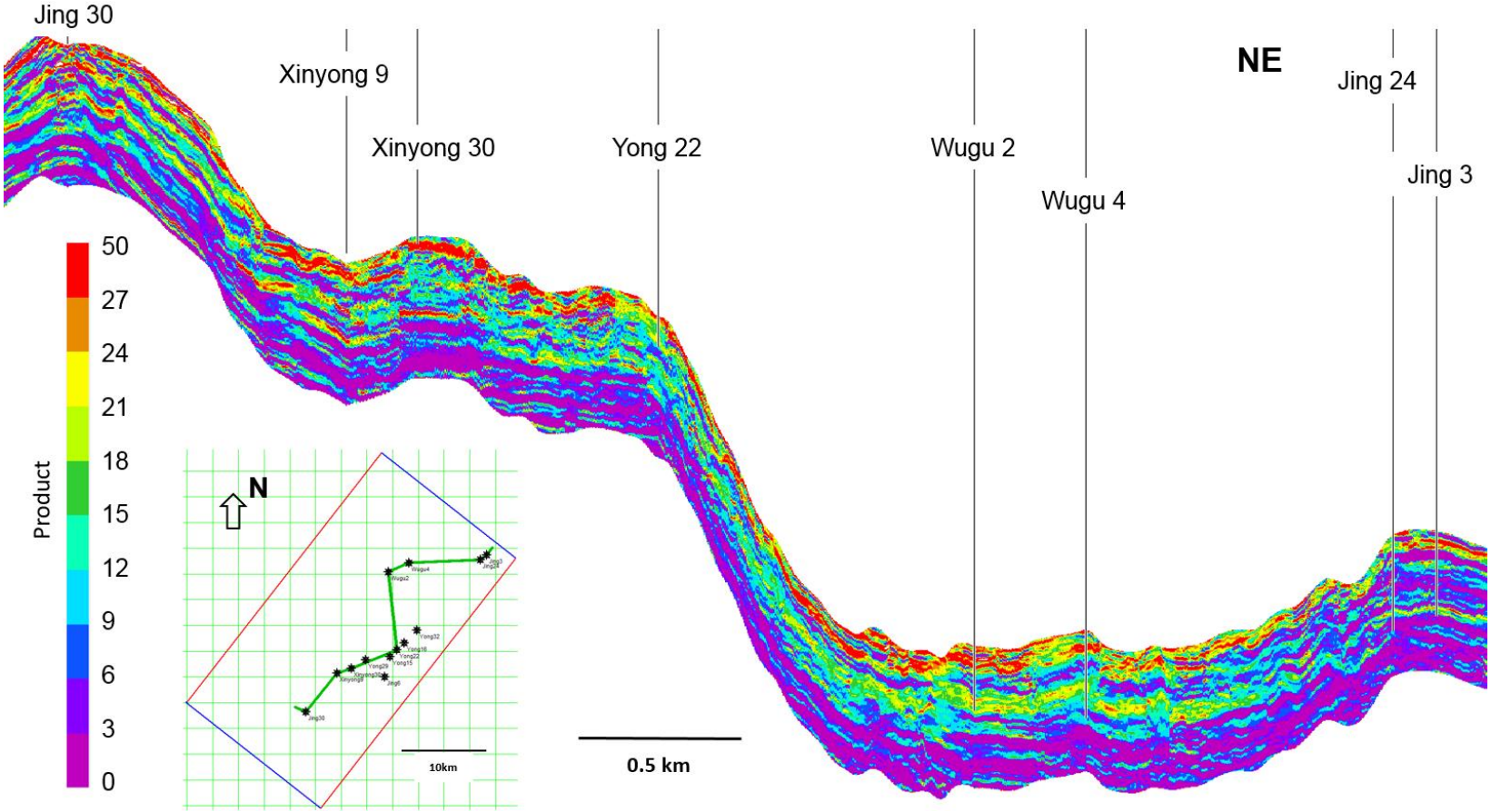

Figure 4.68. A profile of the product of porosity and pore structure parameter from high-resolution seismic data cutting through Jing 30, Xinyong 9, Xinyong 30, Yong 22, Wuug 2, Wugu 4, Jing 24, and Jing 3.

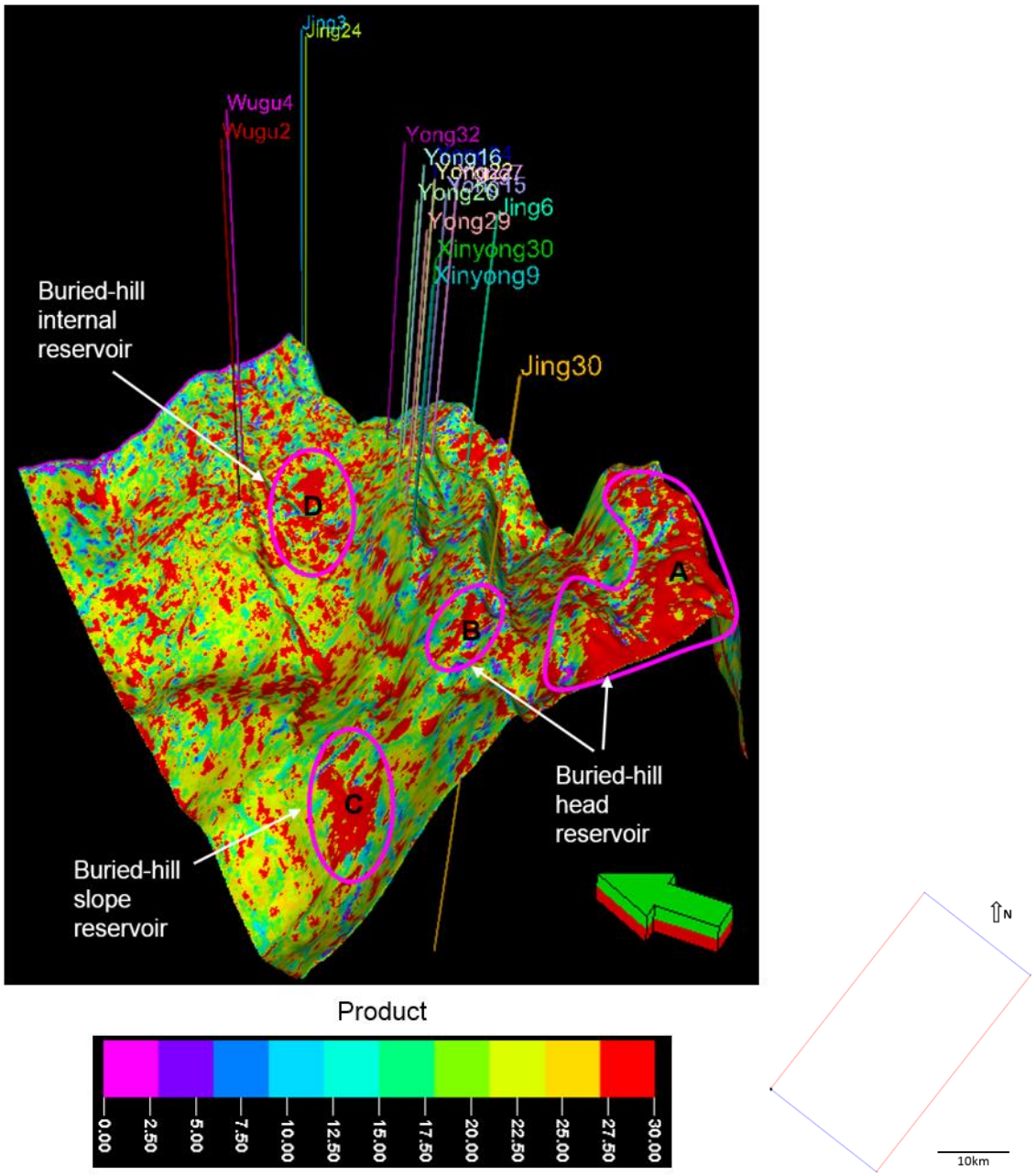

Figure 4.69. The interpretation of product of porosity and pore structure parameter from high-resolution seismic inversion. The slice is cutting through the top cavity zone.

4.5.2.4 Geobody extraction

Geobody extraction is a practical approach to show body interest in 3D view. It has been widely used to show the salt body and sand body geometry (channel or fan). In this research, geobody with low impedance (less than 15,500 (g/cc)×(m/s)) and geobody with high product of porosity and pore structure parameter (greater than 30) is extracted with the assistance of Petrel software to show the 3D distribution of reservoir zones in the Hexiwu area.

Ordovician strata, including Fengfeng Formation, Upper Majiagou Formation, and Lower Majiagou Formation, experienced several uplifting and subsidence in the Hexiwu area. During the uplifting, the exposed carbonates underwent erosion. Figure 4.70 shows the location of residual Ordovician strata in the Hexiwu area. Figure 4.71 shows the structure in the Hexiwu area.

Three different volumes of impedance or product of porosity and pore structure parameter are used to conduct the geobody extraction and analysis: 1) volume I is within the strata from the Ordovician top horizon to 250 ms, which includes older strata than Ordovician strata; 2) volume II is within the residual Ordovician strata from the Ordovician top horizon to 250 ms; and 3) volume III within the residual Ordovician strata from the Ordovician top to bottom horizon. The interpretation horizons are provided by Huabei Oilfield.

Figure 4.72 and 4.73 shows the low impedance (less than 15,500 (g/cc)×(m/s)) geobody extracted from volume I. It is different from the geobody of a salt body or a sand body (channel or delta), which shows a large 3D geometry. The low impedance

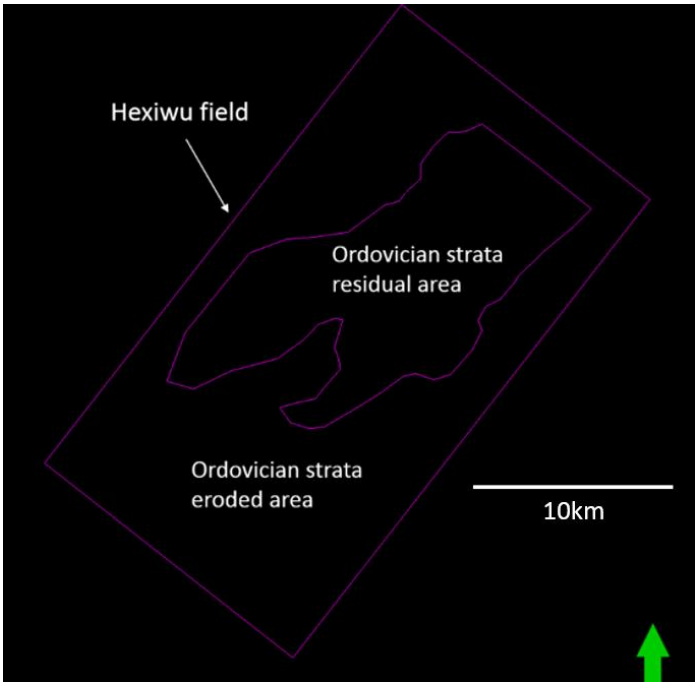

Figure 4.70. A plane map showing the location of residual Ordovician strata in the Hexiwu field.

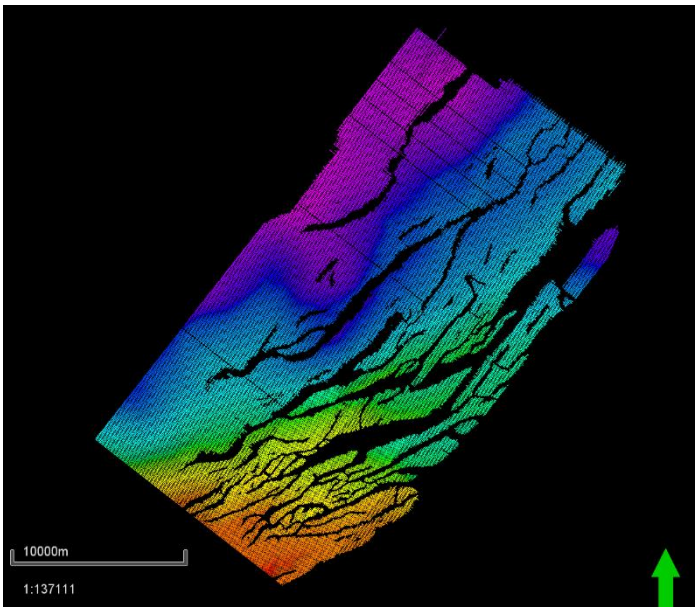

Figure 4.71. The structure map in the Hexiwu area. The interpretation is provided by PetroChina.

geobody consists of many low impedance bodies. The top view of this geobody shows low impedance covering most of the area except the faults. However, the rotated view of the same geobody shows low impedance located along with structure belts. As we discussed before, the buried-hill carbonates experienced long time diagenesis. The depositional pore system and mineralogy are greatly altered by strong diagenesis. The hydrocarbon storage space is fracture and fracture related dissolution pores (vugs, molds, and cavities). The geobody of low impedance indicates the distribution of reservoir rocks has close relationship with faults. The impedance inversion from high-resolution seismic successfully confirms that the distribution of porous carbonates in the Hexiwu area is controlled by faults, which increase the dissolution of vugs and/or molds and increase the permeability in the rock. Recall the four low impedance zones interpreted based on the slice cutting though the top cavity zone in Figure 4.63, they all show large low impedance boy in Figure 4.73.

Figure 4.74 and 4.75 show the low impedance geobody extracted from volume II. The place of Wugu 2 has a larger body than that of Wugu 4. Recall the highlighted data in Figure 4.44. The inversion result successfully demonstrates that the place of Wugu 2 is more fractured than that of Wugu 4. From the rotated view, the geobody is mainly following the pattern of faults. Figure 4.76 and 4.77 show the low impedance geobody extracted from volume III. It is very similar to the geobody extracted from volume II in Figure 4.74 and 4.75.

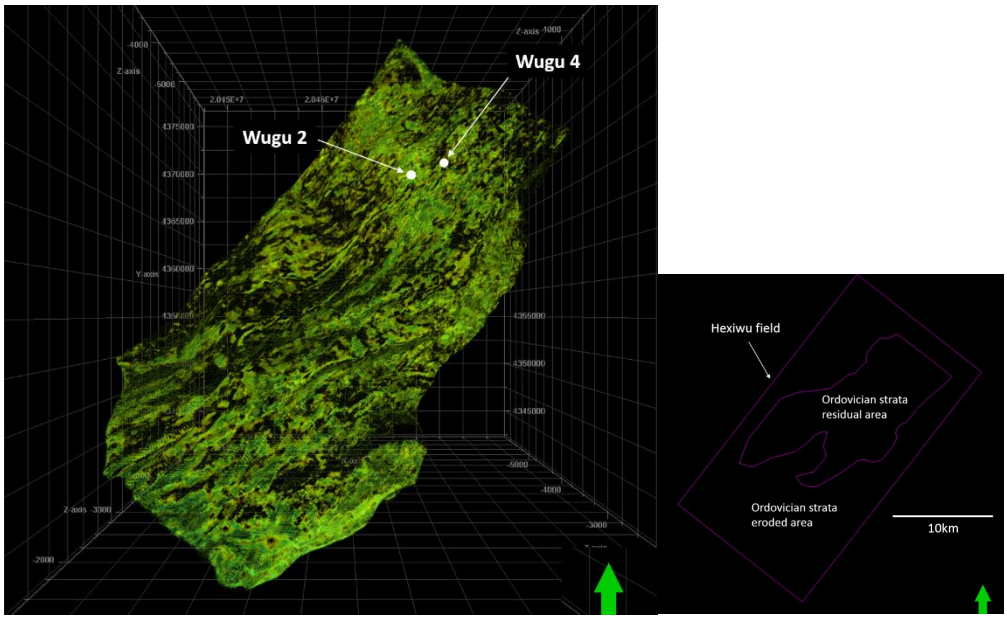

Figure 4.72. A top view of low impedance zone (less than 15,500 (g/cc)×(m/s)) in the Hexiwu area. The geobody is extracted within the strata from the Ordovician top horizon to 250 ms below.

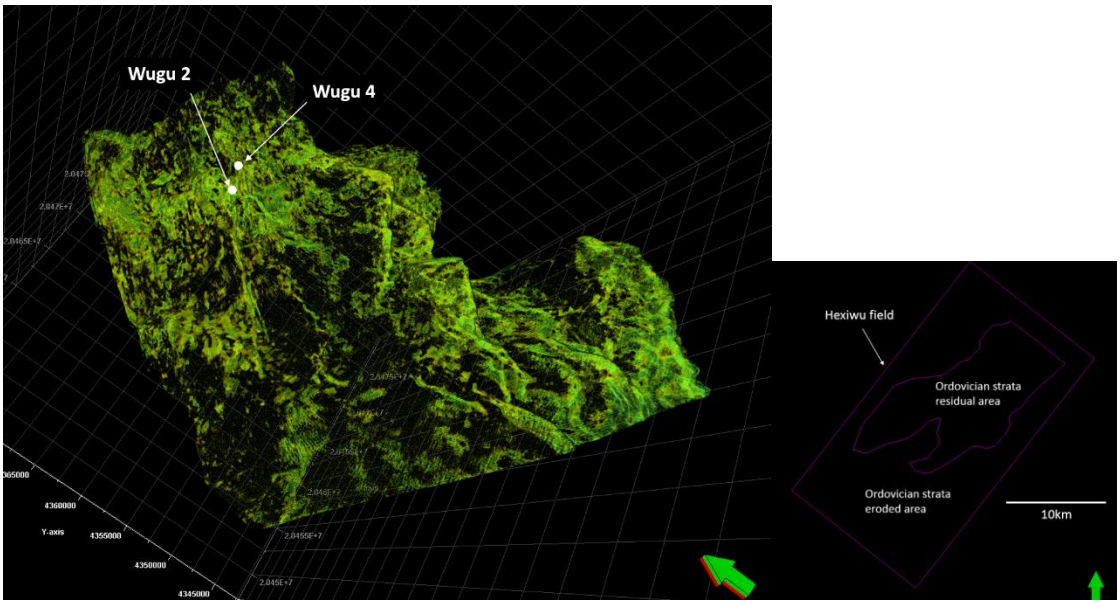

Figure 4.73. A rotated view of low impedance zone (less than 15,500 (g/cc)×(m/s)) in the Hexiwu area. The geobody is extracted within the strata from the Ordovician top horizon to 250 ms below.

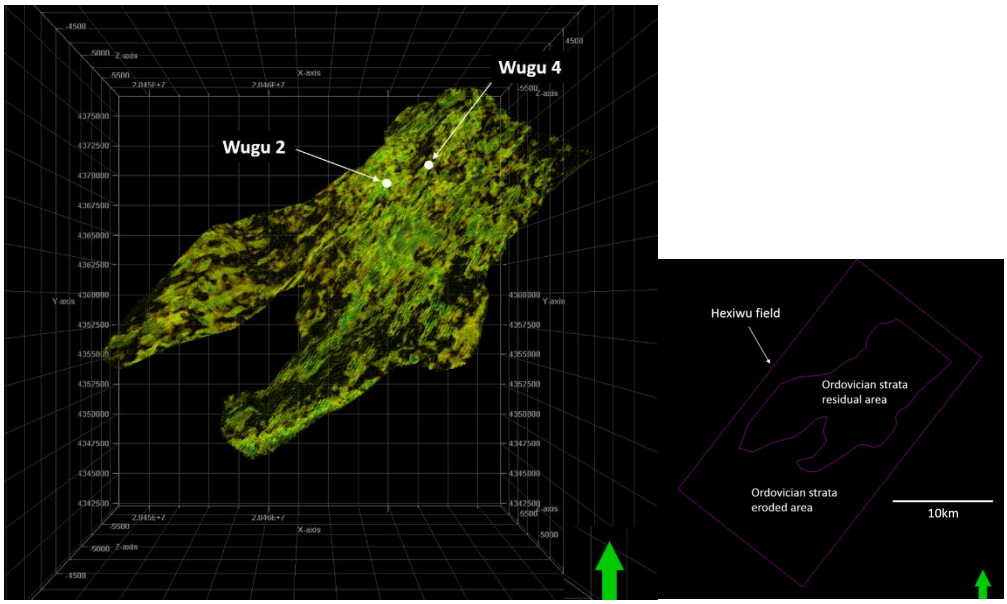

Figure 4.74. A top view of low impedance zone (less than 15,500 (g/cc)×(m/s)) in residual Ordovician strata. The geobody is extracted within the strata from Ordovician top horizon to 250 ms below.

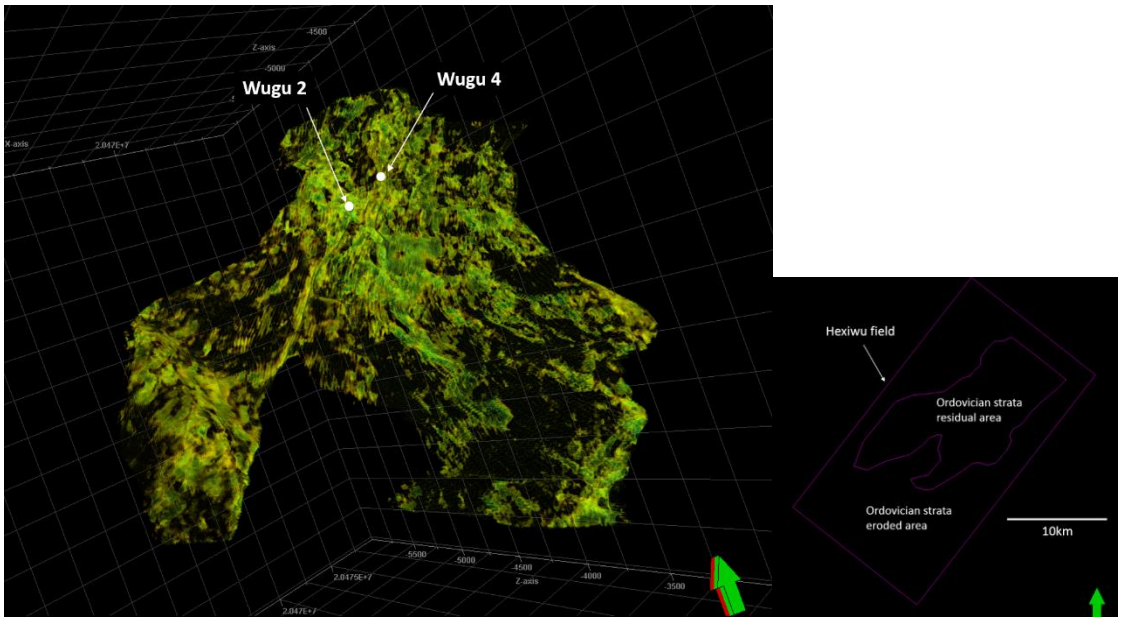

Figure 4.75. A rotated view of low impedance zone (less than 15,500 (g/cc)×(m/s)) in residual Ordovician strata. The geobody is extracted within the strata from Ordovician top horizon to 250 ms below.

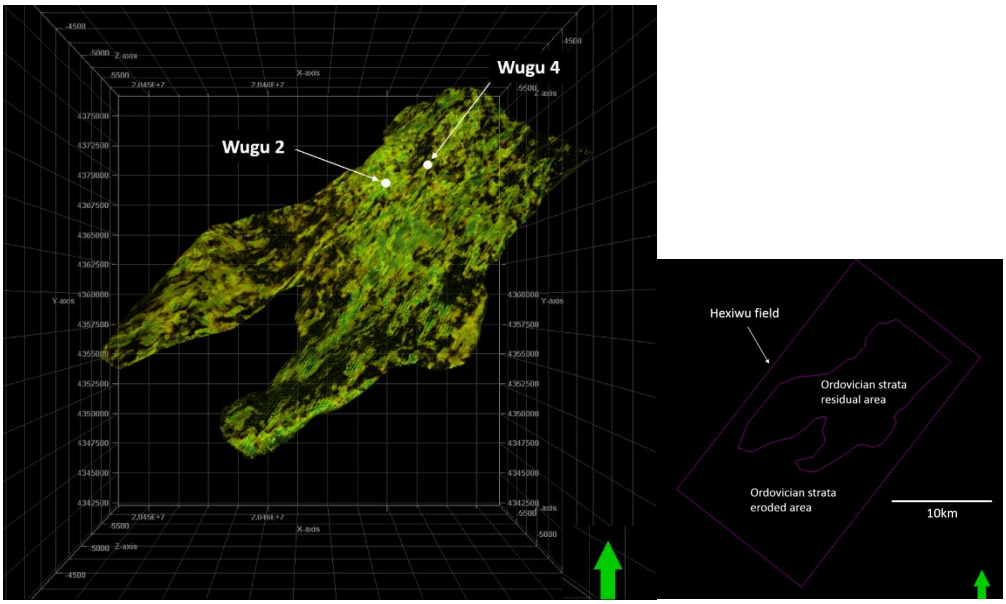

Figure 4.76. A top view of low impedance zone (less than 15,500 (g/cc)×(m/s)) in residual Ordovician strata. The geobody is extracted within the strata from Ordovician top to bottom horizon.

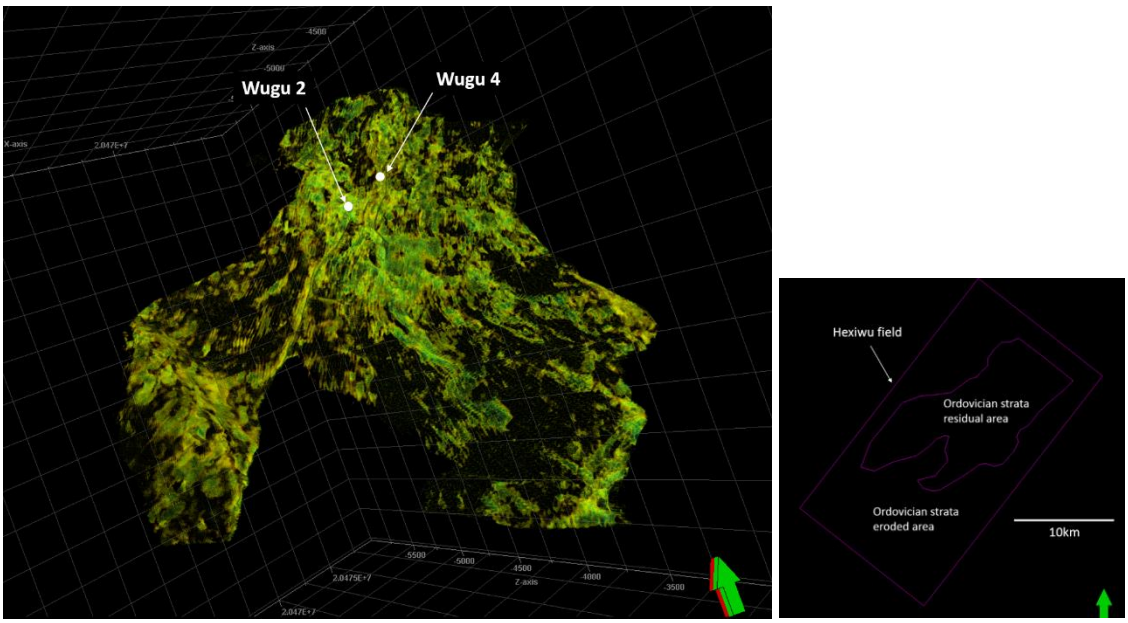

Figure 4.77. A rotated view of low impedance zone (less than 15,500 (g/cc)×(m/s)) in residual Ordovician strata. The geobody is extracted within the strata from Ordovician top to bottom horizon.

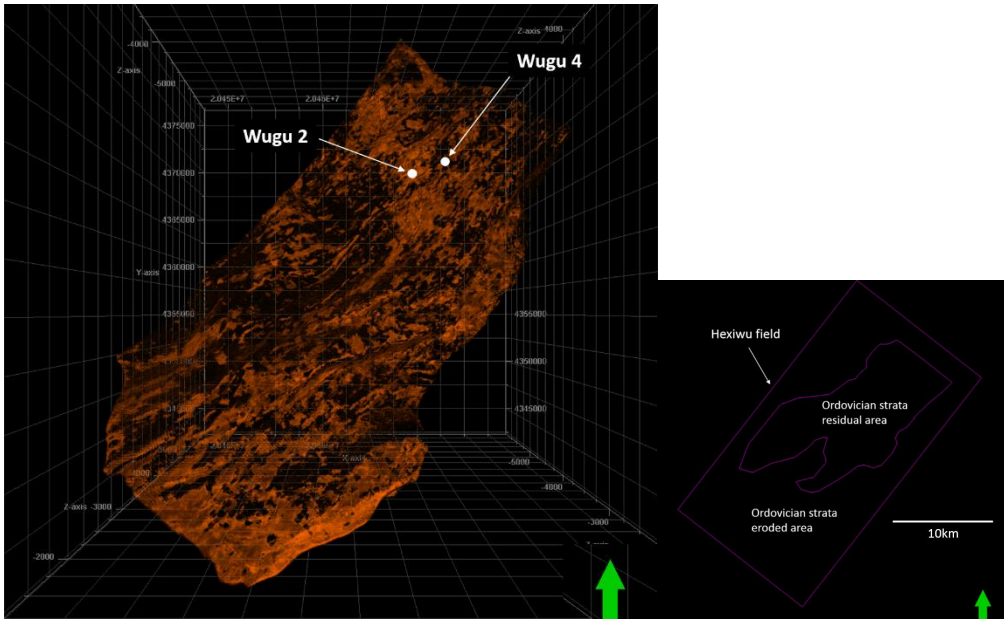

Figure 4.78. A top view of high product zone (greater than 30) in the Hexiwu area. The geobody is extracted within the strata from the Ordovician top horizon to 250 ms below.

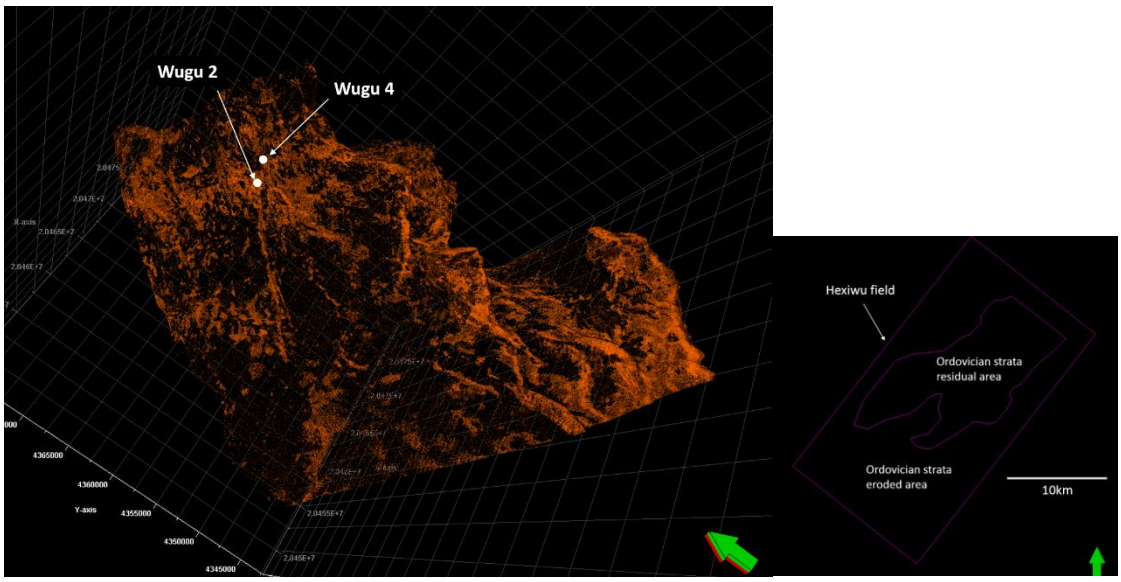

Figure 4.79. A rotated view of high product zone (greater than 30) in the Hexiwu area. The geobody is extracted within the strata from the Ordovician top horizon to 250 ms below.

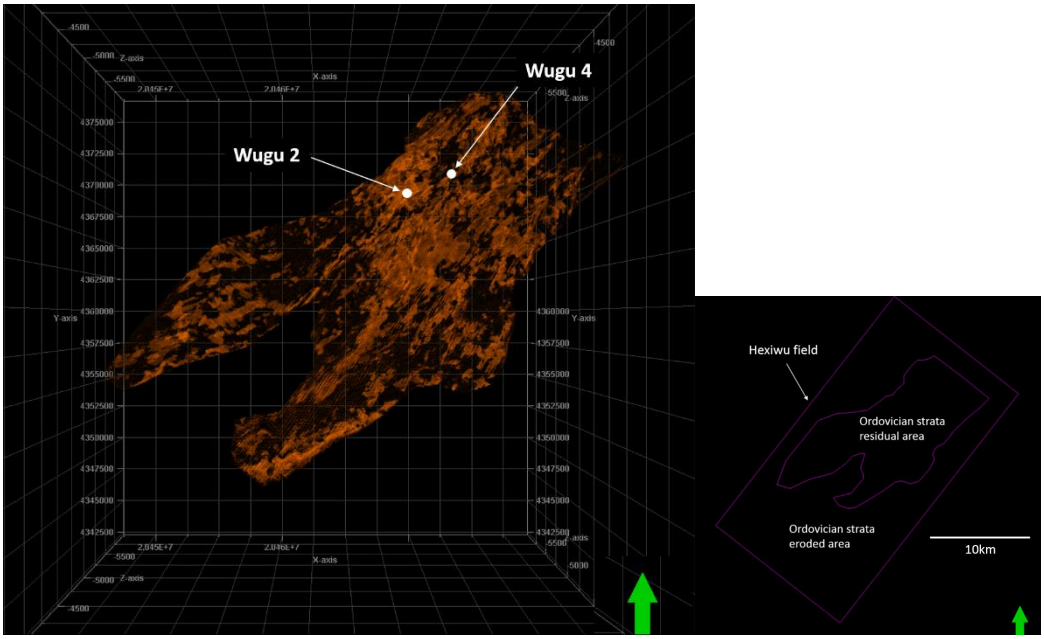

Figure 4.80. A top view of high product zone (greater than 30) in residual Ordovician strata. The geobody is extracted within the strata from the Ordovician top horizon to 250 ms below.

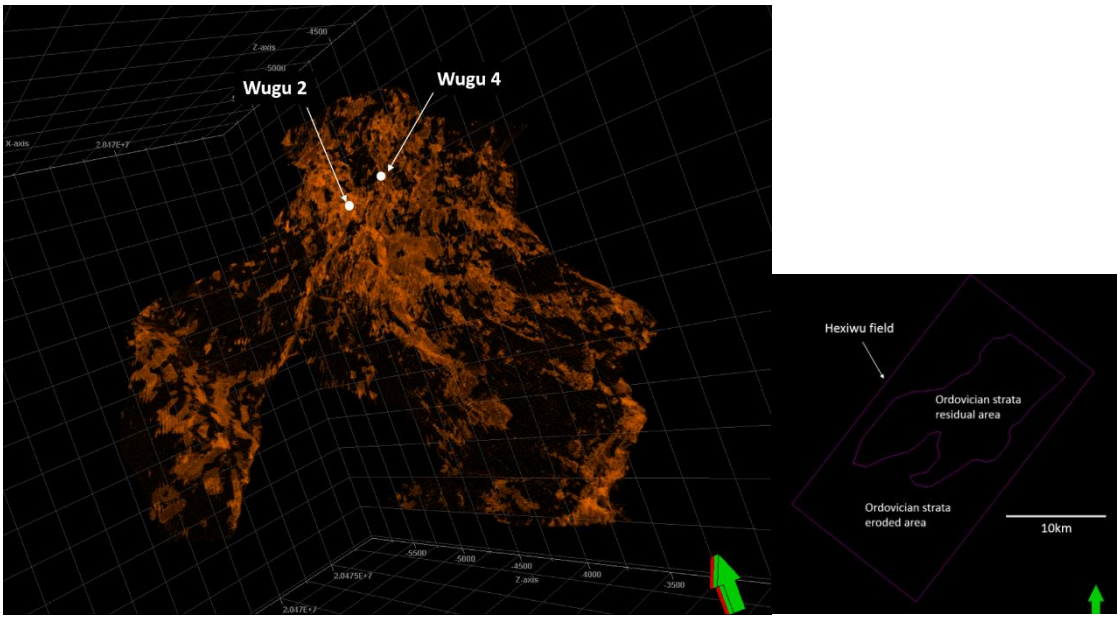

Figure 4.81. A rotated view of high product zone (greater than 30) in residual Ordovician strata. The geobody is extracted within the strata from the Ordovician top horizon to 250 ms below.

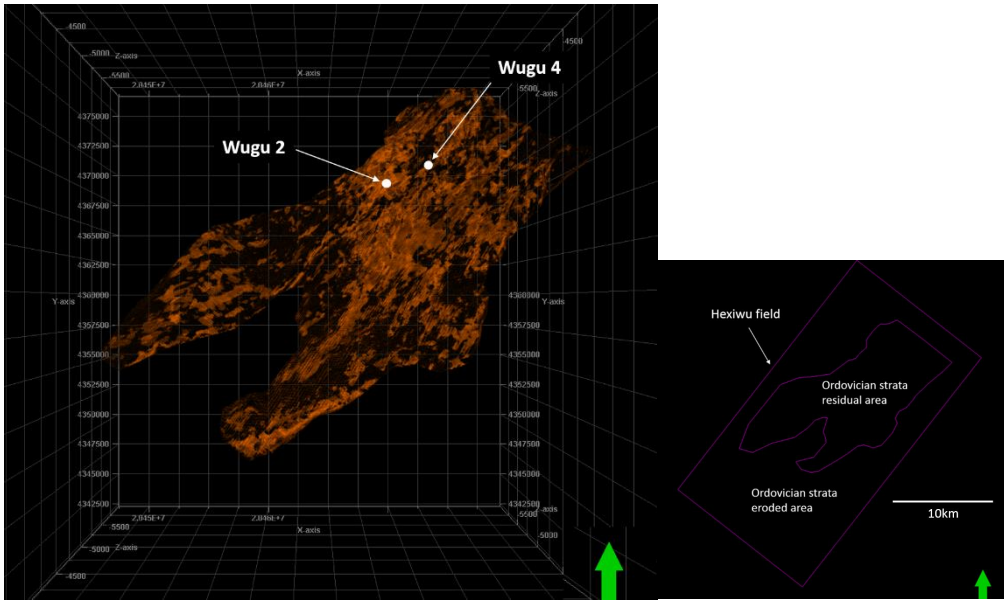

Figure 4.82. A top view of high product zone (greater than 30) in residual Ordovician strata. The geobody is extracted within the strata from the Ordovician top to bottom horizon.

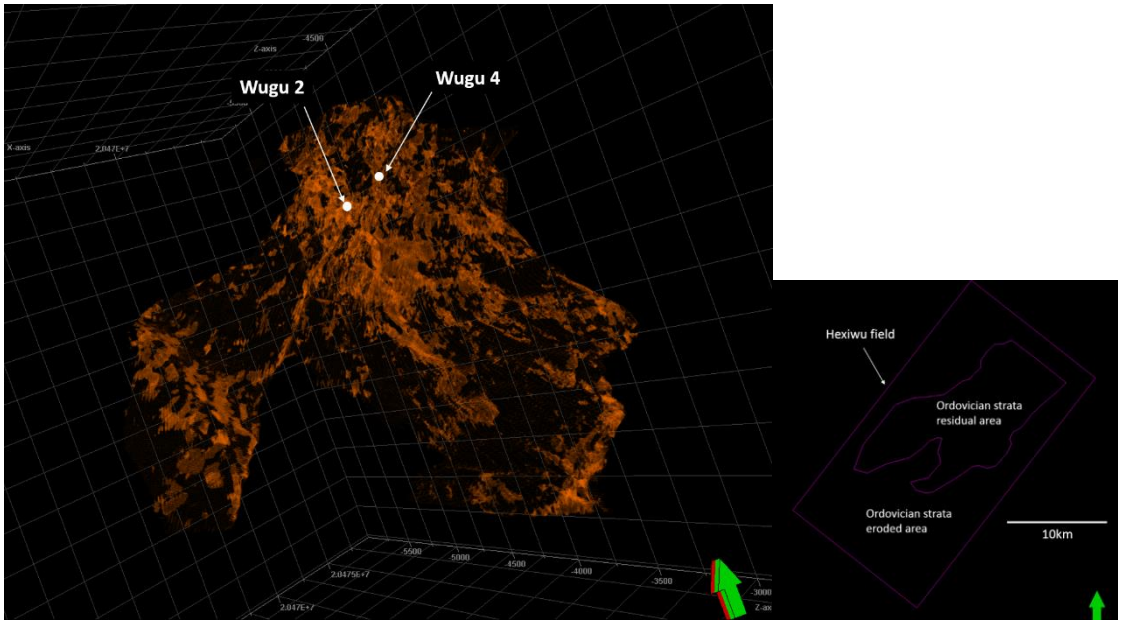

Figure 4.83. A rotated view of high product zone (greater than 30) in residual Ordovician strata. The geobody is extracted within the strata from the Ordovician top to bottom horizon.

Figure 4.78, 4.79, 4.80, 4.81, 4.82, and 4.83 are the geobody of the product of porosity and pore structure parameter. The geobody of Figure 4.78 and 4.79 is extracted from volume I; the geobody of Figure 4.80 and 4.81 is extracted from volume II; and the geobody of Figure 4.82 and 4.83 is extracted from volume III. A value of 30 is set as the threshold to extract geobody. From those figures, it is clear that high product geobody follows the structural patterns and proves the controlling of structure on reservoir rocks in the Hexiwu area.

4.5.3 Prestack seismic inversion

A better understanding of the influence of fractures on rock velocity-porosity complexity and permeability heterogeneity can be achieved by the estimation of porosity and pore structure parameters in the field. Natural fractured zones will be mapped within the carbonate buried hill based on the good estimations of porosity and pore structure diversity. The improved approach of rock-physics-based log and seismic inversion of

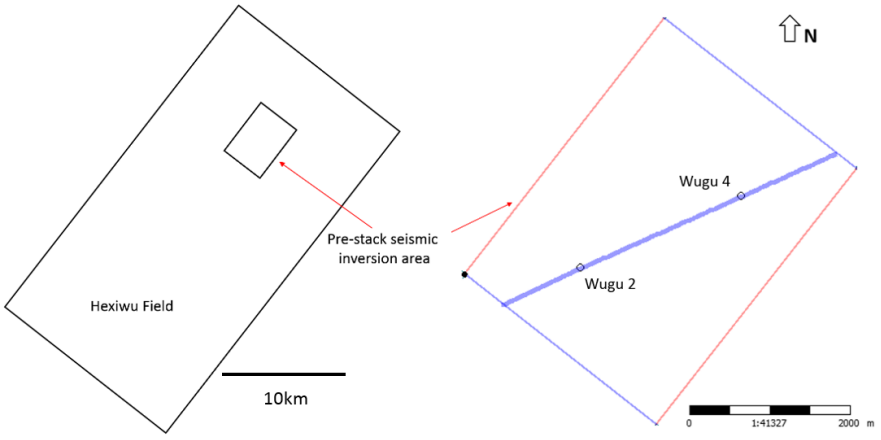

Figure 4.84. The map showing the prestack seismic inversion area and the position of 2-D line cutting through Wugu 2 and Wugu 4.

reservoir porosity and pore types has been successfully applied to the log set in the Hexiwu area, which is documented in the methodology part. With a better understanding of inversion theory, the prestack seismic inversion is carried out, which will provide more information on porosity and pore structure parameter.

Due to the seismic data availability, prestack seismic inversion was only applied to a small area around Wugu 2 and Wugu 4 (Figure 4.84). The synthetic seismograms of Wugu 2 and Wugu 4 are implemented with band-pass wavelet in Figure 4.85. Two wells both show good correlations with seismic angle stacks (Figure 4.86 and 4.87).

Elastic impedances (EI5, EI12, and EI19) are acquired by model-based inversion from near-angle stack, mid-angle stack, and far-angle stack respectively with band-pass wavelet (Figure 4.88, 4.89, and 4.90). The all stack seismic volume contains the information of EI11, as we stacked the 2 to 21 degree traces (Figure 4.91). These four elastic impedances look very similar. They all show low impedance belts at the top of the profiles. However, the patterns of low impedance belts are different from each other, which indicates the AVO characteristics in this formation. For the purpose of

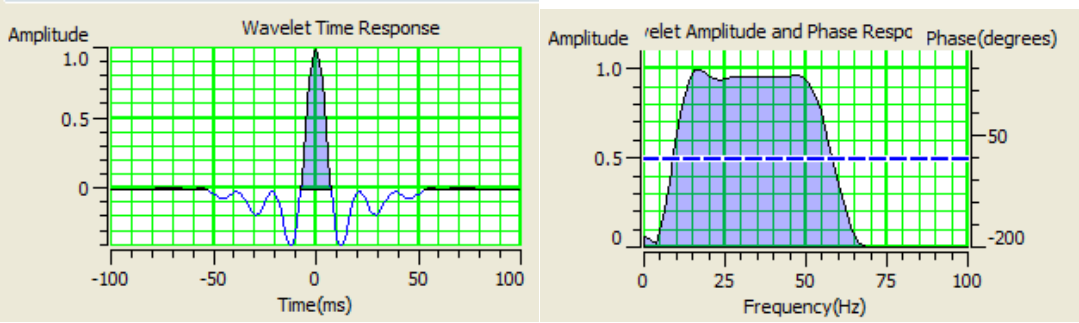

Figure 4.85. The wavelet (band-pass 5-15-50-70 Hz) used in prestack seismic inversion.

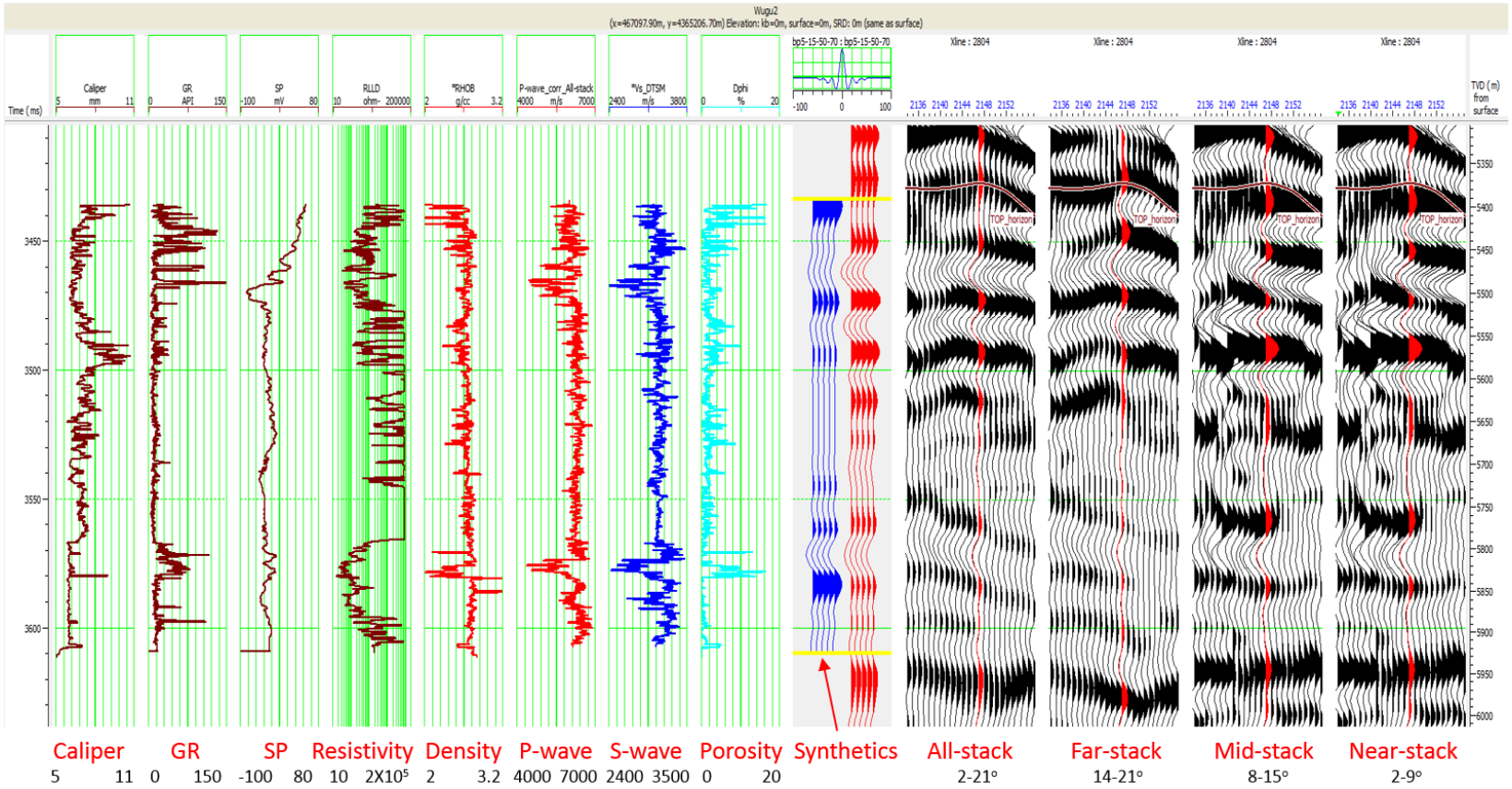

Figure 4.86. Synthetic seismogram of Wugu 2. The wavelet used is band-pass 5-15-50-70 Hz.

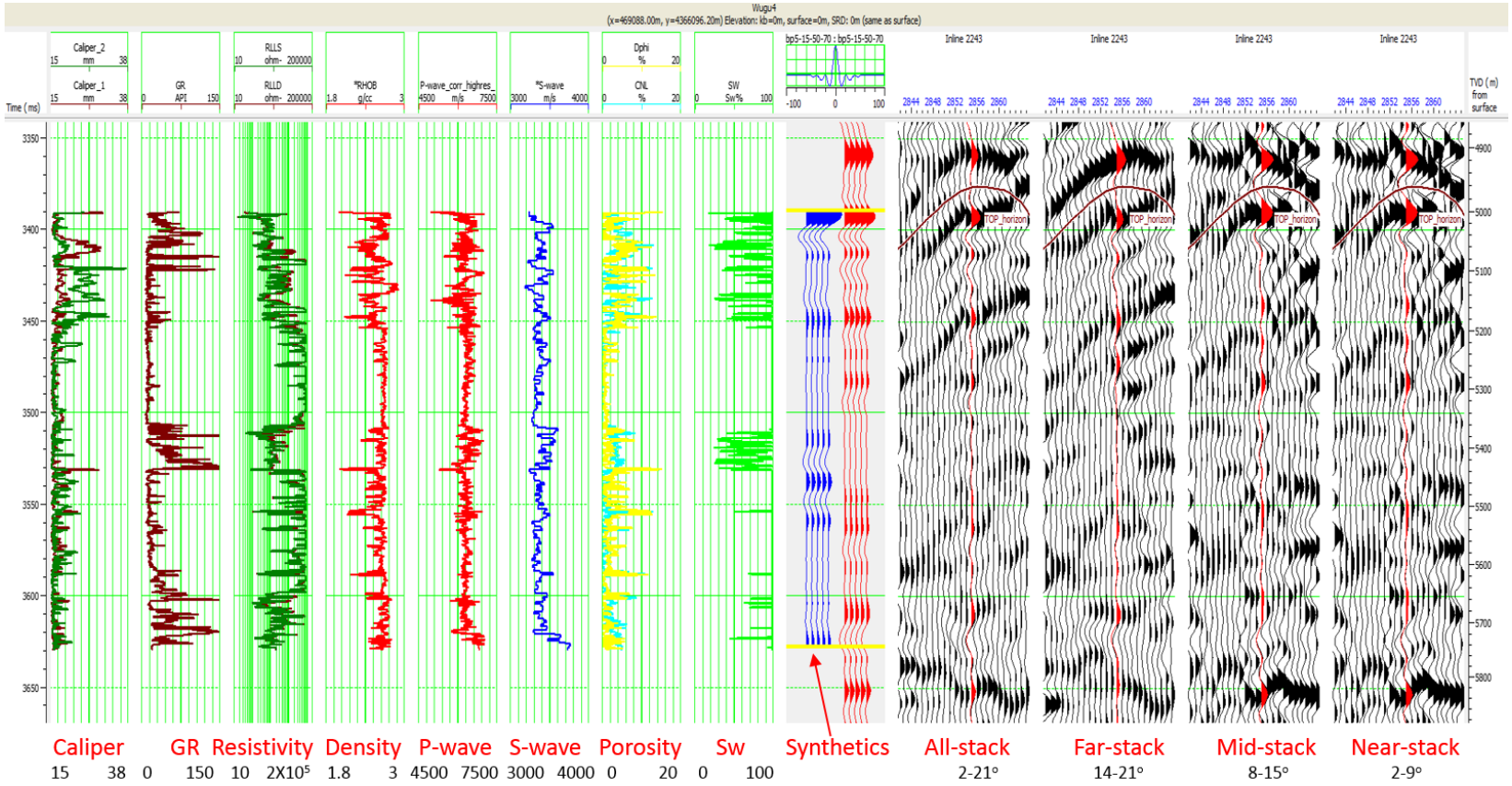

Figure 4.87. Synthetic seismogram of Wugu 4. The wavelet used is bandpass 5-15-50-70 Hz.

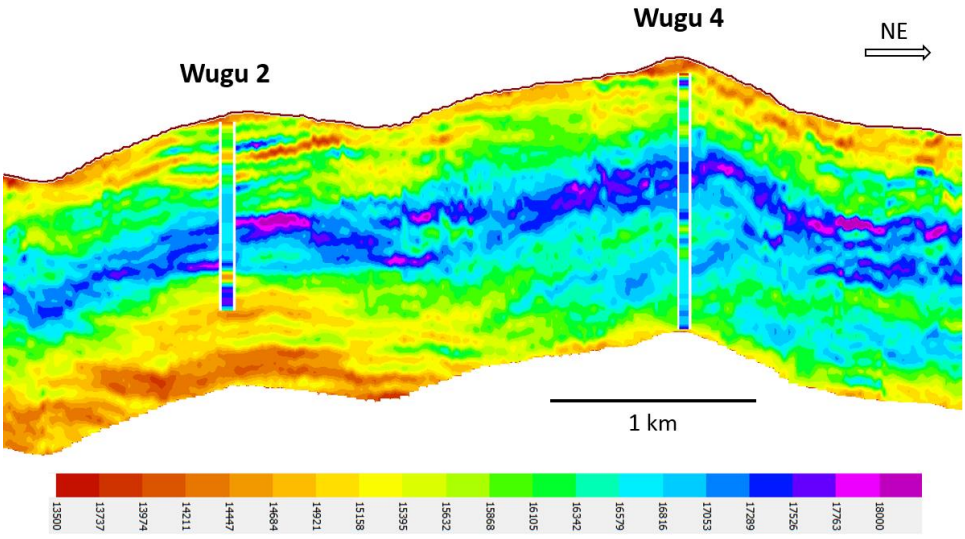

Figure 4.88. A 2D profile of EI5 from near angle stack seismic. The inserted color column is the filtered EI5 log by high-cut filter 50-70 Hz. The position of 2D line is shown in the right figure in Figure 4.84.

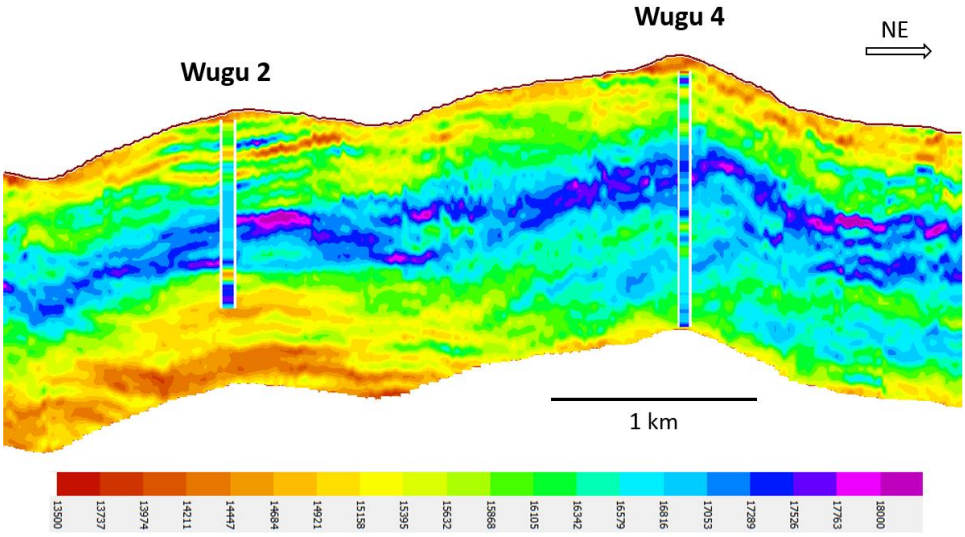

Figure 4.89. A 2D profile of EI12 from middle angle stack seismic. The inserted color column is the filtered EI12 log by high-cut filter 50-70 Hz.The position of 2D line is shown in the right figure in Figure 4.84.

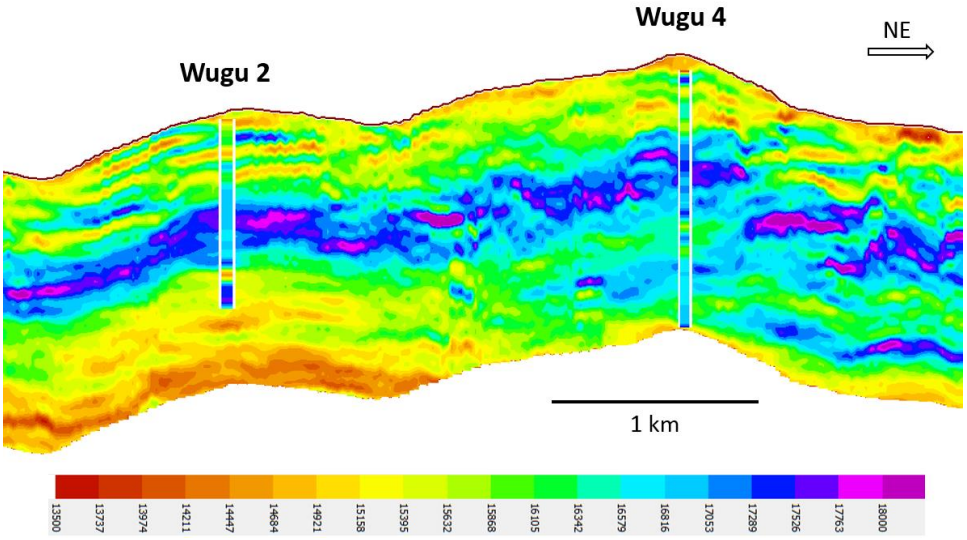

Figure 4.90. A 2D profile of EI19 from far angle stack seismic. The inserted color column is the filtered EI19 log by high-cut filter 50-70 Hz. The position of 2D line is shown in the right figure in Figure 4.84.

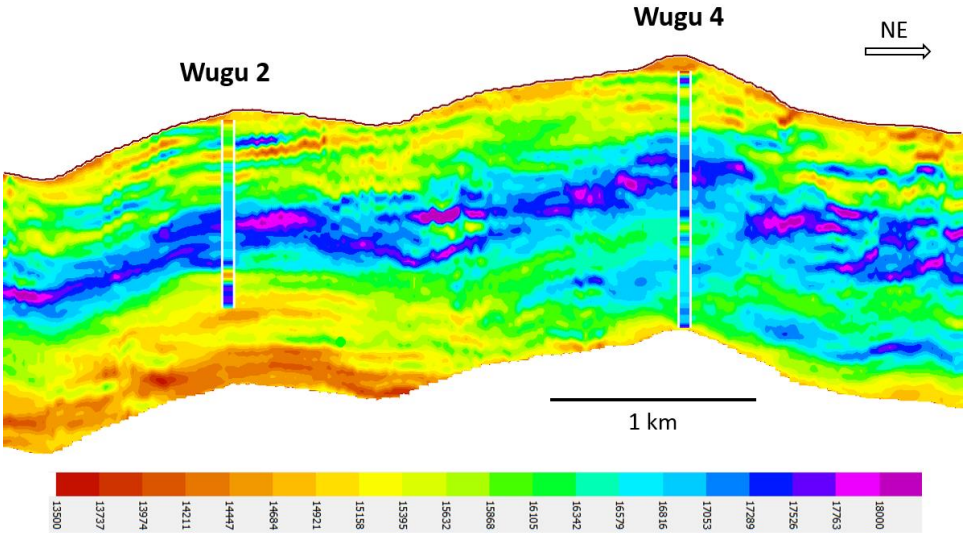

Figure 4.91. A 2D profile of EI11 from all stack seismic. The inserted color column is the filtered EI11 log by high-cut filter 50-70 Hz. The position of 2D line is shown in the right figure in Figure 4.84.

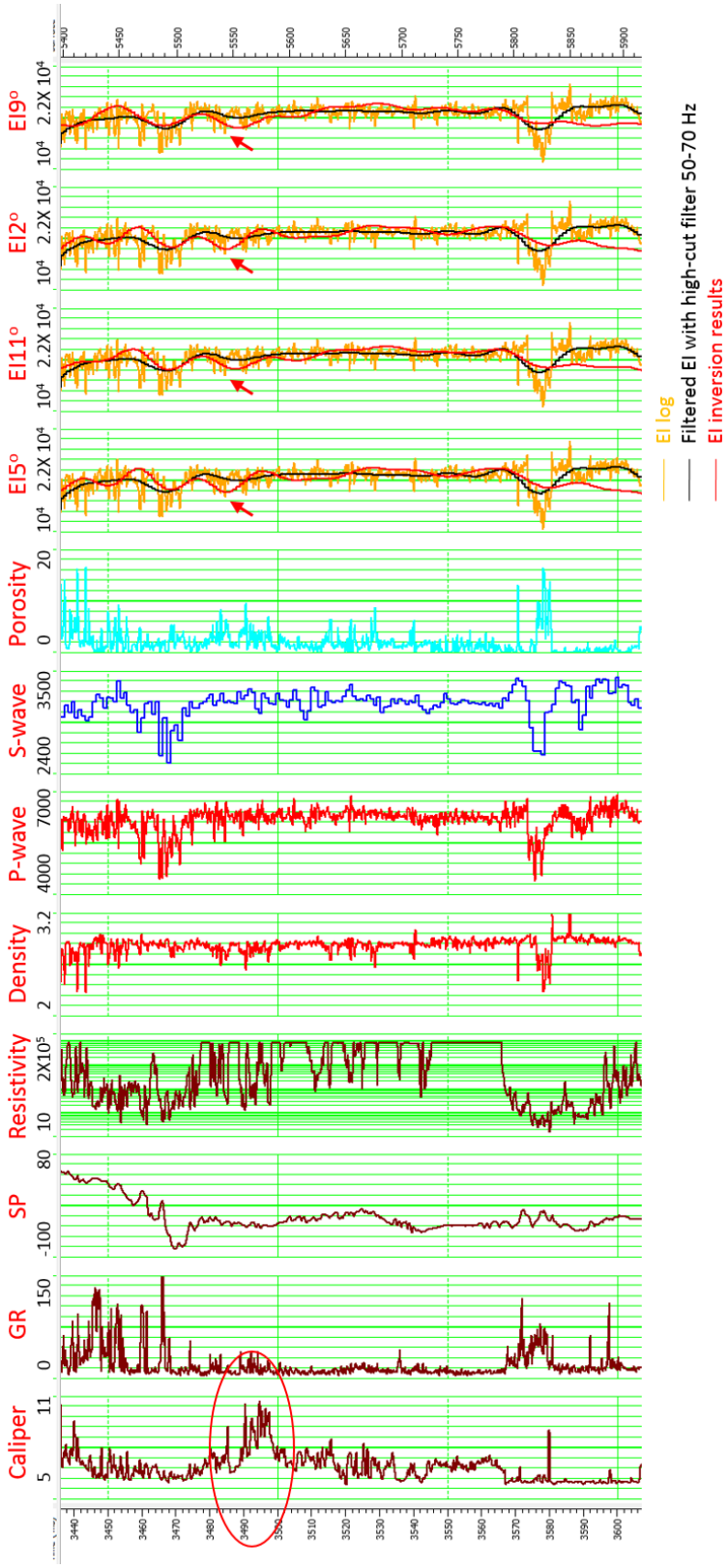

Figure 4.92. Elastic impedance (EI5, EI11, EI12, and EI19) inversion QC at Wugu 2.

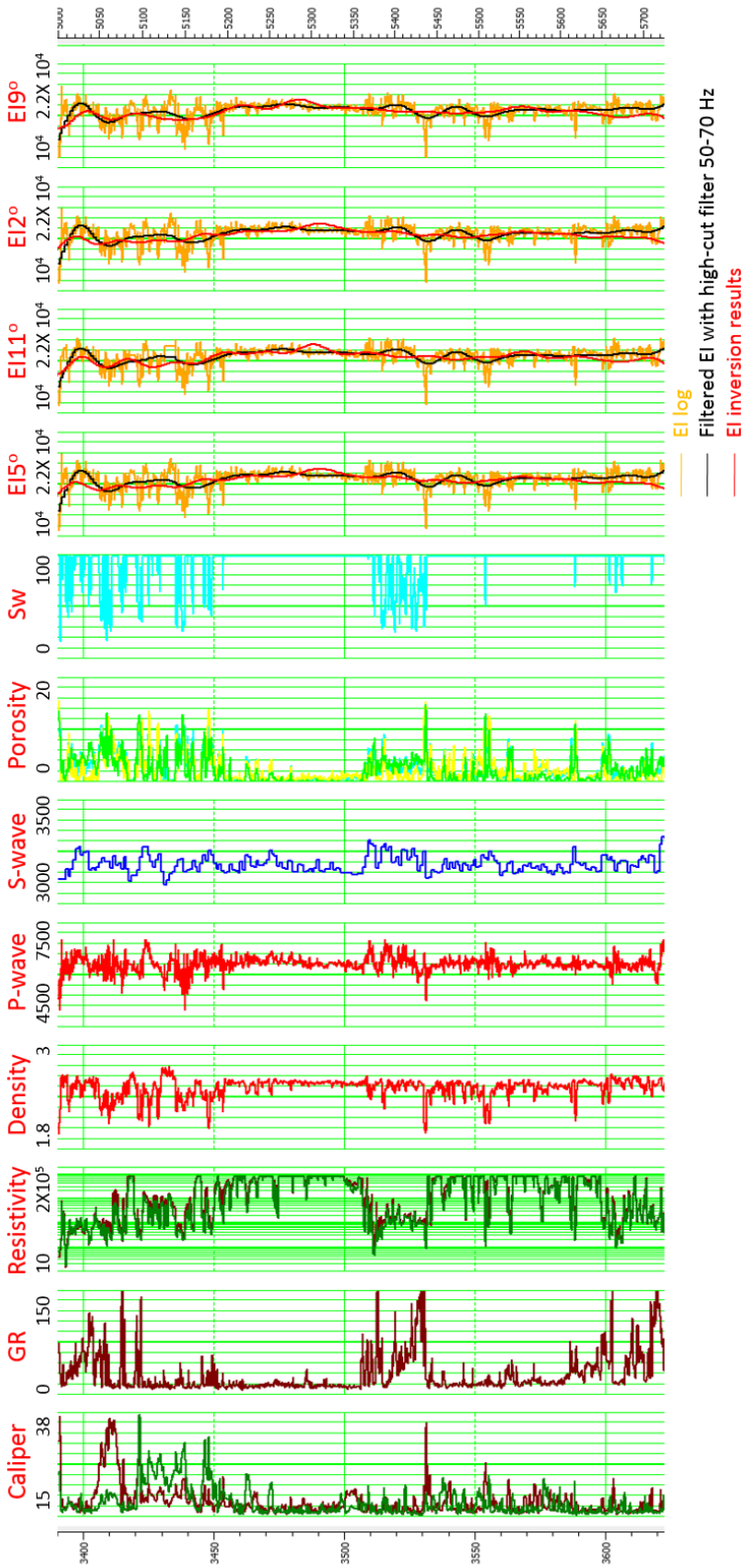

Figure 4.93. Elastic impedance (EI5, EI11, EI12, and EI19) inversion QC at Wugu 4.

detecting fractured zones, EI5, EI12, and EI19 are further used for calculation and estimation of reservoir parameters (e.g. porosity and pore structure parameter).

The inversion results at Wugu 2 and Wugu 4 pick out the major lithology variations (Figure 4.92 and 4.93). One obvious difference between inversion results and impedance logs is at the bottom of Wugu 2. The EI inversion results are all much higher than the EI logs. That is also why we see low EI in the left bottom on four profiles of Figure 4.88, 4.89, 4.90, and 4.91. One possible reason is it may be caused by the log length. Wugu 2 and Wugu 4 all have limited length of standard logs and sonic logs, which greatly decrease the control of inversion from log data. Therefore, the low EI areas in the bottom left should be carefully neglected when characterizing carbonate reservoirs. The second obvious miss-match is at the arrows in Figure 4.92. The reason has been discussed before when QC the poststack seismic inversion.

After acquiring EI5, EI12, and EI19, GI is estimated from EI5 and EI19. The estimation result shows in Figure 4.94. The comparison between the estimation and the GI log shows a big difference, which will influence the porosity and pore structure parameter prediction. The reason for less accuracy estimation of GI is the inversion error in elastic impedance inversion for EI5 and EI19. A substitution of GI is to invert shear impedance (SI) from far angle-stack based on model-based inversion. The inversion result of SI is shown in Figure 4.95. A good match between the SI inversion and SI log. The Vs-Vp ratio is calculated by $\frac{Vs}{Vp} = \frac{SI}{AI}$ (Figure 4.96). The estimated bulk and shear modulus are shown in Figure 4.97 and 4.98 respectively.

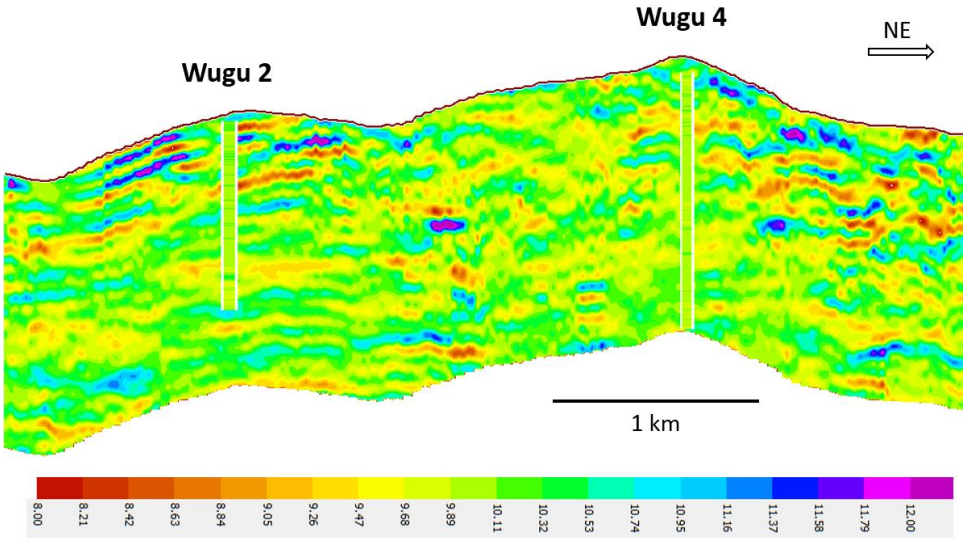

Figure 4.94. A 2D profile of GI estimated from EI19 and EI5. The inserted color column is the filtered GI log by high-cut filter 50-70 Hz. The position of 2D line is shown in the right figure in Figure 4.84.

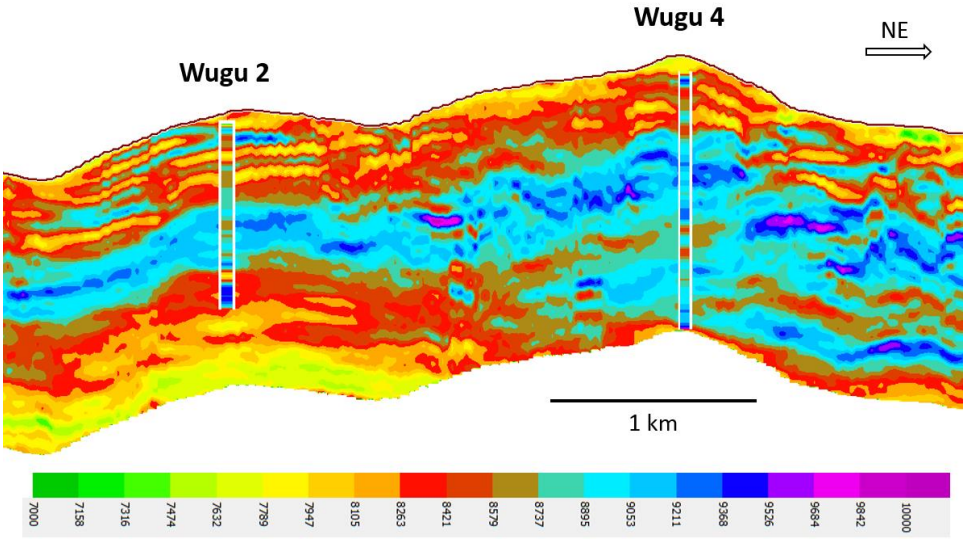

Figure 4.95. A 2D profile of SI from far angle stack seismic. The inserted color column is the filtered SI log by high-cut filter 50-70 Hz. The position of 2D line is shown in the right figure in Figure 4.84.

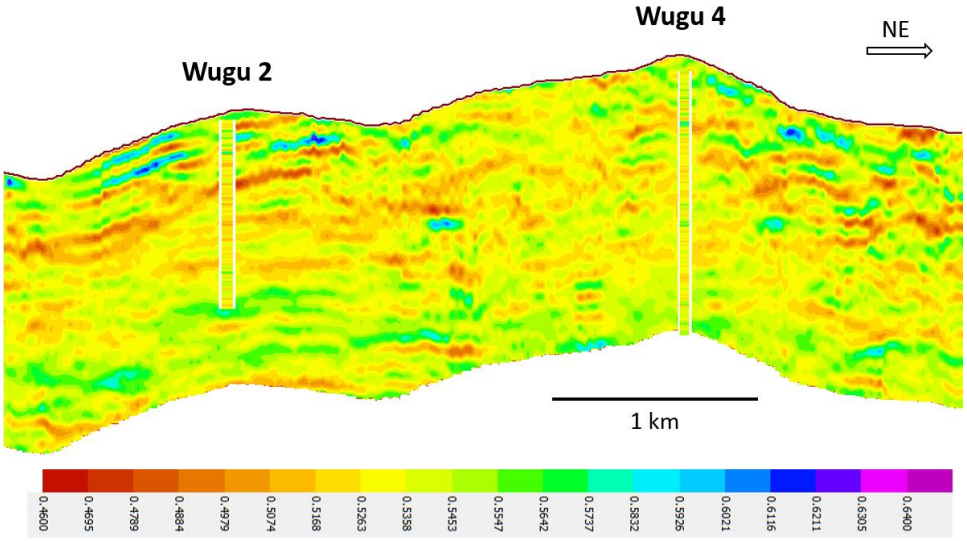

Figure 4.96. A 2D profile of estimated Vs-Vp ratio from EI5 and SI. The inserted color column is the filtered Vs-Vp ratio log by high-cut filter 50-70 Hz. The position of 2D line is shown in the right figure in Figure 4.84.

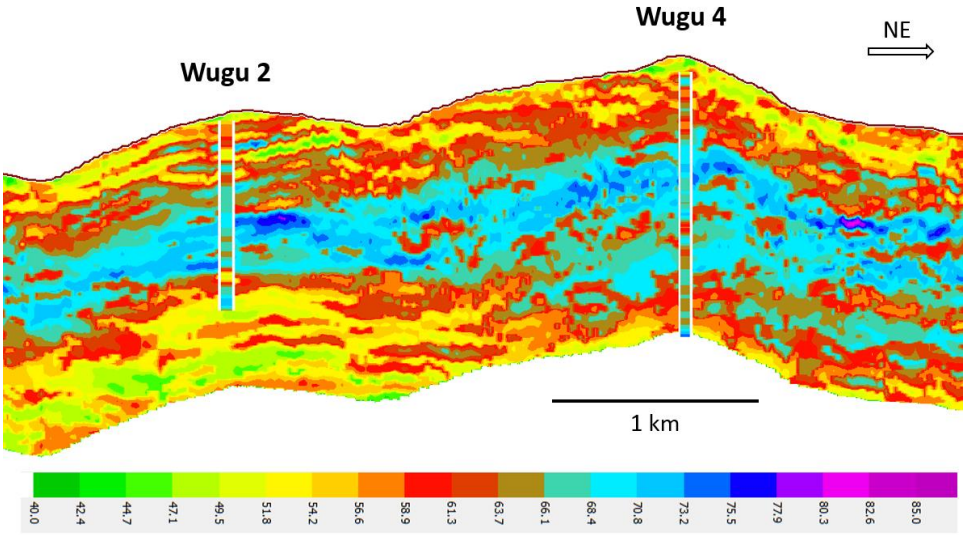

Figure 4.97. A 2D profile of estimated bulk modulus from EI5 (≈ AI). The inserted color column is the filtered bulk modulus log by high-cut filter 50-70 Hz. The position of 2D line is shown in the right figure in Figure 4.84.

Following the algorithm in the methodology part for porosity and pore structure parameter estimation, the porosity and pore structure parameter volumes are further calculated from acoustic impedance (AI) and bulk (K) and shear modulus (μ). And the results are shown in Figure 4.99 and 4.100.

The estimation of porosity and pore structure parameter from prestack seismic are shown in Figure 4.99, 4.100, 4.101, and 4.102. The porosity inversion at Wugu 2 picks most of variations except the bottom interval. The miss-match in the bottom interval is the result of low elastic impedance inversion. The porosity inversion at Wugu 4 also picks most of the porosity variations. Figure 4.100 specifically plot the original porosity and the porosity inversion by side of well path. From top to bottom of Wugu 2 and Wugu 4, the overall change of porosity log and inversion are similar. Pore structure parameter inversion has less accuracy compared to porosity prediction. However, the pore structure parameter inversion picks out the high values of pore structure parameter at wells. Figure 4.102 specifically plot the original pore structure log and the inversion result. The inversion result keeps most of the change at both well locations.

Figure 4.103 puts acoustic impedance profile, porosity profile, and pore structure parameter profile together for reservoir characterization. The red circle and arrow indicate low impedance zones with low porosity but high pore structure parameter. It is interpreted as fractured zones. The blue circle and arrow indicate a low impedance zone with more high porosity but less low pore structure parameter. It is interpreted as a high-porosity zone.

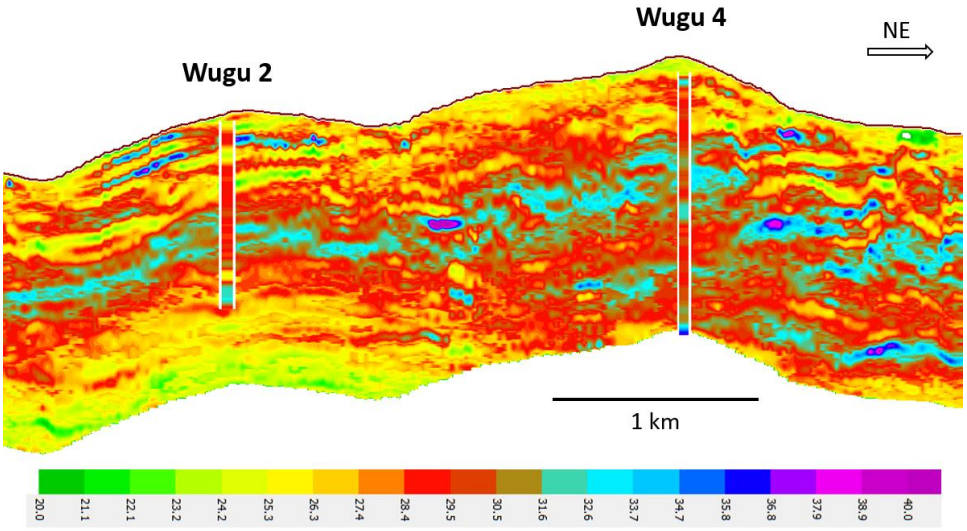

Figure 4.98. A 2D profile of estimated shear modulus from bulk modulus and Vs-Vp ratio. The inserted color column is the filtered shear modulus log by high-cut filter 50-70 Hz. The position of 2D line is shown in the right figure in Figure 4.84.

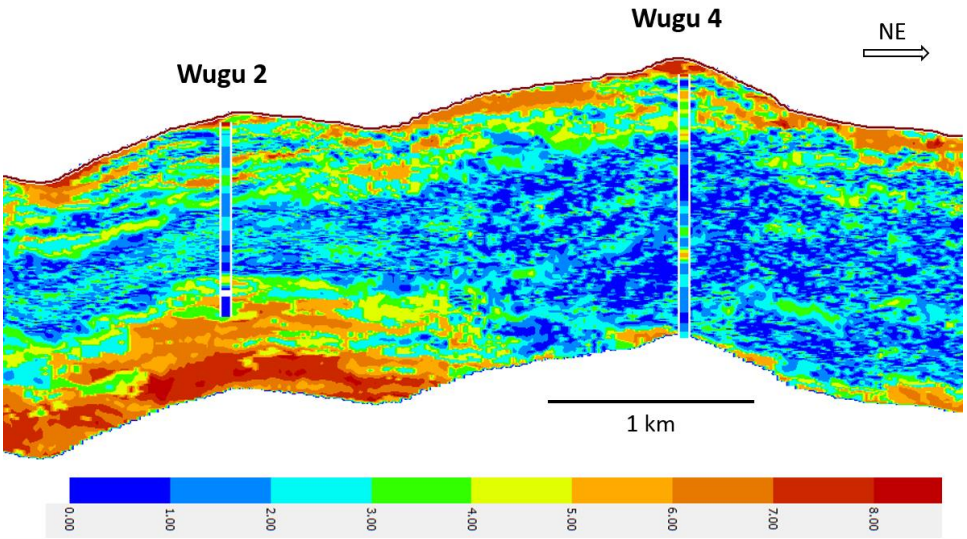

Figure 4.99. A 2D profile of predicted porosity. The inserted color column is the filtered density porosity log by high-cut filter 50-70 Hz. The position of 2D line is shown in the right figure in Figure 4.84.

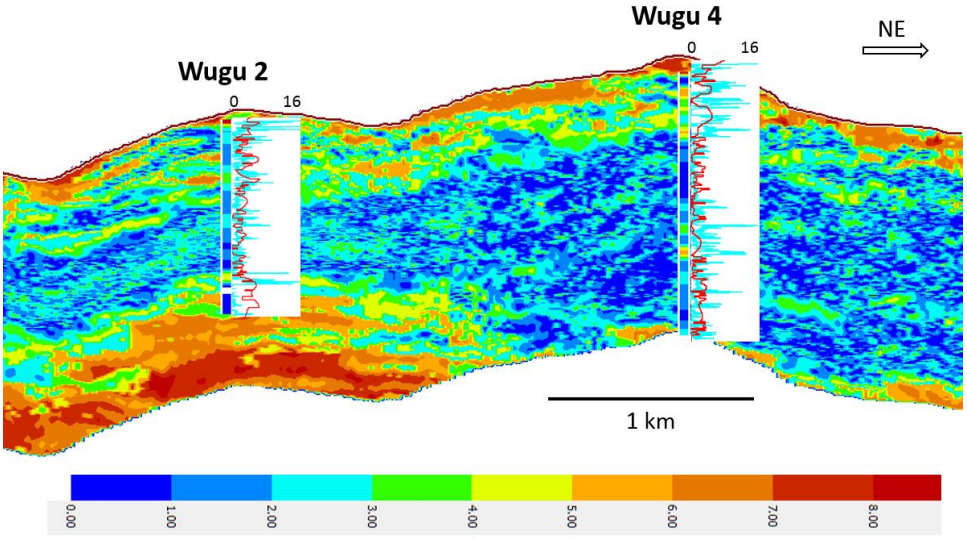

Figure 4.100. The same profile of porosity as in Figure 4.99. The original density porosity log and the inversion result are compared by side of the well path. The position of 2D line is shown in the right figure in Figure 4.84.

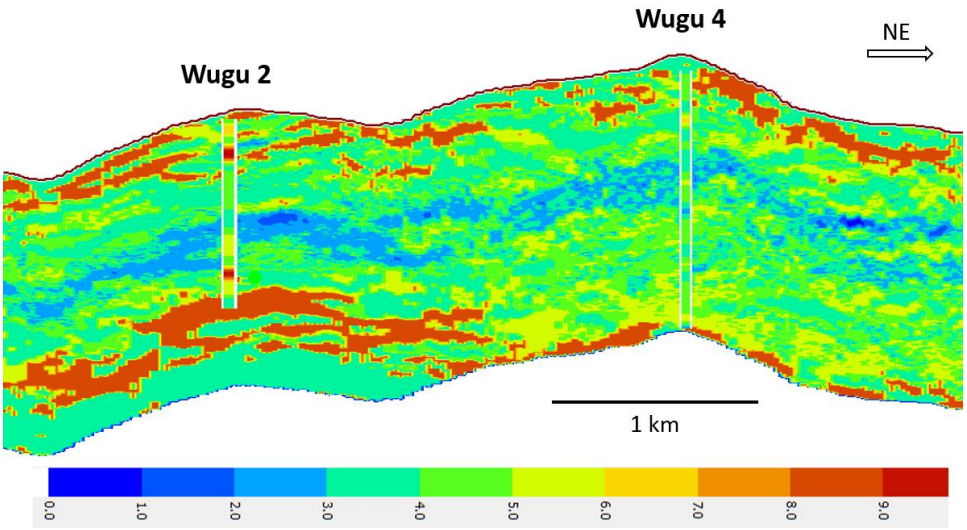

Figure 4.101. A 2D profile of predicted pore structure parameter. The inserted color column is the filtered pore structure log by high-cut filter 50-70 Hz. The position of 2D line is shown in the right figure in Figure 4.84.

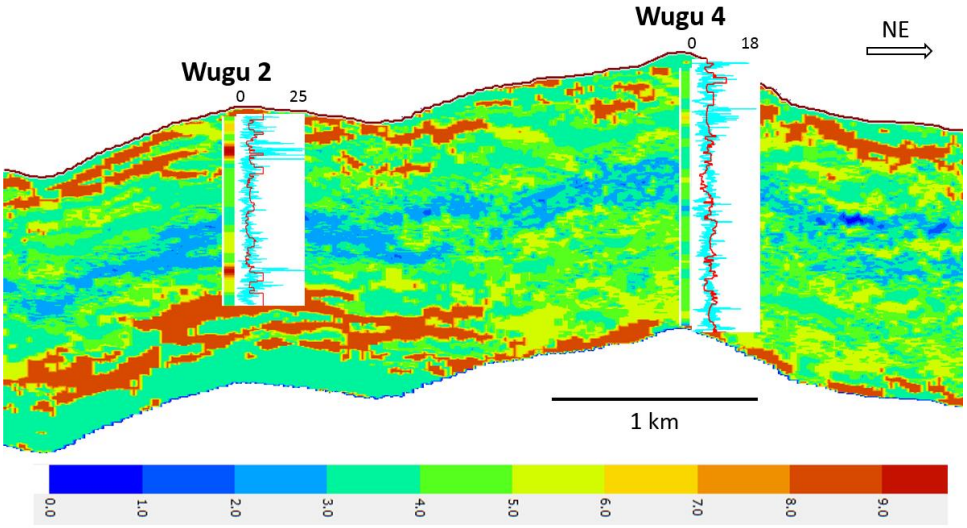

Figure 4.102. The same profile of pore structure parameter as in Figure 4.101. The original pore structure log and the inversion result are compared by side of the well path. The position of 2D line is shown in the right figure in Figure 4.84.

A carbonate hill internal reservoir can be identified at the intersection of inline 2140 and xline 2805 (Figure 4.104). It has lower impedance than 15,500 (g/cc)×(m/s). It has a thin layer of high porosity and a thick layer of high pore structure parameter. It is interpreted as a mixture of high-porosity zone and fracture zone.

Map views of acoustic impedance, porosity, and pore structure parameter are created by horizon slice processing at 38 ms below the Ordovician top (Figure 4.105). The low impedance in left picture points to either high porosity in the middle picture or high pore structure parameter in the right picture. The low impedance at Wugu 2 is caused by high-porosity zone while that at Wugu 4 by fracture zone. From the comparison, we can see the low impedance zone generally is a mixture of high-porosity zone and fracture zone.

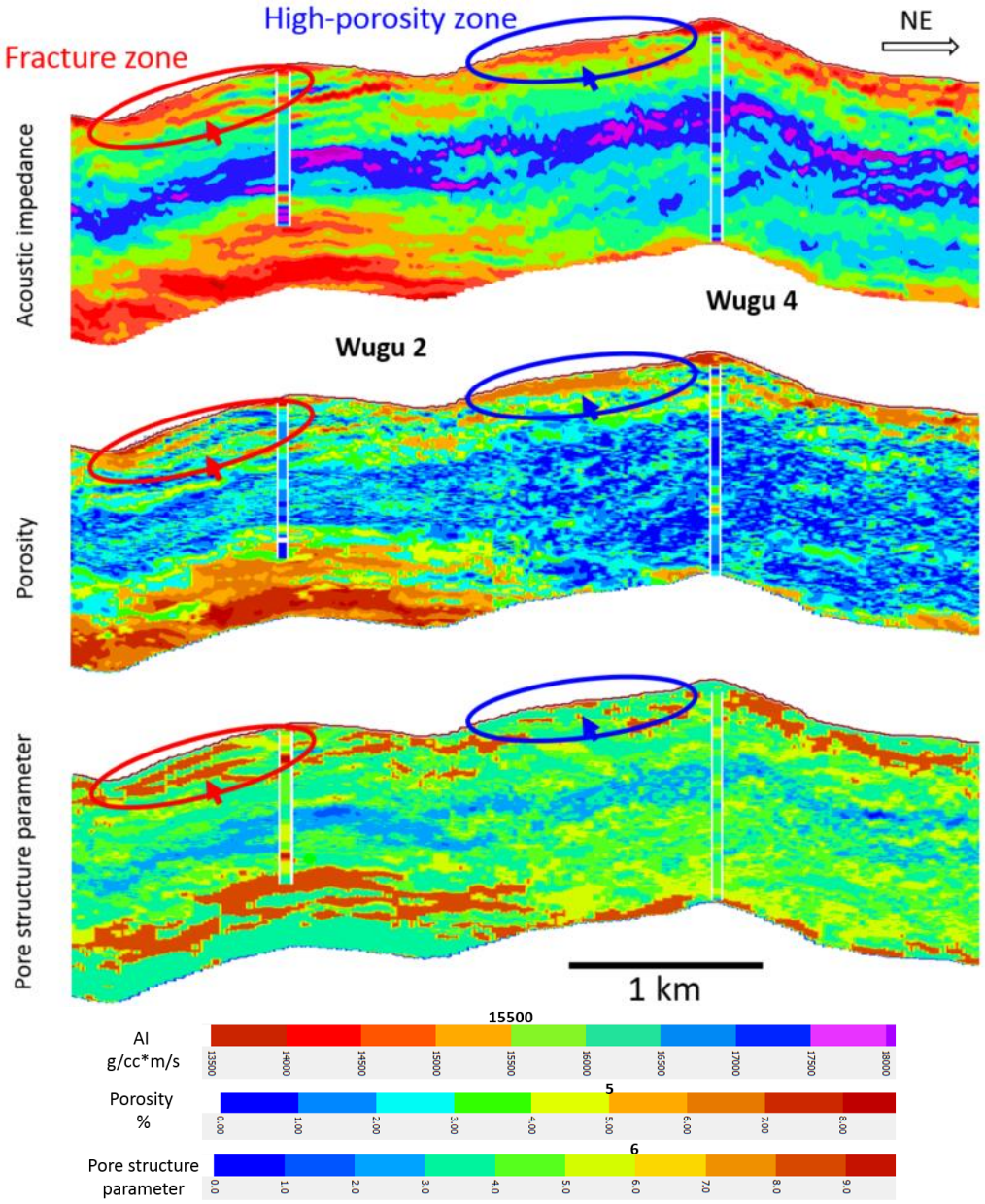

Figure 4.103. The reservoir characterization of 2D line cutting through Wugu 2 and Wugu 4. Top is acoustic impedance profile; middle is porosity profile; and the bottom is pore structure parameter profile. The position of 2D line is shown in the right figure in Figure 4.84.

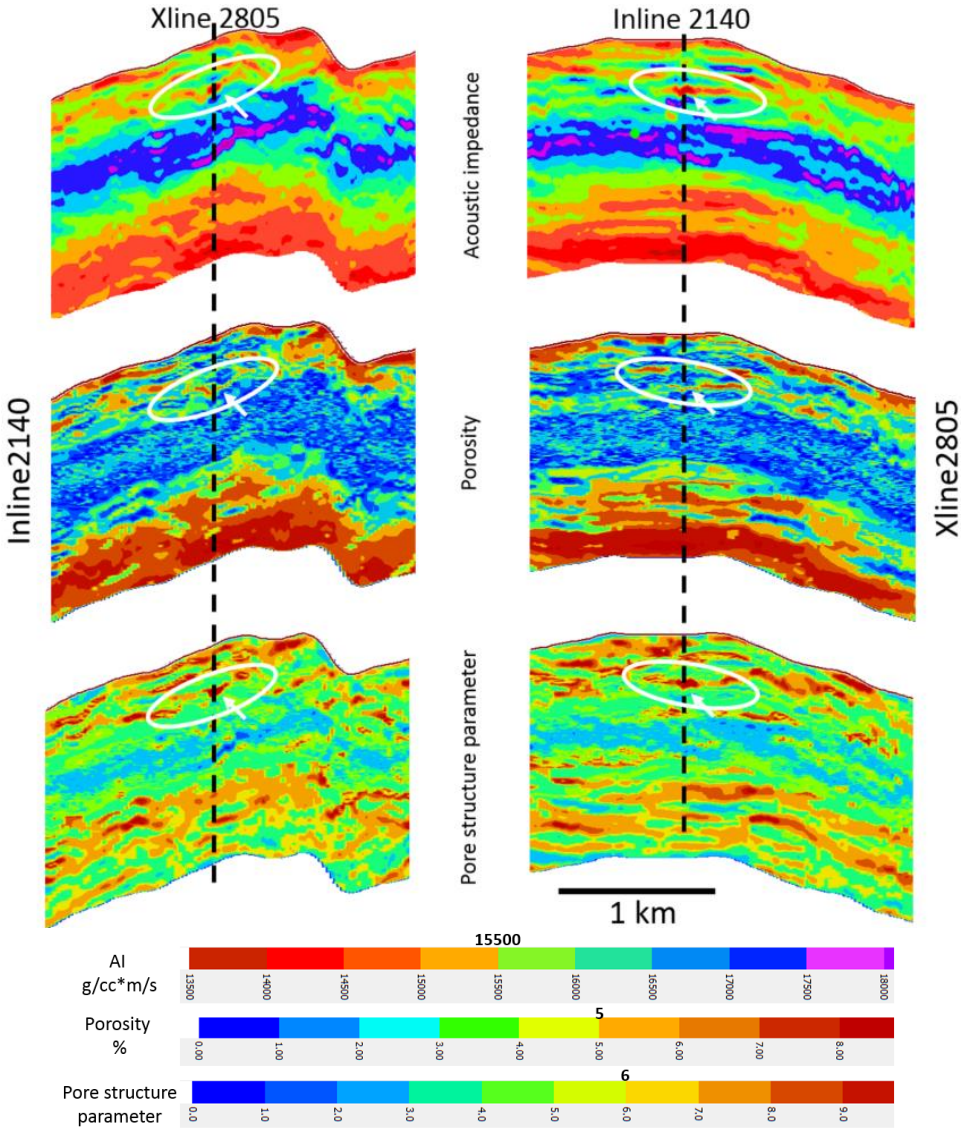

Figure 4.104. The reservoir characterization of inline 2140 and xline 2805. Top is acoustic impedance profile; middle is porosity profile; and the bottom is pore structure parameter profile.

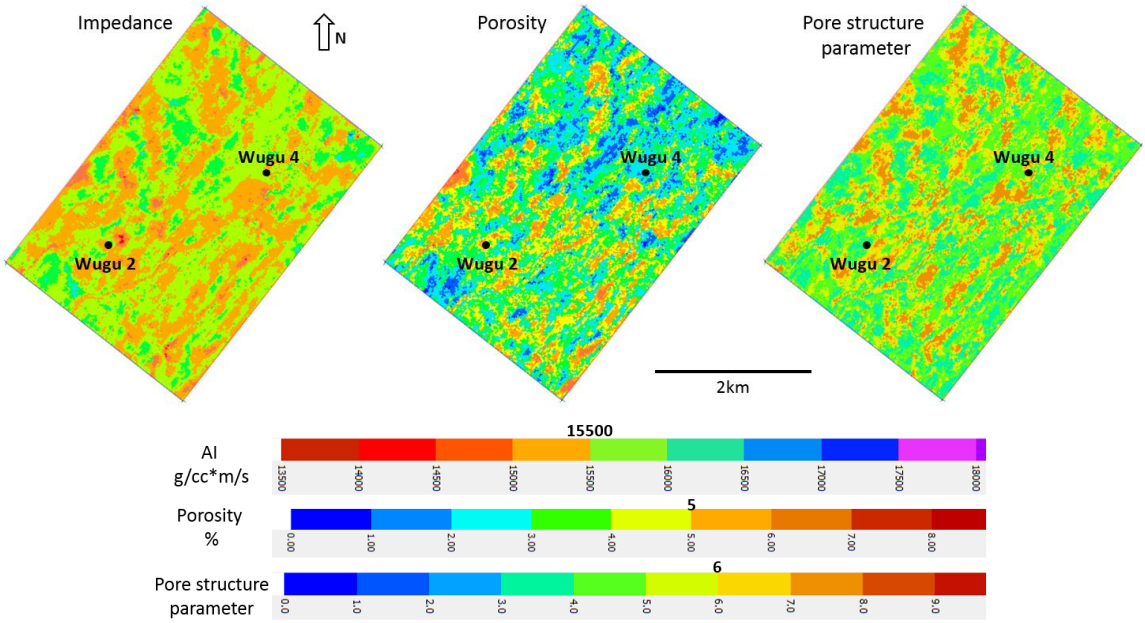

Figure 4.105. Map views of acoustic impedance, porosity estimation, and pore structure parameter estimation. The slices are created at 38 ms below the Ordovician top.

The uncertainty of porosity and pore structure parameter estimation mainly comes from four aspects: 1) elastic impedance inversion (log and seismic data quality); 2) the porosity estimation methodology (the approximation of C difference); 3) the interpretation of the Ordovician top; and 4) the limited angle of angle stack gathers. The maximum angle used in this project is only 21^{o}, which contains less information of poison ratio. In this situation, the shear impedance inversion has less accuracy and therefore influences porosity and pore structure estimation.

4.5.4 Seismic inversion and attribute extraction

Seismic attribute analysis in recent decades has become an instrumental tool in regional and local structure analysis. Coherency and curvature are two common geometric attributes recording seismic reflection discontinuity and are therefore used to map the structure and shape of geological interest, such as faults and channels. The major porosity in Hexiwu buried-hill reservoir is from fracture related dissolution pores (cavities, vugs, and molds) and minor from fractures. In this case, the mapping of local major faults and minor faults in the Hexiwu area plays an important role in identifying reservoir zones.

For the purpose of mapping major fractured zones in the Hexiwu area, Li (2014) extracted coherency and curvature from conventional and high-resolution seismic (Figure 4.106). Li (2014) tested the differences between eigenstructure coherence and most-positive curvature by using 3 different sets of parameters. He found out that generally the attributes from high resolution data show more detail (Figure 4.106b), however, the low resolution coherence volume (top left, Figure 4.106a) shows a better description of minor faults in the study area. He also found out most-positive curvature identifies minor faults accurately (Figure 4.107).

We combine Li's attribute analysis and high-resolution poststack impedance inversion results together (Figure 4.108, 4.109, 4.110, and 4.111). For those low-impedance zones, if their attributes show they are highly fractured zones, they are interpreted to be fracture dominated zones (Figure 4.108 and 4.109). However, if their attributes show less faults and/or fractures, low-impedance zones are interpreted to be

high porosity zones with less fractures (Figure 4.110 and 4.111). The combination of impedance inversion and attribute analysis provides a quick way to separate highly fractured zones and high porosity zones.

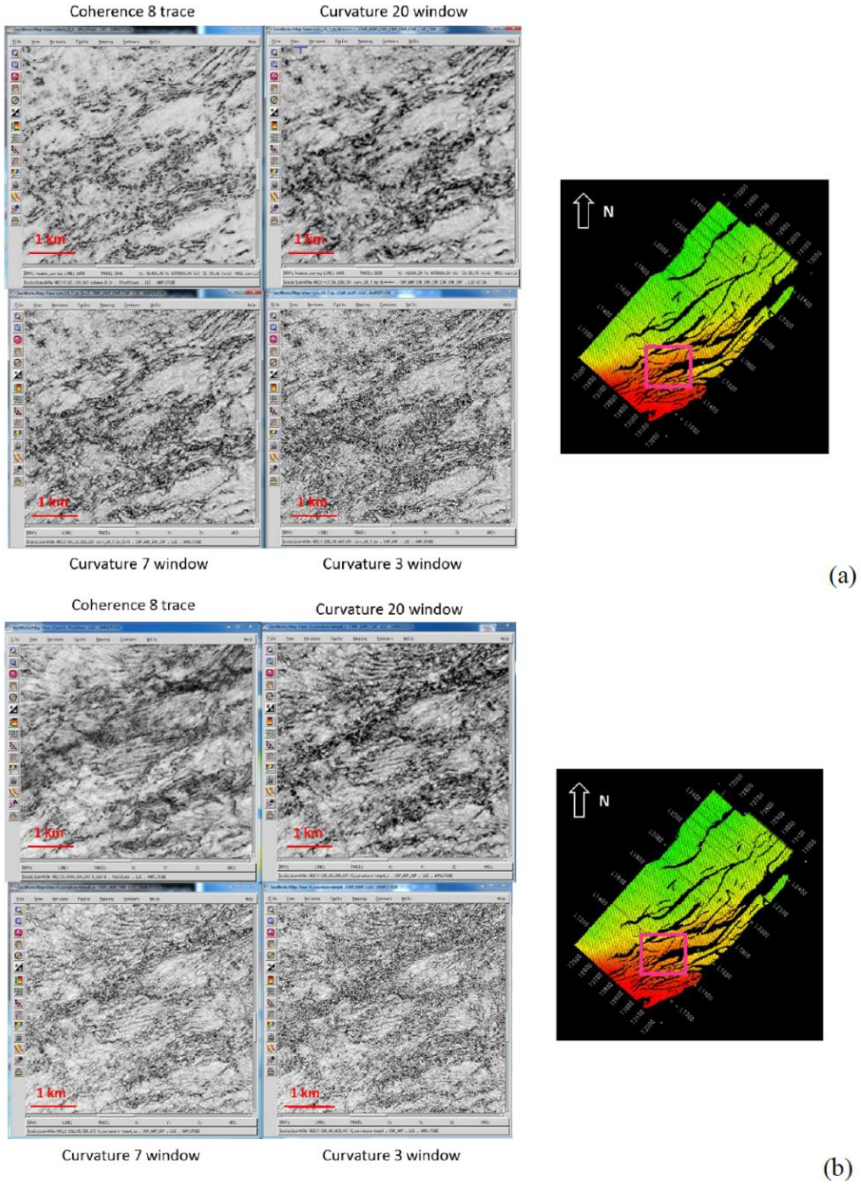

Figure 4.106. Comparison of eigenstructure coherence and parameter testing for most-positive curvature in the low resolution data (a) and high resolution (b) (Li, 2014).

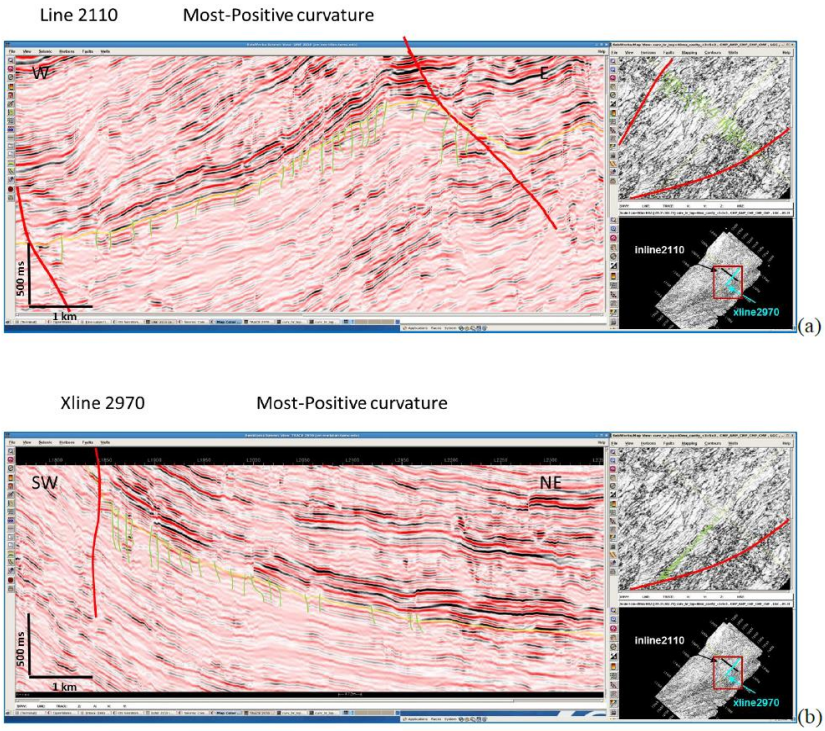

Figure 4.107. The tie of structure interpretation of inline 2110 (a) and crossline 2970 (b) to most-positive curvature at Ordovician horizon top, immediately below which a cavity zone is interpreted from impedance inversion. Green lines indicate the minor faults and red lines regional faults (Li, 2014).

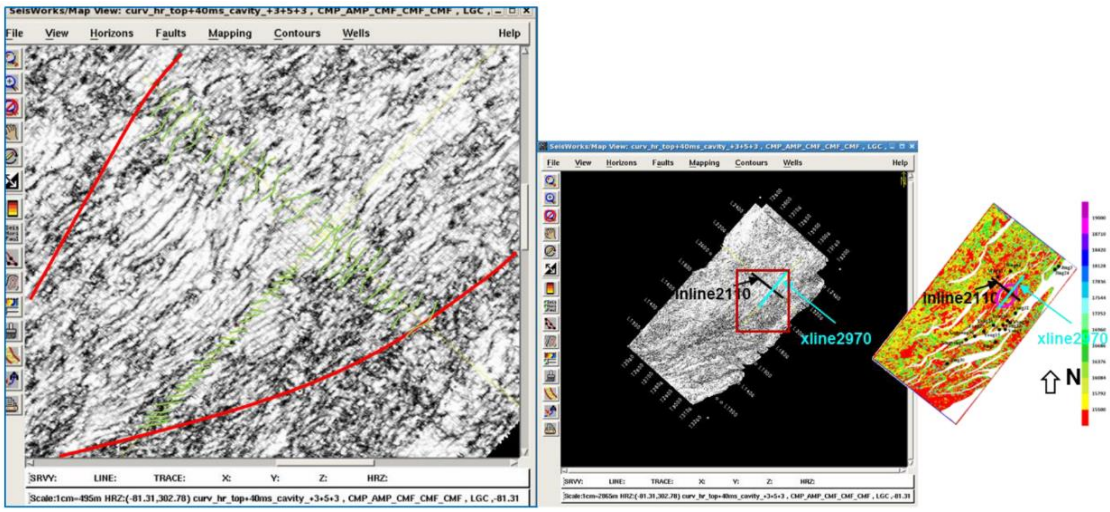

Figure 4.108. The zone D with low-impedance is a highly fractured zone (Li, 2014). The horizon used is the Ordovician top horizon.

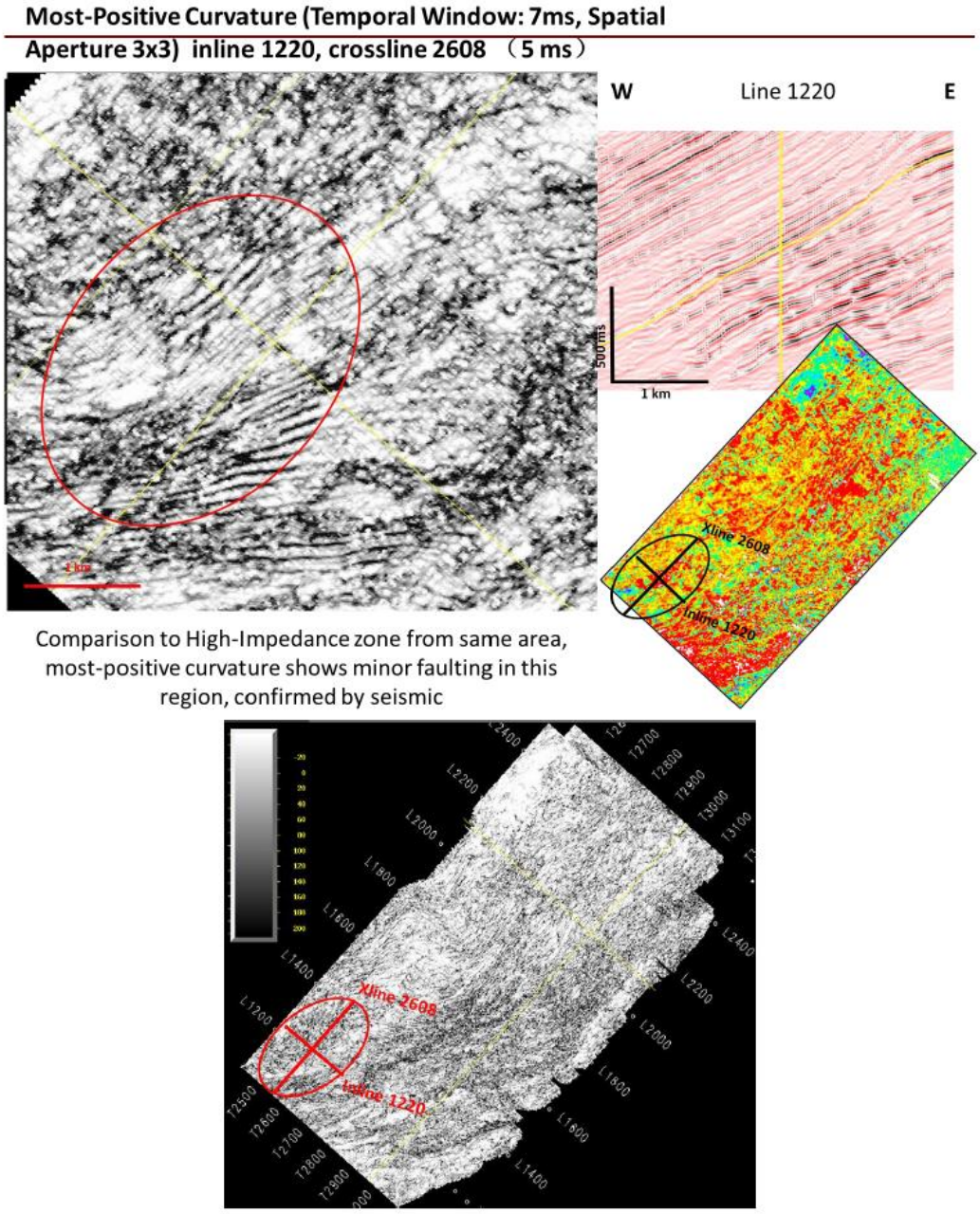

Figure 4.109. A typical zone with low-impedance is a highly fractured zone (Li, 2014). The horizon used is the one 5 ms below Ordovician top horizon.

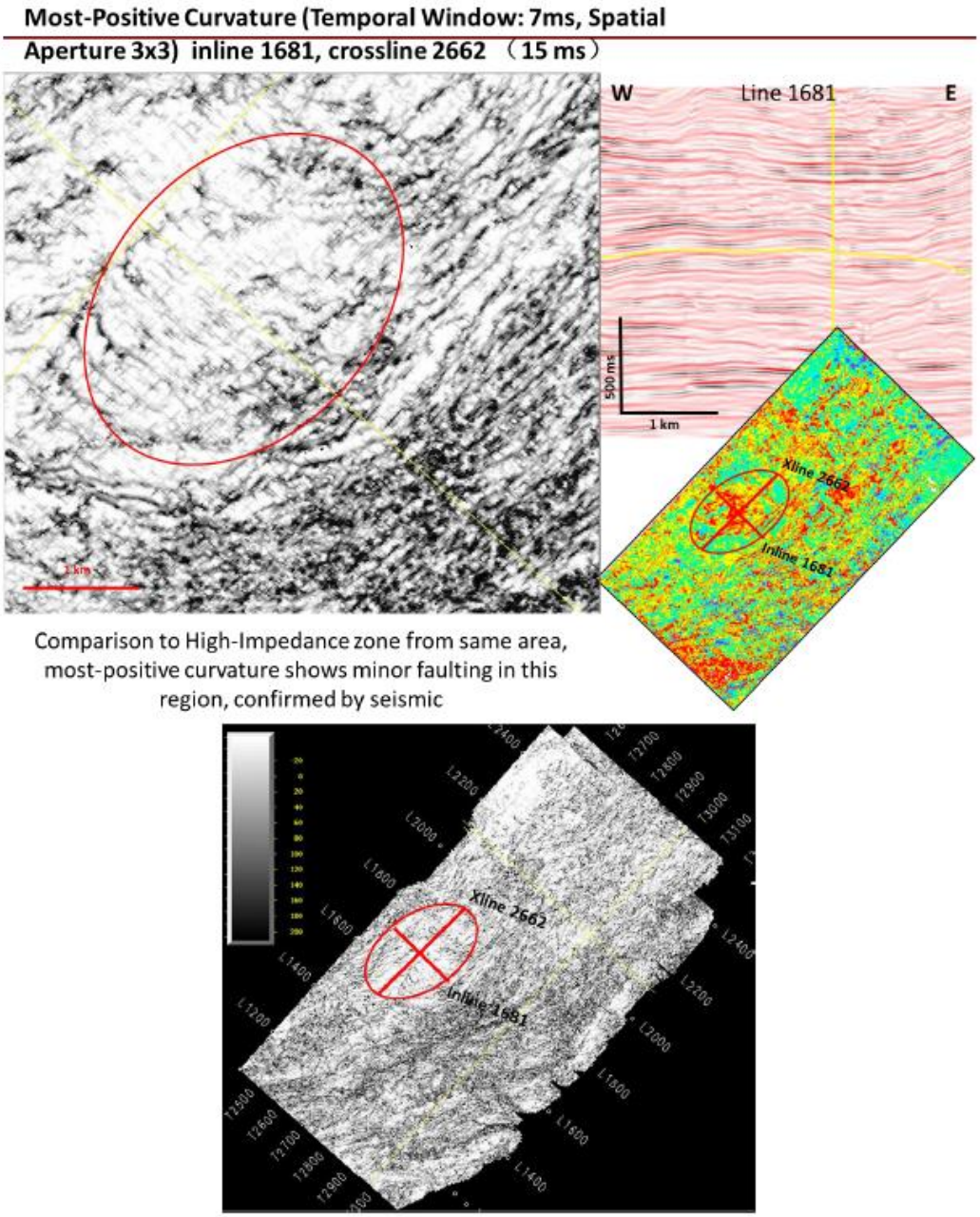

Figure 4.110. A typical zone with low-impedance is not a highly fractured zone (Li, 2014). The horizon used is the one 15 ms below Ordovician top horizon.

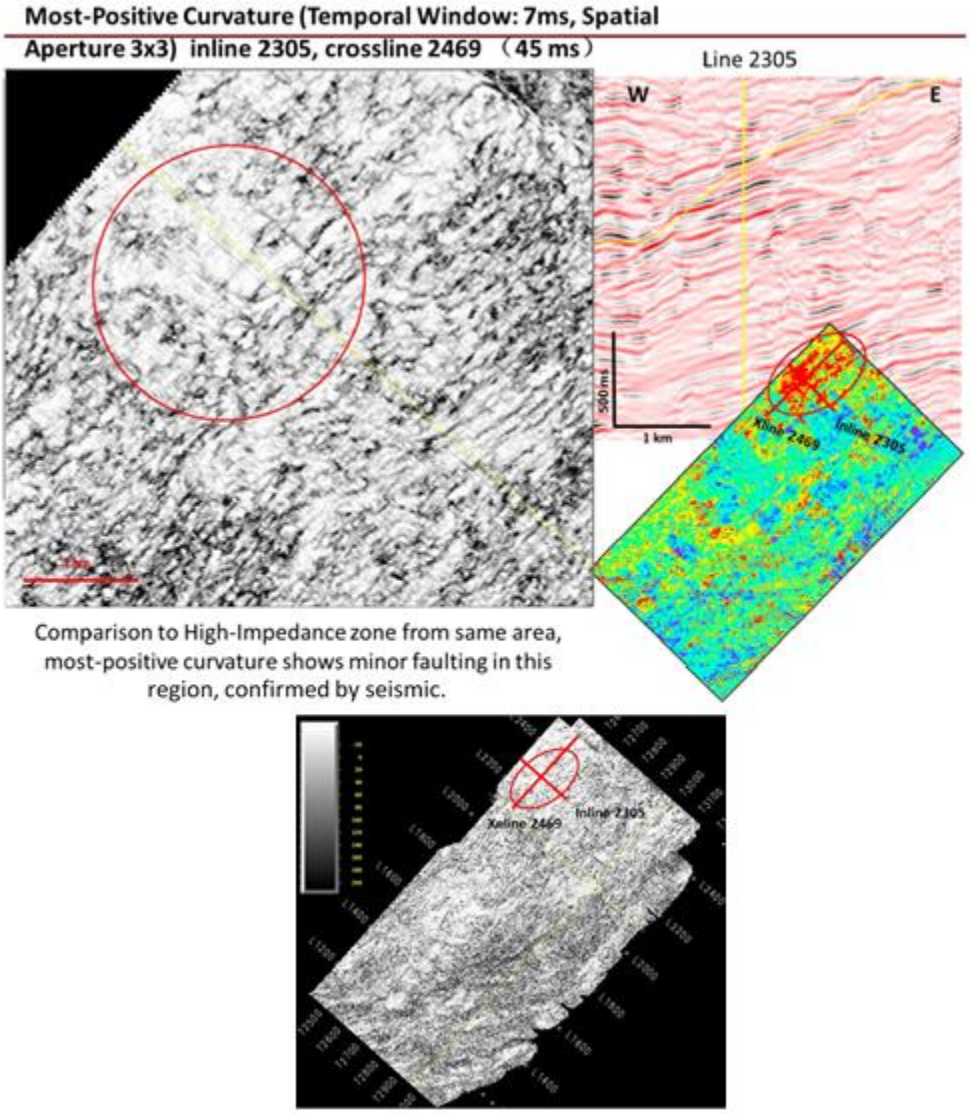

Figure 4.111. A typical zone with low-impedance is not a highly fractured zone (Li, 2014). The horizon used is the one 45 ms below Ordovician top horizon.

4.6 Conclusions

Natural fractures in deep buried carbonate rocks play important roles in the Bohai Bay basin, China. The Hexiwu carbonate hill experienced several tectonic movements, including Lingyuan, Tieling, Jixian, and Caledonian orogeny, and Indosinian-Himalayan movement. Faults and fractures are well developed in this area due to tectonic movements. Strong diagenesis closes original and secondary pores in residual carbonate rocks during multiple uplifting and burial events. The major hydrocarbon storage spaces are interpreted to be dissolution pores (vugs, molds, and cavities) associated with open faults and fractures. Therefore, open fracture detection is the most important work in this area for hydrocarbon reservoirs. How to identify natural open fractures from seismic data is a key step to characterize carbonate reservoirs in this area. Research on the log set and conventional seismic from the Hexiwu field reveals that elastic properties (e.g., velocity, modulus, and impedance) have a strong response to fractures and that the seismic resolution is the key to resolve fractured zones.

Investigation on two adjacent wells, Wugu 2 and Wugu 4, shows that the well with more fractured zones has more data in the range of low porosity (less than 5%) and low bulk modulus (less than 55 GPa). The fractured zones interpreted with FMI generally have lower bulk modulus than tight carbonate zones at similar porosity. Moreover, the fracture angle also has a strong influence on rock elastic properties. At given porosity, fractured zones with large-angle fractures have apparently lower bulk and shear moduli than those with low-angle fractures. The elastic properties of fractured zones are also sensitive to the open or sealing status of fractures. Fractured zones with

open fractures clearly have lower bulk modulus than those with sealing fractures at similar porosity, although the shear modulus fails to distinguish them. In the low porosity range (less than 5%) carbonate rocks with open- and large-angle fractures are detectable with bulk modulus usually lower than 55 GPa and P-impedance lower than 15,500 (g/cc)×(m/s).

The 3D mapping of fractured zones is restricted by conventional seismic resolution, which is lower than 15 Hz. Impedance log filtering shows that the central frequency has to be enhanced at least 30 Hz to resolve a highly fractured zone 20-m-thick. Resolution enhancement processing was applied to the conventional seismic and increased the frequency up to 55 Hz, enabling it to map the 3D distribution of fractured zones in Hexiwu buried hill. The result shows that the distribution of fractures is closely related to structure belts in this area.

The successful application of this methodology in the Hexiwu area provides a significant demonstration on fracture detection in buried carbonate hill. It is also applicable to detect fractures and find permeable rocks in conventional and unconventional reservoirs all over the world.

CHAPTER V

SUMMARY AND CONCLUSIONS

The study on shallow buried carbonate at the Southern Marion platform with rock physics analysis and seismic inversion helps define the relationships among sea level change, ocean currents, and dolomitization. Dolostone with large pores usually has higher sonic velocity and higher permeability compared to other types of dolostone and limestone. The 2D mapping of three dolostone belts by seismic inversion matches well with three maximum flooding events. The high stand of sea level facilitates the dolomitization process to form large pores. Three dolostone belts follow the ocean topography, demonstrating that the fluid flow system within the platform is driven by oceanographic currents. With increased permeability, the dolostone intervals help the fluid-flow within the platform and therefore accelerate the dolomitization process. This study on how dolomitization is related to sea level change and ocean current circulation is applicable for better understanding subsurface fluid-rock interactions and dolomitization mechanism in other carbonate environments.

A field study of ultra-deep carbonate gas reservoirs in the Sichuan basin of China demonstrates that the frame flexibility factor derived from an extended Biot theory is of great importance for understanding the porosity-velocity complexity in carbonate reservoirs. The correlation between velocity and the product of frame flexibility factor and porosity is much better than that between velocity and porosity alone. The correlation between P-impedance and the product of porosity and frame flexibility factor

is even better than the correlation between velocity and the product of porosity and frame flexibility factor. These results prove to be useful for seismic inversion and they should be applicable to ultra-deep hydrocarbon reservoirs in similar geological settings.

Acoustic impedance and pore structure parameter can help detect fractured zones in a buried carbonate hill in Hexiwu field, Bohai Bay basin, China. Analysis of two adjacent wells where standard logs, shear wave and FMI logs are available shows that fractured zones usually occur where porosity is less than 5%. Fractured zones tend to have lower bulk modulus than tight limestone at similar porosity. The fracture angle and opening influence the elastic property of fractured zones. Generally at given porosity, fractured zones with large-angle fractures have lower bulk and shear moduli than those with low-angle fractures. Fractured zones with open fractures have lower bulk modulus than those with sealing fractures, while shear modulus has no significant difference. Fractured zones with open- and large-angle fractures in the studied low-porosity (less than 5%) carbonate rocks usually have bulk modulus lower than 55 GPa and P-impedance lower than 15,500 (g/cc)×(m/s). Fractured zones as thin as 20-m-thick can be imaged using resolution-enhanced 3D prestack seismic data available for the study. 3D distribution of fractured zones in Hexiwu buried hill reveals that the distribution of fractures is closely related to the faults and is controlled by the regional tectonics. The described methodology may also be applicable for fracture detection in other deep conventional and unconventional reservoirs.

REFERENCES

Adesokan, H. and Y.F. Sun, 2010, Rock-physics-based Estimation of Critical Volume of Shale and Its Effect on Seismic and Petrophysical Properties: a North-Sea Example: 2010 SEG Annual Meeting, 17-22 October, Denver, Colorado, US.

Anselmetti, F.S., A.R. Isern, S.N. Ehrenberg, and G.P. Eberli, 2001, Proceeding of the Ocean Drilling Program, Preliminary Report: Ocean Drilling Program, Texas A&M University, College Station, Texas, Ocean Drilling Program, v. 194.

Anselmetti, F. S., and G. P. Eberli, 1993, Controls on sonic velocity in carbonates: Pure and Applied Geophysics, v. 141, p. 287–323.

Bracco Gartner, G.L., P.D. Wagner, G.T. Baechle, Y.-F. Sun, R. Weger and G.P. Eberli, 2005, Obtaining permeability from seismic data: A new breakthrough in carbonate reservoir modeling: 2005 International Petroleum Technology Conference Proceedings, P937.

Chopra, S., J. Castagna, and O. Portniaguine, 2006, Seismic resolution and thin-bed reflectivity inversion: CSEG RECORDER, January, 19-25.

Conesa, G.A.R., E. Favre, P. Münch, H. Dalmasso, and C. Chaix, 2005. Biosedimentary and paleoenvironmental evolution of the Southern Marion platform from the middle to late Miocene (northeast Australia, ODP Leg 194, Sites 1196 and 1199). In Anselmetti, F.S., Isern, A.R., Blum, P., and Betzler, C. (Eds.), Proc. ODP, Sci. Results, 194, 1–38 [Online]. Available from World Wide Web: http://www-odp.tamu.edu/publications/194_SR/VOLUME/CHAPTERS/005.PDF.

Dou, Q., 2011, Rock physics-based carbonate reservoir pore type evaluation by combining geological, petrophysical, and seismic data: PhD, Texas A&M University, College Station, US.

Dou, Q., Y.F. Sun and C. Sullivan, 2011a, Rock-physics-based pore type characterization and its application in carbonate reservoir permeability heterogeneity evaluation, Upper San Andres reservoir, Permian Basin, west Texas: Journal of Applied Geophysics, 74, 8-18.

Dou. Q., Y.F. Sun, H. Zhang, T. Zhang, T. Guo, and X. Cai, 2011b, Rock-physics-based Permeability Heterogeneity and Fluid Evaluation of an Ultra-Deep Low-Porosity Carbonate Reservoir, Sichuan Basin, China: I. Petrophysical Study: AAPG 2011 Annual Convention & Exhibition, Houston, US; 10-13 April 2011.

Du, J., W. Zou, B. Fei, H. Lei, F. Zhang, and Y. Zhang et al., 2002, The complex accumulation styles of hydrocarbon in Jizhong Depression, Beijing Science Press, P. 481-483.

Editorial committee of Petroleum Geology of China, 1987, Petroleum Geology of China (Five), Beijing Petroleum Industry Press, P. 63-64.

Ehrenberg, S.N., Eberli, G.P., and Bracco Gartner, G.L., 2004. Data report: Porosity and permeability of Miocene . ODP, Sci.Results, 194, 1–217 [Online]. Available from World Wide Web: http://www.odp.tamu.edu/publications/194_SR/VOLUME/CHAPTERS/007.PDF.

Ehrenberg, S.N., Eberli, G.P., and Baechle, G., 2006a. Porosity-permeability relationships in Miocene carbonate platforms and slopes seaward of the Great Barrier Reef, Australia (ODP Leg 194, Marion Plateau), Sedimentology, 53, 1289-1318.

Ehrenberg., S.N., J.M. McArthur, and M.F. Thirlwall, 2006b, Growth, demise, and dolomitization of Miocene carbonate platforms on the Marion Plateau, offshore NE Australia: Journal of Sedimentary Research, v. 76, 91-116.

El-Wazeer, F., A. Vizamora, A. Al-Hamedi, H. Al-Housani, P. Abram, and S. Busman, 2010, Integrating rock physics, seismic reservoir characterization and static modeling of carbonates: A case study from the UAE: AAPG GEO 2010 Middle East, Geoscience Conference & Exhibition, Innovative Geoscience Solutions – Meeting Hydrocarbon Demand in Changing Times, March 7-10, 2010 – Manama, Bahrain, #90105.

Guo, J., Y. Guo, and L. Wang, 2009, Features of buried hill reservoirs in Hexiwu structural belt, Langgu Sag, Jizhong Depression: Petroleum Exploration and Development, Vol. 36, No. 6, P.701-708.

Han., D.H., M.L. Batzel, 2004, Gassmann's equation and fluid-saturation effects on seismic velocities: Geophysics, Vol. 69, No. 2, P. 398-405.

Isern, A. R., F. S. Anselmetti, and P. Blum, 2004, A neogene carbonate platform, slope, and shelf edifice shaped by sea level and ocean currents, Marion Plateau (northeast Australia), in Seismic imaging of carbonate reservoirs and systems: AAPG Memoir 81, p. 291– 307.

Li, A., 2014, Volumetric curvature and coherency assisted fault mapping and fracture prediction of carbonate reservoir Huabei field, North China: master thesis, Texas A&M University, College Station, US.

Lu, S., J. Li, K. Wu, Y. Cui, and W. Du, 2011, Tectonic evolution of buried hill in Jizhong Depression and the petroleum geological significance: Journal of Oil and Gas Technology (J. JPI), Nov. 2011, Vol. 33, No. 11, P.35-40, 50.

Lucia, F. J., 1999, Carbonate reservoir characterization: Berlin, Springer-Verlag, 226.

Ma, Y.S., X.S. Guo, T.L. Guo, R. Huang, X.Y. Cai, and G.X. Li, 2007, The Puguang gas field: New giant discovery in the mature Sichuan Basin, southwest China: AAPG BULLETIN, v.91, no. 5, pp. 627-643.

Shipboard Scientific Party, 2001. Leg194 Preliminary Report. ODP Prelim. Rpt., 94 [Online]. Available from World Wide Web: http://www-odp.tamu.edu/publications/prelim/194_prel/194PREL.PDF.

Qi, J. and Q. Yang, 2010, Cenozoic structural deformation and dynamic processes of the Bohai Bay basin province, China: Marine and Petroleum Geology 27 (2010) 757-771.

Ren, J., K. Tamaki, S. Li, and J. Zhang, 2002, Late Mesozoic and Cenozoic rifting and its dynamic setting in Eastern China and adjacent areas: Techonophysics 344 (2002) 175-205.

Russell, B.H., 1988, Introduction to seismic inversion methods: Society of Exploration Geophysicists.

Sun, Y.F., 2000, Core-log-seismic integration in hemipelagic marine sediments on the eastern flank of the Juan De Fuca Ridge: ODP Scientific Results, 168, 21-35.

Sun, Y. F., 2001, Pore structure effects on velocity-porosity relationship in carbonates, Shell International Exploration and Production B.V., The Hague, the Netherlands, EP 2001-5092.

Sun, Y.F., C.X. Ren, L.C. Li, H.T. Lu, L.L. Yan, 2003, Problems of high-resolution analysis and interpretation in Junggar Basin: Case studies: 2003 SEG Annual Meeting, 26-31 October, Dallas, Texas, US.

Sun, Y.F., 2004, Effects of pore structure on elastic wave propagation in rocks, AVO modeling: Journal of Geophysics and Engineering, 1, 268-276.

Sun, Y.F., 2007, Upscaling of a proxy parameter for pore structure in sedimentary rocks: 2007 SEG Annual Meeting, 23-28 September, San Antonio, Texas, US.

Sun, Y.F., H. Zhang, Q. Dou, T. Zhang and T. Guo, 2011; Geological and GeophysicalCharacteristics of the Ultra-Deep High-Porosity Carbonate Gas

Reservoir, Puguang Gas Field, Sichuan Basin, China: I.Petrophysical Study: AAPG 2011 Annual Convention & Exhibition, Houston, US; 10-13 April 2011.

Wang L., and Q. Zhu, 2003, Reservoir prediction research on Daxing subtle conglomeratic reservoir in Langgu Sag: Computing Techniques for Geophysical and Geochemical Exploration, 25(4):308-311.

Weger R.J., G.P. Eberli, G.T. Baechle, J.L. Massaferro and Y.-F. Sun, 2009, Quantification of pore structure and its effect on sonic velocity and permeability in carbonates: AAPG bulletin, V. 93, No. 10, PP. 1297-1317.

Widess, M.B., 1973, How thin is a thin bed: Geophysics, 38, 1176-1180.

Wood, A. W., 1955. A Textbook of Sound. New York: McMillan Co.

Xu, S., and M.A. Payne, 2009, Modelling elastic properties in carbonate rocks: The Leading Edge, 28, 66-74.

Zha Q., 1984, Jizhong Depression, China—its geologic framework, evolutionary history, and distribution of hydrocarbons: AAPG bulletin, V. 68, P. 983-992.

Zhai G. and Q. Zha, 1981, Buried-hill oil and gas pools in the North China Basin: AAPG Mem., vol. 32, p.317-335.

Zhang, H., Y.F. Sun, Q. Dou, T. Zhang, 2012, Preliminary application of the frame flexibility factor in Puguang gas field, Oil & Gas Geology, Vol. 33, 877-882.

Zhang, T., Q. Dou, Y.F. Sun, and H. Zhang, 2012, Improving porosity-velocity relations using carbonate pore types: SEG 2012 Annual Meeting; 4-9 Nov. 2012.

Zhao, X., F. Jin, Z. Cui, C. Han, J. Zeng, Q. Wang, and K. Guo, 2012, Types of subtle buried-hill oil reservoirs and their accumulation simulation in Jizhong Depression, Bohai Bay basin: Petroleum Exploration and Development, Vol. 39, No. 2, P.137-143.

Zhu, F., H. Najwani, J. Harris, T. Ma'Mary, 2012, Seismic tuning helps predicting thin-sand reservoirs-X channels of the Z field, Oman: 10th Middle East Geosciences Conference and Exhibition, Manama, Bahrain, AAPG Search and Discovery Article #90141, 4-7.

APPENDIX

IDENTIFICATION OF THIN GAS-BEARING BEDS IN AN ULTRA-DEEP CARBONATE RESERVOIR THROUGH HIGH-RESOLUTION SEISMIC INVERSION

Summary

The Puguang gas field, with a depth greater than 5km, is one of the deepest carbonate gas reservoirs discovered in Sichuan Basin, China. One of the most important features of this field is that there exists both high porosity (10-28%) and permeability (up to 3300 mD), but very thin-bedded reservoir units of about 4-10 m consisting of sucrosic dolomite. The detailed spatial distribution and geological origin of such thin, high-porosity beds at such great depths is still not well understood with current seismic technologies. This study reports preliminary results of the fine-structure of the thin bedded reservoirs obtained using high-resolution seismic impedance inversion.

Resolution-enhanced seismic data reveals both vertical and lateral high-frequency lithology changes better than conventional seismic. The observation of a transgressive process at the beginning of the Lower Triassic Formation can be clearly interpreted as a relative sea level rise. Overall, synthetic seismogram with a band-pass wavelet (5-10-110-120 Hz) has a good correlation with high-resolution seismic data in accordance with the high-frequency stratigraphy. Within a thick gas reservoir zone of about 300 m, more than three thin, high-porosity, high-permeability gas-bearing beds, characterized by low density and low P-wave velocity, are identified on both synthetic

and high-resolution seismic data but not on conventional seismic data. Thus, one typical feature of high-porosity, high-permeability gas beds of sucrosic dolomite is their low p-impedance value. On the other hand, oolitic dolomite beds have high p-impedance, low permeability (less than 1mD), with similar porosity. Analysis of the high-resolution seismic inversion result demonstrates that porous gas-bearing beds are well connected horizontally but vertically barricaded by non-porous beds, controlled by depositional environment, diagenesis, and paleohydrology. Further investigation could implement the high-resolution seismic inversion result to interpret the flow direction of the paleo-current and map carbonate reservoir heterogeneity for production monitoring.

Introduction

Hydrocarbon exploration has entered a new and challenging era. More focuses are now on prospecting for potential hydrocarbon reservoirs in remote, deep frontier basins with complex structures or thin beds (Chopra, 2006; Zhu, 2012). The identification of hydrocarbon-bearing thin beds has remained a difficult task for many decades. According to Widess (1970), the thinnest bed that can be identified by conventional seismic data is $\lambda/8$. As an example, consider a 5000m-deep dolomite reservoir. Suppose the seismic frequency is 25 Hz or less at reservoir depth and the average sonic velocity is 6 km/s, the thinnest bed discernible by seismic data is approximately 30 meters. Thus identifying hydrocarbon beds thinner than 30 meters becomes an important challenge not only for hydrocarbon field exploration but also for hydrocarbon field development.

The studied ultra-deep gas reservoir is located in the Sichuan Basin of China. According to Ma (2009), gas is contained in the Lower Triassic and the Upper Permian formations, which consist predominantly of dolomitized oolites deposited in shelf and platform-margin shoal and back reef environments. The thickness of the main gas reservoir in the Lower Triassic Formation can be as great as 329 meters (Ma, 2009), consisting of a vertical assemblage of multiple gas beds partitioned by low porosity limestone. In this paper, we investigate the best way to delineate these thin gas-bearing beds by combining high-resolution enhancement of poststack seismic data with model-based impedance inversion.

Method

The high-resolution enhancement method proposed by Sun et al. (2003) is first used to improve the seismic resolution of the studied dataset. This method is derived from a plane-wave solution of poro-viscoelasticity based on a neural network implementation of solving a Volterra integral equation of the first kind. Two key aspects are the physical wavelet and deterministic approach. The physical wavelet takes into account the dramatic decrease of the high-frequency component in seismic waves with increasing travel distance, caused by the influence of viscoelatic properties of rocks on seismic wave propagation. The deterministic approach integrates four functions including reflectivity function, dominant frequency, quality factor, and rock porosity. This method has been applied to a synthetic theoretical model, a geological model and 3D seismic data with good results.

Second, both a low-resolution and a high-resolution 2D earth model are built using log data from two wells. Conventional and high-resolution enhanced seismic data are compared with synthetic seismograms at the well locations to identify accurately the thin gas-bearing beds.

Third, model-based impedance inversion is then performed (Russell, 1988). In order to determine what controls the final resolution of seismic inversion, we devise three types of inversions: Conventional seismic data combined with high-resolution forward earth model; High-resolution enhanced seismic data combined with low-resolution forward earth model; and high-resolution enhanced seismic data combined with high-resolution forward earth model.

Data Analysis and Results

The studied carbonate gas reservoir has a depth of about 5000 meters. The conventional seismic data at this depth has a dominant frequency of about 15 Hz. Such low-resolution seismic data makes it difficult to identify the targeted thin gas-bearing beds. Compared to conventional seismic data, high-resolution seismic data reveals more geological information (Figure 1). At the location of the two red arrows, the high-resolution seismic data has five reflections while the conventional seismic shows only two. Moreover, it is difficult to perform high-frequency cycle interpretation within sequence boundaries T1f1 and T1f4 using the low-resolution seismic data. However, as indicated by four yellow arrows, a progradational process is evident on the high-resolution enhanced seismic section, which correlates well with the water level increase

at the beginning of the Lower Triassic Formation. Thus high-resolution enhanced seismic data enables us obtain important information on high-frequency cycles and predict high-quality gas-bearing beds within reservoirs that usually have more dolomite content and higher permeability.

The synthetic seismogram of Well A shows a good correlation with the conventional seismic data (Figure 2a). The wavelet used is a Ricker wavelet with a

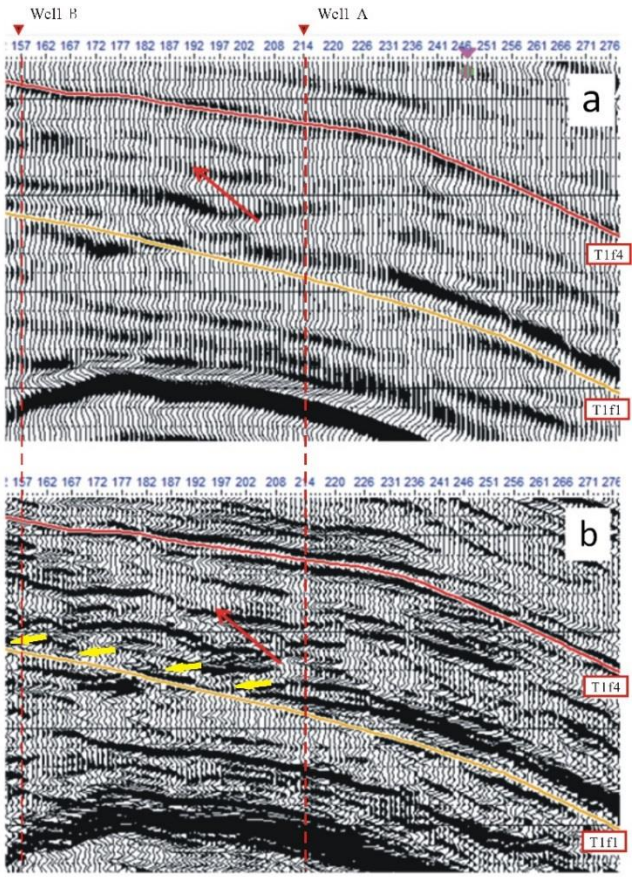

Figure 1. a) Conventional seismic profile through Well A and Well B. b) High-resolution seismic profile of the same location. Dashed red lines indicate well locations. Well A is used to build forward models only.

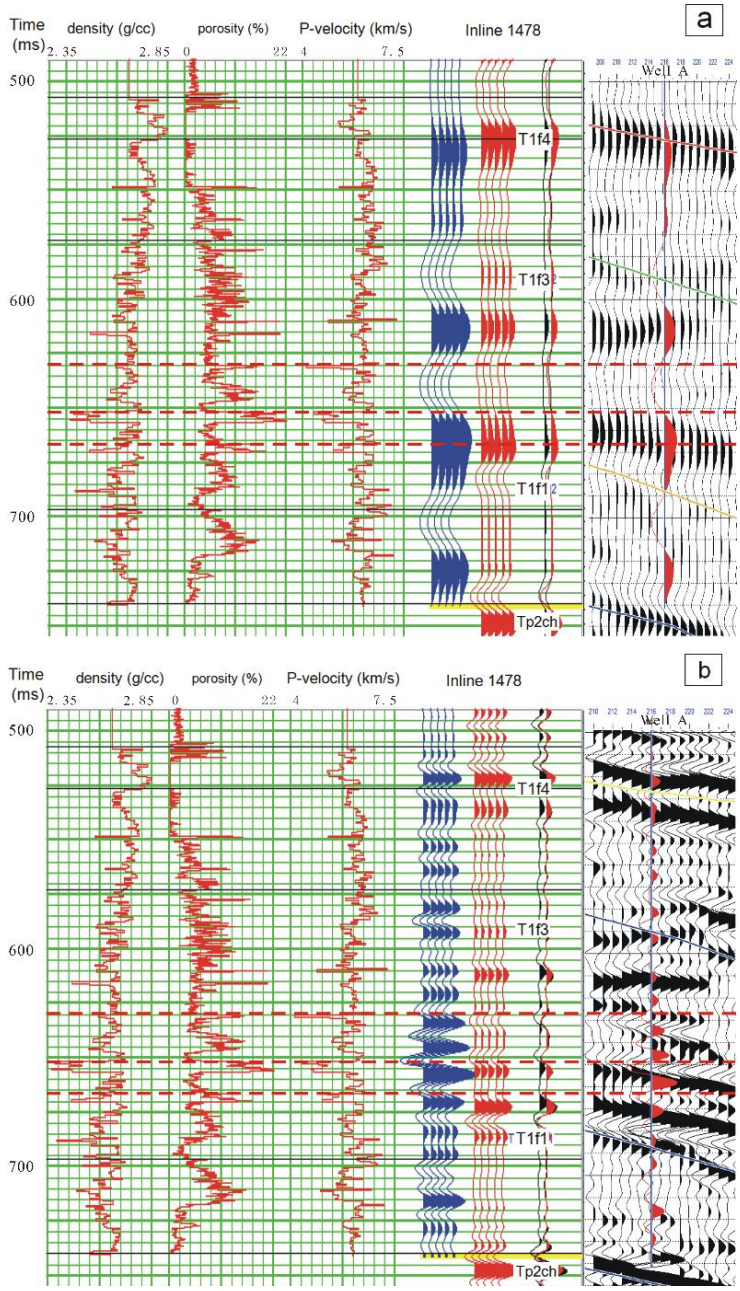

Figure 2. a) Synthetic seismogram of Well A with 15 Hz Ricker wavelet. Right panel shows the conventional seimic. b) Synethci seismogram of Well A with band-pass wavelet (10-15-110-120 Hz). Right panel shows high-resolution seismic data.

central frequency of 15 Hz. This correlation demonstrates that the frequency of conventional seismic at reservoir depth is only 15 Hz. Well A has a thick gas reservoir

from approximately 550 ms to 700 ms (time is relative) (Figure 2). Within the gas reservoir, several layers of gas beds can be identified from log curves (low density, low P-velocity and high porosity). Three dashed red lines represent the tops of three thin gas beds among others. Whereas, the examination of the conventional seismic data shows no indication of these three gas beds. By using a band-pass wavelet (5-10-110-120 Hz), the synthetic seismogram of Well A (Figure 2b) also has a good correlation with the high-resolution seismic data. Notice that the tops of the three thin gas beds point to the wave troughs on the high-resolution seismic profile on the right side of the figure. Of these three beds, the thinnest (the top one) is about 4-meter thick.

To demonstrate impact of high-resolution enhancement seismic data on seismic inversion, we test three scenarios shown in Figure 3. Model A (a in Figure 3) is built with conventional seismic and high-resolution logging data with a blocking size of 2 ms. Model B (b in Figure 3) is built based on high-resolution seismic and low-resolution logging data with a blocking size of 10 ms. Model C (c in Figure 3) is built on high-resolution seismic and high-resolution logging data with a blocking size of 2 ms. Figure 4 shows the inversion results for model A, B, and C. The green color represents low acoustic impedance, which is interpreted to be gas beds. Although model A has high resolution forward earth model, its inversion result (Figure 4a) still shows low resolution vertically and laterally. However, the inversion result (Figure 4b) of the low-resolution forward earth model with high-resolution enhanced seismic data has a much higher resolution. Furthermore, the inversion result B and C (Figure 4b and 4c) have more

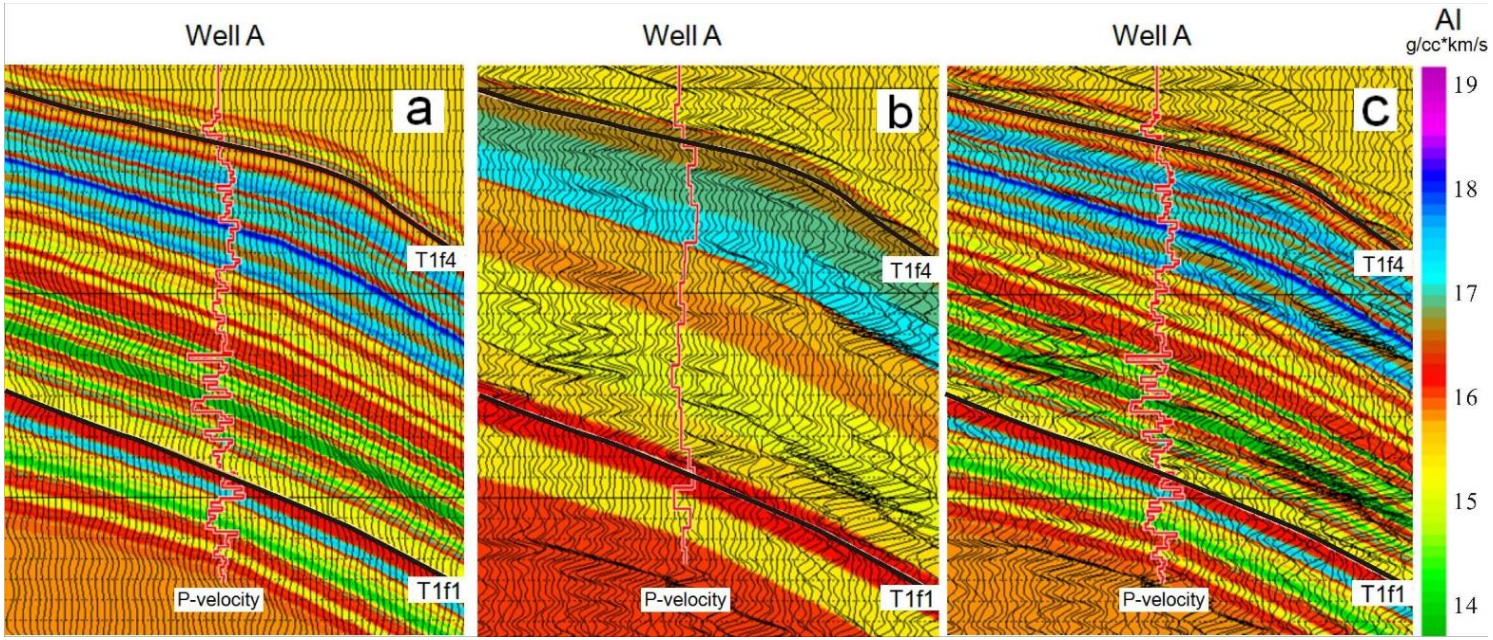

Figure 3. Forward models for inversion: a) model A is built with conventional seismic data and high-resolution logging data (sampling rate: 2 ms); b) model B is built with high-resolution seismic data and low-resolution logging data (sampling rate: 10 ms); c) model C is buit with high-resolution seismic data and high-resolution loging data (sampling rate: 2ms). The inserted log curve is P-velocity.

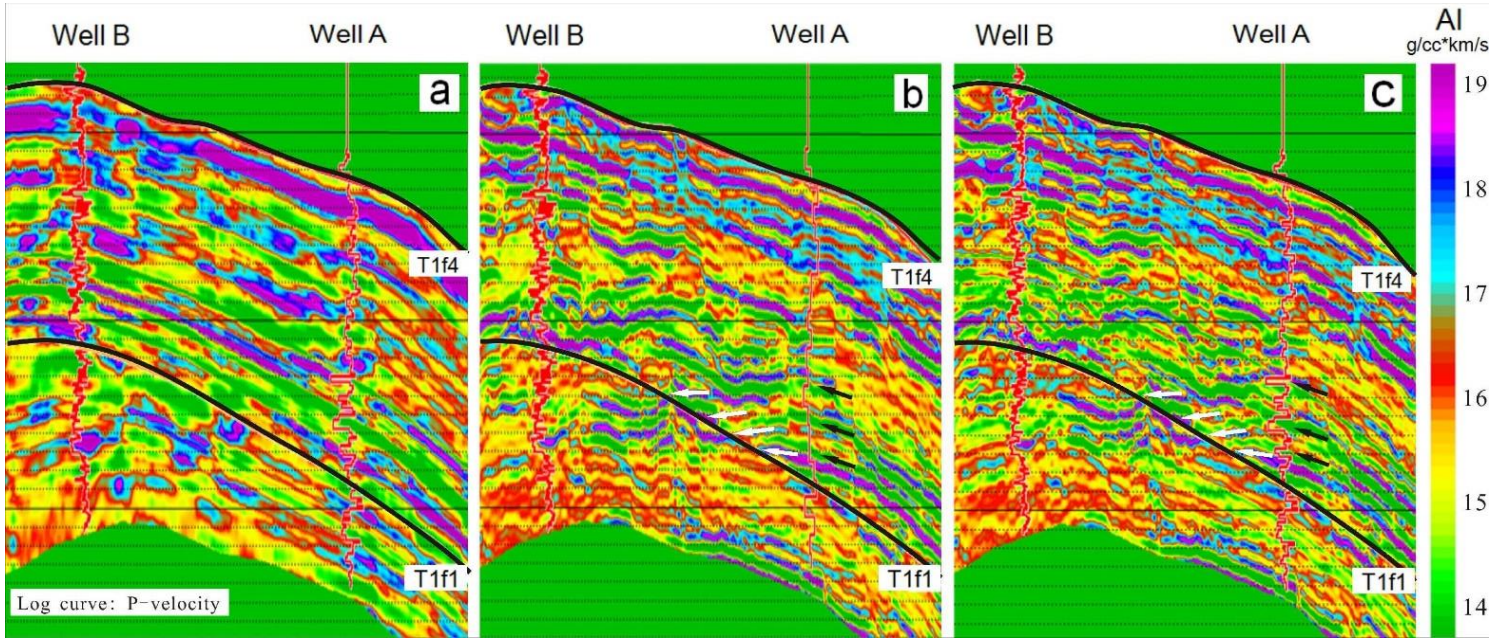

Figure 4. Acoustic impedance inversion results: a) inversion result with model A in Figure 3a; b) inversion result with model B in Figure 3b; c) inversion result with model C in Figure 3c. The inserted log curve is P-velocity.

similarities. Comparatively, the high-resolution logging data used to build the forward earth model C does not contribute much to the inversion result.

Figure 4b and Figure 4c have three black arrows respectively pointing to the three thin beds in Figure 2. Careful examination indicates that Figure 4c clearly shows three beds while Figure 4b does not. Thus, when the seismic data and logging data have similar high resolution, thinner beds are more easily identified.

Vertically, the high-resolution seismic inversion method gives a much better result for multiple thin beds than does conventional seismic inversion. Can high-resolution seismic inversion produce reasonable result laterally? At the location of the test well, Well B, most green colors correspond well with gas beds featured by low P-velocity. Thus the lateral distributions of all beds are reasonable and determined by the depositional process. Compared to Figure 1, the high-resolution inversion results (Figure 4b and 4c) show a much clearer progradational process at the beginning of the Lower Triassic Formation. Therefore, high-resolution seismic inversion can be of great help in interpreting high-resolution seismic data.

Conclusions and remarks

High-resolution seismic data contains much more information about bedding and high-frequency cycles. Successful application of high-resolution enhancement method helps in delineating high quality hydrocarbon beds within current reservoirs and exploring new hydrocarbon fields.

Seismic inversion on conventional and high-resolution seismic data reveals that it is the high-resolution seismic data itself that is the key factor in obtaining high-resolution inversion results. High-resolution logging data and high-resolution forward model have no or limited control on this.